Design of a Multiloop Pyroelectric Neutron Generator Control System

Alice Margaret Darbyshire

Department of Engineering
University of Cambridge

This dissertation is submitted for the degree of
Doctor of Philosophy

Jesus College August 2019

To Pamela, Ian and David.

Declaration

This thesis is the result of my own work and includes nothing which is the outcome of work done in collaboration except as declared in the Preface and specified in the text. It is not substantially the same as any that I have submitted, or, is being concurrently submitted for a degree or diploma or other qualification at the University of Cambridge or any other University or similar institution except as declared in the Preface and specified in the text. I further state that no substantial part of my thesis has already been submitted, or, is being concurrently submitted for any such degree, diploma or other qualification at the University of Cambridge or any other University or similar institution except as declared in the Preface and specified in the text. It does not exceed the prescribed word limit for the relevant Degree Committee.

Alice Margaret Darbyshire
August 2019

As in most academic efforts, there is a team of people behind the research presented here. The major supporters, who have participated in the analytical, planning, data interpretation and reporting phases, include:

My supervisor, Dr Geoff Parks of the University of Cambridge; the report has been substantially improved by the incorporation of many suggestions due to his extremely careful review.

My advisor, Dr Kirk Atkinson, a former member of the Nuclear Faculty, now with the University of Ontario Institute of Technology; his continuous support and encouragement has contributed to the development of this research over the last seven years.

My line manager, Dr Simon Jewer of the Nuclear Faculty, has been instrumental in facilitating the successful scheduling of this research.

Professor Malcolm Smith of the University of Cambridge has contributed to many useful discussions on the dynamics and control of the pyroelectric neutron generator.

Dr Tomas Bily and Dr Lubomir Sklenka of the Department of Nuclear Reactors, at the Czech Technical University, who have contributed to the experimental program and discussions regarding nuclear reactor applications.

I also wish to express my gratitude to Dr David Garrity of STS Defence whose steadfast support over the last couple of years was greatly needed and deeply appreciated.

And finally, last but by no means least, special thanks to my co-workers at the Nuclear Faculty, who I did not mention explicitly; particularly to those who are on the same doctoral path, and to those who have preceded us, for their moral support. It has been a privilege to have had the opportunity to conduct my research alongside you all.

Abstract

Design of a Multiloop Pyroelectric Neutron Generator Control System

Pyroelectric neutron generators are compact, low power systems which may be capable of producing short intense pulses of neutrons from D-D fusion reactions. Initial analysis of pyrofusion dynamics has indicated the potential to manipulate the pulse characteristics through system control. This thesis presents the development of novel pyroelectric neutron generator dynamics models in MATLAB/Simulink that can be used to support the predictability and control of the neutron pulse.

Plant models have been developed using two control system modelling approaches: lumped-parameter and system identification modelling. Describing equations for the pyroelectric subsystem components are detailed and implemented using lumped-parameter modelling. Novel work towards the analysis of the pyroelectric subsystem responses, stability and performance using control system techniques is presented. Frequency-domain studies, stability analysis and time-domain simulations are reported.

The dynamic characteristics of pyroelectric neutron generators have indicated that they could be effective neutron sources for nuclear reactor plants. The development of a prototype pyroelectric neutron source for the purpose of system identification is reported. Plans to progress the work are discussed, including validation against data collected through experiments at an actual zero-power reactor.

The key research areas are: pyroelectric neutron generation; thermoelectric cooler modelling; control system modelling; and controller design.

Alice Margaret Darbyshire

Table of contents

List of figures

List of tables

Chapter 1

Introduction and background to pyroelectric neutron generation

1.1 Project background and purpose

The genesis of this research was the requirement to understand and accurately predict pyroelectric neutron generator dynamics and control. Our approach to this task is constructed upon two bases. The first is an indication of what is known about the actuation of pyroelectric neutron generation; and the second is understanding how the device could behave as a dynamic control component both on the bench, and in nuclear reactor applications.

Since the first publication in 2005 [74], experimental results of various existing pyroelectric neutron generator devices have been reported [20, 23, 24, 28, 31, 36, 42–44, 62, 95]; however, these are only reports of specific test results, and most of the published data are non-transient. It is difficult to extrapolate to new situations, novel device characteristics or applications. The quality of some of these data have been open to question because of the lack of repeatability. Nevertheless, some suitable experimental techniques have been derived and employed in the past to provide us with a limited amount of data.

The history of pyroelectric neutron generation has indicated that these devices are potentially controllable, non-radioactive sources, capable of producing sufficient neutron flux, of around 10^6 n/s [74], for nuclear reactor applications. Their modular design and possible controllability could have distinct advantages, including added flexibility [90] when optimizing neutron flux profiles in the core. Pyroelectric sources have the potential to be geometrically scaled [74] to fit inside the channels of reactor cores and could be dynamically advantageous

sources.

The main advantage of pyroelectric neutron generators for application in nuclear reactors is their potential controllability: the source can be switched on and off, which could allow for operation in a pulsed mode with control over the repetition rate and duration, leading to interesting dynamics in the reactor core. However, to be utilised effectively and safely in a nuclear reactor their dynamical characteristics must be well understood and controlled. With the long history of research from pyroelectric x-ray sources through to neutron sources, there has, to date, been no control system modelling or dynamic analysis of the pyroelectric neutron source, or consideration of the potential effect of such a source(s) on a live nuclear reactor.

It is hoped that, with the knowledge gained from the application of conventional control engineering techniques, we could evaluate the feasibility of the potential use of a pyroelectric neutron generator as a repetitive pulsed neutron source. We could understand what further is needed, and where we go from here.

The work towards our research goals was initiated, on a part-time basis, in October 2012. Almost four years was spent: reviewing the past literature; considering the experiments carried out by previous investigators; designing various control engineering models; developing system identification techniques using the existing experimental data; and considering the potential effects of pyroelectric neutron sources on nuclear reactor dynamics.

In 2017, we reported the first application of a control theory approach to the modelling of pyroelectric neutron sources and presented our initial results [26, 27]. The model was deemed to be serviceable, and the potential uses of this model heightened the desire for a more complete understanding of the mathematically describable aspects of pyroelectric dynamics, and the development of a suitable control system. Over the next two years, we significantly extended our preliminary model with a more presentable mathematical theory; we improved our parameter estimation using empirical data, and carried out substantial model validation. The results of these efforts are reported in the following chapters.

1.1.1 Outline of the thesis

The primary objective of this research is to develop mathematical descriptions for pyroelectric neutron generator characteristics as components in an engineering system.

Chapter 2 discusses the development and current status of the VR-1 experimental program.

Chapter 3 examines, in detail, the dynamic modelling of a thermoelectric cooler (TEC) with the intent to use it as an actuator for the pyroelectric effect. We consider the mathematical theory and compare our model to empirical data.

Chapter 4 starts with a single-loop system for TEC control system design, and updates the model with pyroelectric neutron generator materials, geometries and thermal masses.

Chapter 5 describes the design of an inner loop control system for pyroelectric crystal temperature control.

Chapter 6 extends the model to incorporate the pyroelectric effect and neutron generation. The system dynamics are analysed and the model is validated against empirical data for a specific case. The model presented in this chapter represents the most elaborate dynamic model of a pyroelectric neutron generator, to date.

Chapter 7 considers a multiloop control system design for a pyroelectric device, and discusses the potential controllability of the neutron generation. The chapter ends with a consideration of the effects of repetitively pulsing the pyroelectric neutron source in a zero-energy reactor (ZER), specifically the VR-1 training reactor at the Czech Technical University, in Prague.

Chapter 8 critiques the developed models, and lists the deficiencies, thereby defining the shortcomings and problem areas. Some attempt is made to make this critique constructive by noting, where available, analytic or other approaches which might be adopted to alleviate the shortcomings.

1.2 General nature of the pyroelectric model

The intent of this section is to introduce the basic concepts and phenomena of pyroelectric neutron generation in a primarily descriptive and intuitively understandable manner. The really essential portion of this work is understanding the physical processes that are involved in pyroelectric neutron generation. The lumped-parameter model of the pyroelectric plant

comprises several components, and processes, including: a heater which is driven by a current input to a particular temperature; heat transfer through the crystal altering the surface temperature; a resultant change in electrostatics giving rise to an acceleration potential, which in turn ionises deuterium and accelerates the ions into a target, resulting in a neutron yield.

Figure 1.1 shows a functional block diagram of the main processes involved in pyroelectric neutron generation (the blue blocks). The green blocks show our potential multiloop control system. The system forcing function is a desired neutron output from the device; this can be either a step, pulse or sine-wave based input. The inner control loop drives the crystal temperature by controlling the current applied to the TEC. The outer control loop calculates the difference between the system forcing function and the system output. Typically, the controller's task is to minimise the error signal by trying to keep it matching a set-point. This is accomplished by manipulative control action, which affects the controlled element and gives rise to the system output being controlled. The usual purpose of a system of this nature is to make the system output closely resemble the system forcing function, or, in other words, to make the output follow the input.

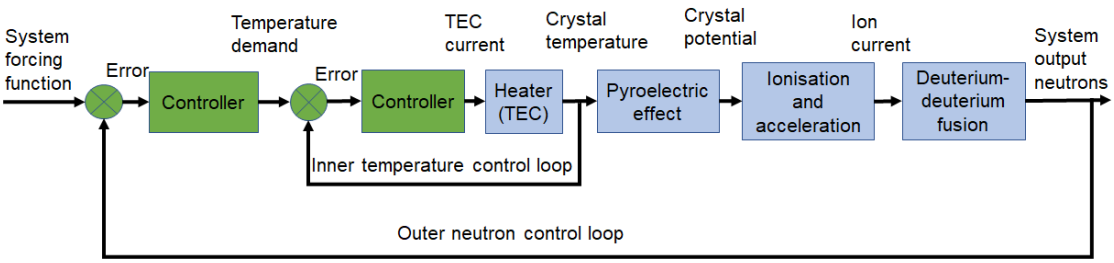

Fig. 1.1 Functional block diagram of processes (blue blocks) in pyroelectric neutron generation and a potential multiloop control system (green blocks).

1.2.1 A control engineering approach

Engineering models comprise analytical descriptions of the phenomenon of interest, expressed such that the key variables are explicit, and both the ranges and rules of application are well defined. Such models should be capable of being validated, augmented or disproved by independent researchers. As predictive tools, they should serve several purposes, including:

1. Estimation or prediction of pyroelectric neutron generator dynamics.

2. Characterisation of past experimental observations with simple analytical forms.

3. Quantitatively describing the connections between model parameters.

A control system approach to modelling the pyroelectric neutron generator system (or the *plant*) will be followed; for each element, a mathematical description will need to be established, working with the physically verified mathematical laws which describe the system's behaviour. There are several good texts and handbooks that describe the various control engineering techniques we will employ in our investigations [9, 10, 30, 34, 64, 77, 97].

It is usual to analyse an idealised equivalent of the physical system in which each element has a single property or function. Considering an idealised system has the advantage that each element has only one independent variable (time) and the system can be described using an ordinary differential equation model. This technique is commonly known as *lumped-parameter modelling*. Block diagrams can be used to represent the Laplace transform equations of the plant. The techniques used in block diagrams are useful as they can be extended to include control equipment and associated feedback paths.

Stability can be tested by examining the linear equations describing the system. A complementary function can result as part of the solution of ordinary, linear differential equations. In control engineering, this complementary function becomes the *characteristic equation*. The characteristic equation, which characterises the system's dynamics, can be determined from a study of the transfer function. A transfer function model is usually obtained from the linear differential equations representing a lumped-parameter model.

The experiments that have been previously undertaken by investigators can provide data that is suitable for developing the open-loop models of the processes (i.e. with no controller feedback). The plant open-loop stability can be examined by applying a bounded input to the system (such as a step, saturated ramp, or sinusoidal signal) and observing the nature of the response; this is called a Bounded-Input-Bounded-Output (BIBO) stability investigation.

As the models develop and further knowledge of the systems is acquired through their analysis, several aspects of control engineering will be required. These have been mapped in Fig. 1.2. The processes by which the model of the system may be developed and the methods by which the controller may be designed are shown contained in the blue boxes. The purple boxes represent alternative aspects that may become necessary as the work develops; for example, following initial modelling, it is known that the pyroelectric plant is nonlinear and

it is anticipated that nonlinear control methods will be required. The green boxes contain a range of methods and techniques of control theory that have potential use in the analysis and design. Orange boxes identify key designer inputs that are required.

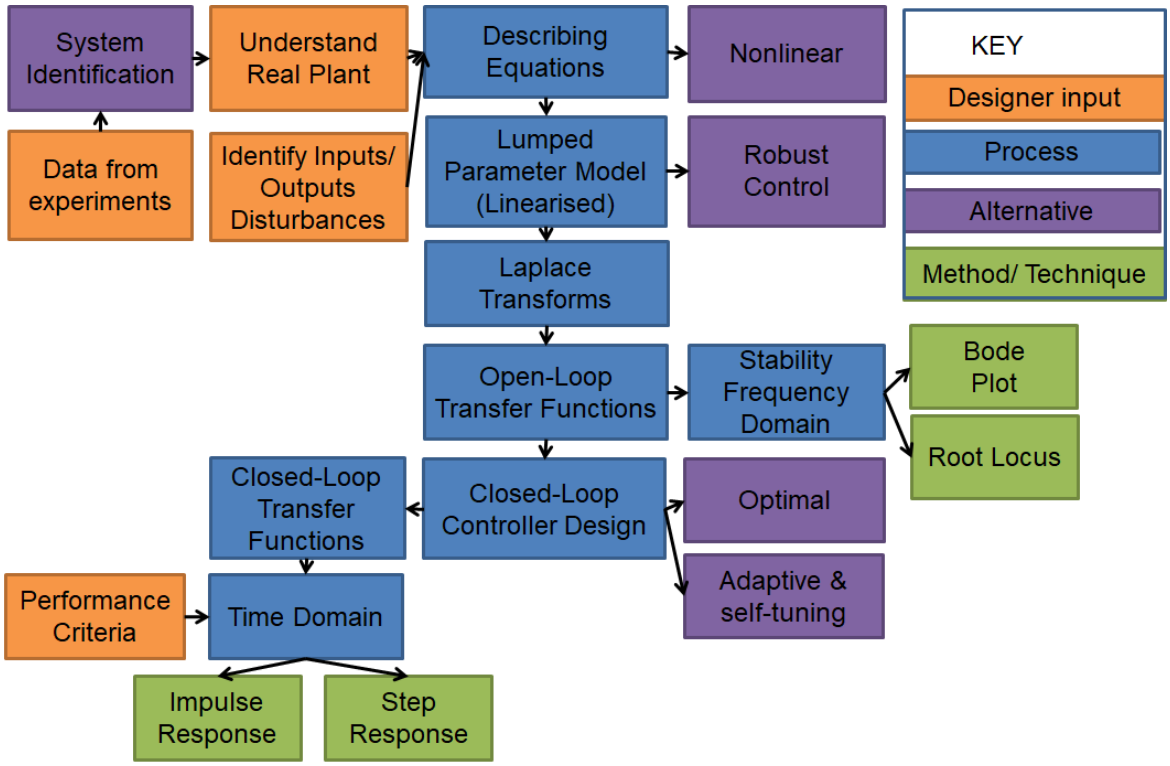

Fig. 1.2 Flow chart showing the process of control engineering.

As shown in Fig. 1.1, we anticipate that two controllers will be required for accurate and safe pyroelectric neutron generation. One in the inner loop to control crystal temperature, and an outer loop controller for neutron generation. Proportional-plus-integral-plus-derivative (PID) -type controllers are commonly used in industry, and in 1942 John 'Zeke' Ziegler and Nathaniel Nichols developed the popular Ziegler-Nichols tuning method [30, 34, 77]. Their manual tuning method has made the PID algorithm the most popular feedback control strategy to be used in industrial applications today [32, 64, 97]. In the 1970's, as PID controllers evolved from electronic and pneumatic devices into fully digital microprocessors, programmers automated the Ziegler-Nichols loop tuning techniques [87].

In the 1980's, Karl Astrom and Tore Hagglund of the Lund Institute of Technology in Sweden [5–7, 49] cited the lack of robustness of methods such as the Ziegler-Nichols tuning method as the reason for many poorly tuned industrial regulators in practice. They

published automated versions of the Ziegler-Nichols closed-loop tuning method. All of the methods forced the process variable into a series of oscillations, known as a limit cycle [10]. The period (time for a single oscillation) and the ultimate gain of the system are calculated from the oscillations. These two parameters are then used instead of the steady-state gain, time constant and deadtime to compute suitable tuning parameters. Variations on the relay method have become standard for commercial auto-tuning controllers, though vendors (such as MathWorks) do not mention which technology they use [32].

In 1966, Gotoh [46] analysed the frequency response of an ionisation chamber. He calculated the break frequency (or corner frequency) of the ionisation chamber, and reported that it was determined by the transit time of positive ions and the applied voltage, and that it could be represented by a first-order lag. We can follow a similar method for developing a transfer function model of a pyroelectric generator, and apply appropriate formulae and standard parameters [71].

We will use the MathWorks [65] tools MATLAB and Simulink to analyse published data, create our engineering models, simulate control algorithms and visualise the results. MATLAB is professionally developed, rigorously tested and fully documented. Simulink is a block diagram environment that supports Model-Based Design for ease of simulation. We can make use of the pre-built functions for analyzing overshoot, rise time, phase margin, gain margin, and other performance and stability characteristics in the time and frequency domains. Root locus and Bode diagrams can be constructed for design and analysis. We can also take advantage of the available automatic tuning features for our controllers.

The application of control design procedures in the frequency domain and the Laplace transform model to investigate the stability and performance of the pyroelectric neutron source plant is a novel approach.

1.2.2 The pyroelectric crystal heater

The change in temperature of a pyroelectric crystal is essentially the actuation mechanism that is responsible for the pyroelectric phenomenon in the device. The most common methods for changing the temperature of a pyroelectric crystal are a resistance heater [74] or a thermoelectric cooler [45]. We will need the ability to simulate thermally cycling our crystal, therefore a TEC with its capability to both heat and cool would be the best option. Figure 1.3 shows a schematic diagram of a typical TEC and a general purpose thermoelectric module. A TEC consists of several pairs of thermoelectric elements which can be used to heat a

pyroelectric crystal. When current flows through a TEC device heat is pumped from one side to the other, so that one side gets cooler while the other simultaneously gets hotter.

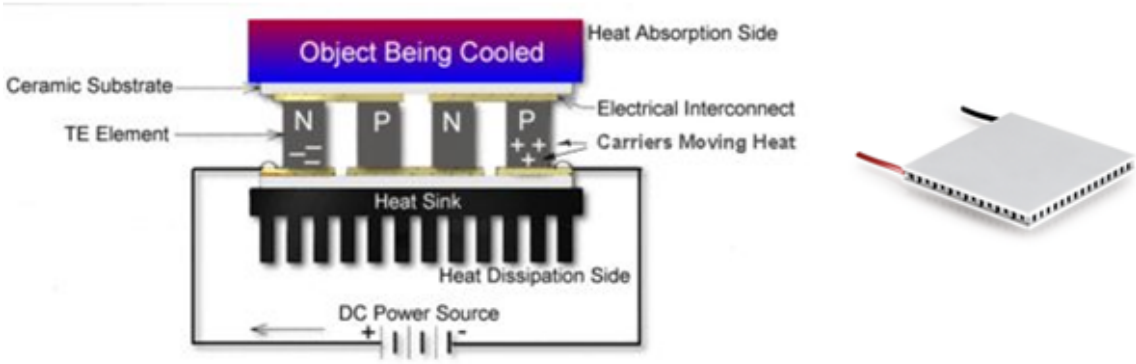

Fig. 1.3 Schematic diagram of a typical thermoelectric cooler and a general purpose thermoelectric module (right) [93].

In 1960, Gray [47] investigated the nonlinear dynamic behaviour of thermoelectric heat pumps and generators. He also performed the first known small-signal analysis and derivation of the linear TEC transfer function. This derivation found application in 1962, by Anderson [2] who performed an analysis, design, and experimental development of a thermoelectric air conditioner for use on submarines. He concluded that the well-known basic relations were a convenient form to explore the performance characteristics and control aspects of a thermoelectric refrigerator. In 1970, Bywaters and Blum [18] successfully applied a similar method when they focused their research on the transient behaviour of cascaded TECs.

In 2000, Huang and Duang [50, 51] developed a linear dynamic model of a TEC including the heat sink and the cooling-load heat exchanger and compared their results to estimated models derived using system identification techniques. Several researchers have applied the transfer function developed by Huang and Duang with varying success [73, 86]. A major part of our model development is to capture the dominant thermal dynamics which actuate our pyroelectric device. The data that is available in the publication by Huang and Duang [50] will be useful for the development, and parameter estimation, of our pyroelectric TEC model in Chapter 3.

1.2.3 The pyroelectric effect

The pyroelectric effect has been observed in various materials (such as tourmaline), and several scientists have studied the phenomenon over the last 24 centuries. Two comprehensive

review articles, written by Whatmore [100] and Lang [62], discuss the history of pyroelectricity, and provide a detailed review of developments, from the earliest known account written by the Greek philosopher Theophrastus in 314 B.C., to David Brewster, who in 1821 was the first author to use the term "pyroelectricity". However, it was John Mothée Gaugain who made the first precise measurements of pyroelectric charges in 1859; he discovered that the total quantity of electricity produced by a crystal of tourmaline depends uniquely upon the limits within which its temperature is varied; within those limits, the amount of electricity produced during heating is the same as that produced during cooling, but with the signs of the charges reversed.

Figure 1.4 shows a triangle diagram that illustrates the thermodynamically reversible interactions that may occur among the thermal, mechanical and electrical properties of a crystal. In 1972, Byer and Roundy [17] developed a direct method for measuring pyroelectric coefficients, and showed that it was possible to accurately measure pyroelectric coefficients for various crystals.

Lithium tantalate (known as $LiTaO_3$, or LT) and lithium niobate ($LiNbO_3$) are pyroelectric crystals that are commonly used in pyroelectric neutron generator experiments. Figure 1.4 shows an example of cylindrical z-cut LT crystal and Table 1.1 shows the similarities between the fundamental thermal and pyroelectric properties of LT and $LiNbO_3$ [80]. Both crystals can grown by the Czochralski method [98] which yields large, high-quality single crystals. The crystals can be manufactured in a cylindrical shape and cut such that the polarization z-axis is perpendicular to its flat faces.

Crystal	Melting point °C	Curie temperature °C	Heat capacity J/kmol	Thermal conductivity W/mK	Pyroelectric coefficient $\mu C/m^2$
Lithium tantalate	1650	605	100	4.6	∼190
Lithium niobate	1253	1133	89	4	∼140

Table 1.1 Fundamental properties of LT and lithium niobate [80].

Pyroelectric crystals, such as LT, are anisotropic dielectric (electrically non-conducting) materials that are spontaneously polarised at equilibrium conditions; that is, they have a built-in, or permanent, electric polarisation (dipole moment per unit volume) with no applied temperature gradient or electric field. When the crystal is held at constant temperature, the polarization is compensated by free charge carriers that have reached the surface of the crystal by conduction through the crystal and from the surroundings; under these equilibrium

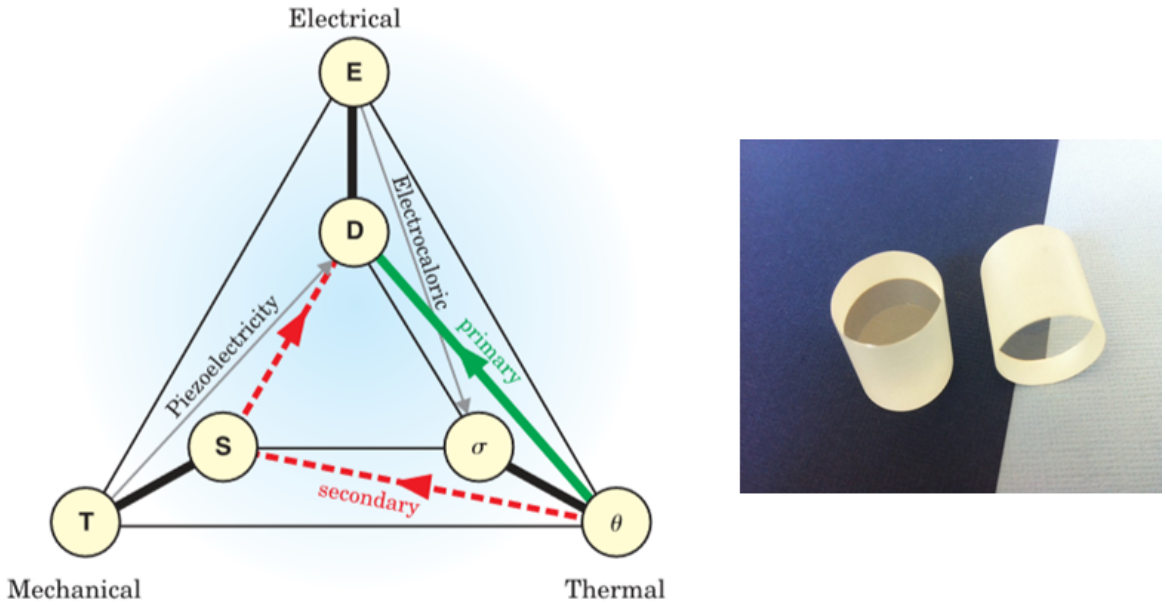

Fig. 1.4 Left: Triangle diagram illustrating the coupled effects of pyroelectricity in a crystal, and Right: An example of a cylindrical z-cut LT crystal (diameter 20 mm, length 20 mm), manufactured by Del Mar Photonics [53].

conditions the polarisation is screened, which prevents the observation of any electrical properties. When LT crystals are subjected to a uniform temperature change, the oxygen, lithium and tantalum ions are displaced within the LT cell; as a result, the crystals become depolarised. The spontaneous polarisation cycle for a pyroelectric crystal is shown in Fig. 1.5. The change in spontaneous polarisation is known as the pyroelectric effect, and it only occurs in crystals which lack a centre of symmetry and also have a polar axis (a so-called z-axis) [15].

In 2001, Brownridge [14] conducted a series of experiments and concluded that, at a given temperature, $LiNbO_3$ and LT crystals will exhibit a definite polarization charge in a *reproducible manner*, as shown in Fig. 1.6.

1.2.4 Ionisation and acceleration in pyroelectric devices

The story of pyroelectric device development begins with *crystal x-ray generation*, which began in 1973 at the Bendix Research Laboratories in Michigan. It was here that Rosenblaum, Braunlich and Carrico [13, 82] discovered that thermally stimulating single pyroelectric crystals of lithium niobate, $LiNbO_3$, resulted in persistent electron emissions from the positive polarised surface (called the +z surface), and electron emission in bursts from the negative

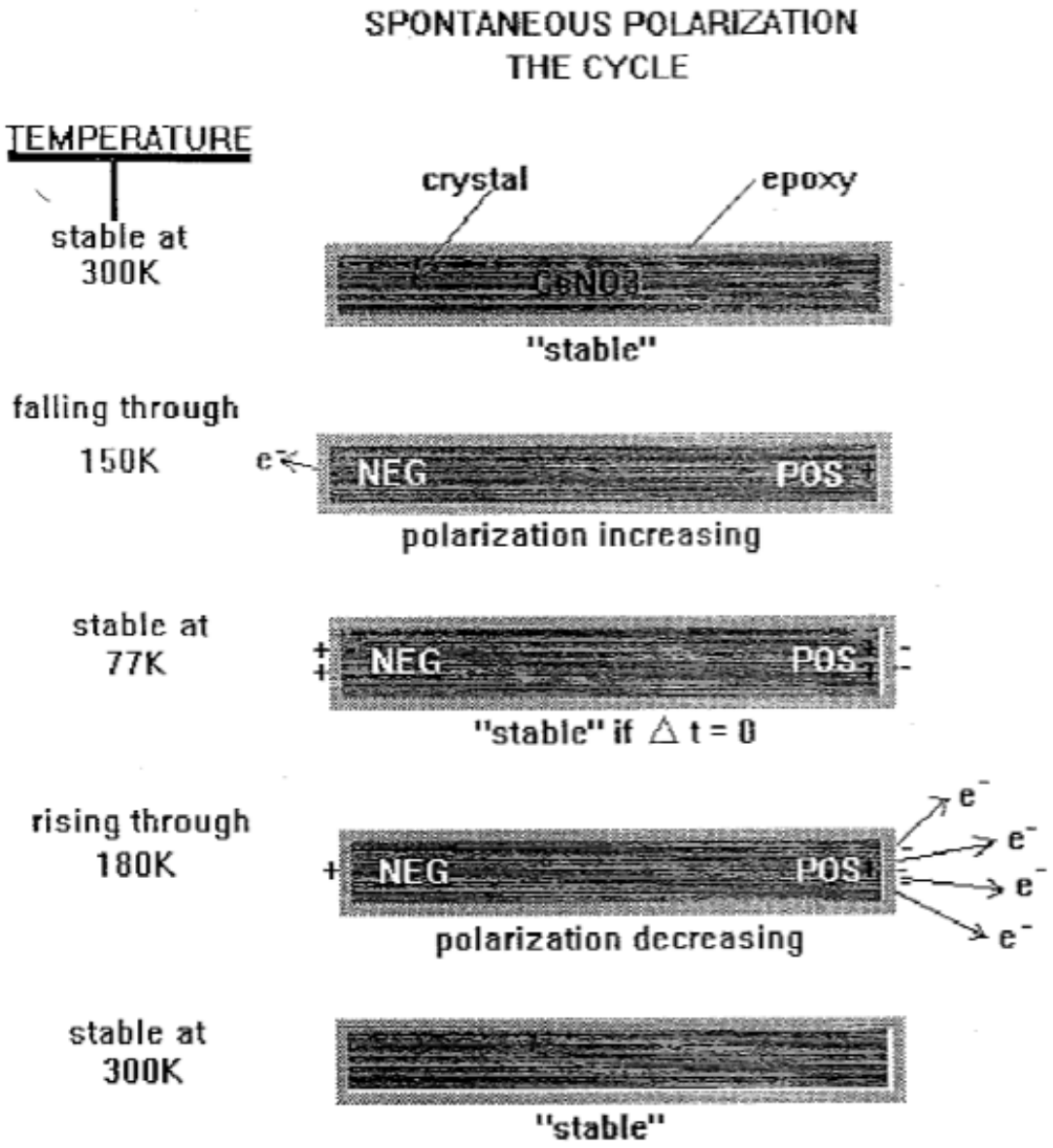

Fig. 1.5 The spontaneous polarisation cycle for pyroelectric crystals [15].

polarised surface (called the -z surface). These results were repeated and confirmed in 1983 [83] and 1985 [58].

In 1992, Brownridge [15] documented the spontaneous polarisation of $LiNbO_3$ and LT. He discovered that when these pyroelectric crystals are subjected to a thermal cycle in a vacuum, the electrons from the surface of the crystal and from the ambient gas remaining

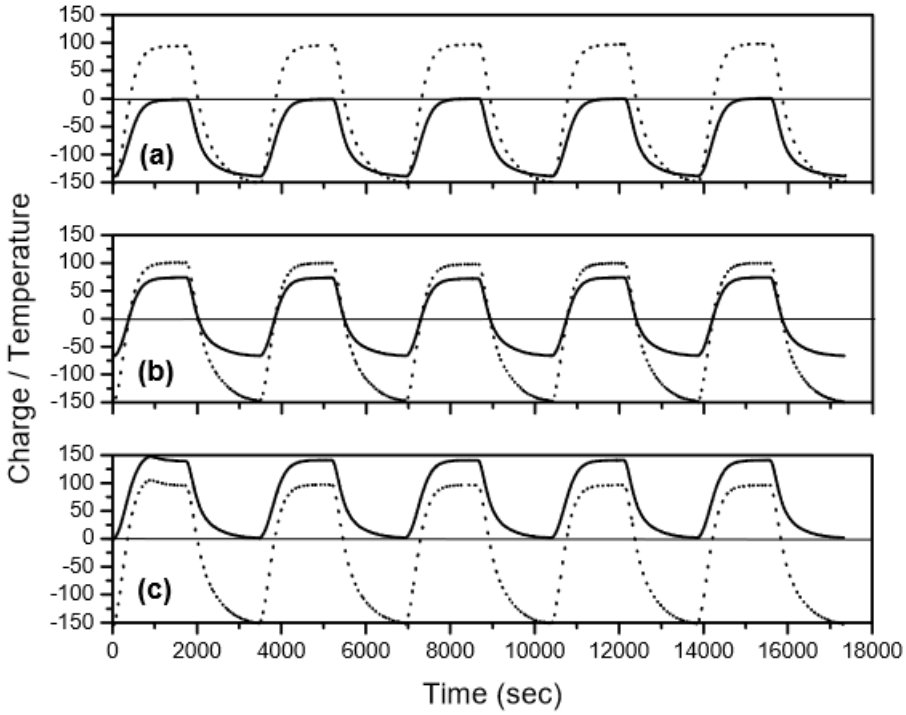

Fig. 1.6 Polarization charge and crystal temperature as functions of time for the -z base of a crystal of LT. In all three zeroing conditions presented the dashed curve represents the temperature of the crystal with the calibration: 100 divisions = 100 °C. The solid curve represents the charge reading of the electrometer with the calibration: 30 divisions = 10^{-7} °C. (a) The crystal was grounded at a temperature of about 100 °C. (b) The crystal was grounded at 0 °C. (c) The crystal was grounded at about −150 °C. [14].

in the vacuum chamber can be accelerated by the potential of the crystal against a metallic target to create x-rays through characteristic x-ray fluorescence and bremsstrahlung.

In 2005, Brownridge and Shafroth [11, 16, 59, 60] conducted several experiments with the aim of understanding the nature of the pyroelectric crystals focusing process and characterisation of the electron beam and its dependence on the environment around its focal spot. They thermally cycled z-cut $LiNbO_3$ and LT crystals in a dilute gas environment, and observed that, on a rising temperature, at the -z base positive ions are accelerated away from the crystal in a focused beam and simultaneously electrons are accelerated to it in a focused beam. The focused beam was reported to strike the crystal near its centre. The reverse process was observed when the crystal was cooled. It was noted that the crystal surface charge produced a very strong electric field at the surface of the crystal, around 1.35×10^7

V/cm. This field was strong enough to ionise the gas molecules close to the crystal surface and produce an ion pair.

Brownridge and Shafroth had pioneered the development of the first fully operational pyroelectric x-ray source as an alternative to isotopic sources. While isotopic sources had been manufactured to provide a wide range of source yield and energy, they required bulky shielding, even when not in use. They demonstrated that their x-ray source could be turned off when not in use, and although it was low in yield, it could be manufactured to fit into a pocket and run on a nine-volt battery. In 2003, Amptek [1] introduced the first commercially produced Cool-X x-ray device based on this design.

1.2.5 Deuterium-deuterium (D-D) fusion

Deuterium exists naturally as molecules of D_2. An important aspect in realizing pyroelectric fusion and neutron generation is the ability to ionise and accelerate deuterium gas towards the deuterated target. Once an atom of deuterium is accelerated above its ionisation energy, its electron is stripped away, leaving just the bare nucleus: the ion. When considering deuterium ionisation it is important to know if D^+ or D_2^+ ions are being produced. A research group at Rensselaer Polytechnic Institute (RPI) [23] conducted an experiment using a novel mass spectroscopy system constructed using pyroelectric crystals as an ion source. It was found that D_2^+ ions were being produced and accelerated to between 65 and 80 keV. There was no evidence that D^+ ions were being produced in large quantities. These results show that D-D fusion neutron yield from a pyroelectric accelerator using tip ionisation sources should be calculated using D_2^+ ions. As a result, the D-D interaction energy is half that of the accelerated ion energy.

In 2005, the University of California, Los Angeles (UCLA) [74] showed that a small pyroelectric crystal could produce deuterium ion beams of sufficient energy and current to drive nuclear fusion via the deuterium-deuterium reaction. There are two branches of the D-D fusion reaction which have the same chance of occurring over a large range of energies:

$$\begin{aligned} \mathrm{D}+\mathrm{D} &\rightarrow \mathrm{He}^3(0.82\ \mathrm{MeV})+\mathrm{n}(2.45\ \mathrm{MeV}) \\ \mathrm{D}+\mathrm{D} &\rightarrow \mathrm{T}(1.01\ \mathrm{MeV})+\mathrm{H}(3.02\ \mathrm{MeV}). \end{aligned} \tag{1.1}$$

These branches are called the *neutron branch* and the *proton branch* respectively. The cross section for the reaction varies with accelerating potential. The D-D neutron branch produces neutrons at comparable energies ($\sim$2.45 MeV) to the fast neutrons that are produced

from fissions in a nuclear reactor. Following moderation, in a reactor, to thermal energies these neutrons would initiate fission reactions [29, 33, 48, 56, 72, 78, 88, 89, 99].

1.3 Review of existing pyroelectric neutron generators

As we have noted in a previous section, we will need suitable data from an experimental program to provide data for the development and validation of a pyroelectric neutron generator model. Therefore, a necessary preliminary is to consider the status of transient data that is available from the existing literature. This is accomplished in this section by distilling out the best experimental data which represent the essence of current empirical knowledge, and which are based on the efforts of previous investigators.

In 2001, Shafroth [85] first discussed the possibility of achieving fusion and generating neutrons using pyroelectric crystals at a meeting of the American Physical Society. He suggested that pyroelectric crystals could be used to achieve D-D fusion through ionisation of deuterium gas and acceleration of deuterium D_2^+ or D^+ ions into a deuterated target. However, at the time, the lack of both neutron detection equipment and a target put a stop to this research.

Since then, there have been two main research groups who have led the major developments in pyroelectric neutron generation, and we can compare their devices and the published experimental data that is available for our analysis. The lead research groups are:

1. **University of California, Los Angeles (UCLA) [31, 63, 74, 90–92].**
   (a) In 2005, Brian Naranjo, James Gimzewski and Seth Putterman from UCLA published the first professional publication describing pyroelectric generated neutron production [74]. They reported that gently heating a pyroelectric crystal in a deuterated atmosphere can generate nuclear fusion under desktop conditions. It was reported that, although the fusion was not useful in a power-producing sense, it was anticipated that the system would find application as a simple palm-sized neutron generator. Figure 1.7 shows the UCLA vacuum chamber cut-away view, and the arrangement of neutron, ion current (Faraday cup) and x-ray detectors.
   (b) In 2007, researchers at UCLA [90] collaborated with Lawrence Livermore National Laboratory (LLNL), and reported the first results from the operation of the LLNL Crystal Driven Neutron Source (CDNS) based on the pyroelectric effect.

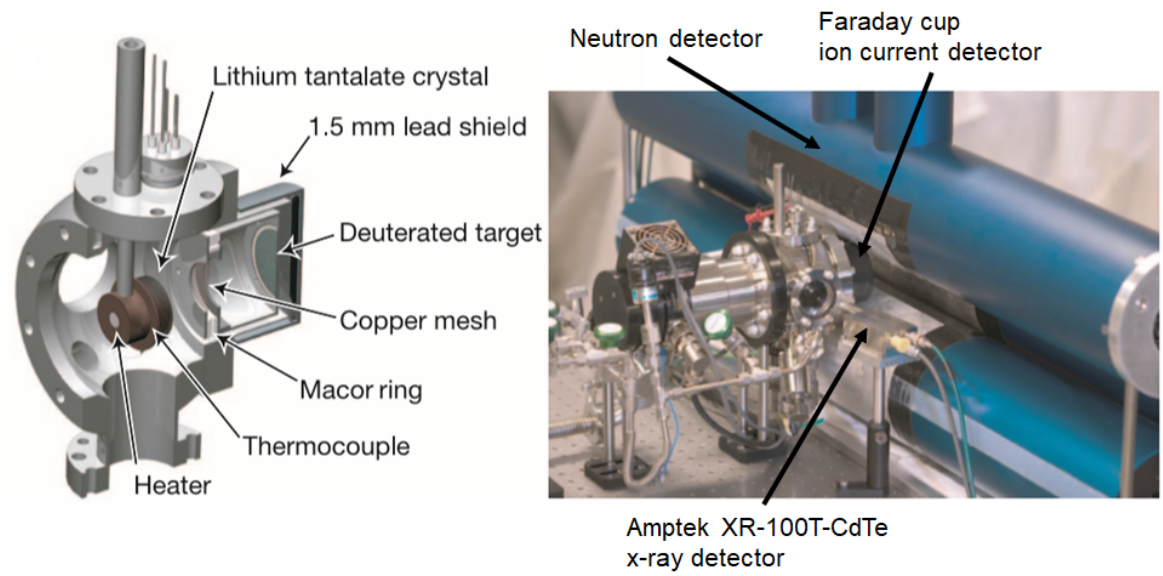

Fig. 1.7 UCLA vacuum chamber cut-away view, and arrangement of neutron and x-ray detectors [74].

The goal of this work was to raise the neutron output by increasing the beam energy and current using different crystal configurations. They incorporated feedback temperature control, socket mounts for rapid changing of field emitters, and the ability of the assembly to traverse the beam axis permitting maximum experimental flexibility. The neutron output of 1.9×10^5 cps was a factor of two higher than had previously been seen. This neutron yield is still the highest yield to date.

(c) In 2009, the researchers [91, 92] demonstrated pulsed operation at a low repetition rate by coupling an independently user-controlled ampere class spark deuterium ion source with a negative high voltage pyroelectric crystal. The yield from their device was $> 10^{10}$ n/s during the neutron pulse, with pulse widths of $\sim$100's ns.

(d) In 2012 [31], they used a decoupled configuration with a target coated crystal and an electrically biased gated tungsten tip to generate neutrons. Their testing additionally showed that dielectric insulation of the crystal reduces flashover.

2. **Rensselaer Polytechnic Institute (RPI) [3, 24, 25, 28, 35–45].**

(a) Research led by RPI has made significant contributions to electron acceleration, optimisation of x-ray production and improvements in the reproducibility of the neutron yields. In 2003-2007, RPI [35–40] reported experiments that showed that the maximum energy and x-ray yield from pyroelectric x-ray generators are

dependent on the thickness of the crystal. They showed that the maximum energy can be doubled with the addition of a second crystal. They also reported that the crystal heating rate had an effect on the x-ray production. They qualitatively discussed the reduction of the counts that was observed per thermal cycle when a crystal was heated very rapidly or very slowly. At rapid heating rates the poor thermal conductivity meant that the exposed crystal surface may not have experienced the same thermal cycle as the surface contacting the heater. At slow heating rates the crystal may re-mask its polarization through the accumulation of free charges, and by gradual electrical conduction through the crystal. The group observed that the optimal heating rate was around 0.27 K/s, half the rate at which the crystal could no longer react to the entire thermal cycle.

(b) Between 2007 and 2009, RPI [41–45] demonstrated a paired-crystal device that generated an acceleration potential of over 200 keV, which is the highest energy produced using this technology. RPI made contributions to the reproducibility of the neutron yields. Experiments were undertaken that produced $\sim 1 \times 10^4$ neutrons per thermal cycle for a two-crystal system. The group had the ability to reproduce experimental results using a new thermal management system, meaning thermal cycles could replicated from one experiment to another. Research at RPI had focused on the practical application of a portable pyroelectric neutron source with emphasis on improvements in the neutron production yield, reproducibility and controlled emission length. Such sources could find uses in neutron detector calibration, research and education and security applications.

(c) In 2009, RPI [25] published steady-state equations that were used to predict the potential and electric field in an idealized one-crystal and two-crystal pyroelectric accelerator. Their mathematical analysis was shown to agree with both finite element calculations and experimental values. They also showed that the accelerating potential is maximised at around 120 keV for crystal thickness between 10 and 20 mm, for a 50 °C temperature change.

(d) In 2011, RPI research [24, 28] focused on improving the neutron yield, the emission reproducibility, and shortening the heating cycle. They showed that D-D and D-T neutrons could theoretically produce $\sim 10^7$ n/cycle and could reach $\sim 10^7$ n/s for the D-T reaction. They demonstrated that the neutron emission during heating or cooling could be shortened to ~ 30 seconds during a typical heating/cooling cycle of about 2-3 minutes. They also developed an educational accelerator device in collaboration with the United States Military Academy, and the Defense Threat Reduction Agency at West Point [3]. They discussed a

method to optimise the acceleration potential by precisely controlling the thermal cycle of the crystals through a proportional thermal controller implemented in LabVIEW.

The most recent advances in associated fields have focused on: optimising various aspects of the hardware associated with pyroelectric x-ray radiation sources [4, 19, 55, 57, 75, 95, 96]; the modelling and simulation of pyroelectric detectors [76]; and reconverting solar energy into nuclear fusion energy using pyroelectric devices [94].

The number of devices studied by the principal investigators of pyroelectric neutron generation, through the years 2005-2019, are summarised in Table 1.2. The transient data from these devices are shown in Fig. 1.8.

The UCLA 2005 device [74] data, presented in Fig. 1.8a, shows (from top to bottom): the crystal temperature; the x-rays detected; the Faraday cup current; and the neutrons detected.

The UCLA and LLNL 2007 device [90] data, presented in Fig. 1.8b, shows the measured beam current (right), detected neutrons per 10 s (left), and rear crystal temperature (left).

The UCLA and LLNL 2012 device data [31], presented in Fig. 1.8c, shows (from top to bottom): the measured crystal temperature; the ion source bias voltage; the neutron production averaged over 1 s time intervals; and the crystal voltage measured from bremsstrahlung emission.

In the RPI 2008 [36] device data presented in Fig. 1.8d, the dashed line shows the counts from a CdTe x-ray detector, the dotted line shows the counts from the proton recoil detector without pulse-shape discrimination, and the solid line represents the proton recoil detector counts with pulse-shape discrimination (neutron counts) [36].

Comparison of devices and data available in Table 1.2 and Fig. 1.8 indicates that, as a starting point, the UCLA group's 2005 device [74] will serve as the best baseline from which to identify the typical components for the processes involved in, and the data available from, pyroelectric neutron generation.

Investigator	Device and experiment	General results and remarks
ULCA 2005 [74]	$LiTaO_3$ z-cut crystal, (diameter, 3.0 cm; height, 1.0 cm), with copper disk, and tungsten tip. Resistance heaters on -z face. Heated from 240 K to 265 K. Heating rate 0.2 K/sec. Cooled naturally. Deuterium pressure 5.2 mTorr.	1. Ion beam >100 keV, >4 nA. 2. Neutron yield $\approx$ 800 cps. 3. Transient data results are shown in Fig. 1.8a.
UCLA and LLNL 2007 [90]	$LiTaO_3$ z-cut crystal, (diameter, 3.0 cm; height, 1.0 cm), platinum coated crystal faces, copper disk (diameter 1 cm) and tungsten tip. Feedback temperature control. TEC on -z face. Heated from 10 °C to 110 °C. Heating rate 0.2 K/sec. Cooled naturally. Deuterium pressure 3 mTorr.	1. Ion beam >80 keV, $\sim$9.5 nA. 2. Neutron yield $\approx$ 924 cps. 3. Transient data results are shown in Fig. 1.8b.
UCLA and LLNL 2012 [31]	$LiTaO_3$ z-cut crystal, (diameter, 3.0 cm; height, 3.0 cm), copper disk and tungsten tip. Feedback temperature control. TEC on -z face. Heated from 20 °C to 65 °C. Heating rate 0.3 K/sec. Cooled naturally. Deuterium pressure 2.25 mTorr.	1. Ion beam >80 keV, 3 nA. 2. Neutron yield 1.6 $\times 10^2$ cps. 3. Transient data results are shown in Fig. 1.8c.
RPI 2007 [36]	$LiTaO_3$ z-cut crystal pair, (diameter, 2.0 cm; height, 1.0 cm), platinum coated crystal faces, copper disk (diameter 1.6 cm) and tungsten tip. Heated from 25 °C to 160 °C. Heating rate 0.27 K/sec. Cooled naturally. Deuterium pressure 3 mTorr.	1. Ion beam >100 keV, $\sim$9.5 nA. 2. Neutron yield $\approx 5.9 \times 10^3$ cps. 3. Transient data results are shown in Fig. 1.8d.

Table 1.2 Summary of pyroelectric neutron generator devices.

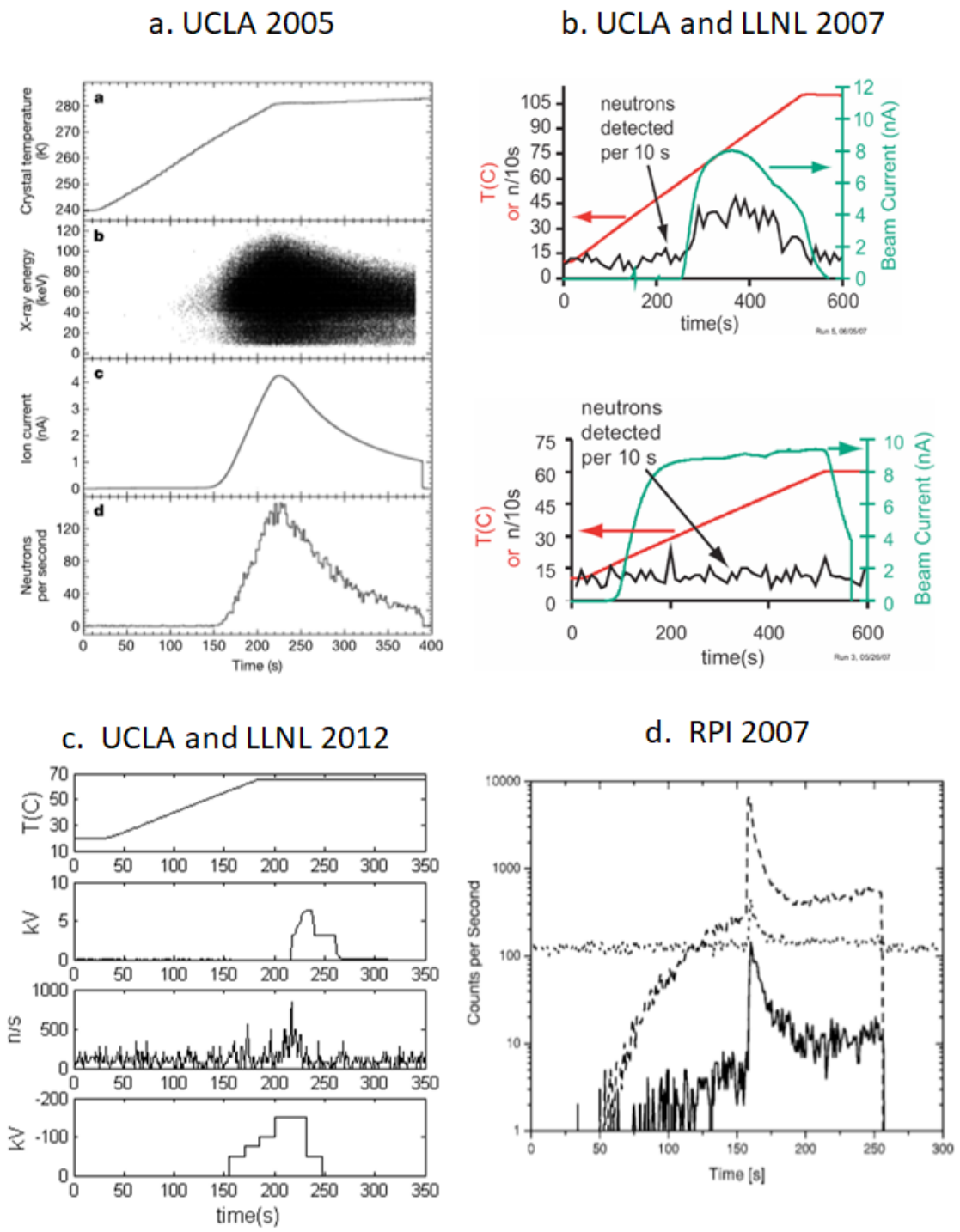

Fig. 1.8 Comparison of published transient data: a) UCLA 2005 [74]; b) UCLA and LLNL 2007 [36]; c) UCLA and LLNL 2012 [31]; d) RPI 2007 [36].

1.3.1 Overview of the VR-1 reactor

A Zero Energy Reactor (ZER) is one which generates insufficient power to materially alter its own thermal energy and can be modelled using the reactor kinetics subsystem. For the ZER system there is no feedback path; hence, for some real plants, the control of the neutron level can be entirely in the hands of the Reactor Panel Operator. The VR-1 reactor at the Czech Technical University [52] operates as a ZER, as does a Pressurised Water Reactor (PWR) during start-up and critical operation in the sub-power range. The VR-1 ZER is convenient for performing pulsed-source experiments and making corresponding calculations for systems ranging from delayed critical to highly subcritical [12, 54].

The training reactor VR-1 is operated by the Department of Nuclear Reactors of the Faculty of Nuclear Sciences and Physical Engineering at the Czech Technical University (CTU) in Prague. The reactor is principally used for training of university students and there is a focus on education and research in the field of nuclear engineering [52]. The Defence Academy's Nuclear Faculty has research links with the CTU's Department of Nuclear Reactors, and there is an ongoing programme of experimental collaboration.

The VR-1 training reactor, shown in Fig. 1.9, is a pool-type, light water thermal reactor with enriched uranium fuel. The neutron moderator is light de-mineralised water, which is also used as a neutron reflector, as biological shielding, and as a coolant. There are two pools containing identical, 2.3 m diameter, 4.7 m height, stainless steel reactor vessels; one vessel houses the active core, and the other is a handling vessel. The reactor shielding is made up of water and a specialised type of heavy concrete. The reactor is at ambient temperature; it sits at atmospheric pressure and the cooling is via natural convection only. The current neutron source is an americium-beryllium mix, with an activity of 185 GBq [s^{-1}]. The fuel is type IRT-4M, ^{235}U, with an enrichment of 19.7%, just below the threshold classed as highly enriched. The average neutron lifetime in the reactor is around 10^{-4} seconds. The reactor has a low nominal power of 1 kW thermal (up to 5 kW thermal for a short period). A detailed description of the VR-1 reactor is available online [52].

In the field of nuclear reactor dynamics it is common to use the term *kinetics* for short-time phenomena without feedback, and the term *dynamics* with feedback [29, 48, 78, 88, 99]. Short-time phenomena typically occur in time intervals of seconds to minutes. This timescale is appropriate for rapid changes in the neutron flux due to intended or accidental changes in the system, and flux transients important for: certain accident analyses (critical excursions); experiments with time-dependent neutron fluxes; reactor operation (such as start-up, load

Fig. 1.9 Photographs of the VR-1 training reactor, at CTU [52].

change, and shut-down); and analysis of stability with respect to neutron flux changes. It is this short timescale that we will be considering for our application of pyroelectric neutron generators to nuclear reactors.

The short-time phenomena include changes in the neutron flux as well as causally related changes in the reactor system, i.e. composition or temperature. This causal relationship can occur in either direction. Changes in the system can also be externally induced, for example, by the motion of an independent neutron source, or of control or shut-down rods, resulting in neutron flux changes. Nuclear reactors are designed to initiate, maintain and control a nuclear fission chain reaction. Uranium-235 is a fissile isotope that is commonly used; on absorption of a neutron it can undergo fission; this can be expressed as

$$ {}^{1}_{0}\mathrm{n} + {}^{235}_{92}\mathrm{U} \rightarrow \left[{}^{236}_{92}\mathrm{U}^{*}\right] \rightarrow FF_1 + FF_2 + \nu\mathrm{n}(5\,\mathrm{MeV}) \tag{1.2} $$

The reaction generates highly charged and energetic fission fragments (referred to as FF_1 and FF_2), and between one and five neutrons (on average $\nu = 2.4$ neutrons) are produced with a total energy of 5 MeV. The neutrons produced in the fission reaction are referred to as

prompt, and can be used to propagate a fission chain reaction. The majority of these neutrons appear instantaneously, within 10^{-14} seconds of the fission event. A small quantity, less than 1%, of the neutrons appear with an appreciable time delay, from the subsequent decay of radioactive fission fragments; these are called *delayed neutrons*.

The probability of a neutron-induced nuclear fission reaction taking place can be expressed in terms of its *microscopic cross section*, σ (units of barns); this expresses the probable reaction rate for neutrons travelling with a certain speed over a distance in a particular material. The microscopic fission cross section is a measure of the probability that a neutron and a nucleus interact to form a compound nucleus which then undergoes fission. The variation of the fission cross section for ^{235}U with neutron energy is shown in Fig. 1.10.

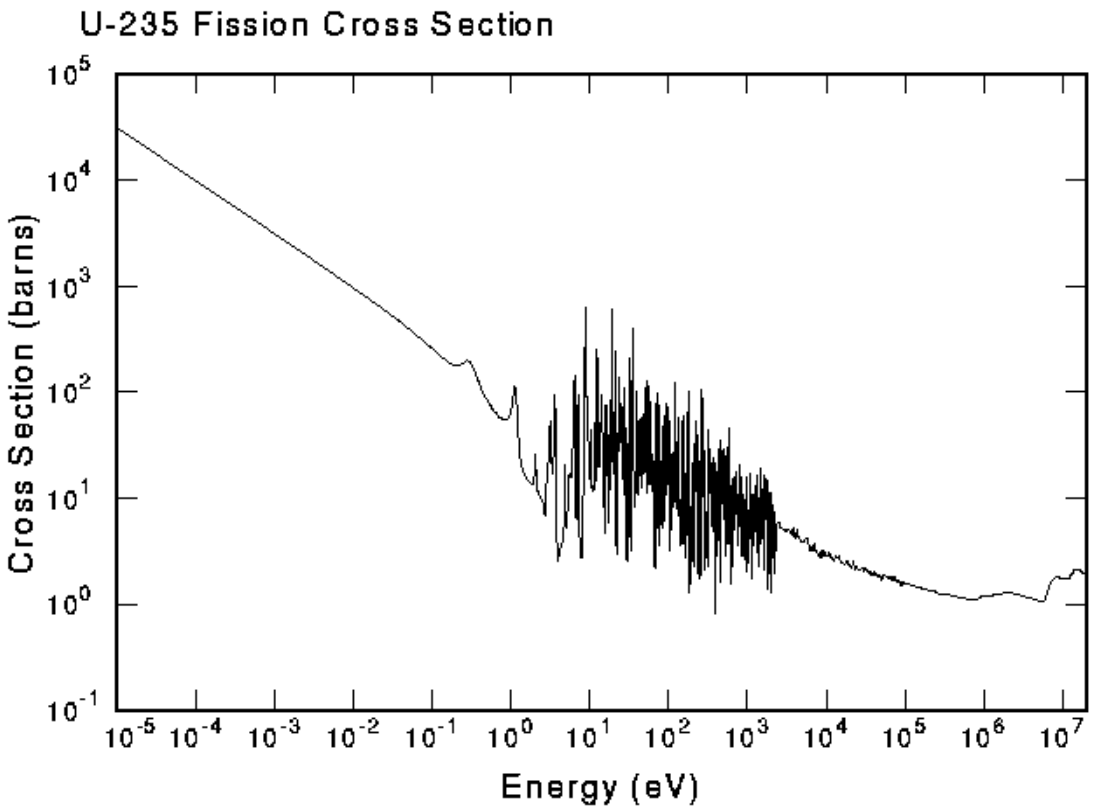

Fig. 1.10 The microscopic fission cross sections for ^{235}U, for a range of neutron energies [61].

The low energy neutrons, < 1 eV, are known as *thermal neutrons*, and for these the fission cross sections are largest. The intermediate energy region is known as the *slowing down region*, which contains the resonance region, and the high energy region is known as the fast

energy region. Neutrons produced in the fission reaction are usually in the high energy region, around 2 MeV, and need to be moderated to lower energies. Fission can occur at these high energies; however, it is much easier for a neutron to be absorbed and for a fission reaction to occur at thermal energies. In thermal light water reactors the moderation is carried out by the water that surrounds the fuel, which acts both as a coolant and a moderator. Reactor fuel enrichment levels have a large effect on the number of neutron-induced nuclear fissions. In reactors, such as the VR-1, with highly enriched fuels (i.e. those enriched to $\sim 20\%$), more neutrons will be captured in the resonance region, where the cross section is lower than the thermal region.

In the 1960's and 1970's, researchers [33, 72, 89] conducted experimental and analytical study of pulsed-source techniques for measuring shut-down reactivities in, and the frequency response of, nuclear reactors. The studies demonstrated the feasibility of using pulsed-source experimental techniques in a wide range of nuclear reactors.

It is anticipated that pyroelectric neutron sources will have distinctive dynamic effects when operated in the core of the VR-1 reactor. In this thesis, we will present the first model and simulations of these combined dynamic responses.

Chapter 2

Status of the VR-1 experimental program and recommendations for future work

Pyroelectric neutron generators are not commercially available; however, as previously mentioned, groups at UCLA, NNL and RPI have built devices for on-the-bench testing. These groups have focused on the improvement of the ionisation mechanisms to achieve reproducibility of results in the system. One of the primary challenges for our future experimental work will be to replicate the pyroelectric systems hardware that has been previously developed, with adaptations for the size and material constraints associated with live nuclear reactor applications.

Since this programme of PhD work started, in October 2012, two initial proof-of-concept demonstrators have been designed and manufactured at the Nuclear Faculty, Defence Academy. The first was assembled using adapted commercial, off-the-shelf components at the end of 2012 (referred to as Demonstrator One (DI) from hereinafter) and experiments were carried out in Prague in February 2013. The system was re-designed later in 2013 and a second system (referred to as Demonstrator Two (DII) from hereinafter) was fabricated at the end of 2013 and tested in February 2014.

2.1 Initial proof of concept demonstrator manufacture

The two demonstrators, DI and DII, were designed to understand the new designs that would be required for nuclear reactor applications, and to enhance the system analysis. The demon-

strators have helped to narrow down our recommended design options, avoiding those which will not work, and to highlight where further development and testing is necessary. They helped with the familiarisation with the experimental applications of the work. Challenges were added to the design of these demonstrators, as the application to a nuclear reactor introduces size and material constraints. This PhD work took the lead on the build of the hardware between 2012 and 2014; this facilitated real system experience to improve the pyroelectric model. The ongoing build of this hardware will continue at the Nuclear Faculty and the author will provide the control system design and implementation.

Both of our demonstrators have included many of the same standard vacuum system components such as pumps, controllers, gauges, flanges and fittings. Commercial, off-the-shelf vacuum components have been purchased and adapted to build the DI chamber, crystal and heater mountings and system connections to gauges, and controllers. The main constraint placed on the design was that the chamber should fit in a dry 50 mm diameter, cylindrical vertical channel in the reactor. Figures 2.1 and 2.2 show the DI system hardware, vacuum system and connections.

The DI vacuum chamber was assembled using a modular approach, by adding the aluminium flanges and fittings, as necessary. The main chamber was an aluminium KF-40 intermediate flange (Note: KF stands for Kwik-Flange). Kwik-Flanges were chosen as they are easily accessible: the vacuum seals consist of re-usable polymer-metal o-rings and clamps. The chamber had a 40 mm outer diameter and was 100 mm in length. The ends of the chamber were two aluminium DN 40 to DN 16 reducers, where DN is the European designation equivalent to American Nominal Pipe Size (NPS); it stands for diamètre nominal/nominal diameter, which is measured in millimetres. Two 30 mm sections of aluminium bar of 30 mm outer diameter served both as the heat sinks and provided the mounting platforms for the two $LiTaO_3$ crystals. A segment was cut from each bar to allow enough space for the wires to pass through and to provide the penetration into the chamber required to pump down and introduce the deuterium gas. This design of chamber had a high vacuum integrity and repeatedly held suitable vacuum pressures down to 10^{-4} mTorr (which is equal to 10^{-6} mbar). The geometry and small size of this chamber made it difficult to access the internal pyroelectrics and make adjustments or repairs during testing.

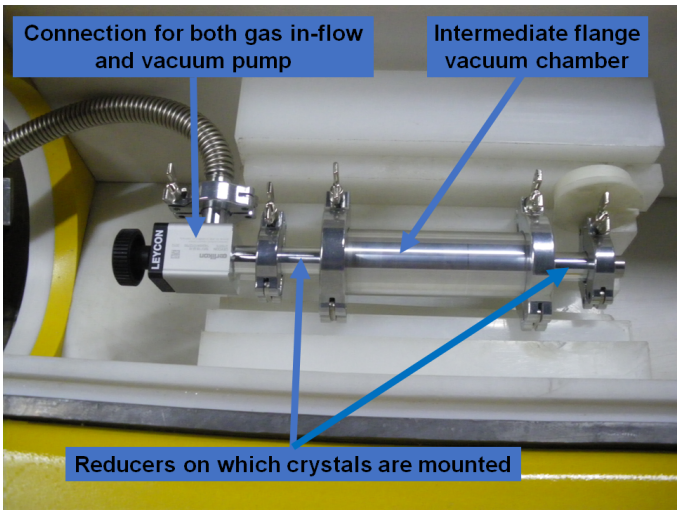

Fig. 2.1 The DI device at the Nuclear Faculty, February 2013.

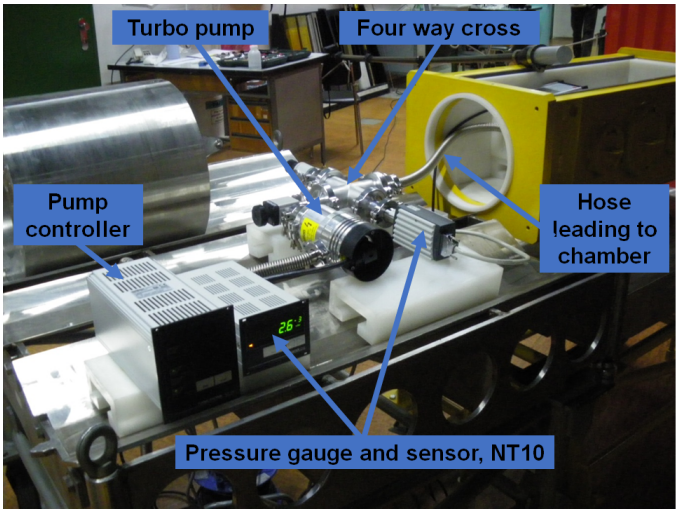

Fig. 2.2 DI device vacuum system and connections at CTU in Prague, February 2013.

The DI device produced neutrons above background during a bench test at the Czech Technical University, in Prague. However, problems with multiple TEC failures at peak transient temperatures, and difficulty accessing the internal pyroelectrics made repetition infeasible in the time frame that was available for conducting the experiments.

Following the DI experiments the opportunity to use the radial channel of the VR-1 reactor was proposed. This altered the main constraint placed on the design from a dry 50 mm diameter vertical channel to a dry 250 mm diameter horizontally oriented channel in the reactor. Figure 2.3 shows the DII prototype and Fig. 2.4 shows the position of the VR-1 radial reactor channel. The geometrical constraint of the new channel size was the main driver behind the increased geometry of the vacuum chamber. This larger rectangular vacuum chamber made the internals of the chamber more accessible during experimentation.

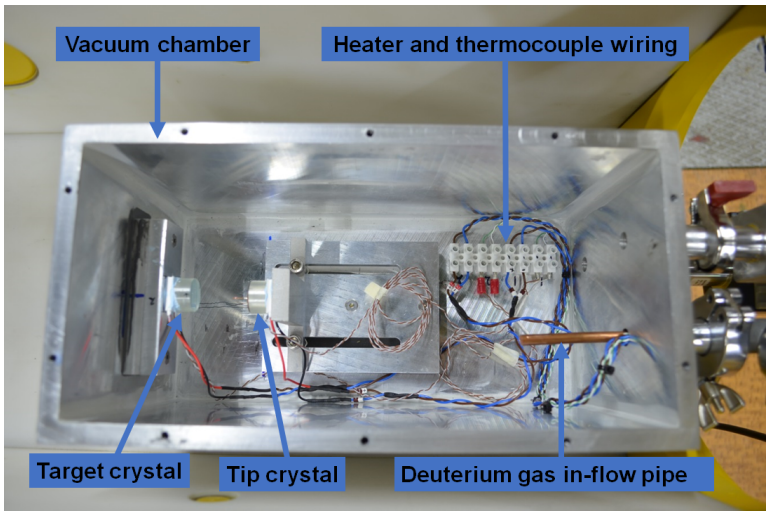

Fig. 2.3 DII device during bench testing at CTU in February 2014 (photograph courtesy of H. Bull, Nuclear Faculty).

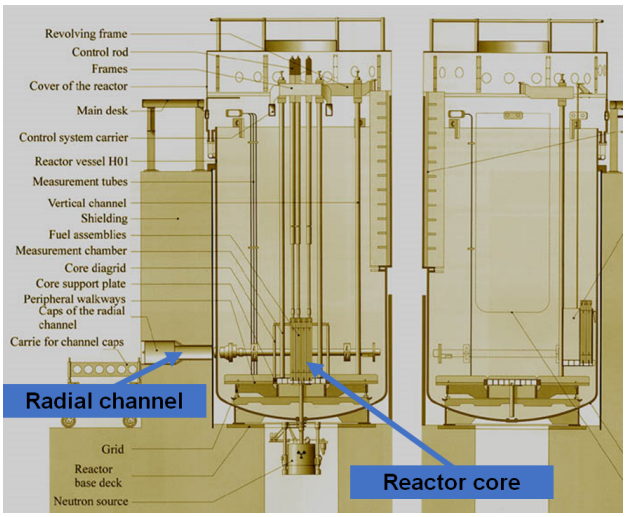

Fig. 2.4 Reactor vessels H01 and H02, Reactor VR-1, adapted from source [52].

2.2 Pyroelectrics hardware

Two 1 cm thick, 2 cm diameter, z-cut $LiTaO_3$ crystals were mounted on TECs and housed inside the vacuum chamber, see Fig. 2.5. TECs were chosen for the neutron generator because it was envisaged that later designs would benefit from the capability of the TEC to both heat and cool. The maximum size of heater that would fit inside the DI chamber was 2 cm by 2 cm, and a heater[1] from Farnell was chosen. These heaters were also used in the later DII system. It was necessary to provide a cooling-load aluminium mass capable of sinking all the heat produced by the devices. A silver-filled adhesive acted as a thermal compound and improved the thermal contact between the devices and the cooling load. Thermocouples (T/C in Fig. 2.5) were attached to the front of the TECs.

The DII design incorporates a removable aluminium plinth heat sink onto which the crystals are attached. The z+ face of the tip crystal has a 18 mm diameter, $\sim$ 0.8 mm thick copper disk and a 70 nm radius tungsten (chemical symbol W) tip[2] attached. The copper disk collects the charge from the z+ face and the tip locally enhances the electric field with the aim of improving the ionisation of the D_2 gas. Figure 2.6 is a photograph of the pyroelectric set-up for DII.

A Dual Inline Package (DIP) socket was soldered to the copper disk, which was cut to size using the Electric Discharge Machine (EDM) at the Nuclear Faculty. The tungsten tip could then easily be inserted and removed. The copper disk was mounted to the crystal using JB Weld epoxy, which is electrically non-conductive. The crystal was also mounted to the TEC using thermally conductive epoxy. The back side of the TEC was glued to the heat sink using the same thermally conductive epoxy to ensure thermal conductivity. A T-type thermocouple was epoxied to the upper side corner of the TEC and was used to measure the temperature of the back of the crystal. A deuterated target of deuterated polystyrene (DPS) was deposited onto the surface of the target crystal in preparation for the neutron production experiments.

[1] Part no. MCPE-071-10-13, from uk.farnell.com.
[2] Part no. 15864, Ernst R. Fullam, Inc., http:www.fullam.com (Dec 2013) as by Gillich 2009

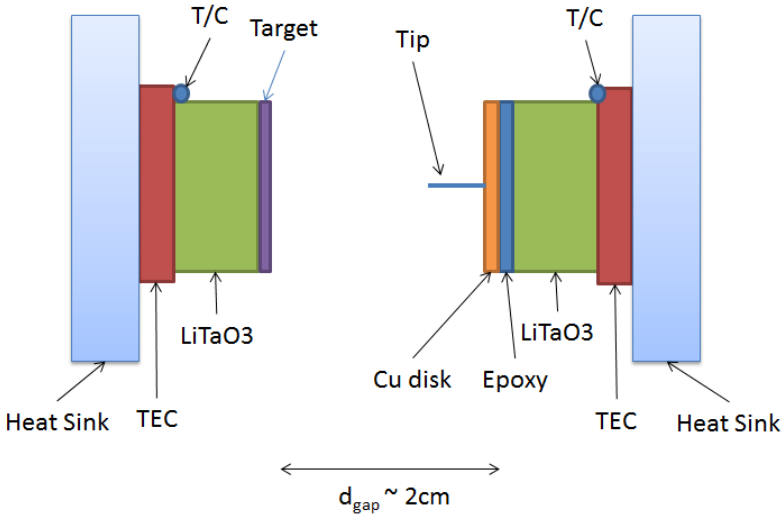

Fig. 2.5 Pyroelectrics experimental set-up for DII, February 2014.

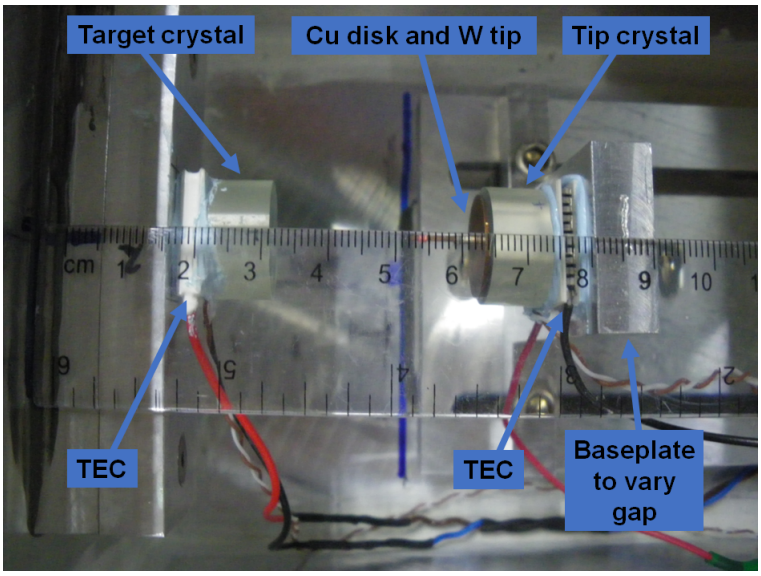

Fig. 2.6 Photograph of the DII pyroelectrics, February 2014.

2.3 Target preparation

The target material was deuterated polystyrene, deposited in a $\sim$ 45 µm layer on the surface of the target crystal. To prepare the target we heated 100 mg of DPS in a flat-bottomed flask containing 75 mL of xylene. The mixture was heated to around 100 °C, just below the boiling point of xylene (at around 135 °C). Within half an hour the DPS was fully dissolved. At this point, the xylene was gently boiled to thicken the solution. A pipette was then used to transfer three drops of the solution to the surface of the target crystal. The surface tension was enough to keep the solution from running down the sides of the crystal. The coated crystal was left in a fume cupboard to dry through evaporation of the xylene.

2.4 Vacuum chamber

The vacuum chamber houses the pyroelectric neutron generator and is an integral part of the system. The standard commercially available chambers are generally made of stainless steel and are too large in size for the nuclear reactor application. We designed and manufactured a custom-built chamber for DII using on-site expertise at the Nuclear Faculty, Defence Academy and HMS Sultan.

The most common materials used in the manufacture of vacuum chambers are austenitic steels. However, this material would not be suitable for the nuclear reactor application, due to the reactor neutron flux. The high activation of stainless steels by neutrons rules them out as suitable materials for this application. For radioactive backgrounds, aluminium with its substantially lower neutron absorption cross section is favoured. Aluminium is a good choice for thermal conductivity and allows the vacuum chamber to act as a heat sink for the TECs. Aluminium has a sufficiently high maximum service temperature of 200 °C, and may be used up to this value without significant property degradation.

A rectangular chamber, with a box lid configuration, was fabricated from welded thin plate (10 mm thick) aluminium material (150 mm by 150 mm by 300 mm (W H L)). We designed the chamber to be rigid enough to withstand the differential pressure, with operating pressure of around 1-10 mTorr inside and atmospheric pressure acting externally. The gasket sealing the lid was made from Viton, which is a standard material used in vacuum systems. Viton has suitability over a wide temperature range of -20 °C to 200 °C. One end-plate was adapted with ports for: entry of deuterium gas, attachment of the vacuum pump line, pressure gauge and electrical feed-through for thermocouple output and power to heaters, see Fig.

2.7. The removable lid facilitated easy access to the pyroelectric crystals and TECs mounted inside the chamber.

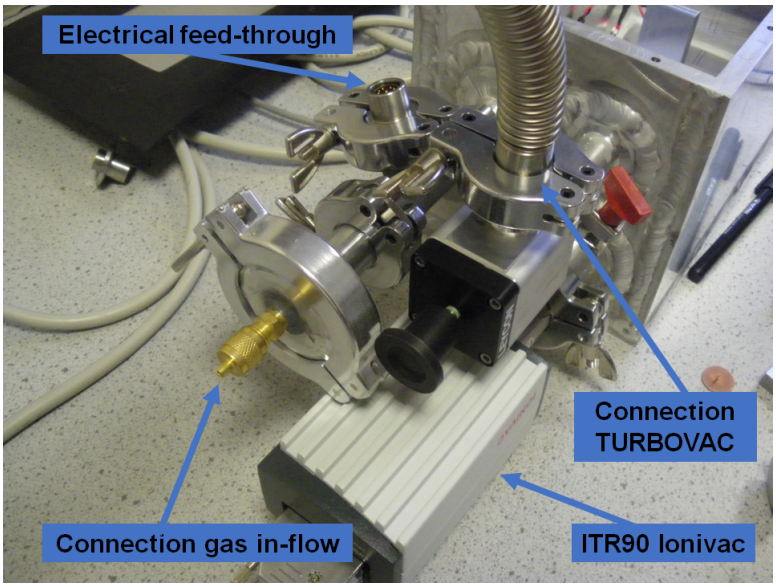

Fig. 2.7 End-plate attachments of DII, February 2014.

After manufacture, all chamber surfaces and components were thoroughly cleaned with a mild detergent and wiped down with acetone to remove gross deposits of cutting oils left by machining. Activation of material by such particles would hamper the functioning of the equipment and produce radioactive components that are difficult to handle.

Leak tightness of a vacuum chamber is essential; however, this is difficult given that the weldability of aluminium is poor. Gas can easily flow through a wall of the vessel via any imperfections such as holes, cracks or bad seals. For a vacuum chamber, leaks from atmosphere into the evacuated chamber are of concern. The welds between the aluminium plates on DII were coated with TorrSeal to improve their integrity. The chamber was leak tested using a water immersion bubble test. This method consisted of pressurising the system with a high pressure of nitrogen, then the chamber was isolated from the gas supply and its internal pressure monitored over time. A leak detection liquid was applied along the welds of the plates and flanges to identify any leak sites. The chamber was evacuated to around 3 mTorr, stabilised, isolated and then the increase in pressure was measured; over 24 hours the pressure increased to 100 mTorr and stabilised. This pressure would be too high for the pyroelectric system application, and the vacuum pumps would have to remain on during the

experiments in order to maintain a high vacuum.

During DI experiments the deuterium gas cylinder was connected to the system via a flexible plastic hose and clips. The connection point for the gas was remote from the chamber and the proximity of the pump could have prevented the gas from reaching the chamber; this may have compromised the experiments in February 2013. During testing it was found that this was an air ingress leak point to the system. The DII system was designed with improved gas connections and used a high integrity refrigeration hose with a Schrader valve, two ball valves and a needle valve connection: this resulted in better leak integrity and improved manual control over the gas flow.

2.5 Vacuum system

A Leybold TURBOVAC 50[3] portable, high-vacuum pump was used to achieve the necessary vacuum environment for the experiments. This turbomolecular pump is designed to pump vacuum chambers down to pressures in the high-vacuum range. The aluminium DN 16 vacuum hose running to the chamber is connected to the pump using an ISO-K 40 to 16 reducer. The TURBOVAC was operated and controlled with the corresponding Leybold NT 10 (200-240 V) TURBOTRONIK frequency converter[4] using a 1 m connecting cable. A dual-stage, oil-sealed roughing pump was connected to the system via the forevacuum line and used to reduce the pressure in the vacuum chamber to below 5 mTorr before the TURBOVAC pump was turned on.

Experiments were conducted on the bench using the DII chamber to determine how well the vacuum held following pump-down and system isolation. These experiments were able to determine that the pressure rise over 24 hours became significant (above 100 mTorr). It is possible that atmospheric gases were permeating the gasket or other seals in the vacuum chamber, and it was also likely that the epoxies and crystal assemblies were out-gassing into the system. Out-gassing is the liberation of gases and vapours from the walls of a vacuum chamber or other components on the inside of a vacuum system. This quantity of gas is also characterized by the increase in pressure resulting from the introduction of gases into this volume. The gas molecules bonded to the surface of the materials have a large effect at pressures in the 10^{-3} mbar range (which is equivalent to 1 mTorr). Degassing of glue joints can be a problem, even for high-performance epoxies which are commonly used to

[3]From www.leyboldproducts.oerlikon.com, Part number 85400
[4]From www.leyboldproducts.oerlikon.com, Part number 89500

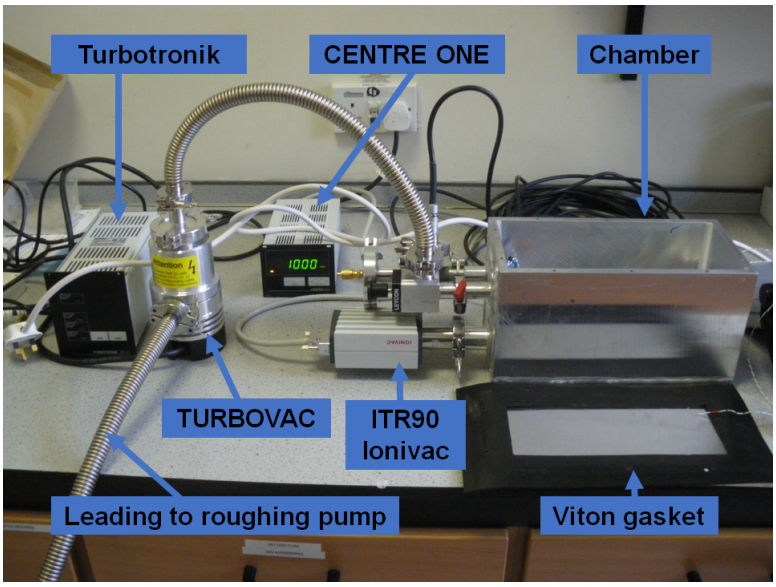

Fig. 2.8 Photograph of the DII vacuum system on the bench, February 2014.

repair leaks, such as the TorrSeal used on the DII chamber welds. This out-gassing limits the lowest achievable pressure in the vacuum chamber, and considerably extends the time for high and ultra-high vacuum to be reached. Similar issues in maintaining the required vacuum were experienced by RPI [25]. During experiments on DII the chamber took 3 hours to pump down to 6 mTorr. Evacuation to 100 mTorr was quick (taking around 30 mins), then it took 90 minutes to reduce to the 6 mTorr limit.

2.6 Data acquisition and control

A LabJack U9[5] data acquisition device was used for data acquisition and control for DI; it was relatively easy to use and low cost. An electronics box was built to house the TEC 10 V power supplies and relays. This was connected on its input port to the LabJack for a control signal and on the output port to the neutron generator via the electrical feed-through as shown in Figs. 2.9 and 2.10.

When developing the DII system, the decision was made to upgrade to the National Instruments cDAQ, see Fig. 2.11. With this new data acquisition platform, a direct interface with any sensor can easily be controlled via LabVIEW or MATLAB, which is advantageous as the control system modelling and control design is carried out using MATLAB software. A LabVIEW program was written to provide two modes of control: ramp and soak. The

[5]From www.LabJack.com, Ue9

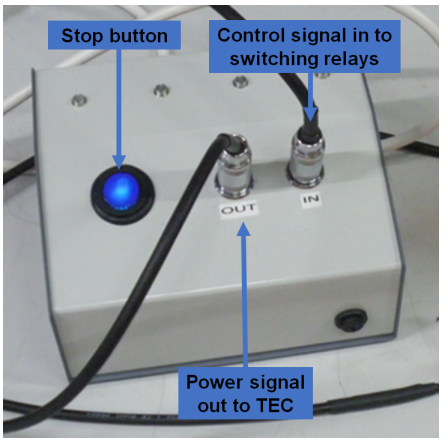

Fig. 2.9 Photograph of the DI data acquisition hardware, February 2012.

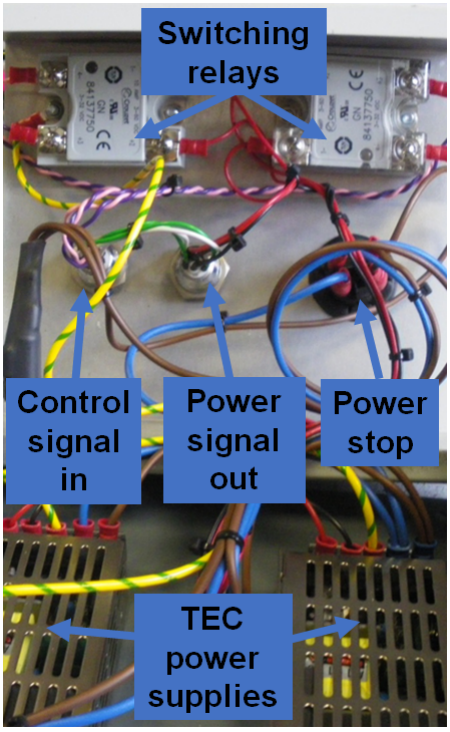

Fig. 2.10 Photograph of the electronics hardware, February 2014.

program manages the temperature set point and generates a signal to the relays based on an on/off control algorithm. The program interfaces with the cDAQ and its thermocouple and digital output modules. The graphical user interface generated is shown in Fig. 2.12.

Figure 2.14 shows the LabVIEW block diagram for the temperature while loop; the target crystal diagram is shown for clarity, some sections of the wiring shown are duplicated

Fig. 2.11 Photograph of the National Instruments cDAQ.

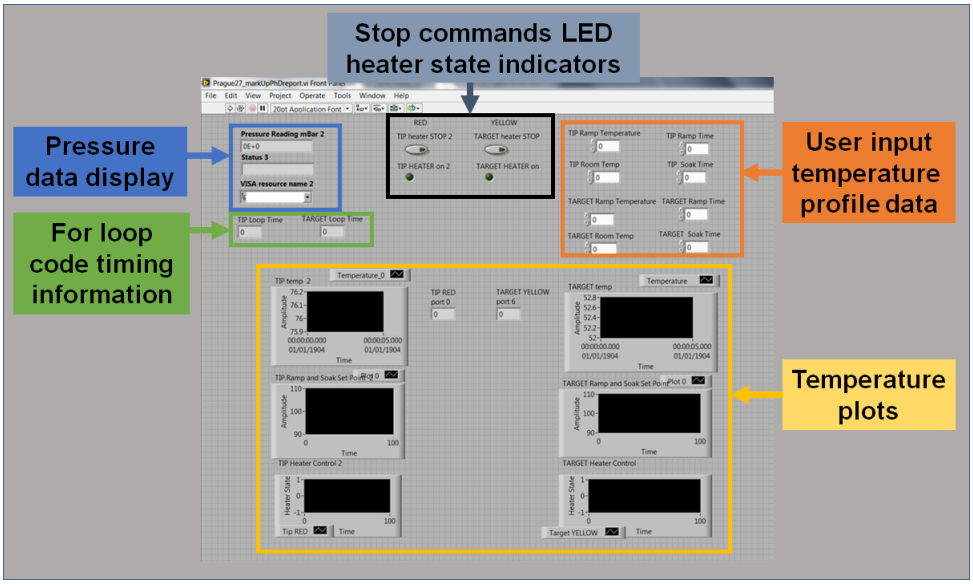

Fig. 2.12 Screen shot of the LabVIEW program graphical user interface.

for independent control of the tip crystal temperature. The program receives a user input temperature profile and raises or lowers the current to the thermoelectric cooler based on whether the crystal needs to be heated or cooled to match the command profile. Using this program, the thermal cycles were reproducible. Part of the program establishes communication between the computer and the cDAQ modules via a device driver. The program takes the set temperature and the desired time to get to that temperature and then calculates the required ramp rate. It uses this ramp rate and a measurement of current time to determine a set-point value. The program samples the current temperature and displays it to the front panel. It then calculates the difference between the set-point and the current temperature and a PID controller with pulse width modulation determines the required on/off state of the heaters. Figure 2.13 shows the LabView block diagram for the pressure loop.

At this stage, before we had carried out our model simulation and controller design, the TECs were controlled using on-off control. The DII hardware was redesigned to more precisely control the thermal cycle for each crystal independently. We noticed that with on-off control the TECs would not last long. There were lots of “hard” oscillations caused by this program; it is believed that this caused damage to the TEC heaters, which compromised the February 2014 DII experiments. These could now be removed through the design of an appropriate PI controller.

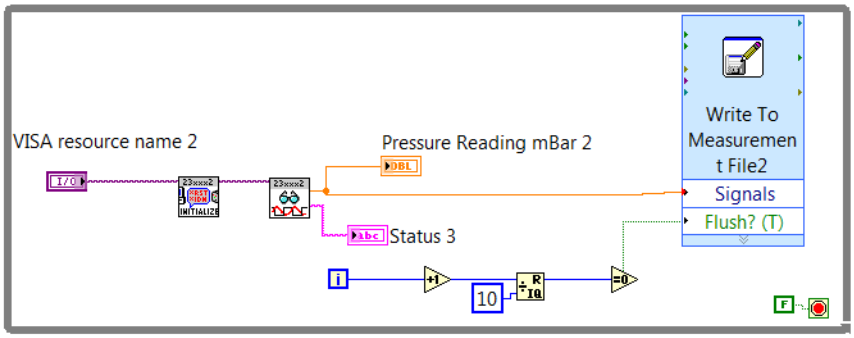

Fig. 2.13 Screen shot of the LabVIEW pressure loop.

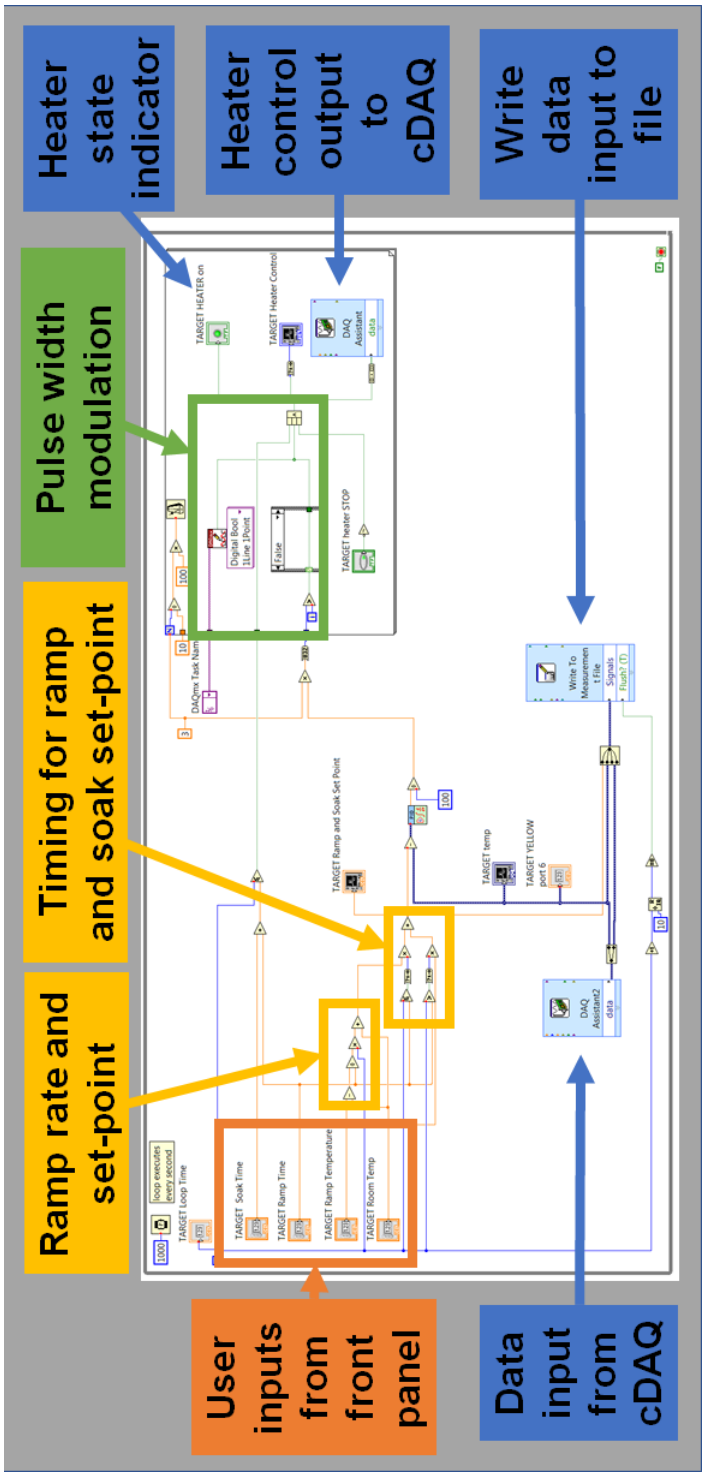

Fig. 2.14 Screen shot of the LabVIEW temperature loop (showing target crystal only for clarity).

2.7 X-ray experiments

X-ray fluorescence occurs when an electron bound to a target atom is expelled by incident x-ray or electron radiation. When an outer electron falls in energy to fill the empty shell, radiation is emitted in the form of x-rays. Every element has a characteristic set of electron energy levels, so the x-rays emitted as the electrons move between levels are specific to the target atom. The beam electrons eject inner-shell electrons that are then replaced by outer-shell electrons. If the voltage is too low, then the beam energy may not be capable of generating the characteristic radiation.

Since the acceleration potential changes as the crystal heats and cools, the x-ray emission is cyclical. With the +z surface of the tip crystal facing the target crystal, emission is observed during heating. As the heating cycle progresses, the pyroelectric effect causes an increase in the acceleration potential until the charge emitted as electrons balances with the charge generated due to the change in polarisation. After this point, the acceleration potential will decrease as the excess charge is emitted more rapidly than it can be replenished.

We purchased an Amptek X-123 detector for use in the DII experiments. The Amptek X-123 (see Fig. 2.15) is a complete x-ray detector system housed in an aluminium box. It combines a XR100CR detector and pre-amplifier, digital pulse processor and multichannel analyser (MCA), and power supply into a single package. Two connections were required: power (+5 VDC) and USB to the computer. To accurately calibrate the x-ray spectrum, we used two known sources: a copper source (at 8.9 keV), and an americium-241 source (at 14 keV).

Fig. 2.15 Photograph of the X-ray Detector, X-123 from Amptek [1].

Following the pump-down sequence, x-ray studies were completed to determine if the system could attain the 100 to 200 keV end-point energies for ionisation and fusion. All experiments were carried out at the CTU, in Prague. The crystals were given a 5 minute ramp to 90 °C, a 5 minute soak time at that temperature and then allowed to cool naturally.

The x-ray yield data is presented in Fig. 2.16, as the number of x-ray counts plotted against energy, and is indicative of the ion current impacting the target.

The resulting x-ray output consists of a continuous bremsstrahlung spectrum falling off to zero at the 65 keV end-point voltage. Characteristic x-ray emission lines can also be seen superimposed on the continuous bremsstrahlung spectrum. The x-ray results from the DII experiments can be compared with those of RPI [45], see Fig. 2.17. An end-point energy was observed to be about 200 keV and the k-shell x-ray lines for tantalum can be seen.

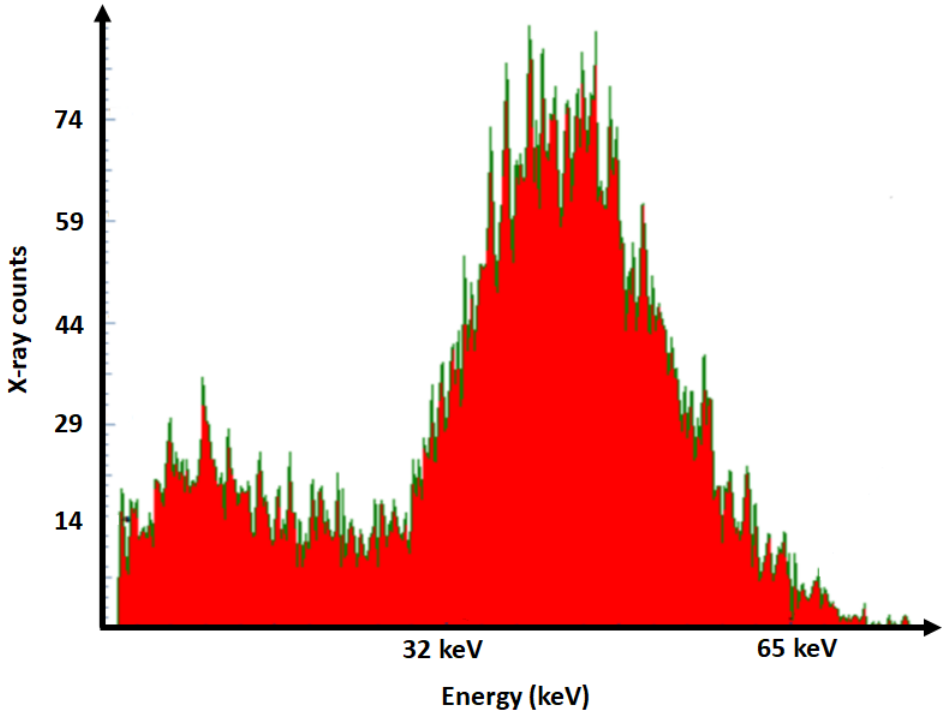

Fig. 2.16 X-ray emission from experiment using DII, 2014 - test 19.

Changing the heating rate was seen to have a detrimental effect on the x-ray production. The drop in production when rapid heating rates were applied may have been due to the poor thermal conductivity of the crystal, which means that the crystal surface facing the detector may not have experienced the same thermal cycle as the surface contacting the TEC. During slow thermal cycles, the crystal may have had time to re-mask its polarization through the accumulation of free charges from the gas, and by gradual electrical conduction through the crystal. Increasing gas pressure was seen to have a great effect on x-ray intensity.

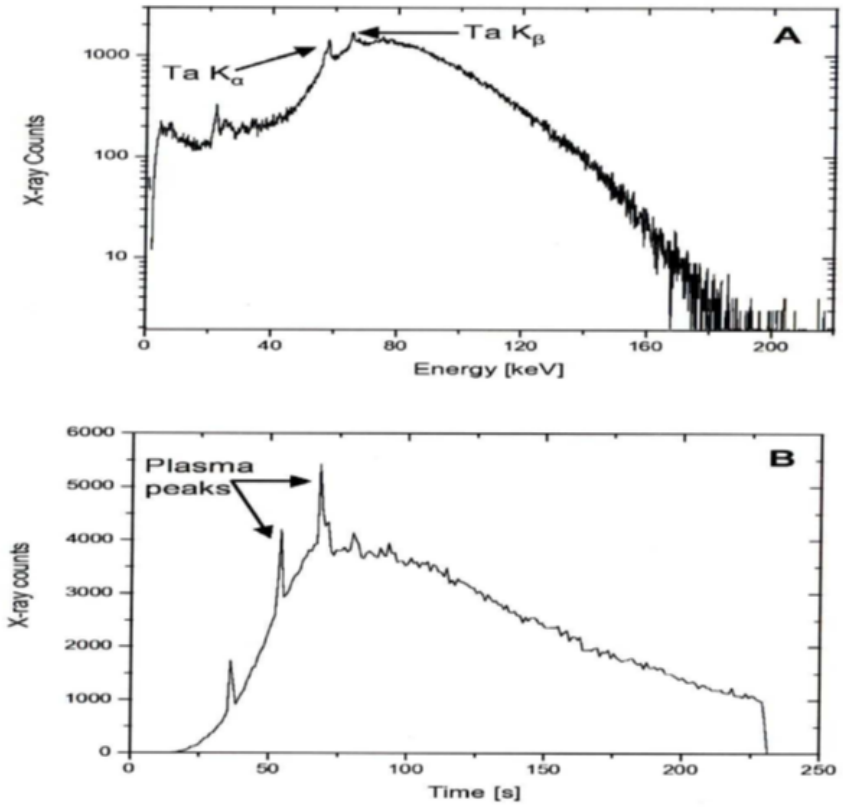

Fig. 2.17 X-ray energy (A) and yield (B) for one of RPI's successful neutron experiments [45].

The results show that the DII system provided an unstable environment, and reproducibility in energy and x-ray yield was not possible. As end-point energies of $\sim$ 65 keV were obtained, this was not deemed high enough for successful neutron experimentation. However, the improved deuterium gas flow and pressure control was tested. The D_2 pressure typically obtained was 10-20 mTorr and it was deemed that the quantity of gas permeating out of the system may have become equal to the amount of D_2 in the system. Under neutron experiment conditions this would have reduced the emission from the sealed system.

Following the DI and DII experiments we identified that modelling the system in order to understand and accurately predict the performance was the priority task. Following our modelling and simulation, it is recommended that the experimental program is improved to further verify the model.

A future device (DIII) would be specifically targeted at on-the-bench testing and designed to validate the pyroelectric neutron generator model. The device would be based around the Kurt Lesker 304L stainless steel CF cube for UHV systems - which has been tested and proven to sustain a suitable vacuum. It is the intention that testing, and development of the device will be begin at the Nuclear Department in late 2020 - early 2021, following appropriate financial approval, and risk assessments. The equipment intended for future purchase and its connection to the CF cube is shown in Fig. 2.18.

The main advantage of using an off-the-shelf cube as a vacuum chamber is the many gauges, instruments, accessories and feedthroughs that are available. The $LiTaO_3$ crystals and TECs will be epoxied on to two DN35CF-KF25 reducers on opposite sides of the cube. There will be connections to the existing pressure gauge and vacuum system via appropriate reducers. The multi-pin instrumentation feedthrough will provide connections to data acquisition and control. The top port can be fitted with a glass viewport for observing the experiments and quick identification of some of the more common TEC failures we experienced with the DI and DII devices.

Although a repeatable neutron yield has yet to be detected, both sets of experiments produced x-rays. The total charge produced by a pyroelectric crystal was observed during the experiments to be independent of the length of the heating or cooling phase; it depended only on the total change in temperature, and the pyroelectric coefficient. This is true if the crystal temperature change takes place over a long enough time for conduction of the heat through the crystal to allow the heating or cooling of the exposed crystal surface. The temperature cycle must also be fast enough such that relaxation current and screening effects remain negligible.

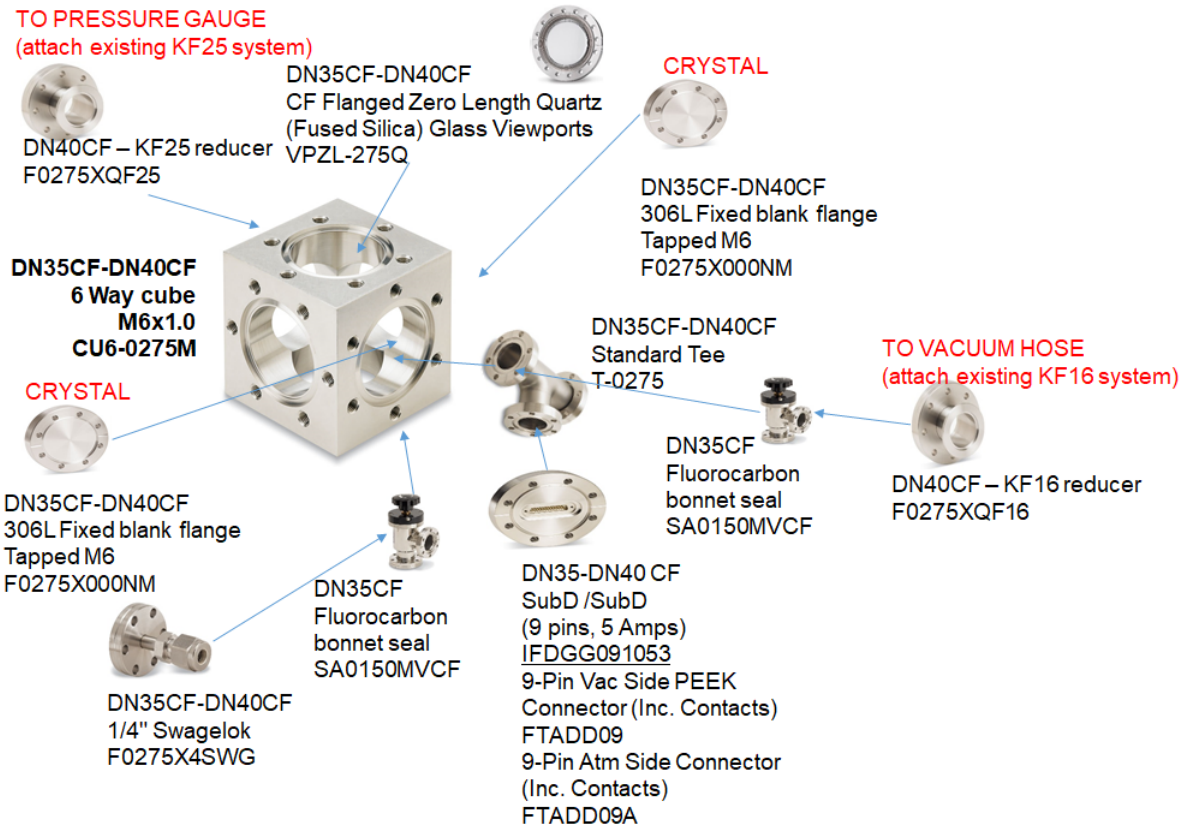

Fig. 2.18 DIII device - schematic of the proposed hardware. Individual images adapted from [22].

Chapter 3

System dynamic model of a thermoelectric cooler

3.1 Introduction

A thermoelectric cooler is a low-power energy conversion device with no moving parts and it has the potential for good controllability; it is therefore the best-possible technical solution to the problem of pyroelectric system actuation. Previous research groups have used thermoelectric coolers to heat pyroelectric crystals and the results of such experiments are readily available in publications. The vital missing stage from these pieces of research is the modelling and simulation of the thermoelectric cooler, and the pyroelectric system dynamics. Another advantage of the thermoelectric cooler, for our application, is the ability to heat or cool simply by switching the direction of the applied current flow. In fact, with the appropriate control the device could be used to cool the crystal to below ambient temperature; something which has been only been done using nitrogen cooling in previous pyroelectric research.

In the control of the thermal aspects of our pyroelectric neutron generator we will have the requirement to establish control over the incremental temperature of the cold-side to which the thermal load (our crystal) is connected; this temperature is known as the *controlled variable*. The *controlling variable* will be the incremental current, since this can be varied by electrical means.

In this chapter we begin by introducing the ideal governing equations for the thermoelectric cooler. Using these, a state-space model is developed specifically for the purpose of controller design and applicability to the pyroelectric system actuation. The validity of

the model with respect to this purpose is then determined. As part of the verification and validation, the outputs of the derived thermoelectric cooler model are compared to another simulation model that was developed by Huang in 2000, which itself has been validated against experimental data [50]. Finally, a parameter variability-sensitivity analysis is used to provide sufficient confidence in our model performance, and the conclusion is drawn that the model can be considered valid for its intended application.

It is difficult to obtain an exact analysis of the dynamic behaviour of thermoelectric coolers. The devices are most accurately described by partial differential equations that contain nonlinear terms and that are subject to boundary conditions that contain product-type nonlinearities [47]. In this research we require to control a thermoelectric cooler for use as the actuator in a pyroelectric system; hence sufficiently modelling the dynamic behaviour of such devices will contribute significant information to our task. Information in a form that is useful for control purposes can be obtained by means of small-signal analysis, which permits the development of transfer function models which can be used in the frequency response analysis or calculation of the device response in the time domain.

Sufficient background material in control engineering for the work to follow will be presented as it is required in this thesis. For further references the reader is referred to the control engineering texts listed in the References section [30, 34].

3.2 Thermoelectric cooler preliminaries

In order to maintain control of the thermoelectric cooler it is first required to understand the dynamic behaviour of the device. There are three closely-related, predominant thermoelectric effects: the Seebeck effect; the Peltier effect; and the Thomson effect, which are well described in the original 1960s modelling work of Gray [47];

1. **The Seebeck effect.** In 1821, Seebeck discovered that an electric current could be produced in a closed circuit composed of two different conductors if one junction of the dissimilar metals was maintained at a temperature different from the other junction, and the effect can be expressed as

$$\alpha(T) = \frac{dV}{dT} \tag{3.1}$$

where α is the Seebeck coefficient of thermoelectric material [V/K];
V is the voltage [V];

T is temperature [K].

2. **The Peltier effect.** In 1834, Peltier observed that an amount of heat Q was either absorbed or evolved at a junction of two dissimilar metals when an electric current I was passed through the junction.

$$Q = \Pi I \tag{3.2}$$

where Π is the Peltier coefficient.

3. **The Thomson effect.** In 1857, Thomson showed the direct relationship between the Seebeck and Peltier effects; the Peltier coefficient at a junction is equal to the Seebeck coefficient multiplied by the operating junction temperature, given by

$$\Pi = \alpha T \tag{3.3}$$

where T is the temperature of the junction. Thomson also predicted what came to be known as the Thomson effect, that heat Q is absorbed or evolved along the length of a material rod whose ends are at different temperatures. This heat was shown to be proportional to the flow of current and to the temperature gradient along the rod. The proportionality factor τ is known as the Thomson coefficient. Practically the thermoelectric behaviour of a device is adequately described using only one thermoelectric parameter, the Seebeck coefficient α. The Thomson effect is comparatively small, and so it is generally neglected [50].

There are two other main heat transfer factors that we must consider in addition to the Seebeck effect when we aim to sufficiently model the thermoelectric cooler dynamics:

1. **Fourier's heat conduction.** The heat conduction in two thermoelectric cooler semiconductor legs between the source and the sink. The thermal flow down these two legs is given by Fourier's heat conduction law:

$$\frac{dQ}{dt} = -kA\frac{dT}{dx} = kA\frac{T_H - T_L}{L} \tag{3.4}$$

where k is the mean thermal conductivity of the p-n pair [W/m-K];
A is the total cross-sectional area of the thermoelectric material [m^2];
T_L is the temperature of the cold-side of the thermoelectric module [K];
T_H is the temperature of the hot-side of the thermoelectric module [K];

L is the length of the thermoelectric elements [m]; and

2. **Joule heating.** Ohmic heating occurs in both of the thermoelectric cooler legs because of the presence of electrical resistance. The heat Q produced in each leg is given by Joule heating:

$$Q = \frac{\rho L I^2}{A} \tag{3.5}$$

where ρ is the average electrical resistivity of the semiconductor materials [Ω·m], and I is the applied electrical current [A]. Approximately half of the resistance-produced heat in each of the two legs flows towards the source, and half towards the sink.

Gray used small-signal analysis to theoretically derive a dynamic model of a thermoelectric module [47]. Bywaters and Blum worked out their control equations for a thermoelectric module based on the assumption that the temperature distribution is linear [18]. We will use the same assumption and follow a similar process for obtaining the linearised thermoelectric cooler model as these previous researchers.

3.3 Governing equations for the thermoelectric cooler model

First, the temperature distribution across the thermoelectric cooler (TEC) must be modelled. With reference to Fig. 3.1, during a cooling cycle, the heat load Q_L is absorbed at the cooling-load heat exchanger and conducted to the cold-end plate of the thermoelectric module; it is then pumped to the hot-side of the module and into the heat sink. In the development of the governing equations for the system dynamic model of the TEC, we can assume that [18]:

- the temperature distributions inside the cold-end plate and the cooling-load heat exchanger are uniform, and
- the temperature distribution in the TEC is linear and the average temperature can be represented as $T = \frac{T_H - T_L}{2}$, and
- the parameters of the device are independent of temperature.

The governing describing equation for the energy balance to the cold-end plate and the cooling-load can now be written as

$$(M_L C_L + M_C C_C)\frac{dT_L}{dt} = Q_L + \frac{kA}{L}(T_H - T_L) - \alpha I T_L + \frac{1}{2}\frac{\rho L}{A} I^2 \tag{3.6}$$

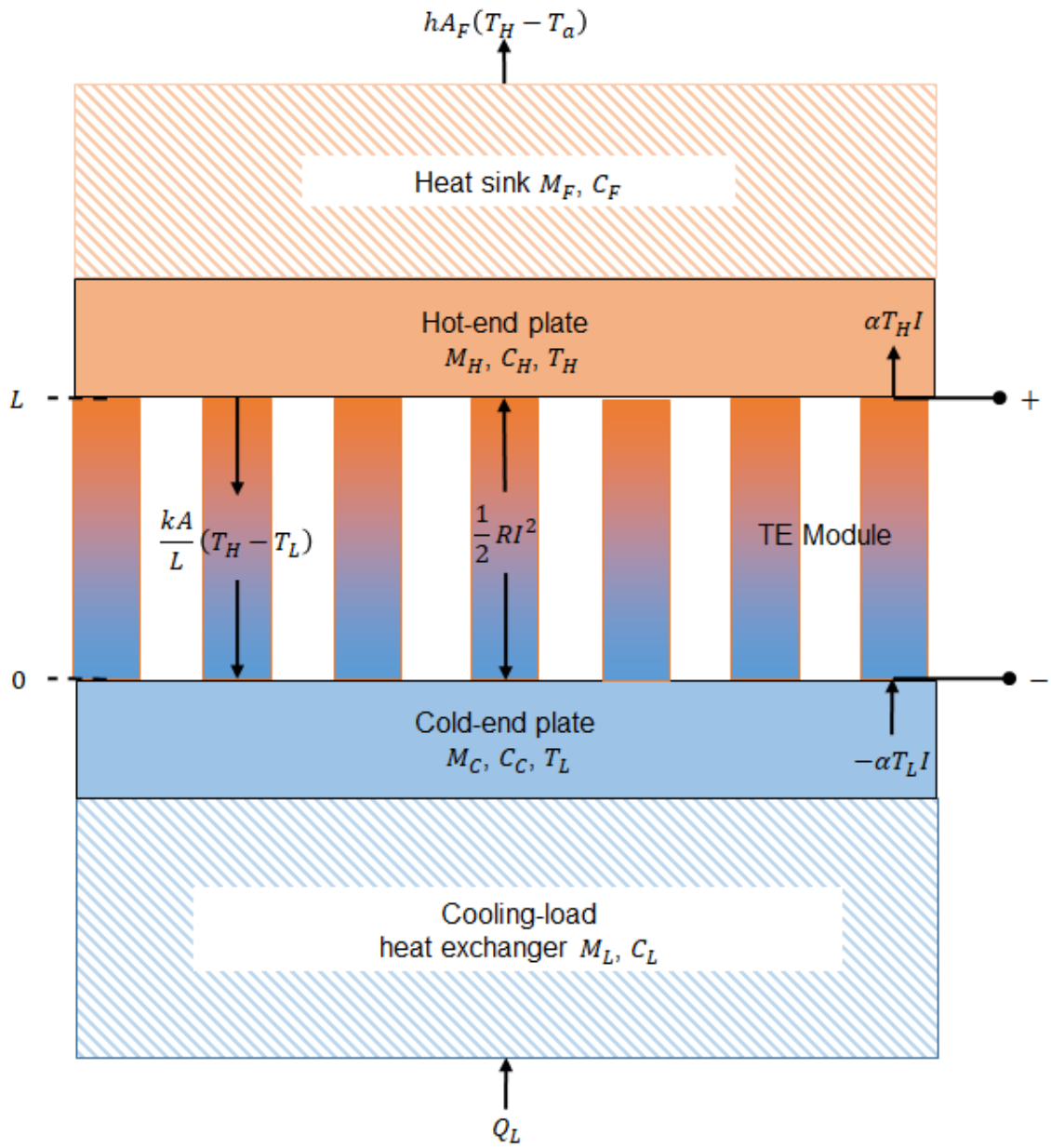

Fig. 3.1 Schematic diagram of the thermoelectric cooler and temperature distribution.

where M_L is the mass of the cooling-load [kg],
C_L is the specific heat capacity of the cooling-load [J/kg-K],
M_C is the mass of the cold-end plate of the thermoelectric module [kg],
C_C is the specific heat capacity of the cold-end plate of the thermoelectric module [J/kg-K],
T_L is the temperature of the cold-side of the thermoelectric module [K],
T_H is the temperature of the hot-side of the thermoelectric module [K],
I is the applied current to the thermoelectric module [A],

α is the Seebeck coefficient of the thermoelectric material [V/K],
k is the mean thermal conductivity of the p-n pair [W/m-K],
A is the total cross-sectional area of the thermoelectric material [m^2],
ρ is the mean electrical resistivity of the thermoelectric material [Ω-m] and
L is the length of the thermoelectric elements [m].

The energy balance to the heat sink and the hot-side plate can be written as

$$(M_F C_F + M_H C_H)\frac{dT_H}{dt} = \alpha I T_H - \frac{kA}{L}(T_H - T_L) + \frac{1}{2}\frac{\rho L}{A} I^2 - hA_F(T_H - T_a) \tag{3.7}$$

where M_F is the mass of the heat-sink [kg],
C_F is the specific heat capacity of the heat-sink [J/kg-K],
T_a is the ambient temperature [K],
h is the convective heat transfer coefficient of the heat sink [Wm^{-2}K^{-1}], and
A_F is the total heat transfer surface area of the heat sink [m^2].

3.3.1 Linearisation of the governing equations

Control design methods are much easier for linear than for nonlinear models; however, the thermoelectric heat transfer process is nonlinear. Therefore, we now need to find a linear model that approximates the nonlinear one.

Linearisation of the TEC governing equations

Lyapunov proved, if a small-signal linear model is valid near an equilibrium and is stable, then there is a region containing the equilibrium within which the nonlinear system is stable [9, 10]. So, we can safely make a linear model and design a linear control for it such that, at least in the neighbourhood of the equilibrium, our design will be stable. Since the role of feedback control is to maintain the process variables near equilibrium, small-signal linear models are a common starting point for control design. Using a small-perturbation analysis a linearised equation set for a typical TEC can be formed. The variables are considered to be the summation of a steady-state value (denoted by $\bar{X}$) and a small change (denoted by $\tilde{X}$) about that operating point, i.e.

$$
\begin{aligned}
T_L(t) &= \bar{T}_L + \tilde{T}_L(t) \\
T_H(t) &= \bar{T}_H + \tilde{T}_H(t) \\
T_a(t) &= \bar{T}_a + \tilde{T}_a(t) \\
Q_L(t) &= \bar{Q}_L + \tilde{Q}_L(t) \\
I(t) &= \bar{I} + \tilde{I}(t)
\end{aligned}
\tag{3.8}
$$

Equation set 3.8 can be substituted into Eqs. 3.6 and 3.7. Taking constant properties for k, ρ, C_L, C_C, C_F, C_H and α, with the preceding considerations, the following equations, Eqs. 3.9 and 3.10, may be realised.

$$
\begin{aligned}
(M_L C_L + M_C C_C)(\dot{\bar{T}}_L + \dot{\tilde{T}}_L) =& (\bar{Q}_L + \tilde{Q}_L) + \frac{kA}{L}(\bar{T}_H + \tilde{T}_H - \bar{T}_L - \tilde{T}_L) - \alpha(\bar{I} + \tilde{I})(\bar{T}_L + \tilde{T}_L) \\
&+ \frac{1}{2}\frac{\rho L}{A}(\bar{I} + \tilde{I})(\bar{I} + \tilde{I})
\end{aligned}
\tag{3.9}
$$

$$
\begin{aligned}
(M_F C_F + M_H C_H)(\dot{\bar{T}}_H + \dot{\tilde{T}}_H) =& \alpha(\bar{I} + \tilde{I})(\bar{T}_H + \tilde{T}_H) - \frac{kA}{L}(\bar{T}_H + \tilde{T}_H - \bar{T}_L - \tilde{T}_L) \\
&+ \frac{1}{2}\frac{\rho L}{A}(\bar{I} + \tilde{I})(\bar{I} + \tilde{I}) - hA_F(\bar{T}_H + \tilde{T}_H - \bar{T}_a - \tilde{T}_a)
\end{aligned}
\tag{3.10}
$$

Eliminating steady-state and high-order terms, we obtain the following

$$
(M_L C_L + M_C C_C)\dot{\tilde{T}}_L = \tilde{Q}_L + \frac{kA}{L}(\tilde{T}_H - \tilde{T}_L) - \alpha\bar{I}\tilde{T}_L - \alpha\tilde{I}\bar{T}_L + \frac{\rho L}{A}\bar{I}\tilde{I} \tag{3.11}
$$

and

$$
(M_F C_F + M_H C_H)\dot{\tilde{T}}_H = -\frac{kA}{L}(\tilde{T}_H - \tilde{T}_L) + \alpha\bar{I}\tilde{T}_H + \alpha\tilde{I}\bar{T}_H + \frac{\rho L}{A}\bar{I}\tilde{I} - hA_F(\tilde{T}_H - \tilde{T}_a) \tag{3.12}
$$

Now, for a TEC performing at a constant cooling load, we have $\tilde{Q}_L = 0$, and for a fixed ambient condition, we can say that $\tilde{T}_a = 0$. Making these substitutions yields the linear set of differential governing equations that we require for our analysis of the TEC dynamics, Eqs. 3.13 and 3.14.

$$
(M_L C_L + M_C C_C)\dot{\tilde{T}}_L = \frac{kA}{L}(\tilde{T}_H - \tilde{T}_L) - \alpha\bar{I}\tilde{T}_L - \alpha\tilde{I}\bar{T}_L + \frac{\rho L}{A}\bar{I}\tilde{I} \tag{3.13}
$$

$$(M_F C_F + M_H C_H)\dot{\tilde{T}}_H = -\frac{kA}{L}(\tilde{T}_H - \tilde{T}_L) + \alpha\bar{I}\tilde{T}_H + \alpha\tilde{I}\bar{T}_H + \frac{\rho L}{A}\bar{I}\tilde{I} - hA_F\tilde{T}_H \tag{3.14}$$

3.4 The TEC Model time constants

The linear time-invariant system of Eqs. 3.13 and 3.14 may be represented in transfer function form. Considering first the equation for the cold-side, Eq. 3.13, by multiplying out all terms, we obtain the following:

$$MC_{LC}\dot{\tilde{T}}_L = \frac{kA}{L}\tilde{T}_H - \frac{kA}{L}\tilde{T}_L - \alpha\bar{I}\tilde{T}_L - \alpha\tilde{I}\bar{T}_L + \frac{\rho L}{A}\bar{I}\tilde{I} \tag{3.15}$$

where, for convenience, we have made the substitution $MC_{LC} = (M_L C_L + M_C C_C)$. Then, collecting like terms, we have

$$MC_{LC}\dot{\tilde{T}}_L + \left(\frac{kA}{L} + \alpha\bar{I}\right)\tilde{T}_L = \frac{kA}{L}\tilde{T}_H + \left(\frac{\rho L}{A}\bar{I} - \alpha\bar{T}_L\right)\tilde{I} \tag{3.16}$$

Putting into standard form, we have the following:

$$\frac{MC_{LC}}{\frac{kA}{L} + \alpha\bar{I}}\dot{\tilde{T}}_L + \tilde{T}_L = \left(\frac{\frac{kA}{L}}{\frac{kA}{L} + \alpha\bar{I}}\right)\tilde{T}_H + \left(\frac{\frac{\rho L}{A}\bar{I} - \alpha\bar{T}_L}{\frac{kA}{L} + \alpha\bar{I}}\right)\tilde{I} \tag{3.17}$$

In this standard form, we can see that the *time constant* of the cold-side of the system (i.e. the time when the response is $1/e$ times the initial value, often denoted by the symbol τ) is

$$\tau_L = \frac{MC_{LC}}{\frac{kA}{L} + \alpha\bar{I}} \tag{3.18}$$

The time constant shows us that the operating point chosen for the applied current $\bar{I}$ affects the rate at which the system will respond to a forcing function. Eq. 3.18 also indicates that the materials and geometry of the whole system are important factors in the rate of heat transfer on the cold-side.

Next we can take the hot-side equation as given by Eq. 3.14 and multiply out all terms, to obtain the following:

$$MC_{FH}\dot{\tilde{T}}_H = -\frac{kA}{L}\tilde{T}_H + \frac{kA}{L}\tilde{T}_L + \alpha\bar{I}\tilde{T}_H + \alpha\tilde{I}\bar{T}_H + \frac{\rho L}{A}\bar{I}\tilde{I} \tag{3.19}$$

where we make a similar substitution as previously done with the cold-side; $MC_{FH} = M_F C_F + M_H C_H$. Then, collecting like terms, we have

$$MC_{FH}\dot{\tilde{T}}_H + \left(hA_F + \frac{kA}{L} - \alpha\bar{I}\right)\tilde{T}_H = \frac{kA}{L}\tilde{T}_L + \left(\alpha\bar{T}_H + \frac{\rho L}{A}\bar{I}\right)\tilde{I} \tag{3.20}$$

Putting into standard form, we have the following:

$$\left(\frac{MC_{FH}}{hA_F + \frac{kA}{L} - \alpha\bar{I}}\right)\dot{\tilde{T}}_H + \tilde{T}_H = \left(\frac{\frac{kA}{L}}{hA_F + \frac{kA}{L} - \alpha\bar{I}}\right)\tilde{T}_L + \left(\frac{\alpha\bar{T}_H + \frac{\rho L}{A}\bar{I}}{hA_F + \frac{kA}{L} - \alpha\bar{I}}\right)\tilde{I} \tag{3.21}$$

The time constant of the hot-side can be seen from Eq.3.21 to be

$$\tau_H = \frac{MC_{FH}}{hA_F + \frac{kA}{L} - \alpha\bar{I}} \tag{3.22}$$

As in the case for the cold-side, the hot-side time constant is dependent on the operating point value of the applied current, $\bar{I}$, and on the materials and geometry of the system.

3.5 The TEC Model state-variable representation

The linear time-invariant system of Eqs. 3.13 and 3.14 may be represented in the more compact, state-variable form as a set of first-order differential equations, expressed as vector-matrix differential equations of the form

$$\dot{x}(t) = f\left[x(t), u(t), t\right] \tag{3.23}$$

where $x(t)$ is an n-dimensional state vector;
$u(t)$ is an r-dimensional control vector;
f is the system function, and
t is time.

With consideration to the physical signals present in the thermoelectric system, an appropriate state vector may be chosen as

$$x(t) = \left[\ \tilde{T}_L(t) \quad \tilde{T}_H(t)\ \right]^T \tag{3.24}$$

First considering the cold-side representation in Eq.3.17, the state-variable form can be written as

$$\dot{\tilde{T}}_L = -\left(\frac{\frac{kA}{L}+\alpha\bar{I}}{MC_{LC}}\right)\tilde{T}_L + \left(\frac{\frac{kA}{L}}{MC_{LC}}\right)\tilde{T}_H + \left(\frac{\frac{\rho L}{A}\bar{I}-\alpha\bar{T}_L}{MC_{LC}}\right)\tilde{I} \tag{3.25}$$

The state-variable form of the hot-side representation in Eq.3.21 can be similarly written as

$$\dot{\tilde{T}}_H = \left(\frac{-\left(hA_F+\frac{kA}{L}-\alpha\bar{I}\right)}{MC_{FH}}\right)\tilde{T}_H + \left(\frac{\frac{kA}{L}}{MC_{FH}}\right)\tilde{T}_L + \left(\frac{\alpha\bar{T}_H+\frac{\rho L}{A}\bar{I}}{MC_{FH}}\right)\tilde{I} \tag{3.26}$$

Then, identifying $\tilde{T}_L$ as x_1, $\tilde{T}_H$ as x_2, and $\tilde{I}$ as u, the state-variable representation as an equation set can be written as Eq. 3.27

$$\begin{aligned} \dot{x_1} &= \left(\frac{-\left(\frac{kA}{L}+\alpha\bar{I}\right)}{MC_{LC}}\right)x_1 + \left(\frac{\frac{kA}{L}}{MC_{LC}}\right)x_2 + \left(\frac{\frac{\rho L}{A}\bar{I}-\alpha\bar{T}_L}{MC_{LC}}\right)u \\ \dot{x_2} &= \left(\frac{\frac{kA}{L}}{MC_{FH}}\right)x_1 + \left(\frac{-\left(hA_F+\frac{kA}{L}-\alpha\bar{I}\right)}{MC_{FH}}\right)x_2 + \left(\frac{\alpha\bar{T}_H+\frac{\rho L}{A}\bar{I}}{MC_{FH}}\right)u \end{aligned} \tag{3.27}$$

For the real physical TEC system, these equations are nonlinear and time-varying. For the linearised, stationary system model, the general expression for the system equations are [99]

$$\begin{aligned} \dot{x}(t) &= Ax(t) + Bu(t) \\ y(t) &= Cx(t) \end{aligned} \tag{3.28}$$

where A = n by n time-invariant system matrix
B = n by r control matrix
C = m by n output matrix
y = m-dimensional output vector

For the derived TEC model, the system matrix A can be written as

$$A = \begin{bmatrix} \left(\frac{-\left(\frac{kA}{L}+\alpha\bar{I}\right)}{MC_{LC}}\right) & \left(\frac{\frac{kA}{L}}{MC_{LC}}\right) \\ \left(\frac{\frac{kA}{L}}{MC_{FH}}\right) & \left(\frac{-\left(hA_F+\frac{kA}{L}-\alpha\bar{I}\right)}{MC_{FH}}\right) \end{bmatrix} \tag{3.29}$$

and the control input matrix B can be written as

$$B = \begin{bmatrix} \left(\frac{\frac{\rho L}{A}\bar{I} - \alpha \bar{T}_L}{MC_{LC}} \right) \\ \left(\frac{\frac{\rho L}{A}\bar{I} + \alpha \bar{T}_H}{MC_{FH}} \right) \end{bmatrix} \tag{3.30}$$

while a suitable output vector y for the TEC system analysis is

$$y = [\ \tilde{T}_L \quad \tilde{T}_H\ ]^T \tag{3.31}$$

The system representation in state-space as given in Eqs. 3.29 and 3.30 will henceforth be referred to as the 'TEC Model' in this thesis.

3.6 Verification and validation of the TEC Model

We will be using the TEC Model derived in section 3.4 for the controller design in Chapter 5 and eventually as the actuator for the pyroelectric system in Chapter 6. Decisions will be based on this model, so we are now concerned with whether the TEC Model and its results are correct. This concern is addressed through model verification and validation in section 3.6.

Model verification is often defined as "ensuring that the computer program of the computerized model and its implementation are correct" and is the definition adopted in this thesis. *Model validation* is usually defined to mean "substantiation that a computerized model within its domain of applicability possesses a satisfactory range of accuracy consistent with the intended application of the model" and is the definition used in this thesis [84].

3.6.1 The Huang model of the TEC [50]

As part of our verification and validation, the outputs of the derived TEC Model will be compared to another simulation model developed by Huang, which has been validated against experimental data. In 1999 B.J. Huang and C.L. Duang published their work on the system dynamic model and temperature control of a thermoelectric cooler [50]. The TEC Model we developed in section 3.4 is for the analysis of a pair of thermoelectric elements. However, Huang's model consists of many pairs of thermoelectric elements, and considers the energy balance to the thermoelectric material, and while this makes it more mathematically complex than required for our application, it should be a more accurate model against which to verify the results of our TEC Model. Both models consider the effect of the thermal masses connected at the cold- and hot-sides of the thermoelectric module and so can be simulated to produce directly comparable outputs. In addition, Huang carried out a set of

experiments to verify his system dynamic model of a thermoelectric cooler using the system identification; we can also make use of these results to further experimentally verify our TEC Model. Huang's model has been successfully used by several groups in later work developing various controllers for thermoelectric coolers [50, 73, 86].

The equations that follow in this section are those that have been developed by Huang and Duang in their manuscript [50]. It is worth noting that we are taking the time to report Huang's equations in full here as they are required to support later discussions in this chapter with reference to potential errors.

The governing describing equation for the energy balance to the cold-end plate and the cooling-load is reported in [50] as

$$(M_L C_L + M_C C_C)\frac{dT_L}{dt} = Q_L - kA\frac{\partial T(x,t)}{\partial x}|_{x=0} - \alpha_{pn} I T_L \tag{3.32}$$

where α_{pn} is the Seebeck coefficient of the thermoelectric material [V/K], and all the other terms are as previously defined.

In [50] the energy balance to the thermoelectric material is reported in the following relation

$$C\gamma\frac{\partial T(x,t)}{\partial t} = k\frac{\partial^2 T(x,t)}{\partial x^2} - \frac{\tau}{A} I\frac{\partial T(x,t)}{\partial x} + \frac{\rho}{A^2} I^2 \tag{3.33}$$

where γ is the mean density of the thermoelectric material [kgm^{-3}] and,
τ is the Thomson coefficient [VK^{-1}].

The energy balance to the heat sink and the hot-side plate is reported as

$$(M_F C_F + M_H C_H)\frac{dT_K}{dt} = I\alpha_{pn} T_H - kA\frac{\partial T(x,t)}{\partial t}|_{x=L} - hA_F(T_H - T_a) \tag{3.34}$$

Linearisation is carried out around a steady-state value. The variables of the thermoelectric cooler are written as the summation of a steady-state value and a perturbed quantity, as in Eq. 3.8 with $T(x,t) = \bar{T}(x) + \tilde{T}(x,t)$

Using an approximate relation of the Seebeck coefficient according to a Taylor's series expansion, the following equations are reported:

$$k\frac{\partial^2 \tilde{T}}{\partial x^2} - \frac{\tau \bar{I}}{A}\frac{\partial \tilde{T}}{\partial x} + \left[\frac{2\rho \bar{I}}{A^2} - \frac{\tau(\bar{T}_H - \bar{T}_L)}{AL}\right]\tilde{I} = C\gamma\frac{\partial \tilde{T}}{\partial t} \tag{3.35}$$

$$(M_L C_L + M_C C_C)\frac{d\tilde{T}_L}{dt} = \tilde{Q}_L(t) - kA\frac{\partial \tilde{T}}{\partial x}|_{x=0} - (\tau + \alpha_L)\bar{I}\tilde{T}_L - \alpha_L \tilde{I}\bar{T}_L \tag{3.36}$$

$$(M_F C_F + M_H C_H)\frac{d\tilde{T}_H}{dt} = (\tau + \alpha_H)\bar{I}\tilde{T}_H + \alpha_H \tilde{I}\bar{T}_H - kA\frac{\partial \tilde{T}(x,t)}{\partial x}|_{x=L} - hA_F(\tilde{T}_H + \tilde{T}_a) \tag{3.37}$$

Following application of Laplace transforms to solve the thermoelectric PDE, the Huang Model is reported as:

$$G_I(s) = \frac{N(s)}{sD(s)} \tag{3.38}$$

where

$$\begin{aligned} N(s) = &\{Akq\,[\alpha_L \bar{T}_L \cosh(qL) - \alpha_H \bar{T}_H] + \alpha_L \bar{T}_L E_H \sinh(qL)\}\, s \\ &+ \frac{Akq\beta}{C\gamma}\,[E_H\,(1 - \cosh(pL)) - Akp \sinh(pL)] \end{aligned} \tag{3.39}$$

$$D(s) = AkqE_L \cosh(qL) + E_H E_L \sinh(qL) + AkqE_H \cosh(pL) + A^2 k^2 pq \sinh(pL) \tag{3.40}$$

$$\begin{aligned} p(s) = &\frac{\frac{\tau \bar{I}}{A} + \sqrt{\frac{\tau^2 \bar{I}^2}{A^2} + 4kC\gamma s}}{2k} \\ q(s) = &\frac{\frac{\tau \bar{I}}{A} - \sqrt{\frac{\tau^2 \bar{I}^2}{A^2} + 4kC\gamma s}}{2k} \end{aligned} \tag{3.41}$$

$$E_L(s) = (M_L C_L + M_C C_C)s + (\tau + \alpha_L)\bar{I} \tag{3.42}$$

$$E_H(s) = (M_F C_F + M_H C_H)s + hA_F - (\tau + \alpha_L)\bar{I} \tag{3.43}$$

$$\beta = \left[\frac{2\rho \bar{I}}{A^2} - \frac{\tau(\bar{T}_H - \bar{T}_L)}{AL}\right] \tag{3.44}$$

A model reduction is then performed using the following approximations:

$$\alpha_H = \alpha_L = \alpha_{pn} \tag{3.45}$$

$$p(s) = q(s) = \lambda(s) = \sqrt{\frac{C\gamma s}{k}} \tag{3.46}$$

$$\sinh(\lambda L) \approx \lambda L \tag{3.47}$$

$$\cosh(\lambda L) \approx 1 + \frac{\lambda^2 L^2}{2} \tag{3.48}$$

The reduced model is then found to be

$$G_I(s) = \frac{\tilde{T}_L}{\tilde{I}} = -K \frac{\frac{s}{z} + 1}{\left[\frac{s}{p_1} + 1\right]\left[\frac{s}{p_2} + 1\right]} \tag{3.49}$$

where

$$K = \frac{\left\{Ak\alpha_{pn}(\bar{T}_H - \bar{T}_L) + L\alpha_{pn}^2 \bar{I}\bar{T}_L \left(\frac{\rho L^2 h A_F}{A} + 2\rho L k\right)\bar{I} + \frac{\rho L^2 \alpha_{pn}}{A}\bar{I}^2 + L\alpha_{pn} h A_F \bar{T}_L\right\}}{AA_F hk + LhA_F \alpha_{pn}\bar{I} - L\alpha_{pn}^2 \bar{I}^2} \tag{3.50}$$

$$z = \frac{AA_F hk + LhA_F \alpha_{pn}\bar{I} - L\alpha_{pn}^2 \bar{I}^2}{\left\{\left[\frac{1}{2}A\alpha_{pn}L^2 C\gamma + L\alpha_{pn}\left(M_F C_F + M_H C_H\right)\right]\bar{T}_L - \frac{\rho L^2}{A}\left(M_F C_F + M_C C_C\right)\bar{I}\right\}} \tag{3.51}$$

$$p_{1,2} = a_{pn} \pm \sqrt{\alpha^2 - b^2} \tag{3.52}$$

It is noted here that in the equivalent of Eq. 3.52 in [50] the symbol α is used rather than α_{pn}. It is assumed that this is a typographical error.

$$a = \frac{\left\{\begin{array}{r} Ak(M_F C_F + M_L C_L + M_C C_C + M_H C_H) + LhA_F(M_L C_L + M_C C_C) \\ + AC\gamma L(Ak + \frac{1}{2}hA_F L) + L\alpha_{pn}(M_F C_F + M_L C_L)\bar{I} \end{array}\right\}}{\left\{\begin{array}{r} AL^2 C\gamma(M_F C_F + M_L C_L + M_C C_C + M_H C_H) \\ + 2L\left(M_F C_F + M_H C_H\right)\left(M_L C_L + M_C C_C\right) \end{array}\right\}} \tag{3.53}$$

$$b = \frac{AA_F hk + LhA_F \alpha_{pn}\bar{I} - L\alpha_{pn}^2 \bar{I}^2}{\left\{\begin{array}{r} \frac{1}{2}AL^2 C\gamma(M_F C_F + M_L C_L + M_C C_C + M_H C_H) \\ + L\left(M_F C_F + M_H C_H\right)\left(M_L C_L + M_C C_C\right) \end{array}\right\}} \tag{3.54}$$

The transfer function model $G_I(s)$ will be henceforth referred to as the 'Huang Model' in this thesis.

The derived TEC Model, given by Eqs. 3.29 and 3.30 in section 3.4, was transformed from a state-space representation to transfer function form. The resultant TEC Model structure was identified to be the same as Eq. 3.49, i.e. both models consist of two poles and one zero.

Simulation of the Huang Model

The next step is to simulate the Huang Model (Eqs. 3.32 to 3.54) in MATLAB in readiness for comparison with our TEC Model and for the purpose of verification. Huang used the values for a typical thermoelectric cooler that have been summarised in table 3.1. Table 3.2 is provided for the purpose of comparing the simulated Huang Model parameter values with those reported and published in Fig. 3.2. The parameter values compared are the model gain K, zero z, and the two poles p_1 and p_2, with reference to the common model $G_I(s)$ structure given in Eq. 3.49. The model steady-state operating point values used for this comparison are $\bar{I} = 1\,A$, $\bar{T_L} = 273$ K and $\bar{T_H} = 273$ K.

Comparison of the values shown in table 3.2 shows:

1. The values of the gains K are in good agreement.
2. The value of the zero z is not in agreement; however, it shows a similar order of magnitude.
3. The values of the poles for the Huang Model are much larger than logically expected for the type of thermal system. These values of poles indicate system time constants of ~ 7 ms, which is rather quick for a typical thermal system. It is known from our initial experiments that TEC time constants are expected to be in the high tens to low hundreds of seconds.
4. The values of the poles for the Huang Graph indicate system time constants of 83 seconds and 400 seconds; these are known to be more realistic values.

Here we can now report two potential mistakes in the published manuscript [50]:

1. The first error is with regard to the format of Eq. 3.49, which has been given in zero-pole-gain format. The value of gain K plotted in Fig. 3.2 and calculated from Eq. 3.50 is given for the standard transfer function form.

Parameter	Symbol	Value	Units
Mean density of the thermoelectric material	γ	200	kgm^{-3}
Mean electrical resistivity of the thermoelectric material	ρ	10^{-5}	Ω-m
Total cross-sectional area of the thermoelectric material	A	0.00145	m^2
Seebeck coefficient of thermoelectric material	α_{pn}	0.02	VK^{-1}
Mean thermal conductivity of the thermoelectric p-n pair	k	1.5	$Wm^{-1}K^{-1}$
Length of the thermoelectric elements	L	0.0025	m
Mass of the cold-end and hot-end plate of thermoelectric module	$M_C = M_H$	0.05	kg
Specific heat capacity of the cold-end and hot-end plate of thermoelectric module	$C_C = C_H$	500	$Jkg^{-1}K^{-1}$
Convective heat transfer coefficient of the heat sink	h	10	$Wm^{-2}K^{-1}$
Mass of the heat sink	M_F	0.4	kg
Specific heat capacity of heat sink	C_F	850	$Jkg^{-1}K^{-1}$
Total heat transfer surface area of the heat sink	A_F	0.3	m^2
Mass of the cooling-load heat exchanger	M_L	0.6	kg
Specific heat capacity of the cooling-load heat exchanger	C_L	400	$Jkg^{-1}K^{-1}$

Table 3.1 Table summarising the TEC values used by Huang [50]

Model	Gain K	Zero z	Pole 1 p_1	Pole 2 p_2
Huang Model	6.1358	0.0013	142.8971	142.8571
Huang Graph	6	0.008	0.0025	0.012

Table 3.2 Comparison of simulated parameter values for the Huang Model and Huang Graph

2. The second error is with regard to Eqs. 3.52, 3.53 and 3.54 calculating the values of the poles, p_1 and p_2. Simulation of the system in MATLAB would indicate that these equations likely calculate the inverse of the poles, i.e. the system time constants. It is thought that the published values in Fig. 3.2 are correct values for the poles. More analysis to support this claim will be carried out when comparing the values for our TEC Model.

The corrected values are now compared in table 3.3. There are now two more problems to be seen with the newly calculated parameter values:

1. The values for the Huang Model and Huang Graph are not exactly the same.

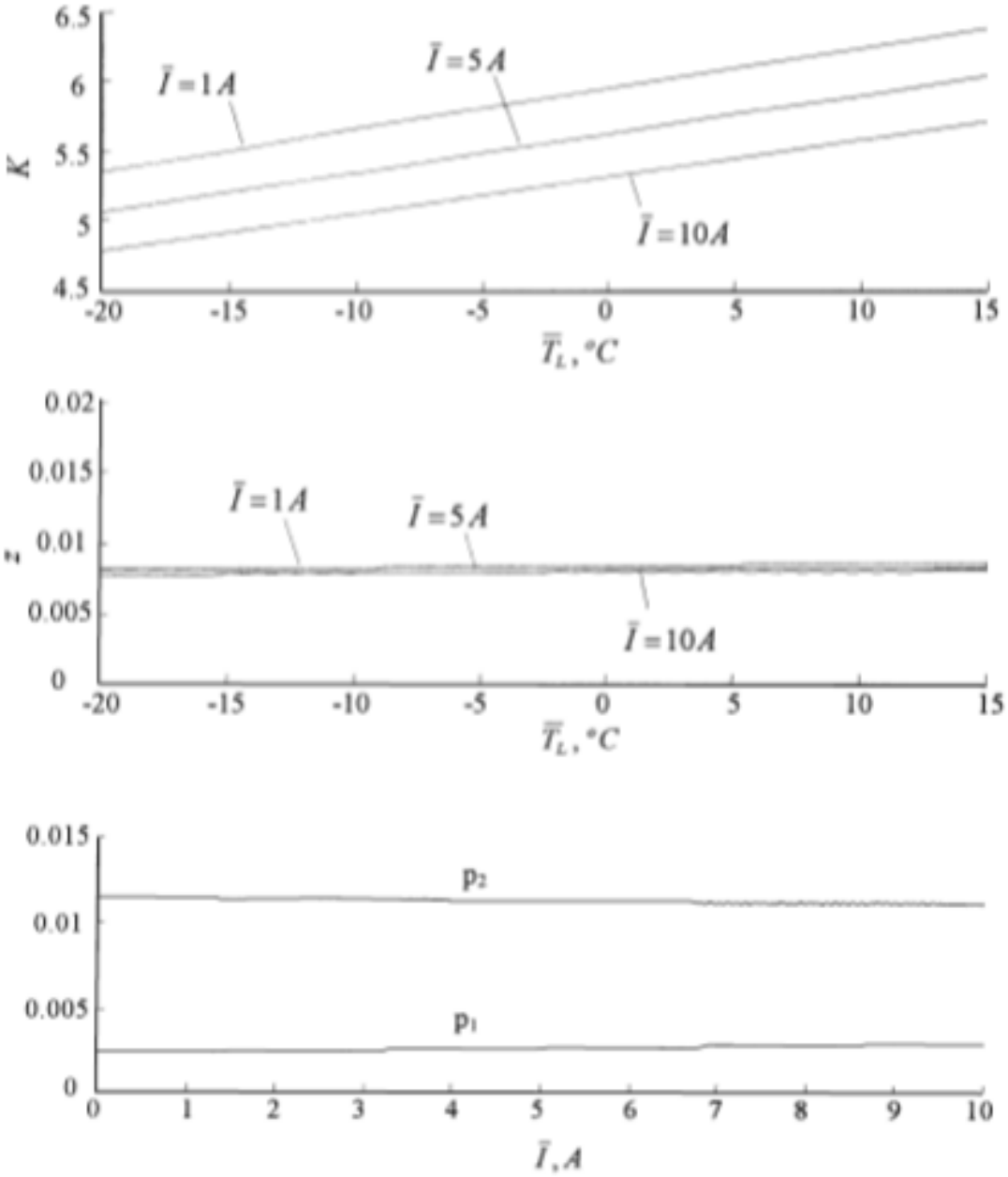

Fig. 3.2 The reported graphed output of the Huang Model [50], referred to in this thesis as the Huang Graph

2. The values for the Huang Model give $p_1 \approx p_2$, but, as we have different thermal masses on the hot- and cold-side, we expect different time constants in the system.

We are using the Huang Model for verification and validation, hence it was decided that it would be prudent to check the correctness of Eqs. 3.35-3.54. We worked through

the equations and section 3.6.2 reports the intermediate steps in the derivation of Huang's mathematics.

Model	Gain K	Zero	Pole 1	Pole 2
Huang Model	**0.22449**	0.001339	**0.006998**	**0.007**
Huang Graph	**0.022**	0.008	0.012	0.0025

Table 3.3 Comparison of the TEC Model parameters with Huang Model and Huang Graph

3.6.2 Derivation of the Huang Model

This section is dedicated to deriving the structural form and numerical correctness of the Huang Model [50], which has not been done in any of the later works that depend on it [73, 86]. In the manuscript [50], it is stated that linearisation is carried out by substituting Eqs. 3.8 into Eq. 3.33 to linearise the energy balance to the thermoelectric material. This substitution yields

$$C\gamma\frac{\partial(\bar{T}+\tilde{T})}{\partial t} = k\frac{\partial^2(\bar{T}+\tilde{T})}{\partial x^2} - \frac{\tau}{A}(\bar{I}+\tilde{I})\frac{\partial(\bar{T}+\tilde{T})}{\partial x} + \frac{\rho}{A^2}(\bar{I}+\tilde{I})^2 \tag{3.55}$$

which can be expanded to give

$$\begin{aligned} C\gamma\left[\frac{\partial\bar{T}}{\partial t}+\frac{\partial\tilde{T}}{\partial t}\right] = k\left[\frac{\partial^2\bar{T}}{\partial x^2}+\frac{\partial^2\tilde{T}}{\partial x^2}\right] - \frac{\tau}{A}\left[\bar{I}\frac{\partial\bar{T}}{\partial x}+\bar{I}\frac{\partial\tilde{T}}{\partial x}+\tilde{I}\frac{\partial\bar{T}}{\partial x}+\tilde{I}\frac{\partial\tilde{T}}{\partial x}\right] \\ + \frac{\rho}{A^2}\left[\bar{I}^2+2\bar{I}\tilde{I}+\tilde{I}^2\right] \end{aligned} \tag{3.56}$$

It is stated in [50] that a linear steady-state temperature distribution in the thermoelectric material can be assumed, such that

$$\frac{d\bar{T}(x)}{dx} = \frac{(\bar{T_H}-\bar{T_L})}{L} \tag{3.57}$$

It is also stated that we can ignore the high-order terms, and eliminate the steady-state term, which leads to

$$k\frac{\partial^2\tilde{T}}{\partial x^2} - \frac{\tau\bar{I}}{A}\frac{\partial\tilde{T}}{\partial x} + \left[\frac{2\rho\bar{I}}{A^2} - \frac{\tau(\bar{T_H}-\bar{T_L})}{AL}\right]\tilde{I} = C\gamma\frac{\partial\tilde{T}}{\partial t} \tag{3.58}$$

Equation 3.58 agrees with Eq. 3.35.

We now linearise Eq. 3.32, by the same method. It is stated in [50] that we can use the approximate relation of the Seeback coefficient according to a Taylor's series expansion:

$$\alpha_{pn}(T) = \alpha_L + \frac{\tau}{\bar{T}_L}\tilde{T}_L = \alpha_H + \frac{\tau}{\bar{T}_H}\tilde{T}_H \tag{3.59}$$

Substitution of Eqs. 3.8 and 3.59 into Eq. 3.32 yields

$$\begin{aligned}(M_L C_L + M_C C_C)\frac{d(\bar{T}_L + \tilde{T}_L(t))}{dt} &= (\bar{Q}_L + \tilde{Q}_L(t)) - kA\frac{\partial(\bar{T} + \tilde{T(x)}(x,t))}{\partial x}|_{x=0} \\ &- (\bar{I} + \tilde{I}(t))\left(\alpha_L + \frac{\tau}{\bar{T}_L}\tilde{T}_L(t)\right)(\bar{T}_L + \tilde{T}_L(t))\end{aligned} \tag{3.60}$$

Expanding Eq. 3.60 yields

$$\begin{aligned}(M_L C_L + M_C C_C)\frac{d\bar{T}_L}{dt} + (M_L C_L + M_C C_C)\frac{d\tilde{T}_L}{dt} &= \\ \bar{Q}_L + \tilde{Q}_L(t) - kA\frac{\partial\bar{T}}{\partial x}|_{x=0} - kA\frac{\partial\tilde{T}}{\partial x}|_{x=0} \\ - \alpha_L\bar{I}\bar{T}_L - \tau\bar{I}\tilde{T}_L - \alpha_L\bar{I}\tilde{T}_L - \frac{\tau}{\bar{T}_L}\bar{I}\tilde{T}_L{}^2 \\ - \alpha_L\tilde{I}\bar{T}_L - \tau\tilde{I}\tilde{T}_L - \alpha_L\tilde{I}\tilde{T}_L - \frac{\tau}{\bar{T}_L}\tilde{I}\tilde{T}_L{}^2\end{aligned} \tag{3.61}$$

Again, we can ignore the high-order terms and eliminate the steady-state terms to obtain

$$(M_L C_L + M_C C_C)\frac{d\tilde{T}_L}{dt} = \tilde{Q}_L(t) - kA\frac{\partial\tilde{T}}{\partial x}|_{x=0} - \tau\bar{I}\tilde{T}_L - \alpha_L\bar{I}\tilde{T}_L - \alpha_L\tilde{I}\bar{T}_L \tag{3.62}$$

Collecting the $\bar{I}\tilde{T}_L$ terms on the right-hand side yields

$$(M_L C_L + M_C C_C)\frac{d\tilde{T}_L}{dt} = \tilde{Q}_L(t) - kA\frac{\partial\tilde{T}}{\partial x}|_{x=0} - (\tau + \alpha_L)\bar{I}\tilde{T}_L - \alpha_L\tilde{I}\bar{T}_L \tag{3.63}$$

Equation 3.63 agrees with Eq. 3.36.

We now linearise Eq. 3.34, the energy balance to the hot-side of the thermoelectric cooler, by the same method. Substitution of Eqs. 3.8 and 3.59 into Eq. 3.34 yields

$$
\begin{aligned}
(M_F C_F + M_H C_H)\frac{d(\bar{T_H} + \tilde{T_H})}{dt} &= (\bar{I} + \tilde{I})\left(\alpha_H + \frac{\tau}{\bar{T_H}}\tilde{T_H}\right)(\bar{T_H} + \tilde{T_H}) \\
&- kA\frac{\partial(\bar{T}(x) + \tilde{T}(x,t))}{\partial x}|_{x=L} \\
&- hA_F((\bar{T_H} + \tilde{T_H}) - (\bar{T_a} + \tilde{T_a}))
\end{aligned} \tag{3.64}
$$

Expanding yields

$$
\begin{aligned}
(M_F C_F + M_H C_H)\frac{d\bar{T_H}}{dt} + (M_F C_F + M_H C_H)\frac{d\tilde{T_H}}{dt} &= \\
\bar{I}\bar{T_H}\alpha_H + \bar{I}\tau\tilde{T_H} + \bar{I}\alpha_H\tilde{T_H} + \bar{I}\frac{\tau}{\bar{T_H}}\tilde{T_H}^2 \\
+ \alpha_H\tilde{I}\bar{T_H} + \tau\tilde{I}\tilde{T_H} + \alpha_H\tilde{I}\tilde{T_H} + \frac{\tau}{\bar{T_H}}\tilde{T_H}^2\tilde{I} \\
- kA\frac{\partial\bar{T}(x)}{\partial x}|_{x=L} - kA\frac{\partial\tilde{T}(x,t)}{\partial x}|_{x=L} \\
- hA_F\bar{T_H} - hA_F\tilde{T_H} + hA_F\bar{T_a} + hA_F\tilde{T_a}
\end{aligned} \tag{3.65}
$$

We may ignore the high-order terms and eliminate the steady-state terms to obtain

$$
(M_F C_F + M_H C_H)\frac{d\tilde{T_H}}{dt} = \tau\bar{I}\tilde{T_H} + \alpha_H\bar{I}\tilde{T_H} + \alpha_H\tilde{I}\bar{T_H} - kA\frac{\partial\tilde{T}(x,t)}{\partial x}|_{x=L} - hA_F\tilde{T_H} + hA_F\tilde{T_a} \tag{3.66}
$$

Collecting the $\bar{I}\tilde{T_L}$ terms and the hA_F terms on the right-hand side yields

$$
(M_F C_F + M_H C_H)\frac{d\tilde{T_H}}{dt} = (\tau + \alpha_H)\bar{I}\tilde{T_H} + \alpha_H\tilde{I}\bar{T_H} - kA\frac{\partial\tilde{T}(x,t)}{\partial x}|_{x=L} - hA_F(\tilde{T_H} + \tilde{T_a}) \tag{3.67}
$$

Equation 3.67 agrees with Eq. 3.37. We have derived Eqs. 3.35, 3.36 and 3.37, which are reported in [50].

Next, the manuscript states that these equations can be solved by Laplace transforms to obtain the transfer function of the perturbed cold-end temperature $\tilde{T_L}$. This technique results in a transformation of the PDE equation in space and time into an ordinary differential equation in space, which can then be solved by conventional methods. When the Laplace transforms of Eqs. 3.58, 3.63, and 3.67 are computed, the following set of equations results:

$$k\tilde{T}_{xx}(x,s) - \frac{\tau\bar{I}}{A}\tilde{T}_x(x,s) - C\gamma sT(x,s) = \left[\frac{2\rho\bar{I}}{A^2} - \frac{\tau(\bar{T}_H - \bar{T}_L)}{AL}\right]\tilde{I} \tag{3.68}$$

$$kA\tilde{T}_x(0,s) = (M_L C_L + M_C C_C)s\tilde{T}_L(x,s) + (\alpha_L + \tau)\bar{I}\tilde{T}_L(x,s) + \alpha_L\tilde{I}(s)\bar{T}_L \tag{3.69}$$

$$-kA\tilde{T}_x(L,s) = (M_F C_F + M_H C_H)s\tilde{T}_H(x,s) - (\tau + \alpha_H)\bar{I}\tilde{T}_H + hA_F\tilde{T}_H(x,s) + \alpha_H\tilde{I}(s)\bar{T}_H \tag{3.70}$$

Where, in accordance with statements in [50], we can let the change in load $\tilde{Q}_L = 0$ and the change in ambient temperature $\tilde{T}_a = 0$.

Equation 3.68 must be solved for the element temperature as a function of the space coordinate x. After the boundary conditions are applied to determine the constants of integration, the temperature at $x = 0$ can be evaluated. The solution of the differential equation by classical methods is straightforward [47]. The equation can be written in the following form:

$$k\tilde{T}_{xx}(x,s) - \frac{\tau\bar{I}}{A}\tilde{T}_x(x,s) - C\gamma sT(x,s) = \left[\frac{2\rho\bar{I}}{A^2} - \frac{\tau(\bar{T}_H - \bar{T}_L)}{AL}\right]\tilde{I} \tag{3.71}$$

The complete solution of this equation is:

$$\tilde{T}(x,s) = A_1(s)e^{px} + B_1(s)e^{qx} + \frac{\beta}{sC\gamma}\tilde{I}(s) \tag{3.72}$$

where A_1 and B_1 are constants, and p and q are the roots of Eq. 3.68. The following definitions are made for convenience:

$$\begin{aligned} p(s) &= \frac{\frac{\tau\bar{I}}{A} + \sqrt{\frac{\tau^2\bar{I}^2}{A^2} + 4kC\gamma s}}{2k} \\ q(s) &= \frac{\frac{\tau\bar{I}}{A} - \sqrt{\frac{\tau^2\bar{I}^2}{A^2} + 4kC\gamma s}}{2k} \end{aligned} \tag{3.73}$$

and

$$\beta = \left[\frac{2\rho\bar{I}}{A^2} - \frac{\tau(\bar{T}_H - \bar{T}_L)}{AL}\right] \tag{3.74}$$

Equation 3.74 agrees with Eq. 3.44.

At this stage, we note that we can make use of the same simplifications in notation that are reported in Eqs. 3.42 and 3.43, where

$$E_L(s) = (M_L C_L + M_C C_C)s + (\tau + \alpha_L)\bar{I} \tag{3.75}$$

and

$$E_H(s) = (M_F C_F + M_H C_H)s + hA_F - (\tau + \alpha_H)\bar{I} \tag{3.76}$$

The transfer function of interest is

$$G_I(s) = \frac{\tilde{T_L}(s)}{\tilde{I(s)}} \tag{3.77}$$

where $\tilde{T_{L0}}(s) = 0$ and $\tilde{T_H}$=0.

Since s is treated as a constant in the solution of the differential equations, the constants of integration $A_1(s)$ and $B_1(s)$, as well as the roots of the characteristic equation q and p are functions of s. They are not functions of x [47]. The boundary conditions that determine the two constants of integration are:

$$\begin{aligned} &\tilde{T}(L,s) = 0 \\ &E_L(s)\tilde{T_L} = -\alpha_L \tilde{I}\bar{T_L} + kA\tilde{T_x}(0,s) \end{aligned} \tag{3.78}$$

When Eq. 3.72 is substituted into Eqs. 3.78 a set of two equations in two unknown coefficients is obtained:

$$A_1 e^{pL} + B_1 e^{qL} = -\frac{\beta}{sC\gamma}\tilde{I} \tag{3.79}$$

and

$$A_1(E_L + kAp) + B_1(E_L + kAq) = \left(-E_L\frac{\beta}{sC\gamma} - \alpha_L \bar{T_L}\right)\tilde{I} \tag{3.80}$$

Solving Eqs. 3.79 and 3.80 yields the coefficients A_1 and B_1. Since the Eq. 3.71 is homogeneous for $\tilde{I} = 0$, each of the coefficients must have $\tilde{I}$ as a factor. Once A_1 and B_1 are known, the control function $G_I(s)$ can be evaluated from its definition [47]. That is

$$G_I(s) = \frac{\tilde{T}_L(s)}{\tilde{I}(s)} = \frac{A_1}{\tilde{I}} + \frac{B_1}{\tilde{I}} + \frac{\beta}{sC\gamma} \tag{3.81}$$

This procedure yields:

$$\frac{\tilde{T}_L}{\tilde{I}} = \frac{(A\beta kp - A\beta kq - A\beta kpe^{Lq} + A\beta kqe^{Lp} - CT_L\alpha\gamma se^{Lp} + CT_L\alpha\gamma se^{Lq})}{C\gamma s(E_L e^{Lp} - E_L e^{Lq} - Akpe^{Lq} + Akqe^{Lp})} \tag{3.82}$$

Re-writing yields:

$$\frac{\tilde{T}_L}{\tilde{I}} = \frac{\frac{A\beta k}{C\gamma}\left(p - q - pe^{Lq} + qe^{Lp}\right) - T_L\alpha(e^{Lp} - e^{Lq})s}{s\left[E_L(e^{Lp} - e^{Lq}) - Ak(pe^{Lq} - qe^{Lp})\right]} \tag{3.83}$$

The transfer function can be expressed in hyperbolic functions, when we recognise that

$$\begin{aligned} \cosh(nx) &= \frac{e^{nx} + e^{-nx}}{2} \\ \sinh(nx) &= \frac{e^{nx} - e^{-nx}}{2} \end{aligned} \tag{3.84}$$

then

$$e^{-nx} = \cosh(nx) - \sinh(nx) \tag{3.85}$$

The transfer function can now be expressed as

$$\frac{\tilde{T}_L}{\tilde{I}} = \frac{N(s)}{sD(s)} \tag{3.86}$$

where

$$\begin{aligned} N(s) =& (T_L\alpha[\cosh(Lq) - \cosh(Lp) + \sinh(Lq) - \sinh(Lp)]s \\ &+ \frac{A\beta k}{C\gamma}[p - q + p\cosh(Lq) + q\cosh(Lp) + q\sinh(Lp) - p\sinh(Lq)] \end{aligned} \tag{3.87}$$

and

$$\begin{aligned} D(s) =& (E_L(\cosh(Lp) - \cosh(Lq) + \sinh(Lp) - \sinh(Lq)) \\ &- Akp(\sinh(Lq) + Akp\cosh(Lq)) + Akq(\sinh(Lp) + \cosh(Lp)) \end{aligned} \tag{3.88}$$

Huang's publication [50] references Gray [47] who, in 1960, conducted the first small-signal analysis of a thermoelectric device. The device consisted of two elements of homogeneous thermoelectric semiconductors. From our studies of the presented Huang solutions, it would appear that he has followed the analysis process of Gray. In our derivation we used Huang's equations and applied the appropriate boundary conditions that were identified by Gray [47]. We consider that the A^2 terms in Huang's solution for $D(s)$ may originate from the definition of β, which incorporates a division through by A in [50]; however, in Gray's publication it does not.

There is good agreement between the general structure of our solution for one thermoelectric element, Eq. 3.83, and the solution presented by Gray [47] for two elements.

3.6.3 Verification and validation using the Huang Model

Three models will be compared:

1. The TEC Model - the thermoelectric cooler derived by this author in section 3.4 simulated in MATLAB.

2. The Huang Model - model derived by Huang and simulated in MATLAB using the published full equations [50].

3. The Huang Graph - model derived by Huang and simulated in MATLAB using the graphed output of the Huang Model reported in [50].

Comparison of the TEC Model parameters

The model parameters of the derived TEC Model were compared to the Huang Model and Huang Graph output values, as shown in table 3.4. Bolded entries indicate cells where the published number has been corrected in accordance with the correction of errors previously identified.

Model	Gain	Zero	Pole 1	Pole 2
TEC Model	0.020604	0.008164	0.01151	0.002398
Huang Model	**0.22449**	0.001339	**0.006998**	**0.007**
Huang Graph	**0.022**	0.008	0.012	0.0025

Table 3.4 Comparison of TEC Model parameters with the Huang Model and Huang Graph

The TEC Model parameters in table 3.4 show very good agreement with the Huang Graph, providing confidence in the validity of the derived model, and further supporting our suspicion of typographical mistakes in [50].

Comparison of the TEC Model frequency response

The frequency response of the Huang Model has also been published and is reprinted here in Fig. 3.3a. Before we discuss our specific system, we will take the time to introduce the basics of frequency response analysis that are required to understand the later discussions of our system analysis.

Frequency response analysis

One of the most commonly used techniques to analyse and design control systems is based upon the response of the system when subjected to a sinusoidal forcing function. Consider a forcing function of $\sin \omega t$ applied to the system represented by the transfer function $H(s) = A(s)/B(s)$, where $f_0(t)$ will be the output.

The Laplace transform of the input is

$$F_i(s) = \frac{\omega_0}{s^2 + \omega_0^2} \tag{3.89}$$

while the output transform is

$$F_0(s) = \frac{\omega_0}{s^2 + \omega_0^2} \frac{A(s)}{B(s)} \tag{3.90}$$

We can take partial fractions, and expand into the form

$$F_0(s) = \frac{\frac{1}{2j}\left[\frac{A(j\omega_0)}{B(j\omega_0)}\right]}{s - j\omega_0} + \frac{\frac{1}{-2j}\left[\frac{A(-j\omega_0)}{B(-j\omega_0)}\right]}{s + j\omega_0} + \frac{C(s)}{B(s)} \tag{3.91}$$

The first two terms of Eq.3.91 are complex conjugates, and the sum of the two is equal to twice the real part of either one. Therefore,

$$F_0(s) = \mathrm{Re}\left[\frac{\frac{A(j\omega_0)}{jB(j\omega_0)}}{(s - j\omega_0)}\right] + \frac{C(s)}{B(s)} \tag{3.92}$$

Now

$$\frac{A(j\omega_0)}{B(j\omega_0)} = H(j\omega_0) = |H(j\omega_0)|e^{j\theta} \tag{3.93}$$

Thus

$$F_0(s) = |H(j\omega_0)|\mathrm{Re}\left[\frac{e^{j\theta}}{j(s-j\omega_0)}\right] + \frac{C(s)}{B(s)} \tag{3.94}$$

where $C(s)/B(s)$ is the transient or homogeneous solution to the system differential equation. If the system is stable, the homogeneous solution is bounded and approaches zero over increasing time. The steady-state component of the solutions is represented by the function

$$F_{0ss}(s) = |H(j\omega)|\mathrm{Re}\left[\frac{e^{j\theta}}{j(s-j\omega_0)}\right] \tag{3.95}$$

This corresponds to a steady-state solution

$$f_{0ss}(t) = |H(j\omega_0)|\sin(\omega_0 t + \theta + \pi) \tag{3.96}$$

So, we can see that the steady-state output response of a linear system to a unit sinusoidal forcing function is a sine wave of the same frequency, only modified in amplitude and shifted in phase. Therefore, the magnitude response of a linear system is defined as the magnitude and phase angle of the transfer function with s replaced by $j\omega$. It also follows that, if we experimentally determine the frequency response of a linear system, we can ascertain its transfer function. In Chapter 6 we will use data from pyroelectric neutron generation experiments to determine various transfer functions of the system. For the reader interested in further information on the fundamentals of frequency response analysis there are many good standard textbooks available on the subject [30, 34].

When analysing the frequency response given in Fig. 3.3a a potential mistake can be identified. The error is with regard to the plotted phase change, which is from 80° at low frequency to 40° at high frequency. The reported total phase change of 40° for this system is not typical for the given structure of the Huang Model. For a system with two poles and one zero, a total phase change of 90° would be expected. With the purpose of comparing the TEC Model frequency response with that of the Huang Model, both were simulated using MATLAB. The resultant frequency responses are shown together in Fig. 3.3.

Comparison between Fig. 3.3a and Fig. 3.3b shows:

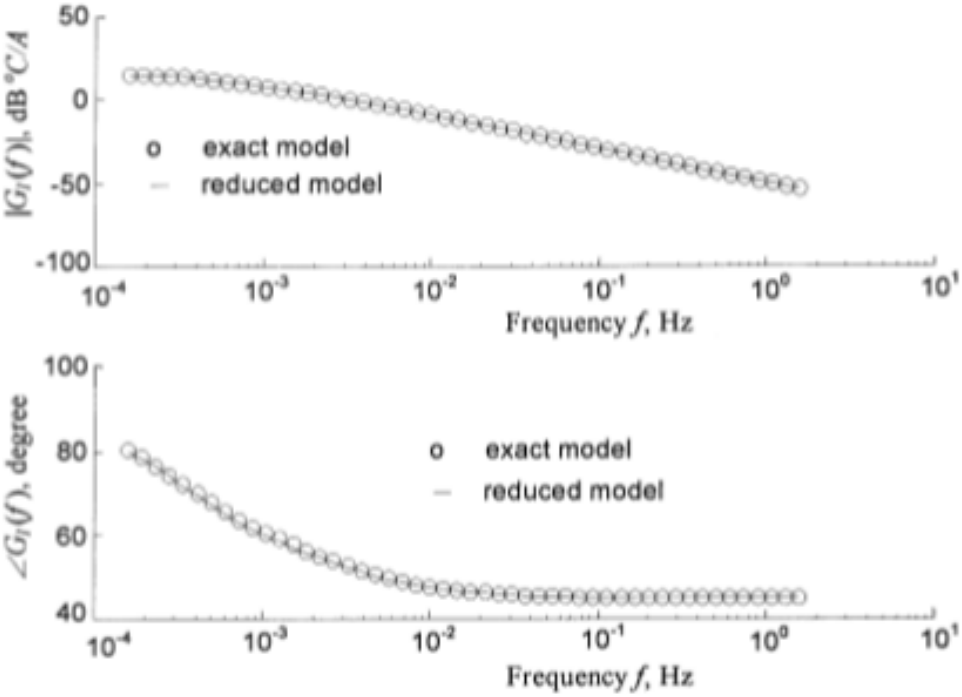

(a) Frequency response of the Huang Model [50].

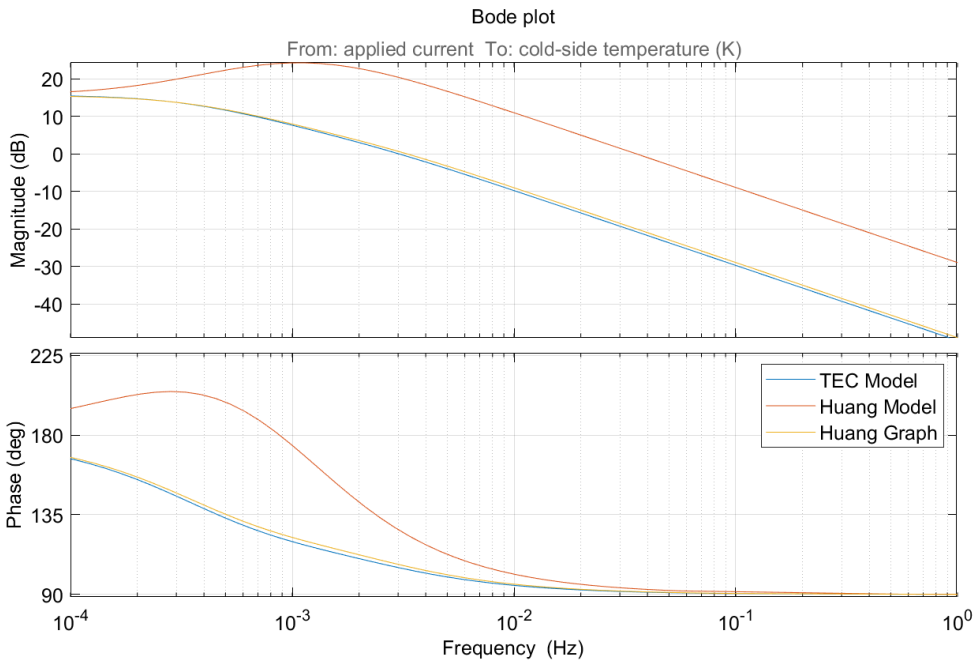

(b) Frequency response of the TEC Model, Huang Model and Huang Graph for comparison.

Fig. 3.3 Comparison of frequency responses of the TEC Model, the Huang Model and the Huang Graph.

1. The gain of the simulated Huang Graph in Fig. 3.3b and that published in Fig. 3.3a are in good agreement.

2. The phase is different for the two figures. The phase in Fig. 3.3b is closer to that expected for the structure of all the models, lending support to the suspicion of error in the frequency response in [50].

We can also see that the frequency response of the TEC Model and simulated Huang Graph shown in Fig. 3.3b are the same. This adds further confidence to the validity of the TEC Model.

The findings of this section lend support to the supposition that the errors are only typographical mistakes and therefore should not have any negative effect on the logical foundations, results or the conclusions of the publication.

3.6.4 Verification and validation using experimental data

The dynamic TEC Model derived theoretically in the present study may not be physically accurate due to many assumptions; experimental verification is therefore required. Huang performed an experimental verification of his model, and reported that the identified model parameters coincided with the test results well [50]. Huang used the experimental set-up shown in Fig. 3.4. We need to take account of the different cooling-load geometry in order to successfully model the frequency response of Huang's experiment. The new geometry results in a cooling-load mass of $M_L = 0.1134$ kg. The other parameters for Huang's experiment are the same as used for the model development, and these are summarised in table 3.1. Huang's experiment number 7 is chosen as this most closely replicates the type of conditions that would be used in pyroelectric neutron generator systems. The specific operating point values required to simulate the Huang Experiment are: $I = 3$ A; $\bar{T_L} = -14.4 + 273$ K; and $\bar{T_H} = 10 + 273$ K. The resulting frequency responses are shown in Fig. 3.5.

System	K	z	p_1	p_2
Huang Experiment	0.255	0.1319	0.0213	0.6600
TEC Model	0.075 (70)	0.1668 (-26)	0.01316 (38)	0.1725 (74)
Huang Model	0.5893 (-131)	0.003007 (98)	0.01761 (17)	0.01759 (97)

Table 3.5 Parameter values comparison for the Huang Experiment, Huang Model and TEC Model; percentage error is given in brackets.

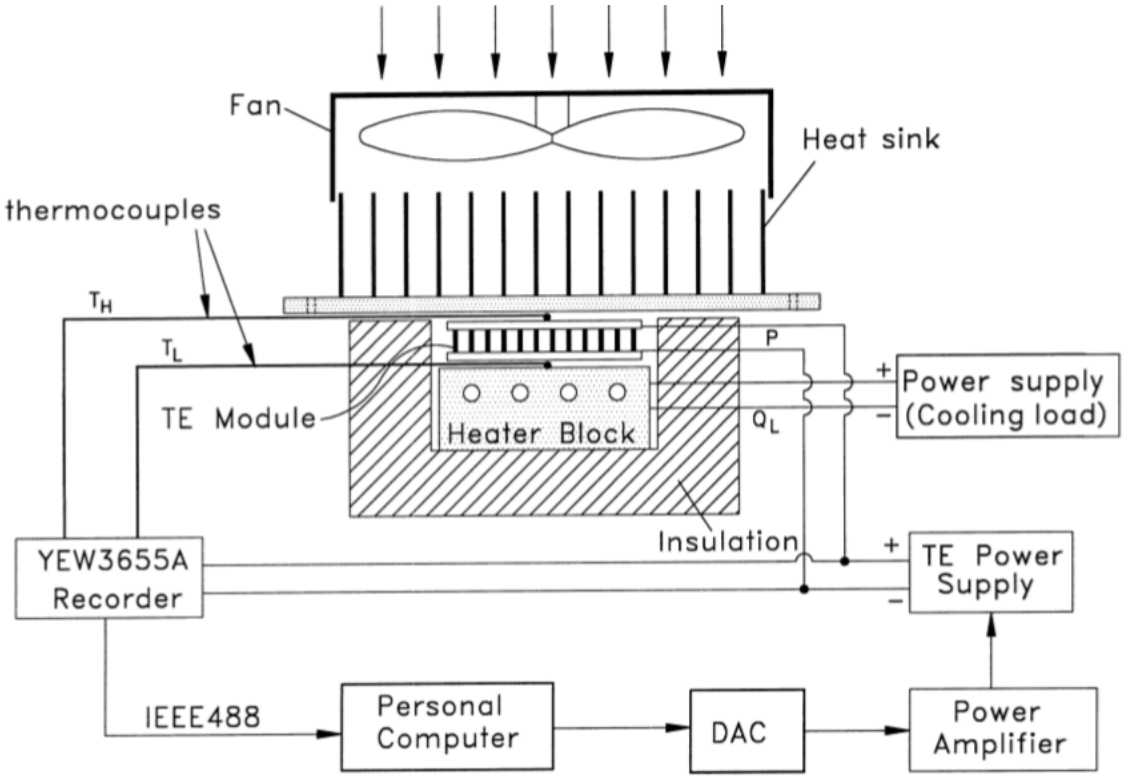

Fig. 3.4 Experimental set-up for system identification of a thermoelectric cooler used by Huang [50].

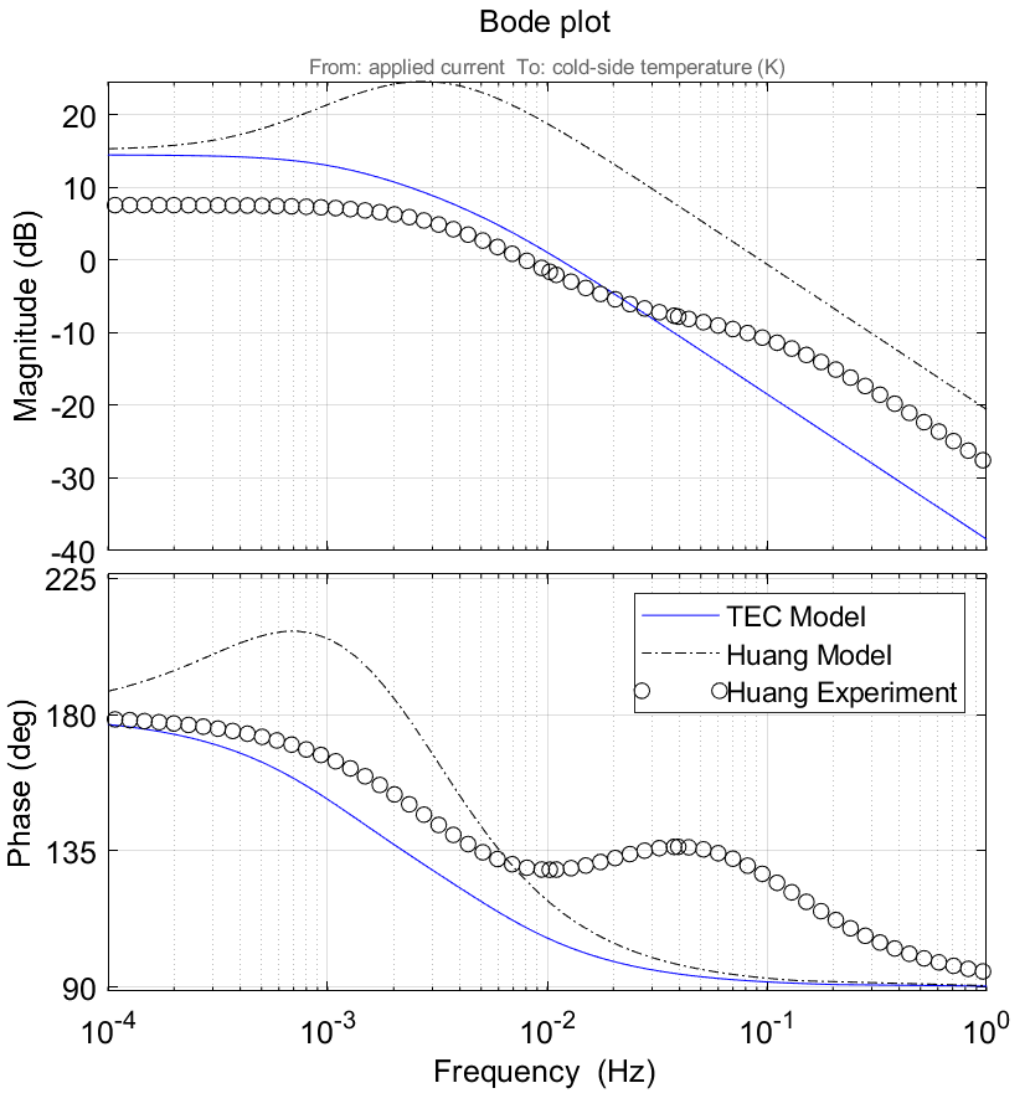

Fig. 3.5 Frequency response comparison of the TEC Model, Huang Model and Huang Experiment.

Note that percentage error values in table 3.5 are calculated using:

$$\frac{\text{experiment value} - \text{model value}}{\text{experiment value}} \times 100\% \tag{3.97}$$

Table 3.5 shows that the TEC Model has better agreement than Huang's Model with the experimental values determined by Huang through system identification methods. What is also important to note is that, at the critical frequency for control (the gain crossover at 0 dB, 10^{-2} Hz), the TEC Model gain matches the experiment. This agreement around crossover is important because modelling errors are most damaging near the gain crossover frequency. However, we see that the Huang Model appears to be worse - this further lends support to the suspicion that there are typographical errors in the reporting of these model equations.

3.7 Parameter variability-sensitivity analysis of the TEC Model

The dynamic model of a TEC is shown to vary with different operating conditions [18, 50, 86]. A parameter variation study of the TEC Model may be conducted in MATLAB using a sampling tuneable model. The selected operating point variations for this study are given by Eq. 3.98; evaluating the system for all combinations of these values results in an array of models. Each entry in the array is a state-space model that represents the system evaluated at the corresponding operating points.

$$\begin{aligned} \bar{T_L} &= [233\,K \quad 253\,K \quad 293\,K \quad 313\,K \quad 343\,K] \\ \bar{T_H} &= [233\,K \quad 253\,K \quad 293\,K \quad 313\,K \quad 343\,K] \\ \bar{I} &= [0\,A \quad 1\,A \quad 2\,A \quad 3\,A] \end{aligned} \tag{3.98}$$

In the following figures:

1. m11 (blue plots on figure) is the response of the model output cold-side temperature, $\tilde{T_L}$, for perturbations in the input applied current, $\tilde{I}$;

2. m12 (red plots on figure) is the response of the model output hot-side temperature, $\tilde{T_H}$, for perturbations in the input applied current, $\tilde{I}$.

3.7.1 The TEC Model step response

The step response plot shown in Fig. 3.6 demonstrates the effect of a step in applied current on the cold- and hot-plate temperatures of the TEC Model. It can clearly be seen that applying

a positive current causes the cold-end plate temperature T_L (m11, blue plot) to decrease, which allows heat to be absorbed from the cooling-load heat exchanger. The absorbed heat is then pumped across the TEC to the hot-end plate, which sees a rise in temperature (m12, red plot).

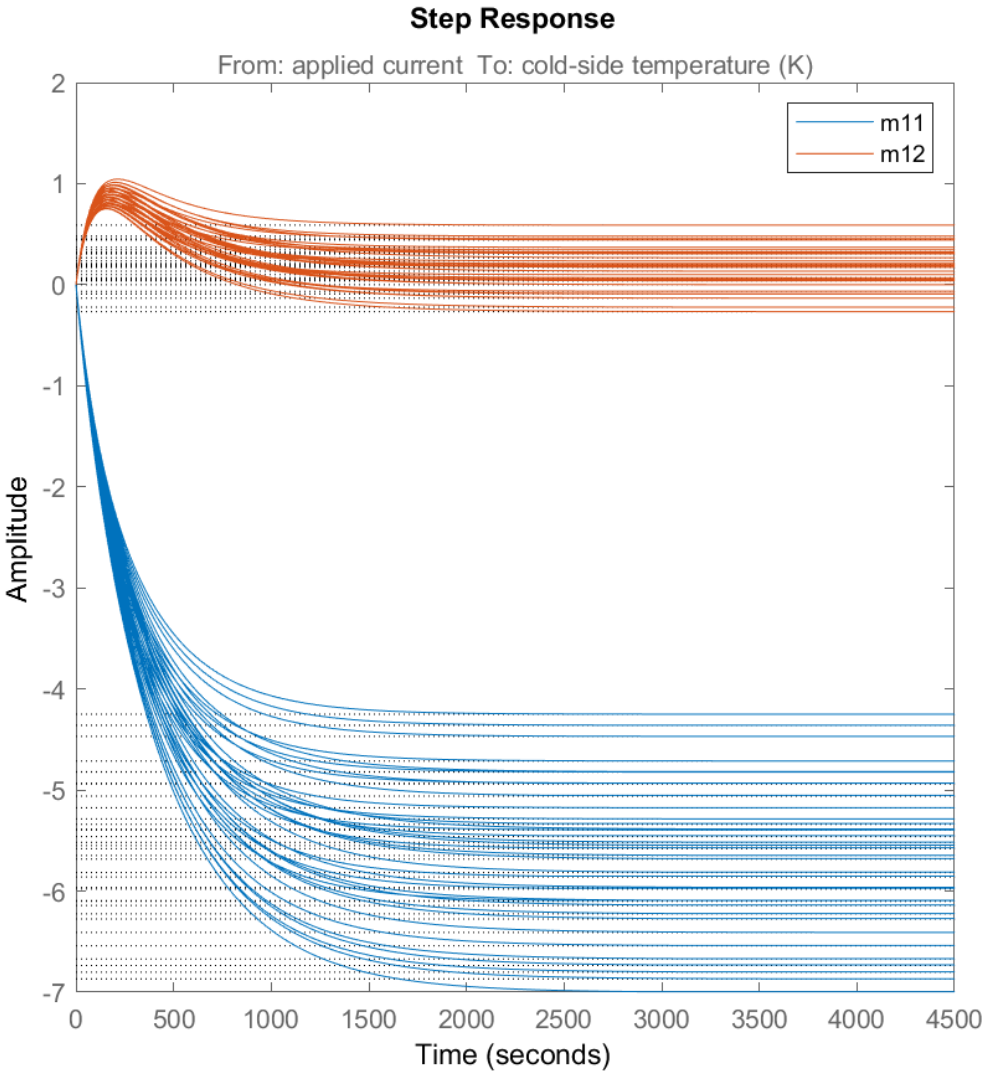

Fig. 3.6 TEC Model step response showing parameter variability-sensitivity.

3.7.2 The TEC Model frequency response

The resulting frequency response plots presented in Fig.3.7 show that:

1. The magnitude difference and phase difference are invariant for changes in current.

2. The sensitivity of the model output in hot-side temperature is more greatly affected by the changes in operating point.

3. The phase margin of m11 is $-81.2°$ at the gain crossover 0.02 rad/s. The negative gain margin indicates that stability will be lost by decreasing the gain for this particular system geometry.

4. m12 will be closed-loop stable, as the frequency response does not pass through 0 dB, $-180°$. The positive gain margins indicate that stability is lost by increasing the gain for this particular system geometry.

3.7.3 The TEC Model phase-plane

We can use a phase-plane plot to further analyse the effects of the model operating point variations on the system internal energy and stability. The system response may be interpreted in terms of a trajectory in the state-space, giving additional physical meaning to the time response of the system. The time response in the phase-plane is generated by starting at an initial condition. The shape of the trajectory depends on the eigenvalues of the system.

The phase-plane portrait for system temperature changes, shown in Fig. 3.8, is characteristic of a stable node, indicating that the eigenvalues of the thermal system are, as expected, real and negative. Variation of the model current operating point $\bar{I}$ does not affect the stability of this particular TEC system.

3.8 Summary

This chapter has introduced the thermoelectric cooler governing equations which have been used to develop the TEC Model. The model performance has been successfully verified through: simulation and comparison with Huang's theoretical model, and with an experimentally derived model. Along the way, potential typographical and modelling errors have been identified and investigated, leading to greater understanding of the TEC performance. A parameter-variation sensitivity analysis has been performed and stability for one particular system geometry has been assessed. It has been shown that the resulting system performance is very dependent on both the model operating point values and the hot-side and cold-side thermal masses. The next step is to apply the TEC Model to the specific geometry and environment appropriate to pyroelectric neutron generator systems

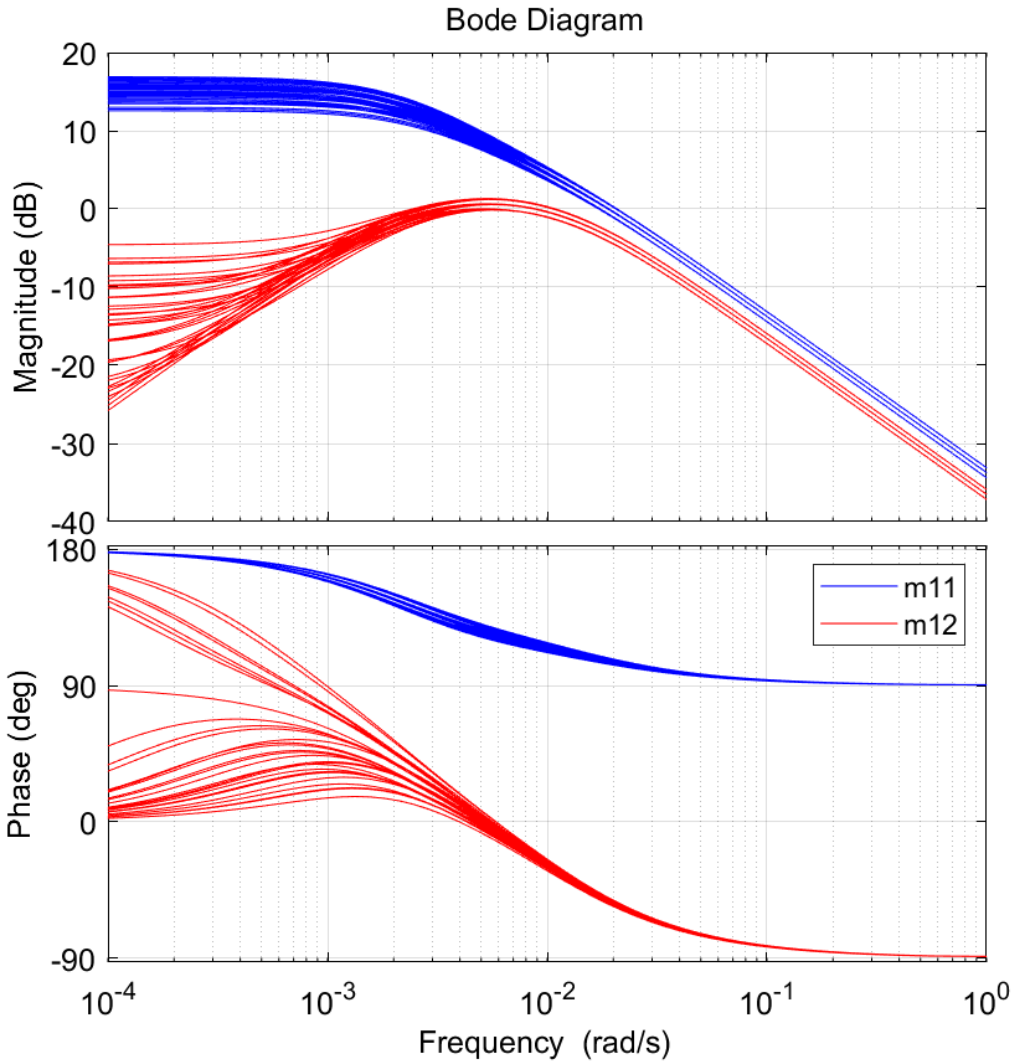

Fig. 3.7 TEC Model frequency response showing parameter variability sensitivity.

with the aim of assessing stability and controllability under these conditions; this is the focus of Chapter 4.

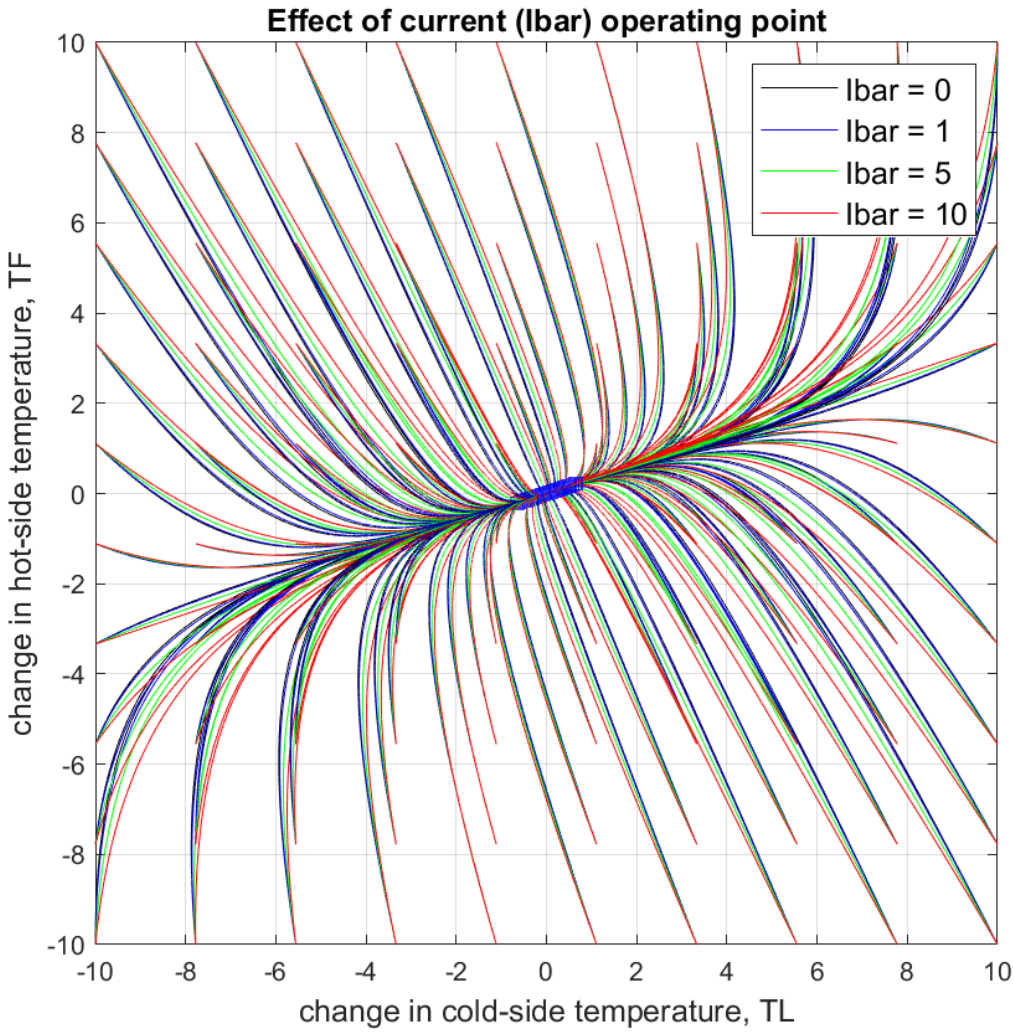

Fig. 3.8 Phase-plane plot of thermoelectric cooler.

Chapter 4

Application of the TEC Model to a pyroelectric system

4.1 Introduction

We will now consider the cooling-load and heat-sink geometry that is relevant to our pyroelectric system application. We will model and simulate the experimental pyroelectric system as investigated by the University of California, Los Angeles (UCLA) group in their 2005 publication in Nature [74]. In their system, the crystal acts as the cooling-load and the vacuum chamber acts as the heat sink. In this arrangement, if we apply a positive current to the system we will cool the crystal, and a negative current will heat the crystal.

First, we must declare the parameters of the pyroelectric system. We will use the same TEC device as was previously modelled in Chapter 3. The parameters for this device are presented in table 4.1; however, the heat-sink and cooling-load parameters will be changed to appropriate UCLA pyroelectric system values.

4.2 Application of the TEC Model to the UCLA pyroelectric system

The UCLA pyroelectric system under consideration consists of a cylindrical (diameter, 3.0 cm; height, 1.0 cm) z-cut $LiTaO_3$ crystal with its negative axis attached to a thermoelectric cooler. On the exposed crystal face, there is a copper disc attached (diameter, 2.5 cm; height, 0.5 mm), allowing charge to flow to a tungsten probe (shank diameter, 80 mm; tip radius,

100 nm; length, 2.3 mm). This single-crystal pyroelectric system is shown in Fig. 1.7.

We can apply the TEC Model (developed in Chapter 3) to this type of pyroelectric system, where the crystal plus the disk make up the cooling-load heat exchanger and the vacuum chamber is the heat sink for the system. To enable suitable verification of our applied model, we will use the single-crystal system arrangement used in the experiments of the UCLA research group [74]. Some of the crystal material properties were not explicitly stated in the UCLA research; these values were taken from the website of Roditi, who are a manufacturer and distributor of photonic crystals [80].

Parameter	**Symbol**	**Value**	**Units**
Crystal radius	r	1.50e-02	m
Crystal depth	z	1.00e-02	m
Pyroelectric coefficient	γ	-1.48e-04	$\mathrm{C/m^2 \cdot K}$
Crystal resistivity	ρ_e	1.3e+12	$\Omega \cdot \mathrm{m}$
Crystal density	ρ	7.47e+03	$\mathrm{kg/m^3}$
Crystal specific heat capacity	c	4.24e+02	$\mathrm{J/kg \cdot K}$
Crystal conductivity	k	4.60e+00	$\mathrm{W/m \cdot K}$
Crystal permittivity	ε_r	5.30e+01	dimensionless ratio
Vacuum permittivity	ε_0	8.85e-12	$\mathrm{F/m}$

Table 4.1 Single-crystal parameter values used in the UCLA experiments [74].

The vacuum chamber geometry is not explicitly stated in [74]; however, we can estimate the geometry using the scale provided in the bottom left-hand corner of the published Fig. 4.1 (inner diameter $\approx$ 7 cm; inner length $\approx$ 5.5 cm; with wall and end-plate thickness $\approx$ 1 cm). The vacuum chamber is stated to have "thick stainless steel walls", i.e. a specific heat capacity of 502 $\mathrm{J/kg \cdot K}$; thermal conductivity of 14 $\mathrm{W/m \cdot K}$; a density of 7999 $\mathrm{kg/m^3}$ and an emissivity of around 0.075 at 300 K. The calculated pyroelectric system values are summarised in table 4.2.

Figure 4.2 shows a schematic of a typical single-crystal pyroelectric system of the type we will investigate in this chapter. Figure 4.3 shows the heat transfer processes involved.

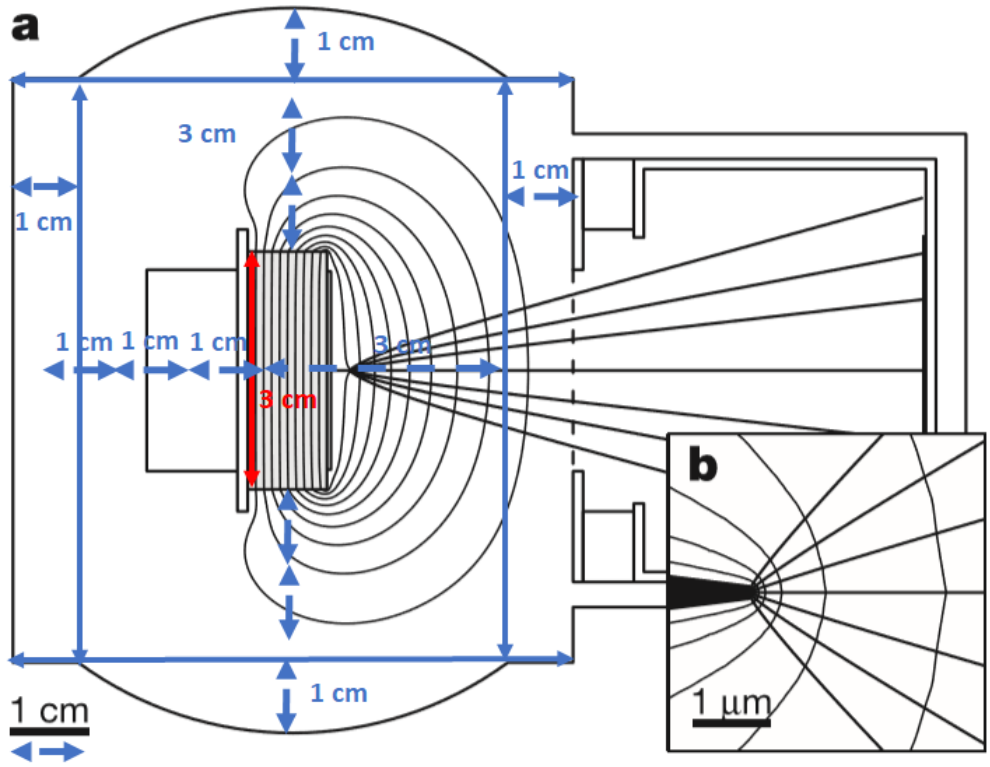

Fig. 4.1 The UCLA experiment geometry (figure adapted from [74]).

Parameter	Symbol	Value	Units
Mass of the heat sink (chamber)	M_F	1.860	kg
Specific heat capacity of heat sink (chamber)	C_F	502	$\mathrm{Jkg^{-1}K^{-1}}$
Total heat transfer surface area of the heat sink (chamber)	A_F	0.0302	$\mathrm{m^2}$
Mass of the cooling-load heat exchanger (crystal)	M_L	0.0528	kg
Specific heat capacity of the cooling-load heat exchanger (crystal)	C_L	424	$\mathrm{Jkg^{-1}K^{-1}}$

Table 4.2 Pyroelectric system parameters.

4.2.1 Consideration of heat transfer via radiation

We shall now consider the radiative heat transfer between the crystal and the vacuum chamber inner wall. The effects of heat transfer via radiation in the vacuum chamber can be modelled using the Stefan-Boltzmann Law, which can be expressed as

$$q = \varepsilon \sigma A T^4 \tag{4.1}$$

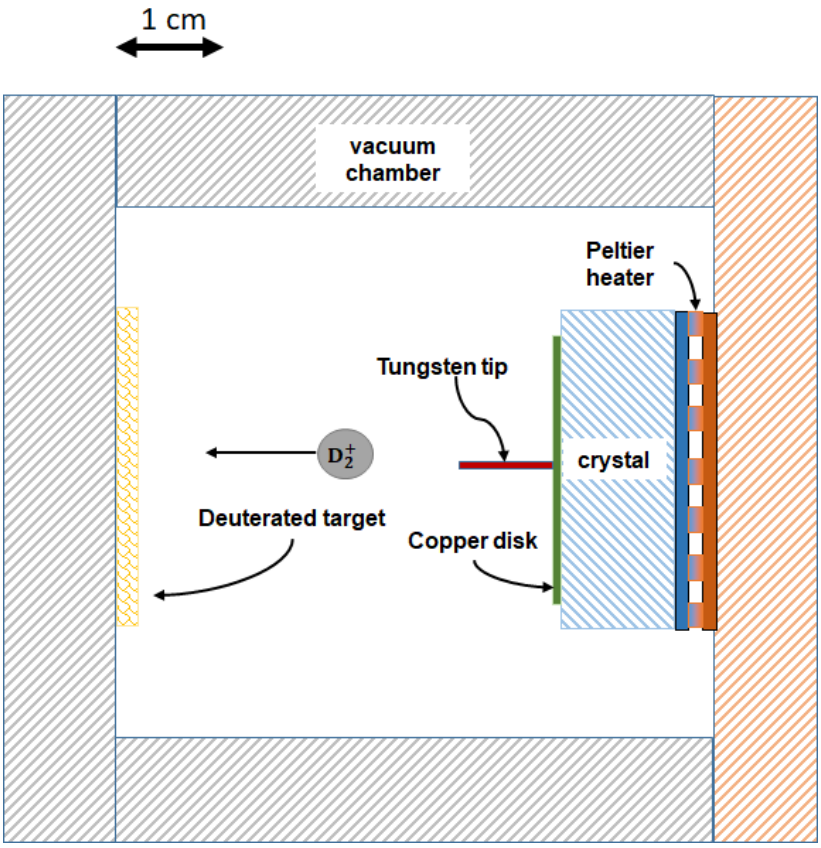

Fig. 4.2 Schematic of the single-crystal pyroelectric system.

where the Stefan-Boltzmann Constant is $\sigma = 5.6703 \times 10^{-8}$ W/m^{2}K^4.

The net radiative heat transfer to a surface is the radiation arriving from other surfaces minus the radiation emitted from the surface:

$$q = q_{absorption} - q_{emission} \tag{4.2}$$

Absorption depends on irradiation, which depends on emission from other surfaces including those far away from the observed surface. The radiation exchange between surfaces' depends not only the radiative properties and temperatures, but also on the surfaces geometry, orientation and the separation distance. To represent these dependencies, we use a geometric function known as a view factor. The view factor is a dimensionless geometric property that determines how much of a surface is visible to another surface, and can be expressed as

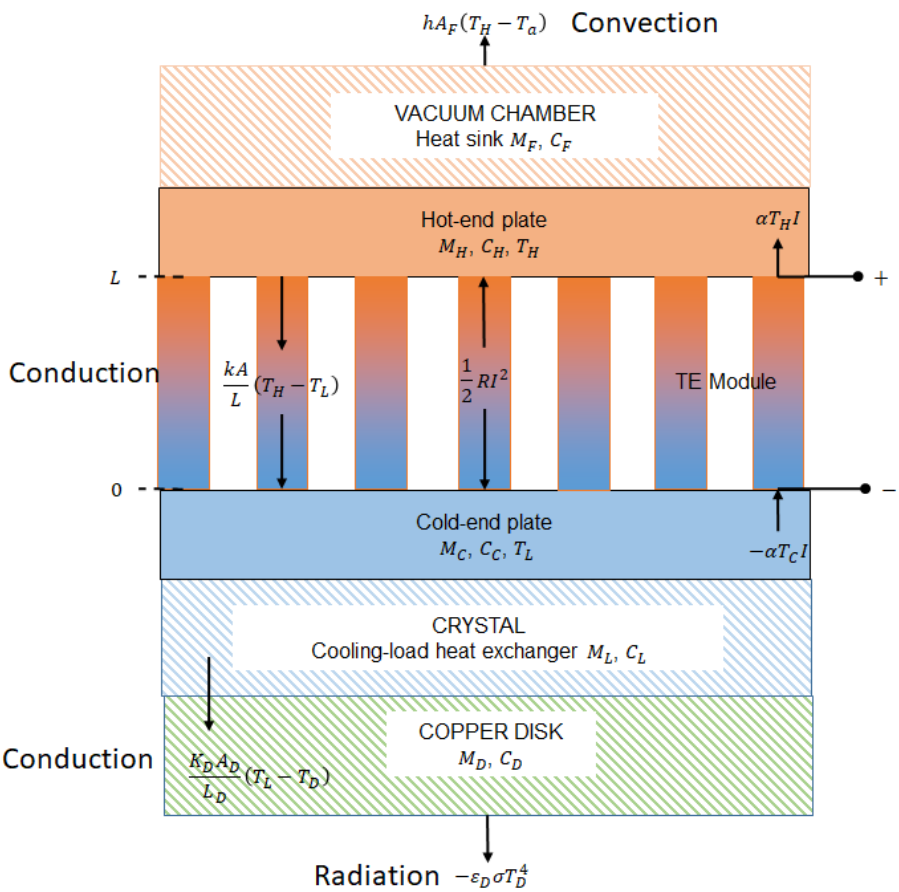

Fig. 4.3 Schematic diagram of the temperature distribution and heat transfer processes in the single-crystal pyroelectric system.

$$F_{i,j} = \frac{\text{radiation leaving } A_i \text{ and intercepted by } A_j}{\text{radiation leaving } A_i} \tag{4.3}$$

where $F_{i,j}$ is the view factor, that is the fraction of energy emitted from surface i which directly strikes surface j,
A_i is the cross sectional area of surface i, and
A_j is the cross sectional area of surface j.

The view factor satisfies two relations.

1. The law of reciprocity:

$$A_i F_{i,j} = A_j F_{j,i} \tag{4.4}$$

2. The summation rule: The sum of all view factors must be one; the summation relation for enclosure of N surfaces is

$$\Sigma_{j=1}^{N} F_{i,j} = 1 \tag{4.5}$$

We can consider the vacuum chamber and the crystal as two concentric cylinders, and we can make the following assumptions:

1. The surfaces under consideration form an enclosure and are separated by a non-participating medium, in which there is no scattering, emission or absorption. A vacuum is such a medium, as are monatomic and most diatomic gases at low and moderate temperatures, which are temperatures before ionization and dissipation occurs. In our system it is the electric field which causes the ionization of the deuterium gas, not the high temperatures directly.

2. The enclosing surface of the vacuum chamber may be composed of complex geometries; however, the enclosure may be idealized by inventing alternative simple surfaces and by assuming the surfaces to be isothermal with constant (average) heat flux values across them.

3. The small body (the crystal) can see only the large enclosing body (of the vacuum chamber) and nothing else. Hence, all radiation leaving the small body will reach the large body, i.e. the representative view factor is $F_{crystal,chamber} = 1$.

4. Part of the radiant energy leaving the inside surface of the vacuum chamber will strike the surface of the crystal; the rest will return to the chamber surface.

5. Heat transfer between the crystal and the chamber by convection is negligible.

To find the fraction of energy leaving the chamber surface which strikes the crystal surface, we apply the law of reciprocity:

$$A_{chamber} F_{chamber,crystal} = A_{crystal} F_{crystal,chamber} \tag{4.6}$$

where $A_{crystal}$ is the area of the crystal, and $A_{chamber}$ is the area of the chamber.

$$F_{chamber,crystal} = \frac{A_{crystal}}{A_{chamber}} F_{crystal,chamber} = \frac{A_{crystal}}{A_{chamber}} \tag{4.7}$$

where, in accordance with our previous assumption that all radiation leaving the crystal will reach the chamber, $F_{crystal,chamber} = 1$.

The inner surface area of the UCLA group's experimental vacuum chamber is estimated to be 0.0198 m^2. The total surface area of the crystal is 0.0024 m^2. By taking the total surface area of the crystal, we knowingly overestimate the view factor to be

$$F_{chamber,crystal} = \frac{A_{crystal}}{A_{chamber}} = 0.1190 \tag{4.8}$$

By the conservation rule, for an N surface enclosure, $\Sigma_{j=1}^{N} F_{i,j} = 1$. The majority of the rest of the heat must therefore be returning to the chamber surface.

Let us consider the crystal (at the cooling-load temperature T_L) and the chamber (at the heat-sink temperature T_H), both emitting radiation towards one another; both will emit radiation according to the Stefan-Boltzmann Law, where the emissivity of the lithium tantalate is estimated to be 0.6 [28]. The variation of the total emitted radiative energy of the cooling-load (i.e. the crystal) with temperature is shown in Fig. 4.4. It can be seen that the maximum total energy for an experiment soak temperature of 100°C is around 0.35 W. Figure 4.4 shows the total emitted radiative energy of the vacuum chamber heat sink, for the same maximum temperature, is around 12 W. The vacuum chamber does not typically reach this temperature during experiments, and, as can be seen from the dashed line plotted in Fig. 4.4, with the view factor, the proportion of this energy that would reach the crystal is much less (around 2 W).

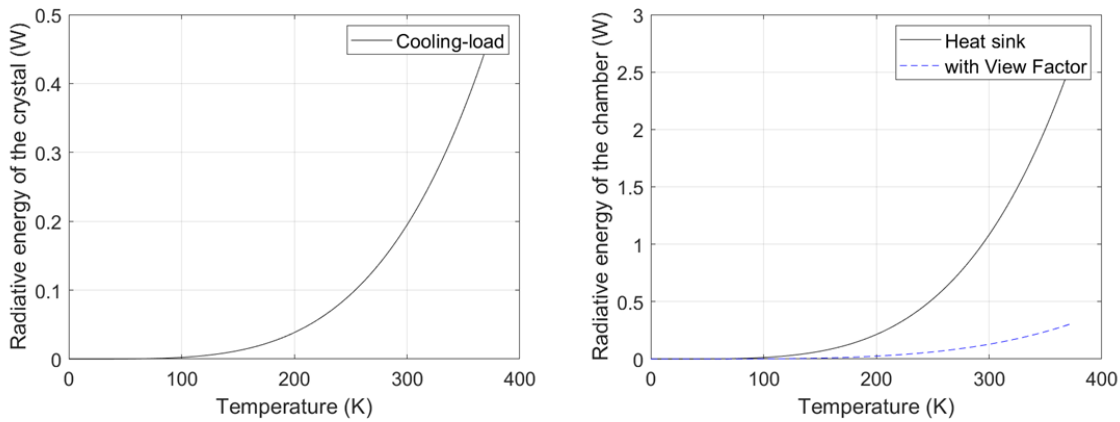

Fig. 4.4 Radiative heat transfer of the crystal (left) and chamber (right) as a function of temperature.

Conduction is considered to be the dominant heat transfer process in the system. We can check this assumption with an estimate of the total rate of conductive heat transfer

$$q_{cond} = \frac{kA}{L}\Delta T \tag{4.9}$$

For a ΔT of 100°C the conduction across the crystal can be calculated to be around 32 W, which confirms the dominance of conductive heat transfer in the system. We can now apply the TEC Model to the UCLA pyroelectric system and analyse the thermal performance.

4.3 Dynamics response analysis

The time response of our control system consists of two parts:

1. The transient response: from the initial state to the final state.

2. The steady-state response: the manner in which the system output behaves as time approaches infinity.

We are trying to predict the dynamic behaviour of the UCLA TEC system from a knowledge of the system components. The most important characteristic of the dynamic behaviour is the stability - whether the system is stable or unstable. The system will be said to be in equilibrium if, in the absence of any disturbance or input, the output stays in the same state. As our system is a linear time-invariant one, it will be considered to be stable if the output eventually comes back to equilibrium when the system is subjected to an initial condition. We will also be interested in the system's relative stability and steady-state error.

4.3.1 Equilibrium points

The phase-plane plot in Fig. 4.5 shows the trajectories of the system given by the nonlinear TEC equations (Eqs. 3.6 and 3.7). These equations have been solved for an ambient room temperature of $T_a = 298$ K, and cooling-load of $Q_L = 0$. The trajectories near an equilibrium point (represented by the black squares) should be approximated well by those of a linearised system at that point. The circles show the starting points for the plotted trajectories. The nature of the system response corresponding to various initial conditions (T_H and T_L) is directly displayed on the phase-plane. We can see that alternative equilibrium points are possible, and these are related to the choice of the important parameters (T_a, Q_L, T_H, T_L and I) of the nonlinear equations.

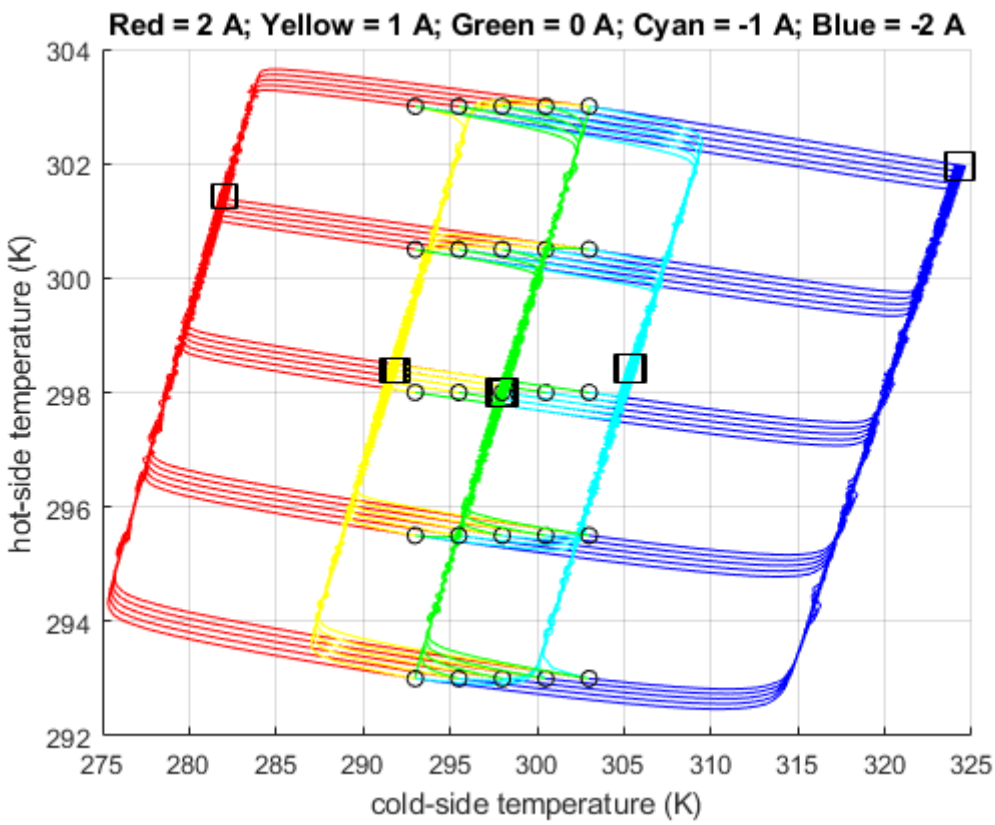

Fig. 4.5 Phase-plane plot for the nonlinear TEC

4.3.2 Transient response analysis

We will study the dynamic response of the pyroelectric thermal system in three domains: Laplace transform (s-plane), the frequency response, and the state-space. The governing equations for the TEC Model were developed in Chapter 3, and are repeated below for convenience. Initially we shall consider both the crystal and the vacuum chamber to be at a room temperature of $\bar{T}_H = 298$ K (i.e. 25°C). The parameters of the system are the UCLA values, which are given in tables 4.1 and 4.2

$$\left(\frac{MC_{LC}}{\frac{kA}{L}+\alpha\bar{I}}\right)\dot{\tilde{T}}_L+\tilde{T}_L=\left(\frac{\frac{kA}{L}}{\frac{kA}{L}+\alpha\bar{I}}\right)\tilde{T}_H+\left(\frac{\frac{\rho L}{A}\bar{I}-\alpha\bar{T}_L}{\frac{kA}{L}+\alpha\bar{I}}\right)\tilde{I} \tag{4.10}$$

$$\left(\frac{MC_{FH}}{hA_F+\frac{kA}{L}-\alpha\bar{I}}\right)\dot{\tilde{T}}_H+\tilde{T}_H=\left(\frac{\frac{kA}{L}}{hA_F+\frac{kA}{L}-\alpha\bar{I}}\right)\tilde{T}_L+\left(\frac{\alpha\bar{T}_H+\frac{\rho L}{A}\bar{I}}{hA_F+\frac{kA}{L}-\alpha\bar{I}}\right)\tilde{I} \tag{4.11}$$

The current-temperature transfer functions with the numerical values input are

$$\frac{\tilde{T}_L}{\tilde{I}} = \frac{-0.12581(s+0.0002974)}{(s+0.01959)(s+0.0003026)} \tag{4.12}$$

$$\frac{\tilde{T}_H}{\tilde{I}} = \frac{0.0055515(s+0.0004223)}{(s+0.01959)(s+0.0003026)} \tag{4.13}$$

Then, we will consider the operating point for the applied current to be $\bar{I} = -1$ A; according to our earlier definitions, a negative value for the current will simulate heating of the crystal. The current-temperature transfer functions with the numerical values input are now

$$\frac{\tilde{T}_L}{\tilde{I}} = \frac{-0.12581(s+0.0003347)}{(s+0.01879)(s+0.0003014)} \tag{4.14}$$

$$\frac{\tilde{T}_H}{\tilde{I}} = \frac{0.0055515(s-0.0004223)}{(s+0.01879)(s+0.0003014)} \tag{4.15}$$

We can see that, for either sign in current input, the value of the gain remains the same. However, the values of the poles and zeros change; this can be seen more easily when these features are plotted on the complex plane, called a pole-zero map. The pole-zero maps of $\frac{\tilde{T}_L}{\tilde{I}}$ for both the cooling and the heating operating point currents are shown together in Fig. 4.6. The system poles are marked by an 'x', and the zeros are marked by a 'o'.

From the pole-zero plot, we can observe that there are two near-cancelling pole-zero pairs close to the imaginary axis, which could be potentially eliminated to simplify the model, with no effect on the overall model response. We will look at this effect when we design the controller for this system in Chapter 5.

1. The p_1 time constant is 53 seconds; this shorter time constant is associated with the smaller thermal mass of the crystal.

2. The p_2 time constant is 2491 seconds (around 41 minutes); this longer time constant is associated with the larger thermal mass of the vacuum chamber, which takes longer to see the effects of changes in operating conditions.

By inspection of the gain of the transfer functions, we can observe that the cooling-load (crystal) sees a larger response from the same forcing function when compared with the heat sink (vacuum chamber). It is worth noting here that, in order to simulate the heating the crystal (the cooling-load), we must apply a negative current to the TEC; this is consistent

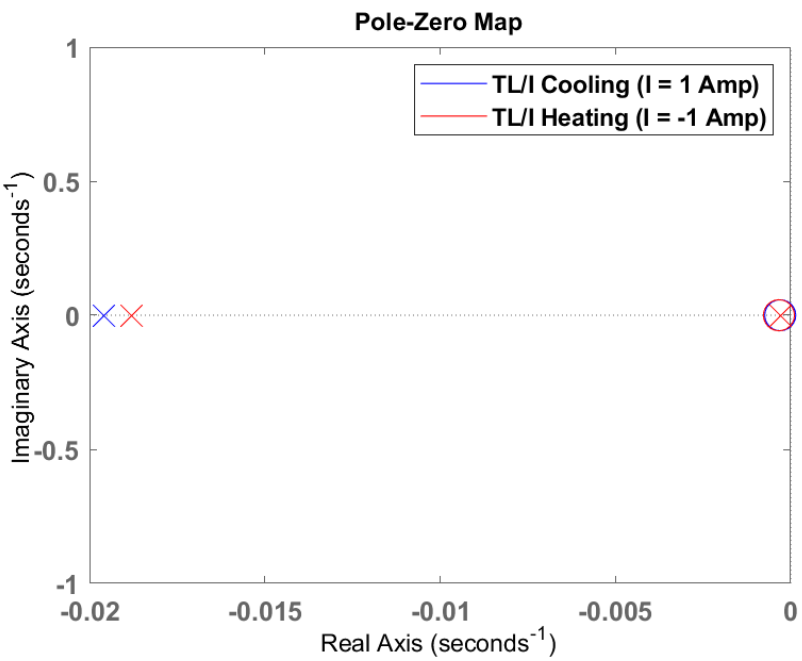

Fig. 4.6 Pole-zero map showing the location of the poles and the zeros for $\frac{\tilde{T}_L}{\tilde{I}}$ for both the heating and the cooling currents.

with the definition of current direction we made during the development of the TEC Model in Chapter 3.

We must also consider the potential effect of the thin copper disk attached to the front of the crystal in the UCLA system. The disk can be neglected in our thermal calculations as the heat capacity of the crystal (22.37 J/K) is about 28 times that of the copper disk (0.8 J/K).

In the experiments conducted by UCLA the crystal was first cooled down to 240 K (i.e. -33°C) from room temperature by pouring liquid nitrogen into the cryogenic feed-through before heating. With $\bar{T}_L = 240$ K, $\bar{I} = -1$ A and $\bar{T}_H = 298$ K the transfer functions become

$$\frac{\tilde{T}_L}{\tilde{I}} = \frac{-0.10132(s+0.0001388)}{(s+0.01879)(s+0.0003014)} \tag{4.16}$$

$$\frac{\tilde{T}_H}{\tilde{I}} = \frac{0.0055515(s+0.003152)}{(s+0.01879)(s+0.0003014)} \tag{4.17}$$

We can see that the greatest effect is on the gain and the largest system pole of $\frac{\tilde{T}_L}{\tilde{I}}$. The pole-zero map of these transfer functions, shown in Fig. 4.7, further highlights the potential

for the pole-zero cancellations to be valid for transients with variations in $\bar{T}_L$.

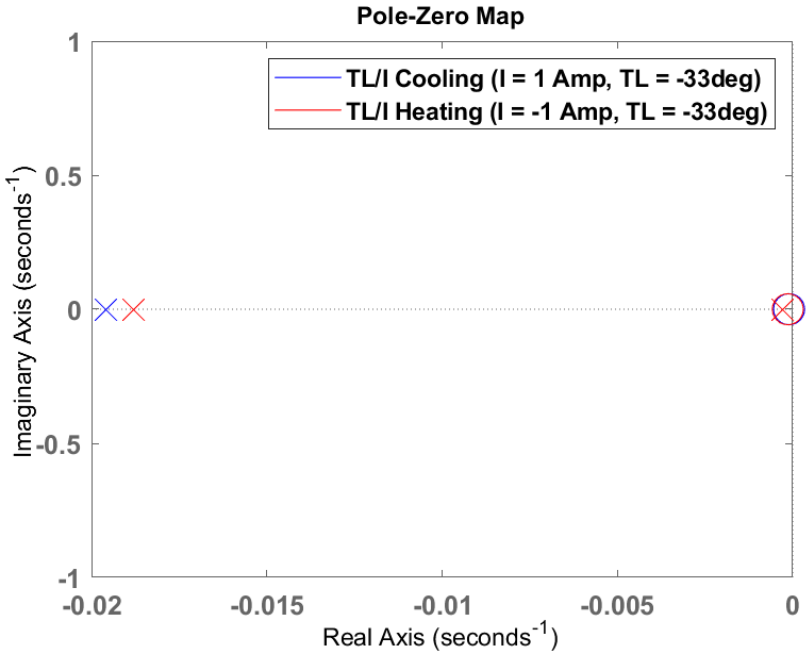

Fig. 4.7 Pole-zero map showing the location of poles and zeros for $\frac{\tilde{T}_L}{\tilde{I}}$ for both heating and cooling currents and with $\bar{T}_L = 240$ K.

In the following sections the emphasis will be on heating and cooling transients about room temperature operating points. That is, we will take $\bar{T}_L = \bar{T}_H = 298$ K, with $\bar{I} = -1$ A for heating transients and $\bar{I} = 1$ A for cooling transients. However, we will investigate the effects of changing these operating points when we undertake our sensitivity analysis towards the end of this chapter. We will first consider the system response to aperiodic signals: step, impulse and ramp functions.

4.3.3 Unit-step response

In this section we shall analyse the system response to a unit-step input, for which the initial conditions are assumed to be zero. Because our system has been linearised, the output for the unit-step case can be multiplied by the magnitude of the input step to derive a step response of any amplitude. We can use MATLAB to simulate the system response to a positive unit-step input in current, and the output is shown in Fig. 4.8. The operating conditions used in this simulation were $\bar{I} = 1$ A, and $\bar{T}_H = \bar{T}_L = 298$ K. Figure 4.8 shows that the system has a rise time of 105 seconds and a settling time of 169 seconds. The final steady-state output

cold-side temperature change for the unit-step input in current is -6.31 K, and, as this is linearly scaled, it would increase with an increase in current.

Figure 4.9 shows that, with $\bar{I} = 1$ A, the response of $\tilde{T_L}$ to a negative unit-step input in current has the same rise time and settling time and has a steady-state change of 6.31 K. However, to more accurately represent the step response to a heating transient, we would ideally need to change our current operating point to be a negative value, i.e. change to $\bar{I} = -1$ A. Figure 4.10 shows the effect of this change in current operating point sign on the negative unit-step response of the cold-side temperature $\tilde{T_L}$. It can be seen that the rise time and settling time are increased. We can also see that the steady-state final value has been slightly increased.

The step response analysis indicates that the open-loop pyroelectric TEC system response is far too sluggish.The difference in step responses for the different operating points highlights the need to conduct a sensitivity analysis to investigate the effects of variation in operating point - particularly the magnitude and the sign of the applied current for both the heating and cooling transients for our pyroelectric system geometry.

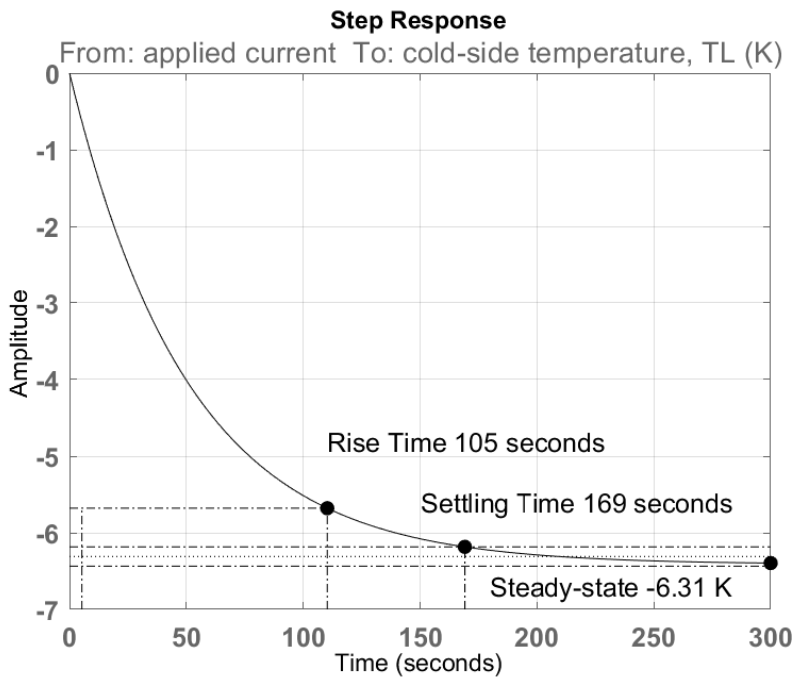

Fig. 4.8 Positive unit-step response of the cold-side (crystal) temperature, with $\bar{I} = 1$ A, and $\bar{T_L} = \bar{T_H} = 298$ K.

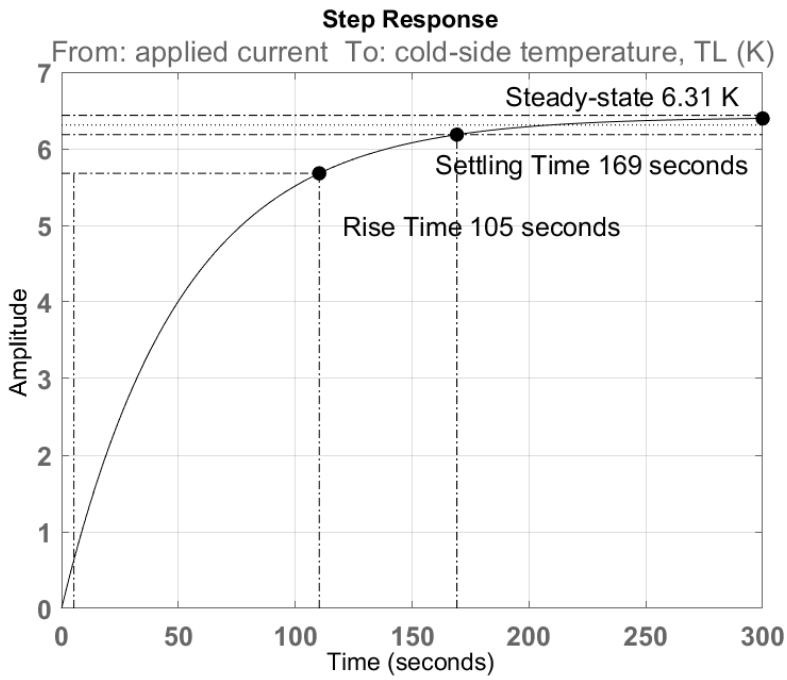

Fig. 4.9 Negative unit-step response of the cold-side (crystal) temperature, for operating point values of $\bar{I} = 1$ A, and $\bar{T_L} = \bar{T_H} = 298$ K.

4.3.4 Unit-impulse response

The system response to a brief input signal (an impulse) can give us some further information about the reaction of the system to an external change. While an impulse input is impossible in any real system, it is actually a useful idealisation, because, in the time domain, a system is described by its Impulse Response Function. Our system can be completely characterised by its impulse response (i.e. any output can be calculated from the input and the impulse response). Again, we will take the operating point values of $\bar{T_L} = \bar{T_H} = 298$ K, with $\bar{I} = 1$ A, and apply a positive impulse to the system. Analysis of Fig. 4.11 shows that the system impulse response peak response is -0.126 K at $t = 0$ and the settling time is 199 seconds. We can compare this with the response for a heating impulse, if we now take the operating point current to be $\bar{I} = -1$ A and apply a negative impulse to the system. Figure 4.12 shows the response of $\tilde{T_L}$. Comparing the two responses, we can see that the peak responses are of equal magnitude; however, the heating transient takes slightly longer to settle (around 14 seconds longer).

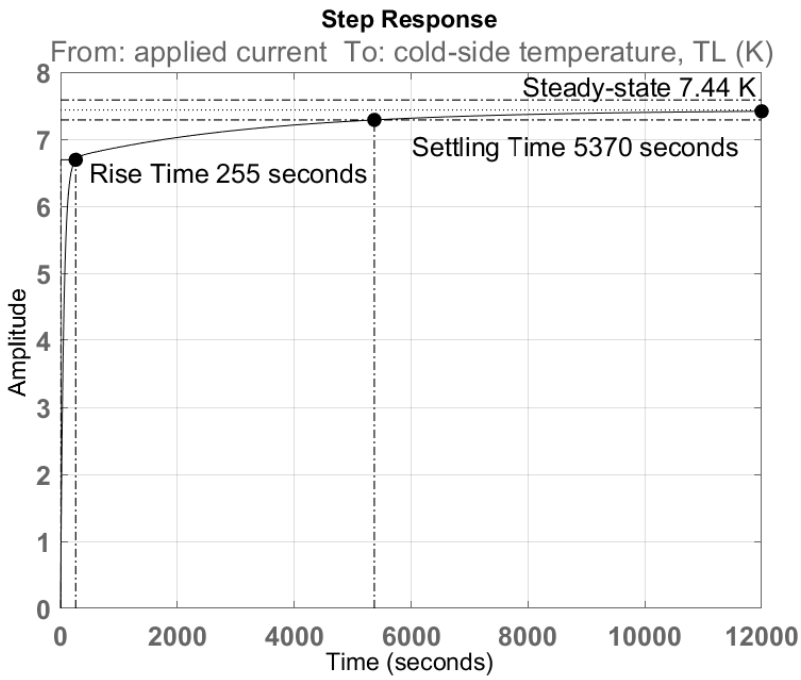

Fig. 4.10 Negative unit-step response of the cold-side (crystal) temperature for operating point values of $\bar{I} = -1$ A, and $\bar{T_L} = \bar{T_H} = 298$ K.

4.3.5 Unit-ramp response

Typical pyroelectric experiments, such as those carried out by UCLA [74], apply temperature ramps to the crystal. Figures 4.13 and 4.14 show that the unit-ramp response curves for the cold-side (crystal) temperature for both cooling and heating transients lead the input curve. As for our previous analysis, we have used the appropriate operating point current. The unit-ramp responses show that the open-loop pyroelectric TEC system is incapable of accurately following a ramp input. We can observe simulated changes of around $\pm \sim$360 K over 100 seconds, which would be unphysical.

4.3.6 Frequency response

One way we can use the exponential response of a Linear-Time-Invariant system is to find the frequency response, or response to a sinusoid. As we are simulating using a heat pump to actuate the pyroelectric crystal, it is feasible that, as we cycle the system, there will be a temperature difference between the hot-side and the cold-side of the system.

Figure 4.15 highlights the difference between the frequency responses of two different current operating points. We can see that with an operating point current appropriate to

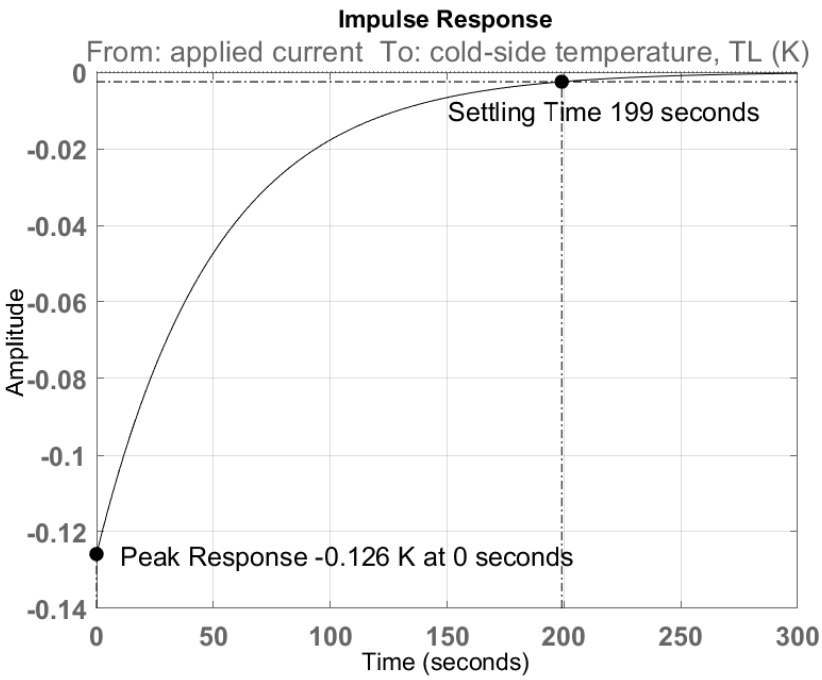

Fig. 4.11 Unit-impulse response of the cold-side (crystal) temperature for operating point values of $\bar{I} = 1$ A, and $\bar{T_L} = \bar{T_H} = 298$ K.

heating the cold-side (crystal) of $\bar{I} = 1$ A, the magnitude of the response is slightly greater at the low frequencies. At the high frequencies, the response of both the magnitudes and the phases are the same. We see that, at a low frequency, the higher magnitude of the heating model is accompanied by a slightly more lagged response. It is important to note that, despite the differences at low frequency, the two responses are the same at the critical frequency, where the magnitude plots cross over the 0 dB line (this occurs at a frequency of 0.124 rad/s); at this point the phase margins of the systems are around 80 degrees.

Although the open-loop pyroelectric TEC system is stable, the principal drawback of open-loop control is a loss of accuracy. A feedback loop would attempt to maintain the process variable (in our case the crystal temperature) at a desired value, thereby increasing the accuracy. Without feedback there would be no guarantee that any control efforts applied to the process will actually have the desired effect. These control system design challenges will be addressed in further detail in Chapter 4.

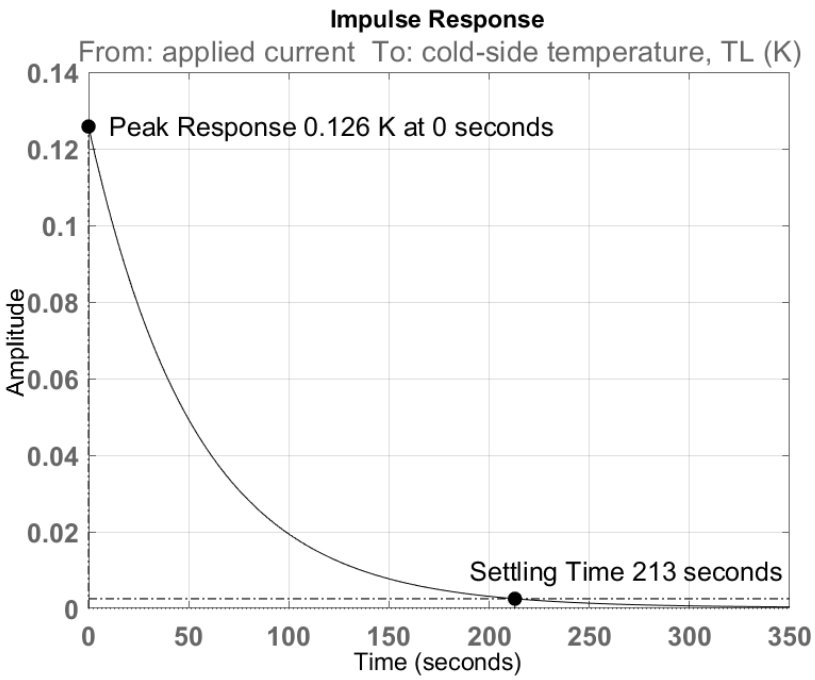

Fig. 4.12 Unit-impulse response of the cold-side (crystal) temperature for operating point values of $\bar{I} = -1$ A, and $\bar{T_L} = \bar{T_H} = 298$ K.

4.4 Sensitivity analysis

In order to explore the behaviour of the model, we will conduct a sensitivity analysis. The analysis will help to examine the robustness of the model output, through the change in cold-side (crystal) temperature $\tilde{T_L}$ with respect to changes of the parameter values: current $\bar{I}$, cold-side (crystal) temperature $\bar{T_L}$ and hot-side (chamber) temperature $\bar{T_H}$. Our nominal set of operating parameters will be $\bar{I} = 1$ A, and $\bar{T_L} = \bar{T_H} = 298$ K, and we will vary one parameter at a time while keeping all other parameters fixed. This approach will reveal the form of the relationship between the varied parameter and the output.

First, we analyse the effects of a $\pm 10\%$ change in each operating point value about the nominal set of parameter values. Figure 4.16 shows the effects of the changes in each operating point about its nominal value. We can conduct the same analysis for a negative unit-step input, and the response is shown in Fig. 4.17. We can see that $\bar{T_L}$ has the greatest effect, followed by $\bar{T_H}$. The response indicates that the model is least sensitive to small changes in $\bar{I}$.

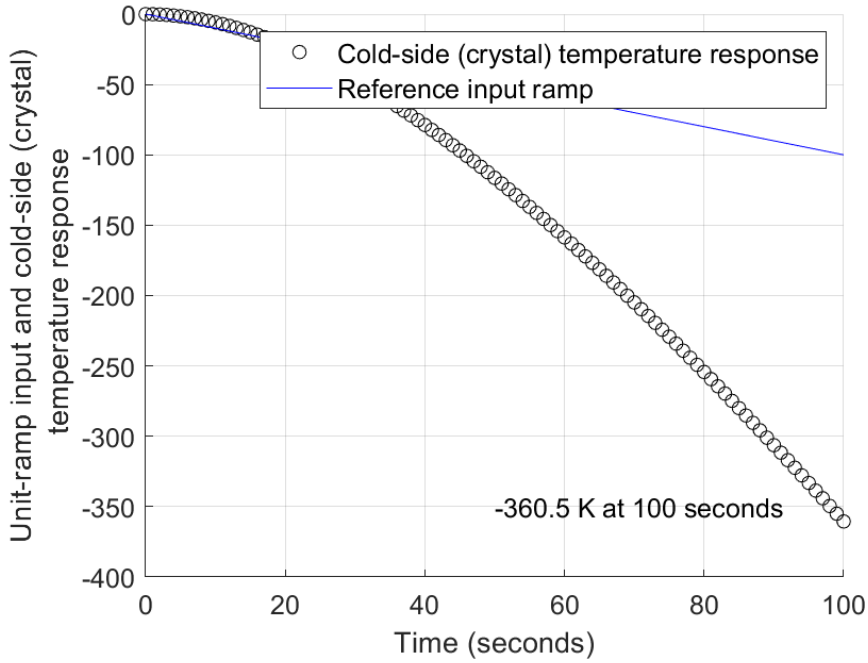

Fig. 4.13 Negative unit-ramp response of the cold-side (crystal) temperature for operating point values of $\bar{I} = 1$ A, and $\bar{T}_L = \bar{T}_H = 298$ K.

4.4.1 Operational current

When we consider the possibility of thermally cycling the crystal in our pyroelectric system, we will need to consider the potential current input range of -10 A to 10 A (the negative currents indicating heating of the crystal, and positive current indicating cooling the crystal). This range for the current is outside the small percentage change that we investigated in the previous section. In fact, we are potentially looking at a 1000% change in current over the typical operating range of the TEC. Also, in a case of thermal cycling, it may be essential to have the sign of the current operating point vary from positive to negative, following along with the sign of the input current. It is anticipated that having the opposite sign for a current operating point could have an unwanted impact on the simulated system dynamic response. In the following two sections we will consider the effect of varying the current operational point sign and magnitude across the stated range.

Positive unit-step input

A positive unit-step input will cool the cold-side of the TEC (reducing the crystal temperature); we can see this in Figs. 4.18 and 4.19. The performance characteristics of these step responses have been tabulated in table 4.3. The most appropriate operating point current for

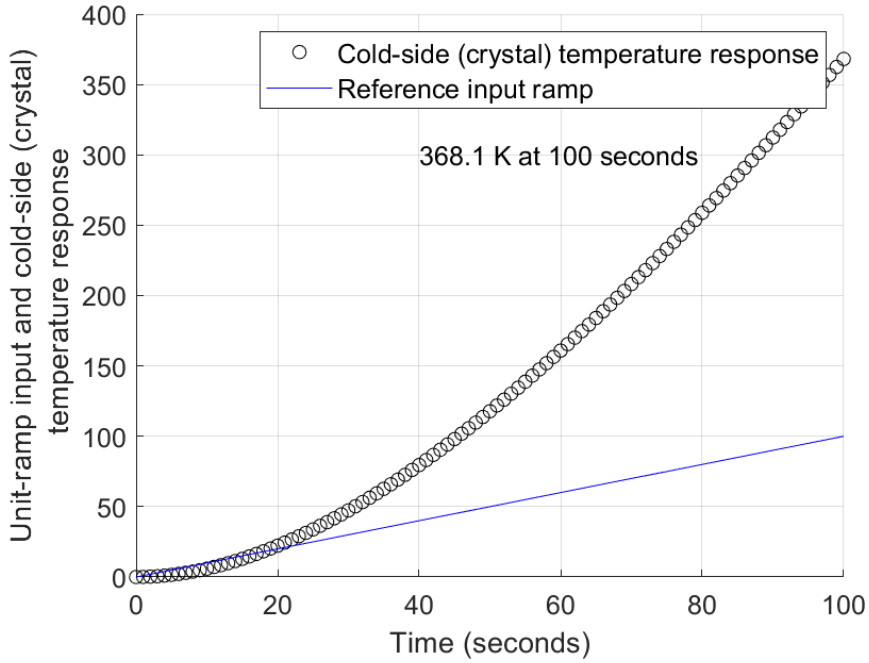

Fig. 4.14 Positive unit-ramp response of the cold-side (crystal) temperature for operating point values of $\bar{I} = 1$ A, and $\bar{T_L} = \bar{T_H} = 298$ K.

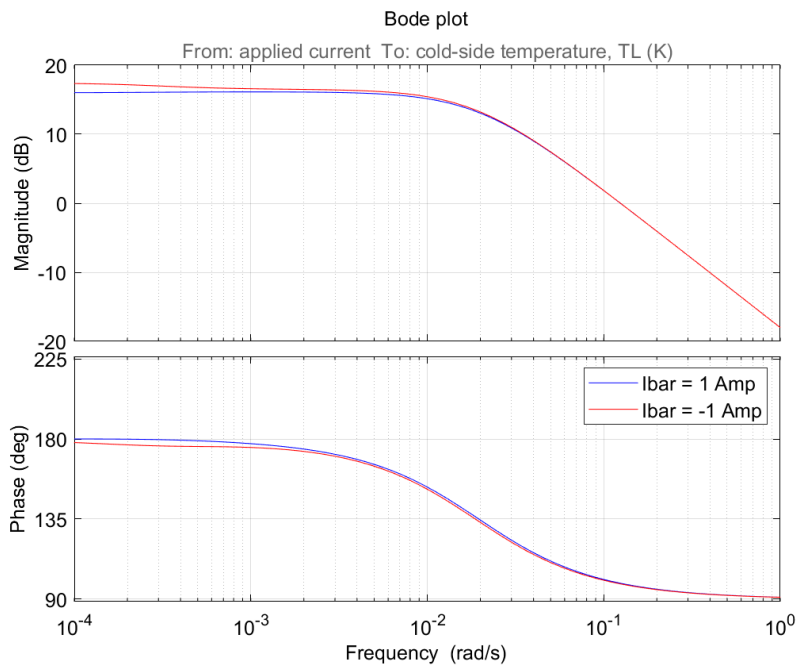

Fig. 4.15 Frequency response of the UCLA pyroelectric TEC system for operating point values of $\bar{T_L} = \bar{T_H} = 298$ K and with both $\bar{I} = -1$ A and $\bar{I} = 1$ A.

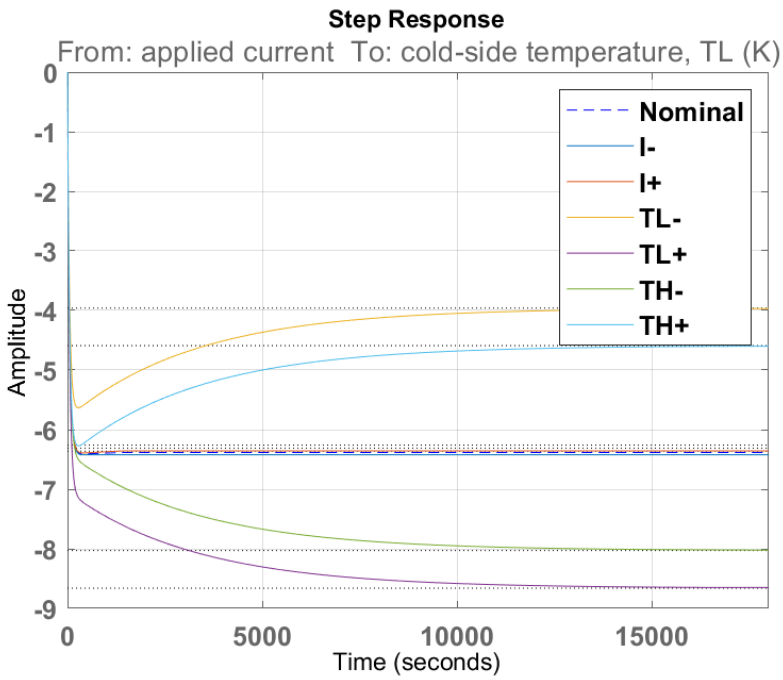

Fig. 4.16 Plot of positive unit-step response curves for $\pm 10\%$ changes in operating point values.

this positive unit-step input is $\bar{I} = 1$ A. All of the $\bar{I}$ values result in reducing the cold-side temperature, as expected. However, we can see some different dynamics between the positive and negative values, which highlights the importance of having the correct operating point current.

1. For positive unit-step transients run with the wrong sign on the operating point current (i.e. simulated with a negative value for $\bar{I}$):

   (a) There are no overshoots present in these transients.

   (b) The settling times are longer, and increase with the magnitude of $\bar{I}$.

   (c) The rise times are longer, and increase with the magnitude of $\bar{I}$.

   (d) The steady-state values are greater, and increase with the magnitude of $\bar{I}$.

   These dynamic responses can be explained by inspection of the governing equations, Eqs. 4.10 and 4.11, (repeated below for convenience).

$$\left(\frac{MC_{LC}}{\frac{kA}{L}+\alpha\bar{I}}\right)\dot{\tilde{T}}_L+\tilde{T}_L=\left(\frac{\frac{kA}{L}}{\frac{kA}{L}+\alpha\bar{I}}\right)\tilde{T}_H+\left(\frac{\frac{\rho L}{A}\bar{I}-\alpha\bar{T}_L}{\frac{kA}{L}+\alpha\bar{I}}\right)\tilde{I} \tag{4.18}$$

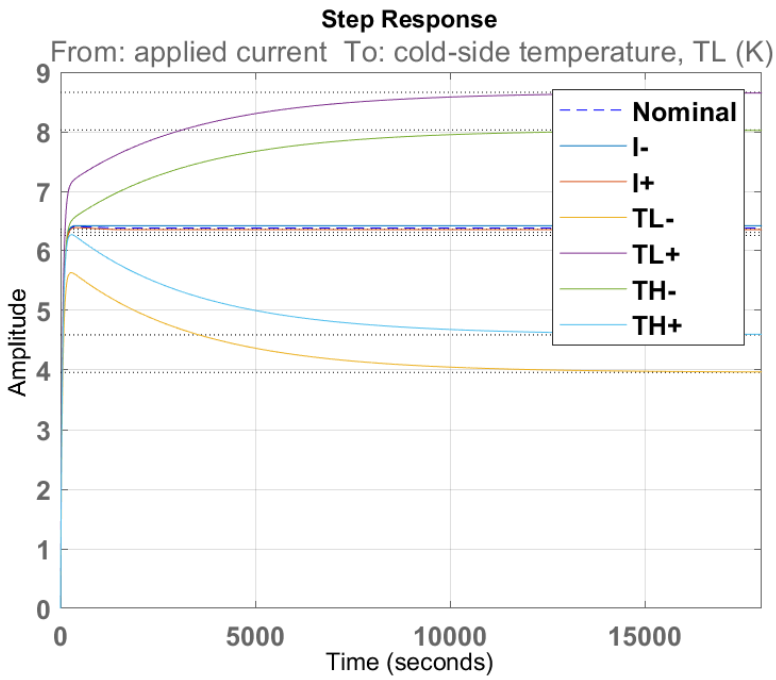

Fig. 4.17 Plot of negative unit-step response curves for $\pm 10\%$ changes in operating point values.

$$\left(\frac{MC_{FH}}{hA_F + \frac{kA}{L} - \alpha\bar{I}}\right)\dot{\tilde{T}}_H + \tilde{T}_H = \left(\frac{\frac{kA}{L}}{hA_F + \frac{kA}{L} - \alpha\bar{I}}\right)\tilde{T}_L + \left(\frac{\alpha\bar{T}_H + \frac{\rho L}{A}\bar{I}}{hA_F + \frac{kA}{L} - \alpha\bar{I}}\right)\tilde{I} \tag{4.19}$$

If we consider the Joule heating term ($\frac{\rho L}{A}\bar{I}\tilde{I}$) which appears on the right-hand side of both equations, it can be seen that if the signs of $\bar{I}$ and $\tilde{I}$ are opposite this term becomes negative. We would, in effect, be simulating removing the Joule heating from both the cold-side and the hot-side, instead of correctly adding this heating power.

2. For transients simulated with the correct sign on the operating point current but larger magnitude than the input (i.e. simulated with a positive value for $\bar{I}$):

   (a) The peak responses of these transients are lower, and decrease with increasing $\bar{I}$.

   (b) The overshoots are larger, and increase with increasing $\bar{I}$.

   (c) The settling times are longer, and increase with increasing $\bar{I}$.

   (d) The rise times are shorter, and decrease with increasing $\bar{I}$.

(e) The steady-state values are lower, and decrease with increasing $\bar{I}$.

In each case the increased magnitude of the operating point falsely drives the transient faster and harder - leading to faster responses, with more overshoot but decreased final steady-state values.

$\bar{I}$ (A)	Peak response (K)	Overshoot (%)	Settling time (s)	Rise time (s)	Steady-state (K)
-10	-17	0	1.35×10^4	6.85×10^3	-17.2
-5	-10.4	0	9.45×10^3	3.84×10^3	-10.4
-1	-7.43	0	5.37×10^3	255	-7.44
0	-6.85	0	2.58×10^3	140	-6.85
1	-6.41	1.55	169	105	-6.31
5	-5.82	30.2	9.5×10^3	50	-4.47
10	-5.24	104	1.46×10^4	21.9	-2.57

Table 4.3 Performance characteristics for a positive unit-step for various operating point currents $\bar{I}$.

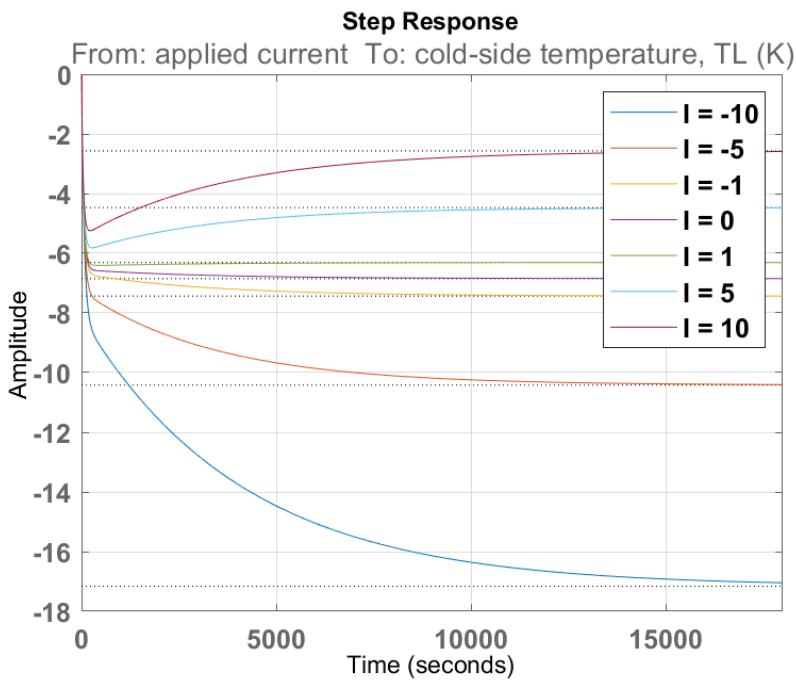

Fig. 4.18 Plot of positive unit-step response curves for various operating point currents $\bar{I}$.

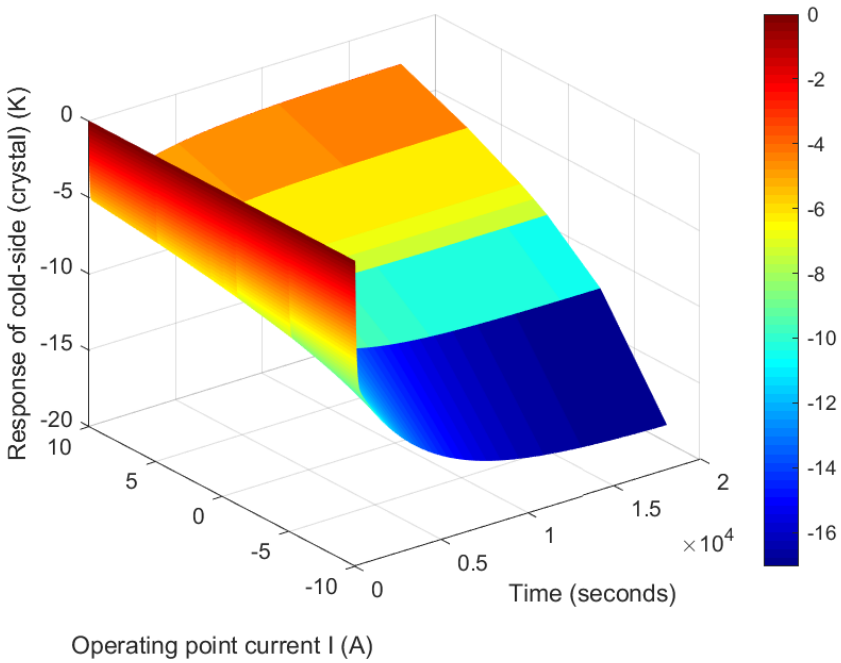

Fig. 4.19 Three-dimensional plot of positive unit-step response curves for various operating point currents $\bar{I}$.

Negative unit-step input

We will now consider a negative unit-step input, which when applied to the TEC will heat the cold-side (increasing the crystal temperature). We can see this response in Figs. 4.20 and 4.21. The performance characteristics of these step responses have been tabulated in table 4.4. In this case, the most appropriate operating point current for the negative unit-step input is $\bar{I} = -1$ A. All of the $\bar{I}$ values can be seen to increase the cold-side temperature. However, once again, the plots highlight the different dynamic responses of the positive and negative operating point values.

1. For negative unit-step transients with positive operating point currents:

   (a) There are overshoots in the response, which increase along with the magnitude of $\bar{I}$.

   (b) The settling times are shorter, and increase with increasing magnitude of $\bar{I}$.

   (c) The rise times are shorter, and they decrease with increasing magnitude of $\bar{I}$.

   (d) The steady-state values are lower, and these also decrease with increasing magnitude of $\bar{I}$.

These dynamic responses can (again) be explained by inspection of the governing equations. The reader is referred back to the earlier discussion of the Joule heating term.

2. For transients simulated with the correct sign on the operating point current but larger magnitude than the input (i.e. simulated with a negative value for $\bar{I}$):

   (a) The peak responses of these transients are higher, and this increases with increasing magnitude of $\bar{I}$.

   (b) There is no overshoot in any of these responses.

   (c) The settling times are longer, and these increase with increasing $\bar{I}$.

   (d) The rise times are longer, and they increase with increasing $\bar{I}$.

   (e) The steady-state values are higher, and these also increase along with $\bar{I}$.

   These responses to negative unit-step inputs show that the increased magnitude of the operating point falsely drives the transient slower and increases the final steady-state values.

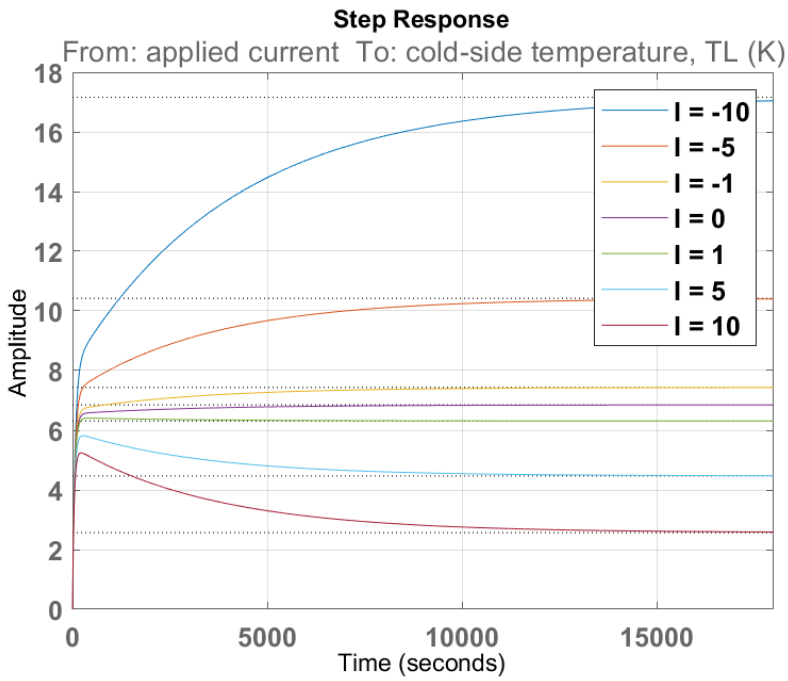

Fig. 4.20 Plot of negative unit-step response curves for various values of operating point current $\bar{I}$.

$\bar{I}$ (A)	Peak response (K)	Overshoot (%)	Settling time (s)	Rise time (s)	Steady-state (K)
-10	17	0	1.35×10^4	6.85×10^3	17.2
-5	10.4	0	9.45×10^3	3.84×10^3	10.4
-1	7.43	0	5.37×10^3	255	7.44
0	6.85	0	2.58×10^3	140	6.85
1	6.41	1.55	169	105	6.31
5	5.82	30.2	9.5×10^3	50	4.47
10	5.24	104	1.46×10^4	21.9	2.57

Table 4.4 Performance characteristics for a negative unit-step for various current operating points.

We can see from tables 4.3 and 4.4 that the magnitude of the responses (the peak responses and steady-states) at each operating point are equal and opposite, and both the settling and rise times are the same. It is very important that we have the correct sign and magnitude of operating point current in our model.

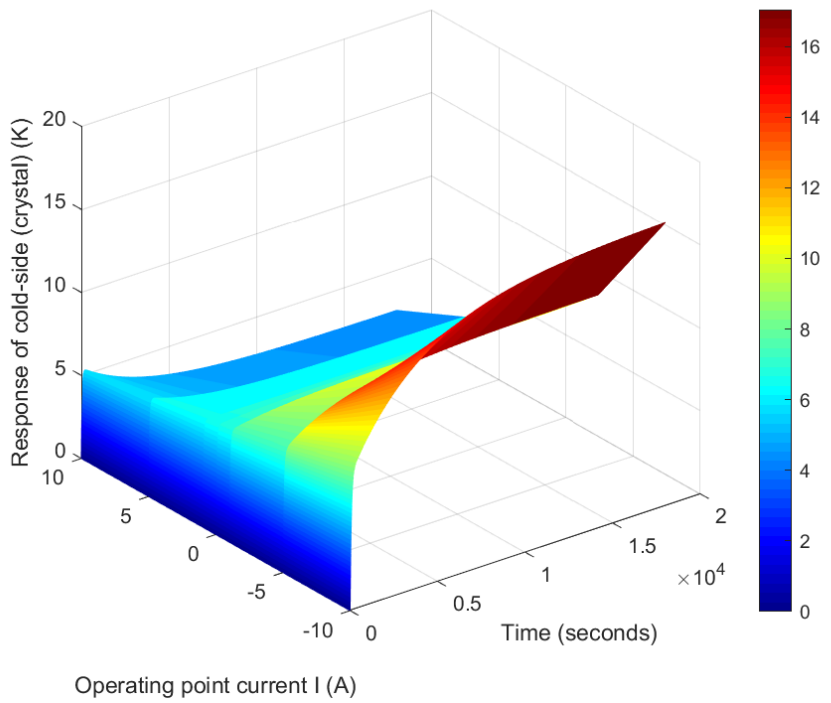

Fig. 4.21 Three-dimensional plot of negative unit-step response curves for various operating point currents $\bar{I}$.

The Bode plot for various operating point currents is shown in Fig. 4.22, and it can be seen that:

1. The current operating point has its greatest effect on the low frequency magnitude, but all the plots have similar high frequency responses.
2. The low frequency magnitudes for each operating point support the steady-state values that are seen in the unit-step responses analysed in the previous section.
3. All plots have the same corner frequency at approximately 0.01 rad/s.
4. All plots come together at the same gain crossover frequency (the 0 dB line) of approximately 0.1 rad/sec; and all have a bandwidth of approximately 0.2 rad/s.
5. The phase crossover (the 180 degrees line) for all plots is at 10^{-5} rad/s.

4.4.2 Operational cold-side (crystal) temperature

The UCLA researchers decreased the temperature of their crystal before beginning the heating cycle, and we may wish to heat our system starting from room temperature. It was therefore deemed prudent to investigate the effect on the response of the TEC model of various operating cold-side temperatures $\bar{T}_L$. The results of this analysis are plotted in Figs. 4.23 and 4.24.

With these simulations carried out, we found that

1. As with the current operating point, the cold-side (crystal) temperature operating point also has its greatest effect on the low frequency magnitude. However, this effect is less than that of the current.
2. The low frequency magnitude response for each operating point is supported by the steady-state values that are seen in the unit-step responses.
3. The corner frequency remains unchanged at approximately 0.01 rad/s.
4. The gain crossover frequency remains unchanged at approximately 0.1 rad/s; and the bandwidth is still approximately 0.2 rad/s.
5. The phase crossover remains unchanged, at around 10^{-5} rad/s.

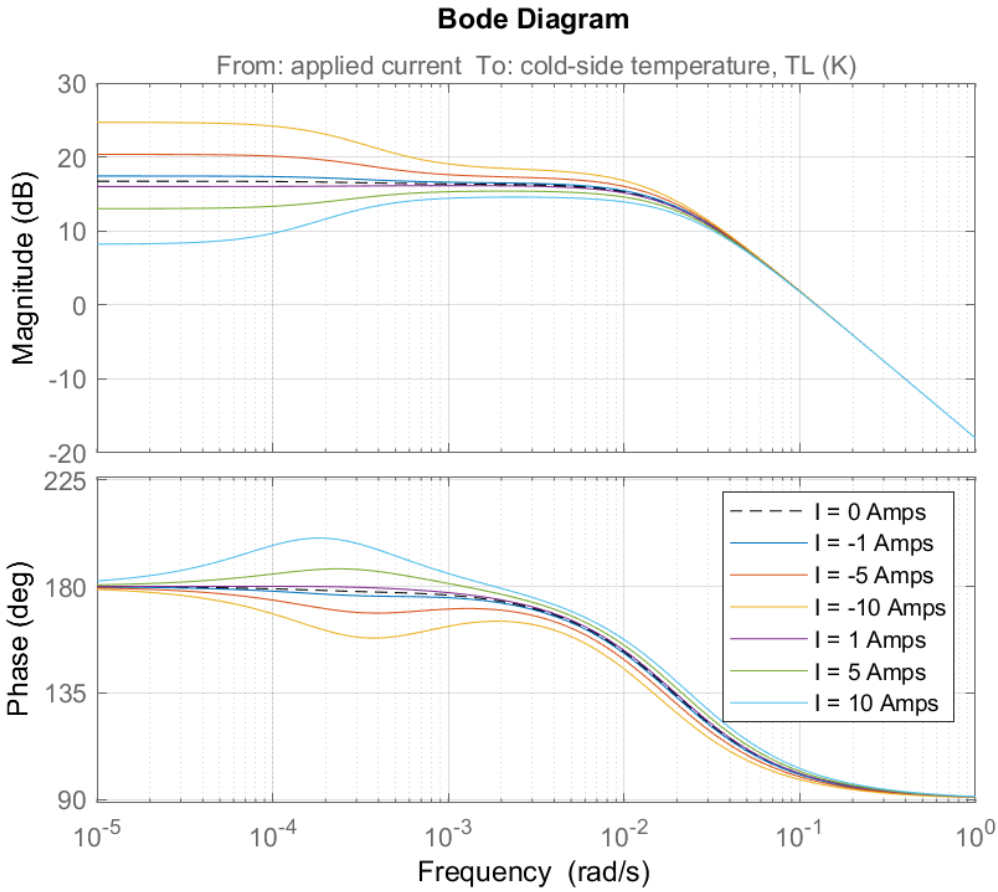

Fig. 4.22 Frequency response sensitivity analysis of the UCLA pyroelectric TEC system model for various values of operational current $\bar{I}$.

4.4.3 Operational hot-side (chamber) temperature

To complete our operating point variation analysis we investigate the effect on the response of the TEC model of various operating hot-side (chamber) temperatures $\bar{T}_H$. The results of this analysis are plotted in Figs. 4.25 and 4.26.

With these simulations carried out, we found that

1. As with the current operating point, the hot-side (crystal) temperature operating point also has its greatest effect on the low frequency magnitude. However, the effect is the least out of all the operating point parameters.

2. The low frequency magnitude response for each operating point is supported by the steady-state values that are seen in the unit-step responses.

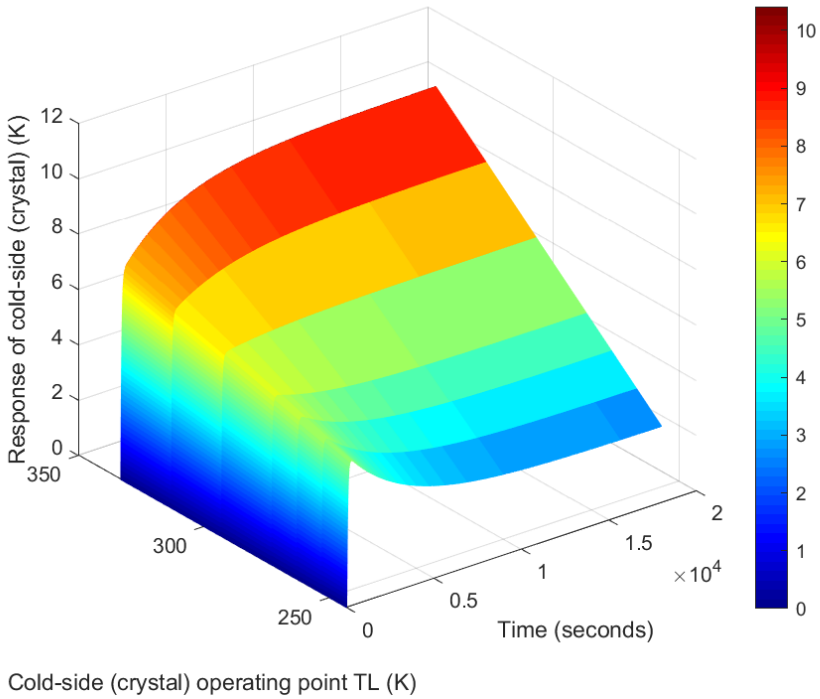

Fig. 4.23 Three-dimensional plot of positive unit-step response curves for various cold-side (crystal) operating point temperatures $\bar{T}_L$.

3. The corner frequency remains unchanged at approximately 0.01 rad/s.
4. The gain crossover frequency remains unchanged at approximately 0.1 rad/s; and the bandwidth is still approximately 0.2 rad/s.
5. The phase crossover remains unchanged at around 10^{-5} rad/s.

State-space

The phase portraits in Figs. 4.27 and 4.28 show trajectories moving directly towards, and converging to the critical point. The trajectories that are the eigenvectors move in straight lines. The rest of the trajectories move, initially when near the critical point, roughly in the same direction as the eigenvector of the eigenvalue with the smaller absolute value. Then, farther away, they would bend towards the direction of the eigenvector of the eigenvalue with the larger absolute value. The trajectories move from infinite-distant out towards, and eventually converge at, the critical point (when the eigenvalues are distinct, real and are both negative). It is an asymptotically stable node. All trajectories of its solutions converge to the critical point as $t \to \infty$. A critical point is asymptotically stable if all of the system

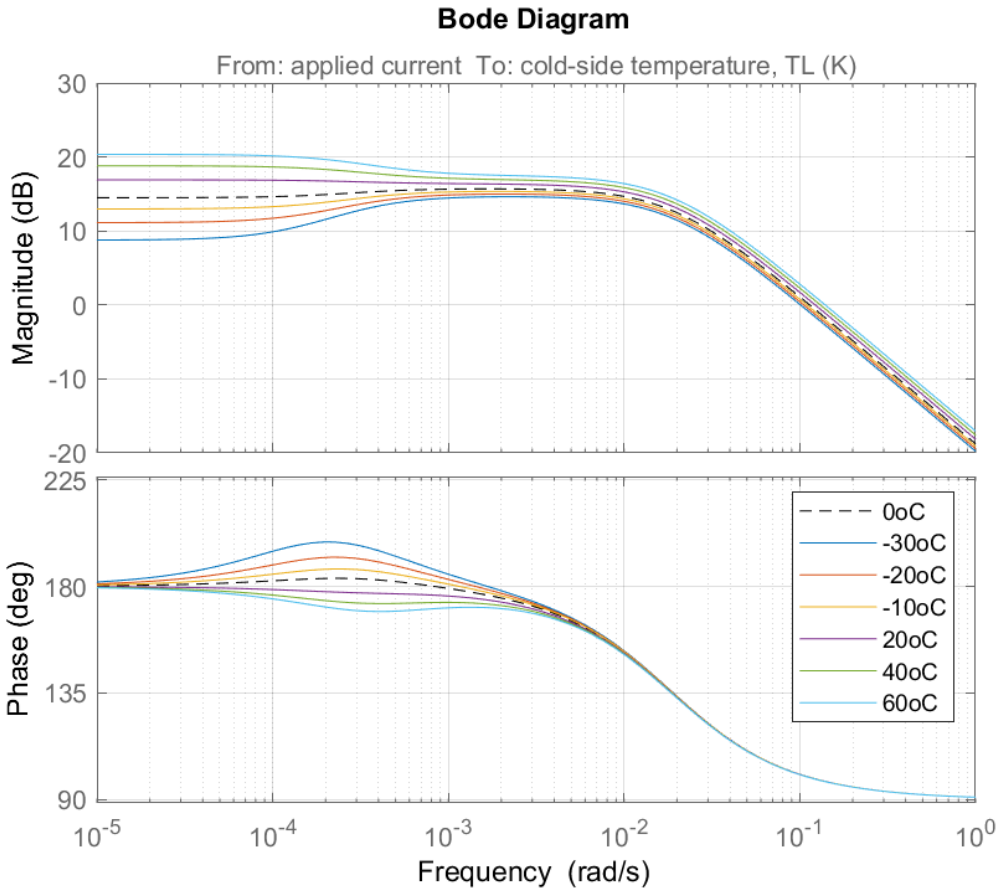

Fig. 4.24 Frequency response sensitivity analysis of the UCLA pyroeletric TEC system model for various values of operational cold-side (crystal) temperature $\bar{T}_L$.

eigenvalues are negative, or have a negative real part for complex eigenvalues.

It can be seen that:

1. For all values of $\tilde{T}_L$ the corresponding temperature change in $\tilde{T}_H$ is small. If we take, for example, the initial change in temperature for the hot-side (chamber) to be $\tilde{T}_H = 0$ K and vary the initial change in the cold-side (crystal) temperature, $\tilde{T}_L$, we can see from Fig. 4.27 that the resultant change in $\tilde{T}_H$ is never more than 5 K.

2. Now, if we take the initial change in temperature for the cold-side (crystal) to be $\tilde{T}_L = 0$ K and vary the initial change in the hot-side (chamber) temperature, $\tilde{T}_H$, by the same amount, Fig. 4.27 shows the change in $\tilde{T}_L$ to be twice that of $\tilde{T}_H$ for the same simulation.

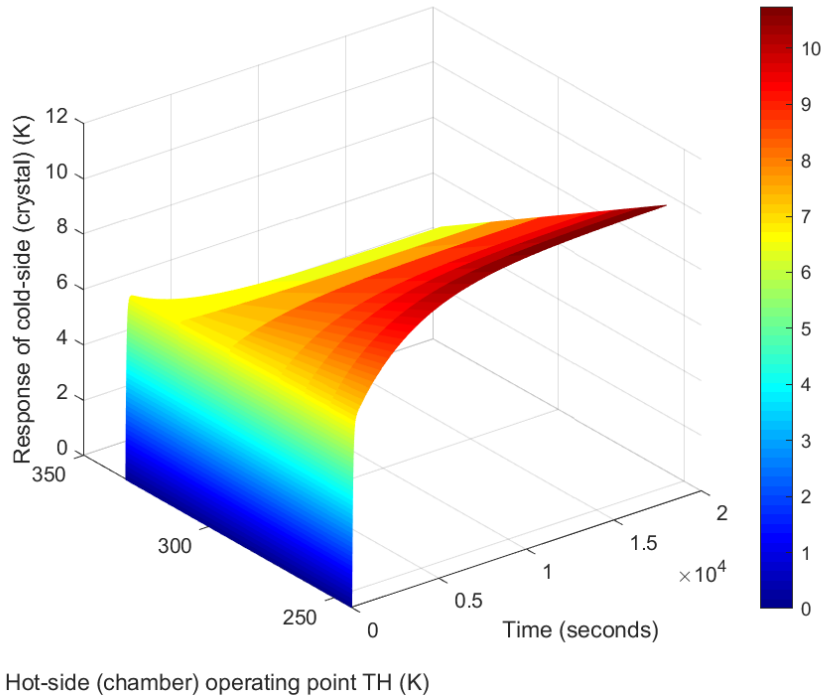

Fig. 4.25 Three-dimensional plot of unit-step response curves for various hot-side (chamber) operating point temperatures $\bar{T_H}$.

3. Figure 4.28 shows the effect of the sign of $\bar{I}$ on the phase-plane trajectories. We can see that the trajectories for the more negative current operating points have the greater magnitude temperature changes.

The phase-plane analysis indicates that the temperature changes seen by the hot-side (chamber) will be much less than those seen by the cold-side (crystal), so we can narrow down the range of potential model operating points for $\bar{T_H}$. We will take $\bar{T_H}$ between $-10°$C and $10°$C.

4.4.4 Combined effects of operational point variation

It is important to now consider the combined effects of the following operational point variations, given in Eq. 4.20; the maximum and minimum values are chosen as they are expected operational values for the pyroelectric system. Figure 4.29 shows the frequency response for all combinations of the operating point values. The large magnitude variation at low frequency is seen in the plot.

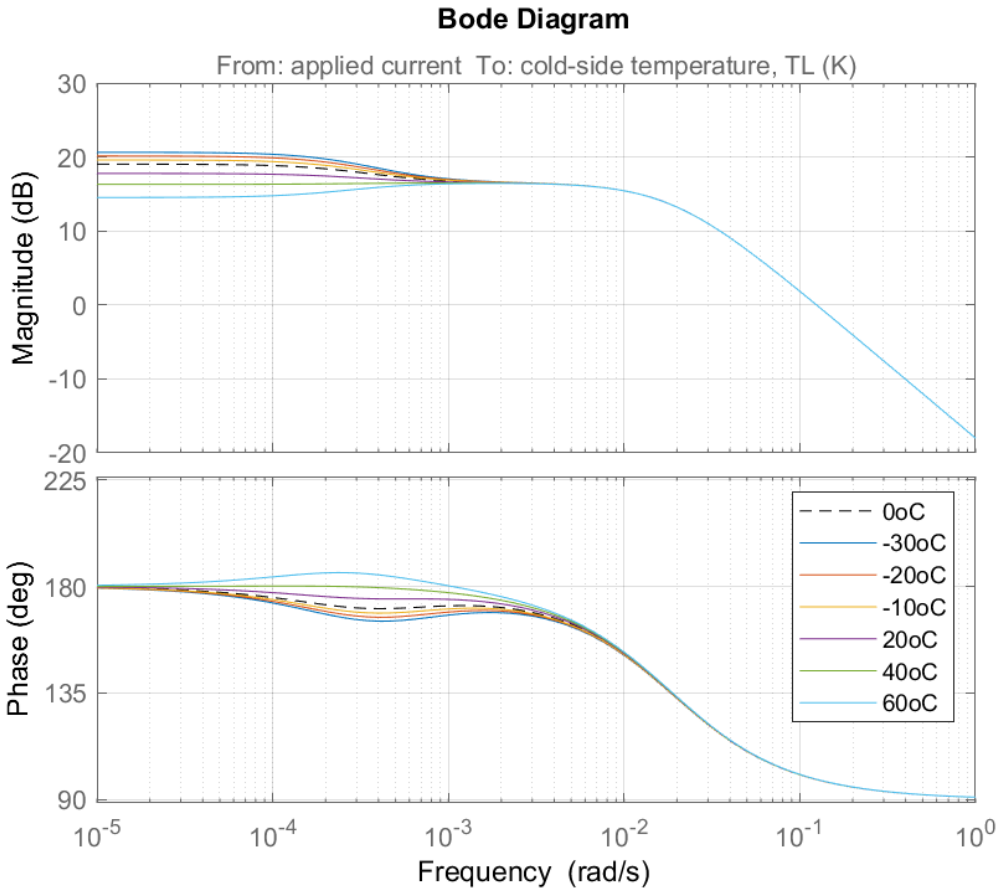

Fig. 4.26 Frequency response sensitivity analysis for UCLA pyroelectric TEC system model operational hot-side (chamber) temperature $\bar{T_H}$.

$$\begin{aligned} \bar{T_L} &= [-30+273\text{ K}, 60+273\text{ K}] \\ \bar{T_H} &= [-10+273\text{ K}, 10+273\text{ K}] \\ \bar{I} &= [-10\text{ A}, 10\text{ A}] \end{aligned} \tag{4.20}$$

However, if we over-plot with the physically realistic variations for room temperature operation (black circles), we see that this range is reduced for our expected 'normal operation'. The analysis reinforces the requirement to vary the operating point of our model over time, if we wish to execute transients with large temperature or current changes.

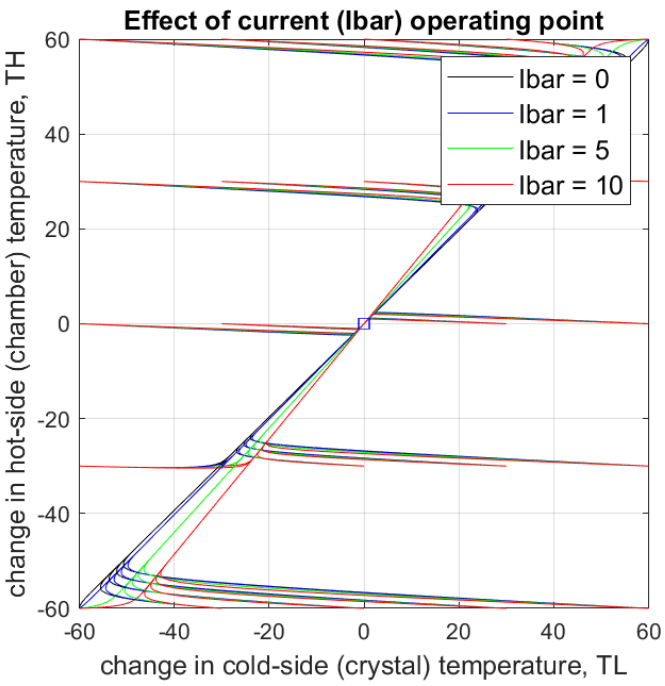

Fig. 4.27 Phase-plane plot for hot- and cold-side temperature changes with positive $\bar{I}$.

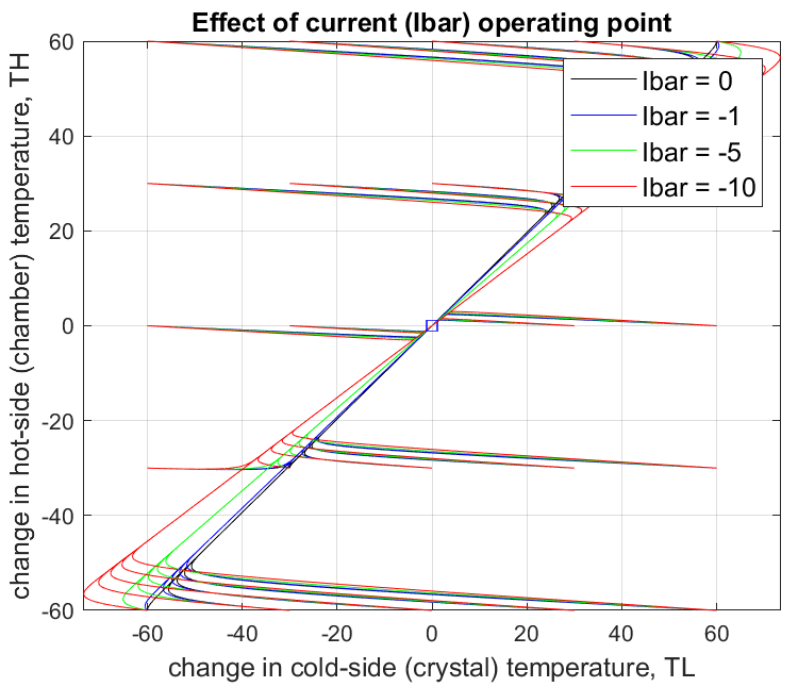

Fig. 4.28 Phase-plane plot for hot- and cold-side temperature changes with negative $\bar{I}$.

$$
\begin{aligned}
\bar{T_L} &= [25+273\text{ K}, 60+273\text{ K}] \\
\bar{T_H} &= [-5+273\text{ K}, 25+273\text{ K}] \\
\bar{I} &= [-10\text{ A}, 10\text{ A}]
\end{aligned}
\tag{4.21}
$$

It is useful to also change the operating point current $\bar{I}$ in the pyroelectric TEC Model to match the input current value. Figure 4.30 shows the expected increase in cold-side (crystal) temperature with increase in current input and the same increase in current operating point. For the -5 A input the steady-state temperature change is 12.4 K, and for -10 A input this is increased to 24.8 K. This change in operating point value causes the change in dynamic response. The operating point variation can be seen to cause the steady-state value to increase.

Performance specification	I = -1 A	I = -5 A	I = -10 A
Peak (K)	5.18	28.8	84.1
Overshoot %	108	31.7	n/a
Time to peak (s)	255	322	9.78×10^3
Settling time (s)	1.33×10^4	9.99×10^3	9.78×10^3
Rise time (s)	26.1	60	3.13×10^3

Table 4.5 Step responses for varying current input along with operating point.

Table 4.5 highlights the increasing damping that is caused by increasing the absolute value of the operating point current. As the current is increased (i.e. becomes more negative), the rise time increases, and the peak response increases along with the time to peak. The amount of overshoot and the settling time both decrease with increasing operating point current.

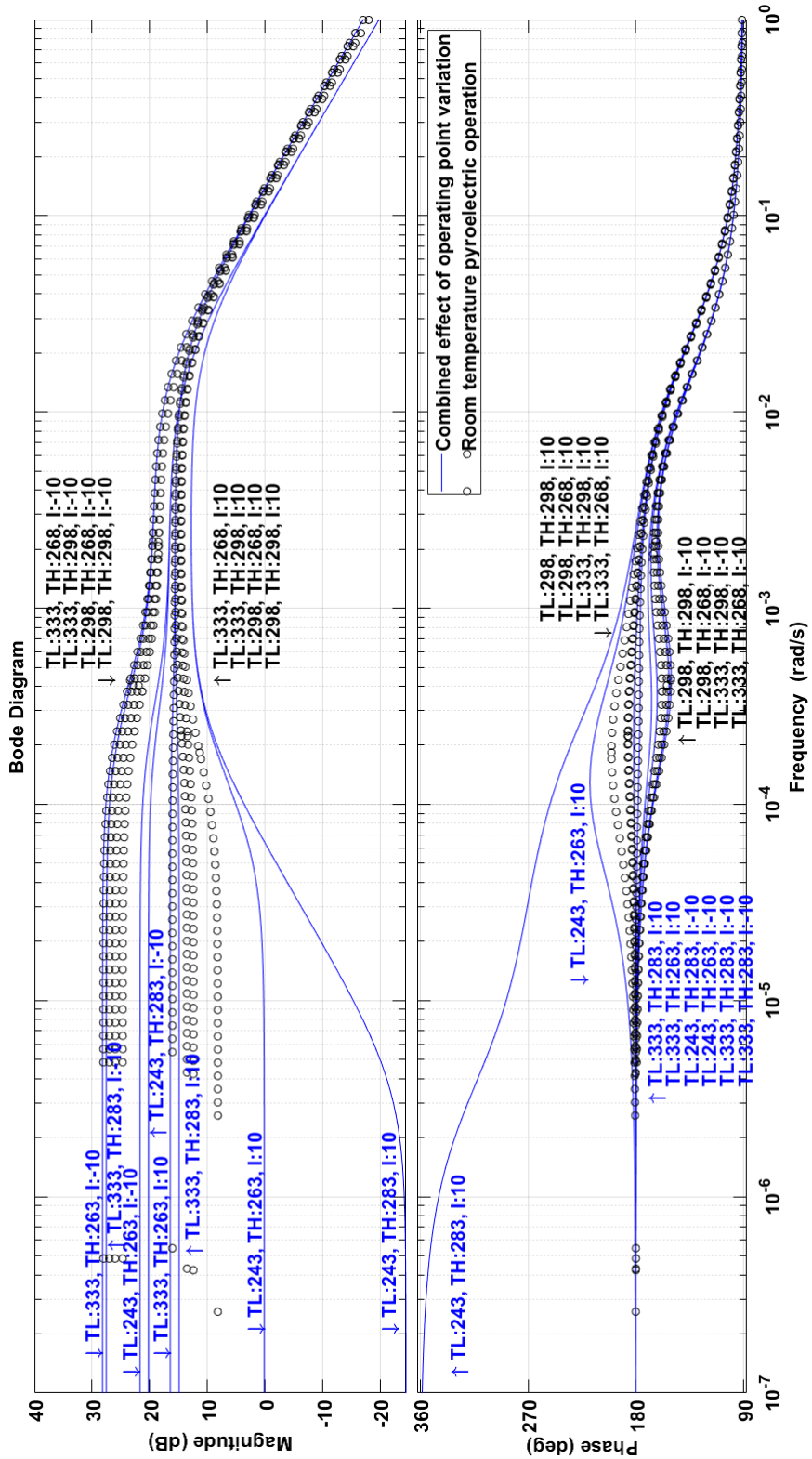

Fig. 4.29 Frequency response combined sensitivity analysis for the UCLA pyroelectric TEC system.

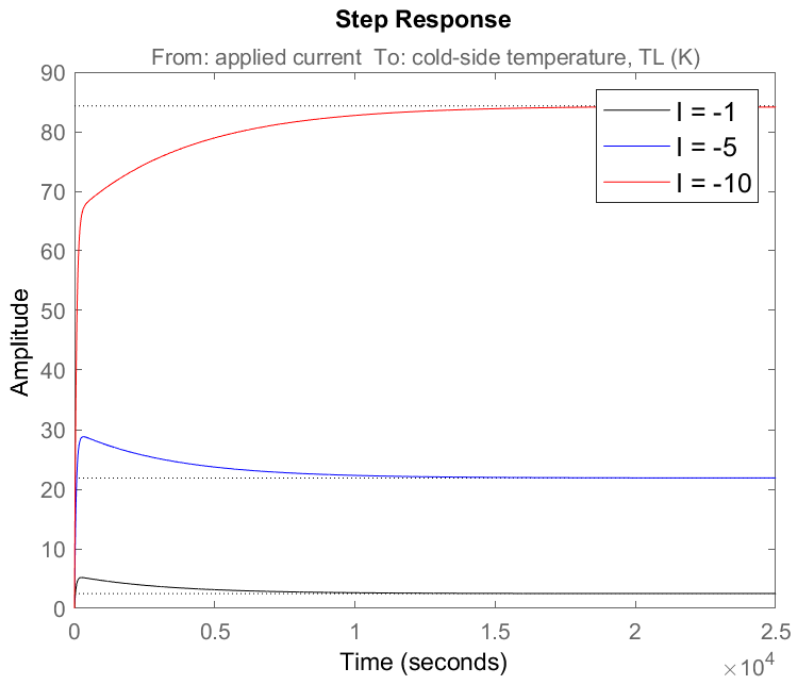

Fig. 4.30 UCLA pyroelectric TEC Model unit-step response.

4.5 Summary

1. The effect of the dynamic behaviour of the thermal masses of the heat sink (crystal) and the cooling-load heat exchanger (chamber) will present a challenge to the control system design.

2. A pole-zero map analysis has shown that we could potentially simplify our model by eliminating near-cancelling pole-zero pairs during our control system design.

3. The linear dynamic model has been shown to vary with operating conditions. We have quantified this output variability and attributed this to the different operating point parameters. We can rank the parameters in terms of their effects on the output. It seems that the magnitude and sign of $\bar{I}$ will be the most important parameter, followed by $\bar{T}_L$ and then $\bar{T}_H$.

The analysis has reinforced the requirement to vary the operating point of our model over time if we wish to execute transients with large temperature or current changes. We will have to design our controller on a nominal parameter set, and then test the robustness of the controller to different operating points to confirm the credibility of the control system design. Designing a closed loop system will allow us the flexibility of placement of poles, which can be used to govern the stability. Chapter 5 is dedicated to controller design for the pyroelectric TEC system that we have just analysed in this chapter.

Chapter 5

Control system design for a pyroelectric TEC model

5.1 Introduction

The control system for our pyroelectric TEC system consists of an automatic controller, an actuator, a plant, and a sensor. The automatic controller compares the actual value of the plant output with the reference input, determines the deviation, and produces a control signal that will reduce the deviation to zero or to a small value. Simulink is the primary tool used in our pyroelectric TEC control system design; it allows us to use a model-based design approach and, with this, we can easily analyse and compare the performance of our various control systems. Figure 5.1 shows the Simulink model block diagram containing the components of our pyroelectric TEC control system. Working through the blocks in Figure 5.1 from left to right, we have:

1. An input signal multiport switch for selecting the temperature input (set point) signal type, which can be programmed using the mfile. The model has been constructed so that the input (reference signal) may be selected from various types, including a step, a sine-wave or a saturated ramp signal. The Simulink model is initiated, and the simulations are automated, using a MATLAB mfile script. The input signal is saved to the MATLAB workspace, and later plotted for use in the analysis of the response of the control system designs.

2. A summing junction which compares the reference cold-side (crystal) temperature change input signal with the actual temperature change, and outputs an error signal. The error signal is acted on by the controller, and it is saved to the MATLAB workspace.

3. A second multiport switch which is for the selection of the controller type. We are considering two common types of industrial controllers which may be used: the two-position (or on-off) controller and the proportional-plus-integral-plus-derivative (PID) controller. Which of these we ultimately select will depend on the nature of our pyroelectric TEC system and the operating conditions. Port 3 on the controller multiport switch is a forward path to the TEC without any controller, and is implemented in open-loop investigations.

4. A saturation block on the output of the multiport switch ensures that the controller cannot demand more than the maximum current in either the positive or negative direction (defined previously to be our cooling and heating currents). The current signal is also saved to the MATLAB workspace.

5. A pyroelectric TEC model which has been implemented as a linear parameter-varying (LPV) system. An LPV system comprises a linear state-space model whose dynamics vary as a function of time-varying scheduling parameters. In our case, it is the sign of the current input $\tilde{I}$ which acts as the scheduling parameter, and initiates the model switching between two stacked, local linear time-invariant (LTI) state-space models. The Simulink block implements a grid-based representation of the LPV system. A grid of values is specified for the scheduling parameter. At each operating point of $\pm\,\bar{I}$ we specify the corresponding linear system as a state-space model object. An array of state-space models, with operating point information, is then generated and used to configure the LPV system block. The structure of the LPV model will allow us to add additional models to the grid as required. We will design a controller based on the LPV model and simulate its performance against the nonlinear model.

6. The nonlinear model represented by Eqs. 3.6 and 3.7 is implemented using two general expression '*Fcn*' blocks and integrators on the outputs. The initial conditions of the integrators are set to the operating point temperatures of $T_H = 298$ K and $T_L = 298$ K.

The first task is to check that the open-loop nonlinear model and the LPV model implementations simulate the system dynamics correctly by comparing the outputs with our previous pyroelectric TEC model in Chapter 4. The open-loop structure has no closed signal path whereby the output influences the control effort. In order to simulate our open-loop system, the controller multiport switch is set to 3 and the feedback gain, H, is set to zero. We applied both a positive and a negative unit-step input current to the system (and correspondingly $\bar{I} = \pm 1$ A in the LPV model of the TEC), and these responses are shown in Figs. 5.2 and 5.3 respectively. These results confirm the correct dynamic response of the open-loop LPV and nonlinear TEC model, when compared with Figs. 4.8 and 4.10 in section 4.3.3.

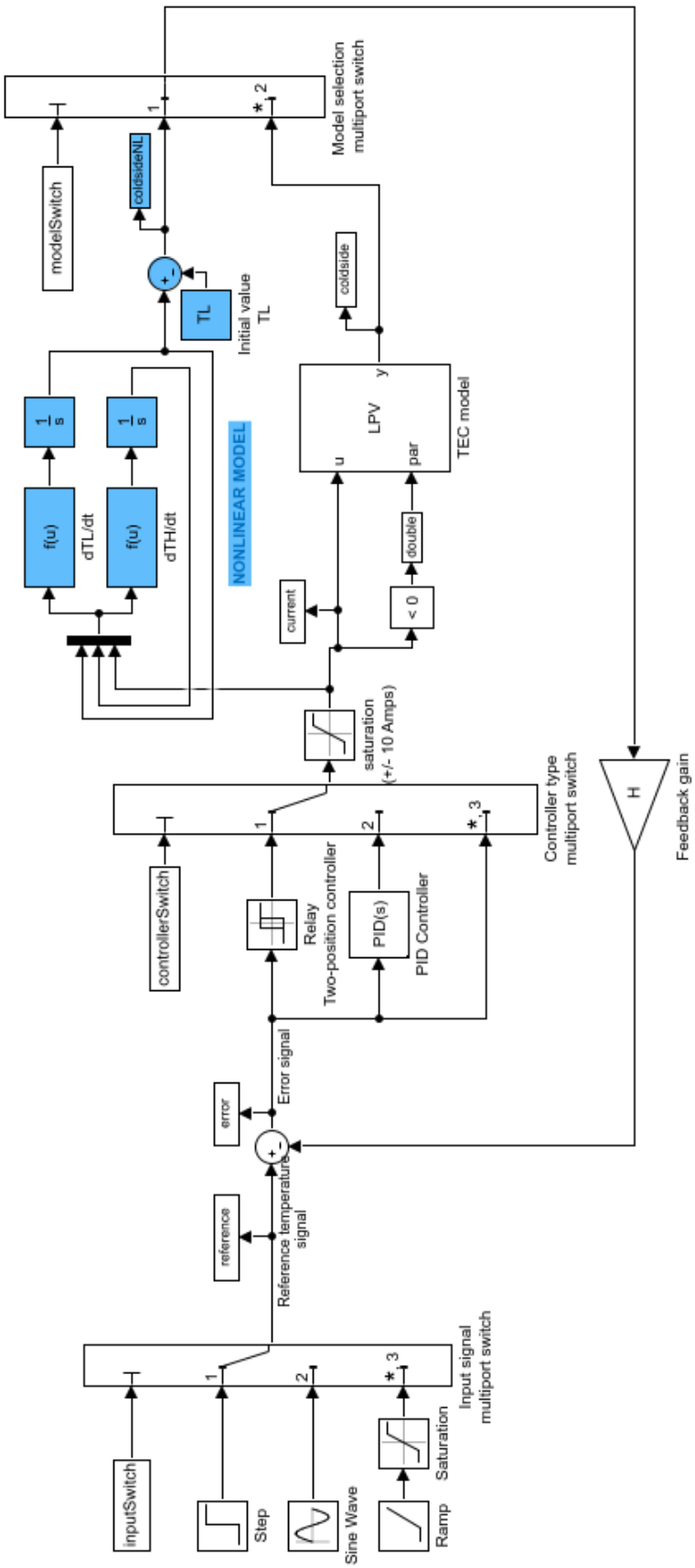

Fig. 5.1 Simulink LPV and nonlinear TEC models.

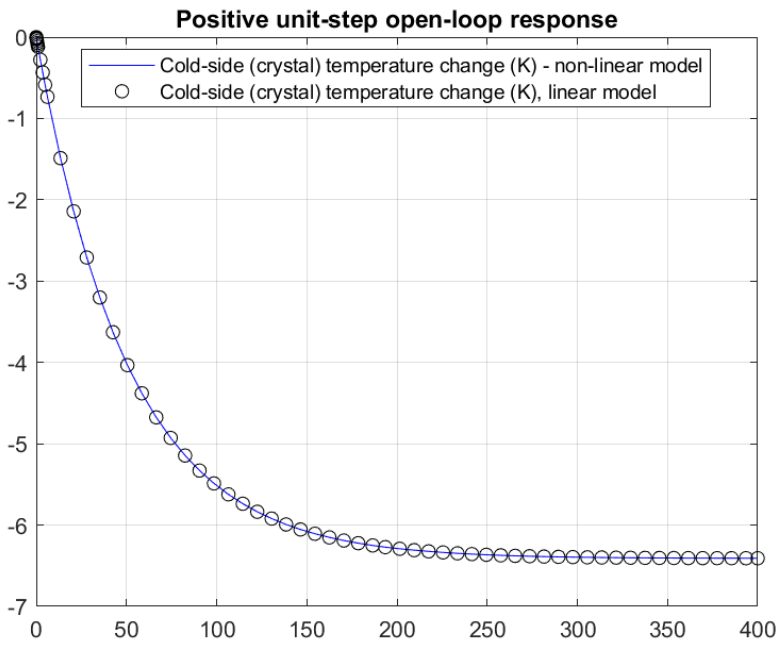

Fig. 5.2 Positive unit-step responses of the open-loop Simulink nonlinear and LPV TEC models.

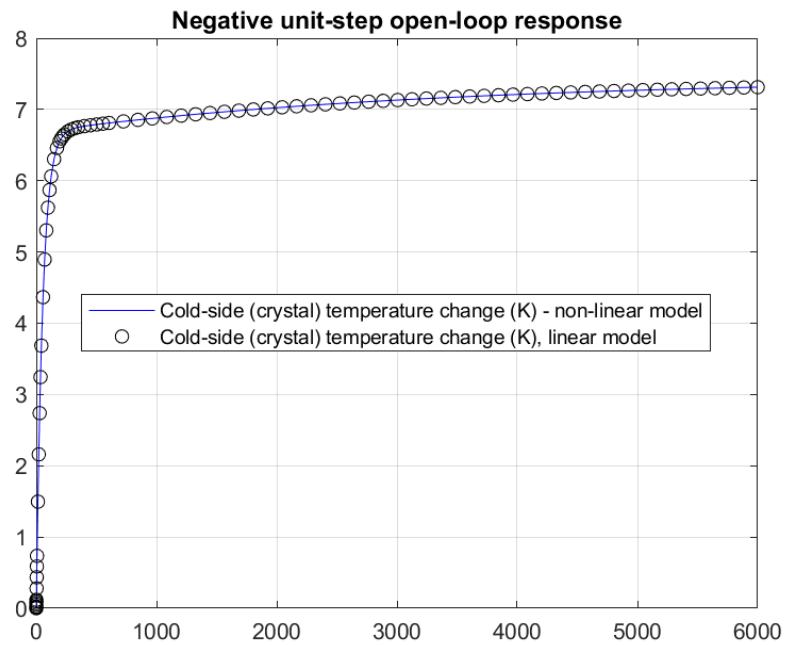

Fig. 5.3 Negative unit-step response of the open-loop Simulink nonlinear and LPV TEC models.

5.2 Two-position control action

In a two-position control system, the actuating element has only two fixed positions. This type of control is relatively simple and inexpensive, and therefore widely used in both industrial and domestic control systems. With reference back to the block diagram of our TEC system in Fig. 5.1, the output signal from the controller is the current $\tilde{I}$ (which is subsequently saturated in the Simulink block labelled TEC Current Saturation), and the actuating error signal is the output from the summing junction. In two-position control, the current signal $\tilde{I}$ remains at either a maximum or a minimum value, depending on whether the actuating error signal is positive or negative.

The range through which the actuating error signal must move before the switching occurs is called the *differential gap*. The differential gap causes the controller output $u(t)$ to maintain its present value until the actuating error signal has moved slightly beyond the zero value. This differential gap is intentionally provided in order to prevent too-frequent operation of the on-off mechanism. The Simulink Relay block behaves like a switch with hysteresis; that is, it has a different condition for switching "ON" than it does for switching "OFF".

5.2.1 Unit-step response

In this case, the dead-band is set to $\pm$ 0.1 K, and we have taken the maximum current allowable for the TEC to be $\pm$ 10 A. The programmed relay schedule is:

1. Switch full negative = $-$ 0.1 K
2. Full negative value = $-$ 10 A
3. Switch full positive = + 0.1 K
4. Full positive value = + 10 A

Figure 5.4 shows the controller response to a positive unit-step input, and Fig. 5.5 shows the negative unit-step response. These on-off controller responses show:

1. The current input to the TEC is either 100% full negative or full positive regardless of where the crystal temperature reading is with respect to the reference temperature input. This has caused overshoots and undershoots in the response.

2. Oscillations and swings of temperature. The temperature swings may be reduced by programming a lower temperature differential, but this would increase the number of switching points and potentially decrease the longevity of control elements through excessive use.

3. The implementation of hysteresis has caused there to be a constant error around the set-point. However, if no hysteresis was implemented, we would probably see damage to the TEC due to rapidly switching it on and off around the set-point.

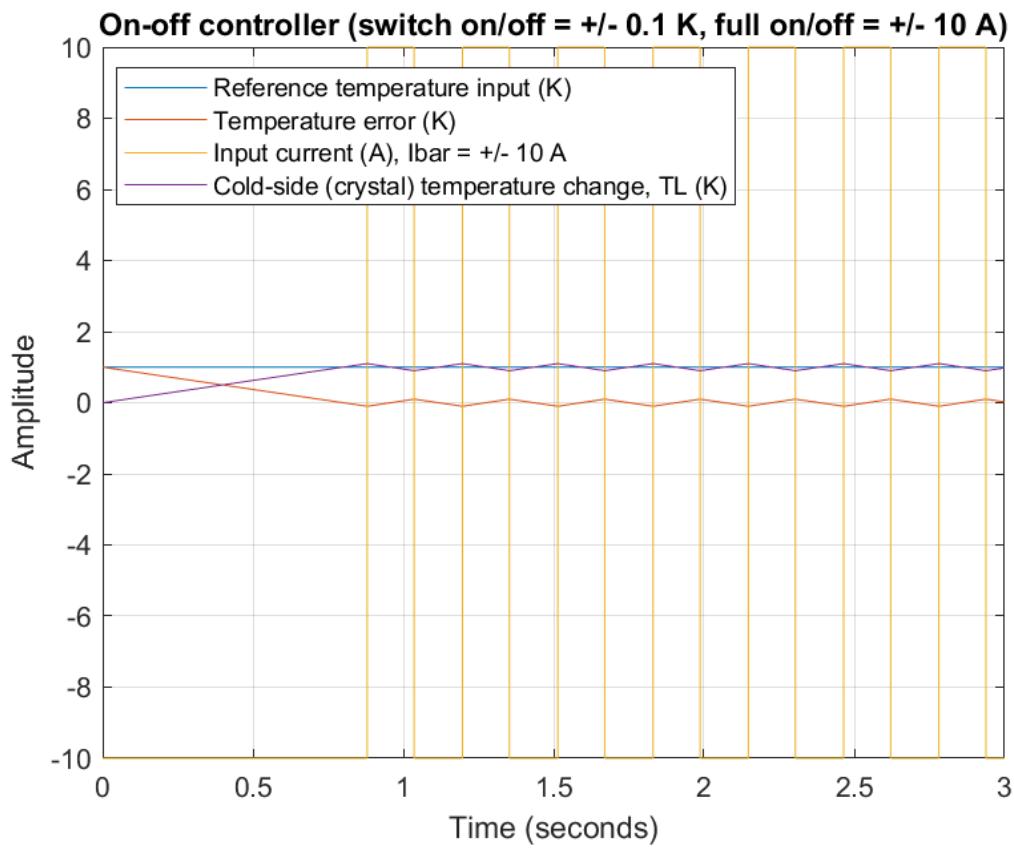

Fig. 5.4 Simulink nonlinear TEC model with an on-off controller - positive step.

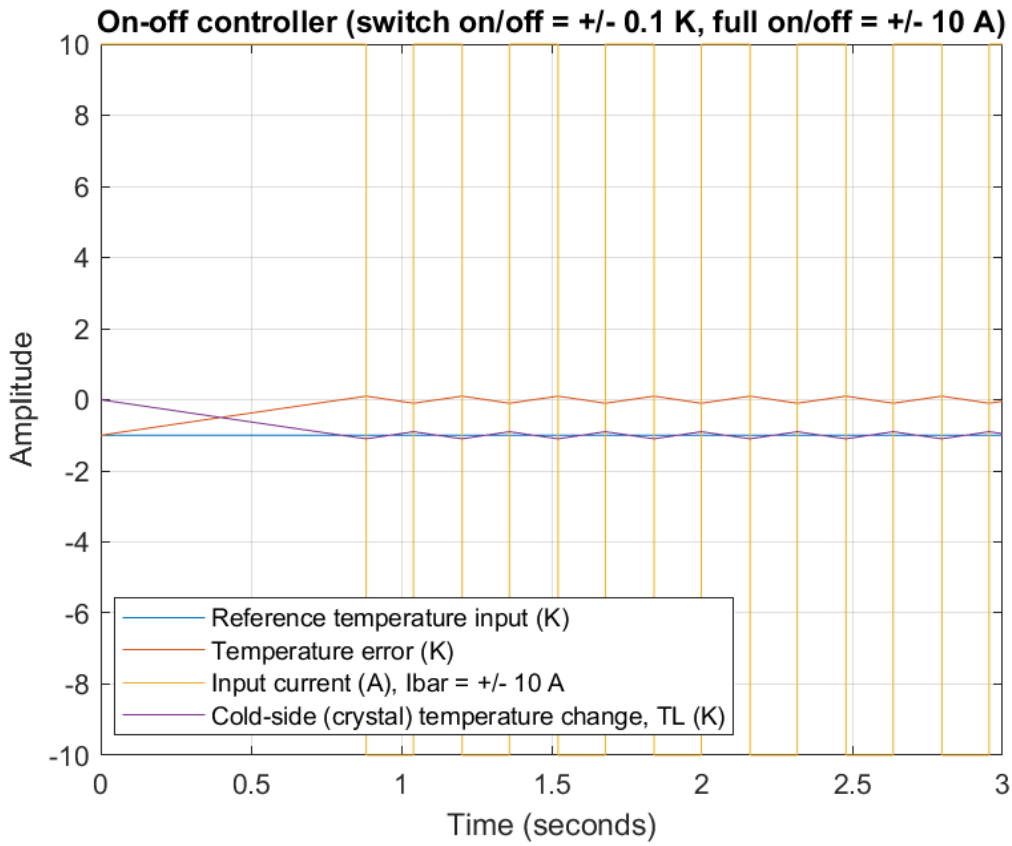

Fig. 5.5 Simulink nonlinear TEC model with an on-off controller - negative step response.

5.2.2 Ramp response

A ramp input of 40 K is commonly applied in UCLA pyroelectric experiments [74]. We expect to operate our system with at least 40 degree temperature changes applied to the pyroelectric crystal, and our open-loop simulations of Chapter 4 demonstrated that we would potentially require up to 10 A of current input for this temperature change. We have taken the maximum possible current input available; however, to avoid excessive over-switching we have allowed a 10% error at steady-state. The on-off controller relay schedule has been initially programmed as:

1. Switch full negative = − 4 K
2. Full negative value = − 10 A
3. Switch full positive = + 4 K
4. Full positive value = + 10 A

Our ramp response analysis shows:

1. The use of the programmed on-off controller has again resulted in oscillations and swings of temperature and a steady-state error, which can be seen in Figs. 5.6 and 5.7. There are, once again, overshoots and undershoots seen in these responses.
2. The difference in the heating and cooling ramp responses can be clearly seen, and it is particularly apparent in the oscillations around steady-state (from 200 seconds). In the cooling ramp response we can see fewer current switching points (less than half the number than in the heating ramp). This is due to the slower responding dynamics of the system in the cooling mode of operation.
3. In order to obtain the best performance of the on-off controller we need to trade off the accuracy and the amount of switching in the response. We can reprogramme the on-off controller relay schedule as:
   (a) Switch full negative = − 4 K
   (b) Full negative value = − 5 A
   (c) Switch full positive = + 4 K
   (d) Full positive value = + 5 A

The effect of decreasing the maximum current input to the TEC on the control system response is shown in Fig. 5.8. Although the overall accuracy of the response has decreased, the amount of switching has reduced to a more tolerable number.

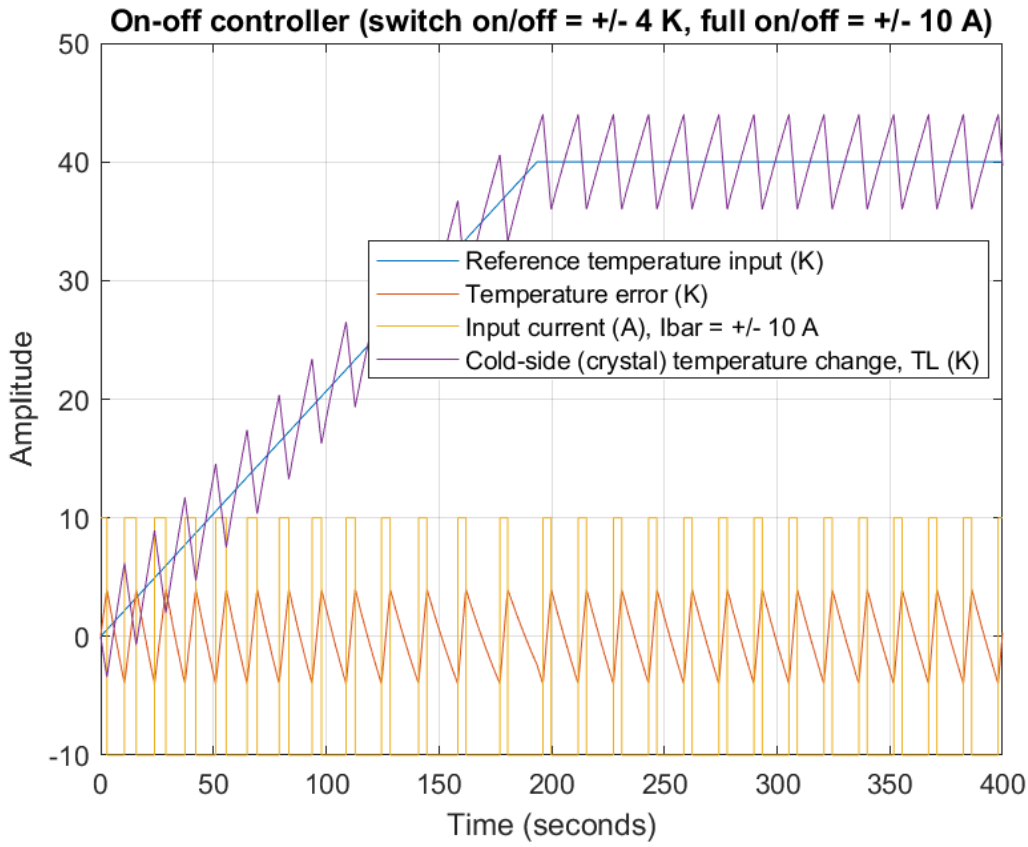

Fig. 5.6 Simulink nonlinear TEC model with an on-off controller - positive ramp response.

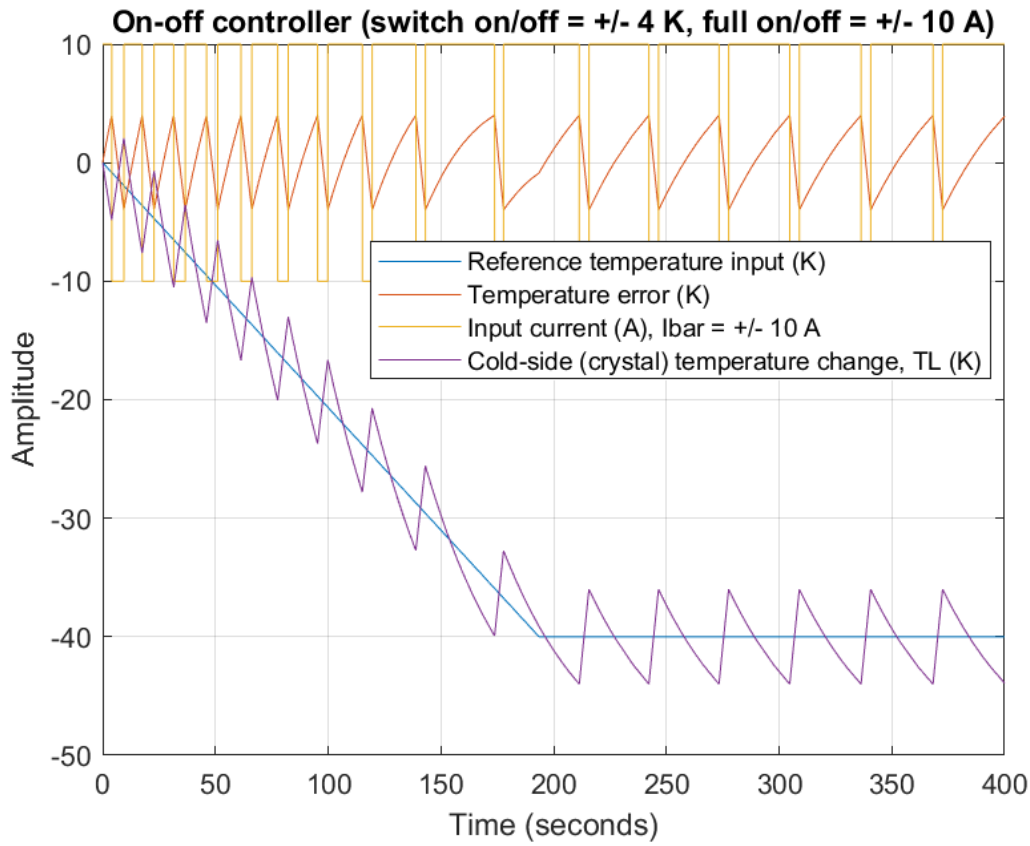

Fig. 5.7 Simulink nonlinear TEC model with an on-off controller - negative ramp response.

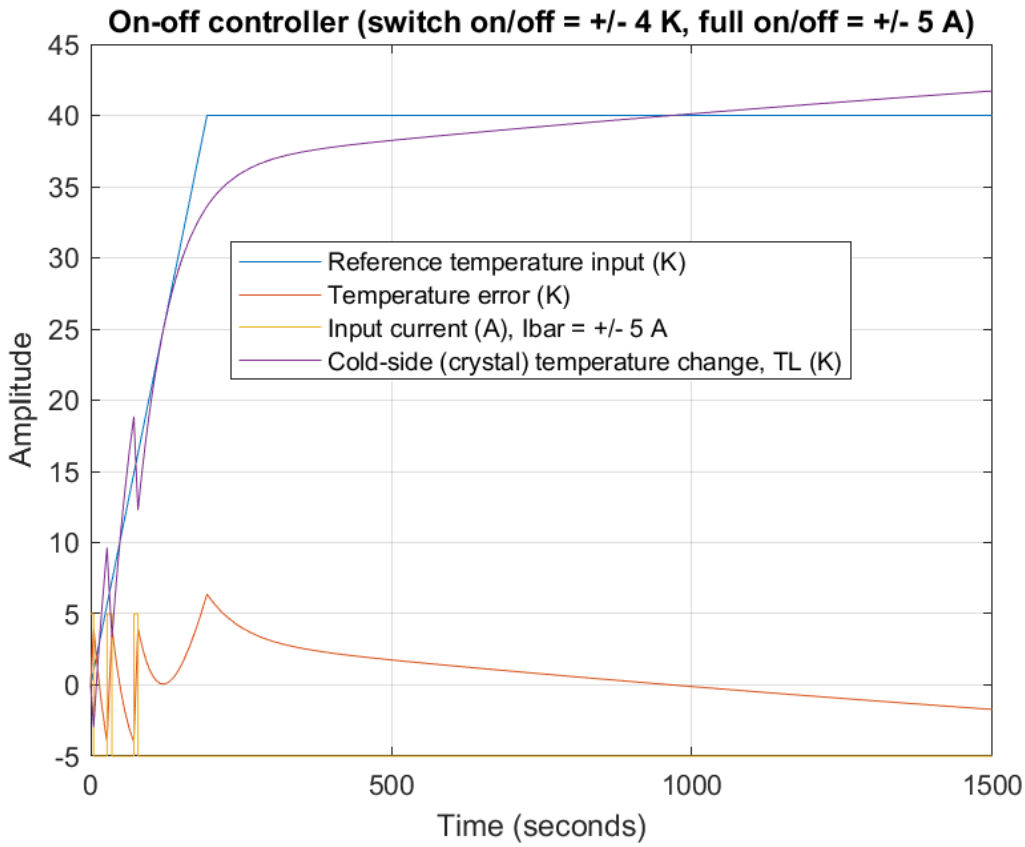

Fig. 5.8 Simulink nonlinear TEC model with an on-off controller - positive ramp response, with limited maximum current at 5 A.

5.2.3 Sine-wave response

Although previous researchers have not continuously cycled their pyroelectric systems, we intend to investigate the feasibility of this mode of operation. A reasonable frequency at which to cycle our system can be determined from the frequency analysis that we conducted in Chapter 4. Referring back to Fig. 4.29, we can see that all the frequency response magnitude plots pass through 0 dB at around 0.1 rad/sec, which indicates that the system cannot be cycled at frequencies above this point. In fact, we can see that 0.01 rad/sec is the highest frequency in the constant magnitude portion (flat region) of the plot. The system attenuates higher frequencies, so this would appear to be the fastest frequency at which we may cycle the pyroelectric TEC and obtain a good response.

Our sine-wave response analysis shows:

1. From Fig. 5.9, it seems that it is possible to keep the system stable, with a reasonable amount of accuracy through implementation of on-off type control. However, the amount of continuous controller switching seen in the response would cause wear on the control-system components and damage to the TEC.

2. In order to obtain the best performance of the on-off controller we need to trade off the accuracy and the amount of switching in the response. We can reprogramme the on-off controller relay schedule as:

   (a) Switch full negative = − 4 K

   (b) Full negative value = − 5 A

   (c) Switch full positive = + 4 K

   (d) Full positive value = + 5 A

   The effect of decreasing the maximum current input to the TEC on the control system response is shown in Fig. 5.10. Although the overall accuracy of the response has decreased, the number of switching points has reduced to a more tolerable number.

3. Figure 5.11 confirms the expectation that reducing the maximum current to ± 1 A will increase the error and reduce the accuracy of the controller. For this transient, the following relay schedule was implemented:

   (a) Switch full negative = − 4 K

   (b) Full negative value = − 1 A

(c) Switch full positive = + 4 K

(d) Full positive value = + 1 A

With these values the controller will not meet the accuracy required of the pyroelectric TEC system.

4. The best on-off control system response for a 40 degree, 0.01 rad/sec sine-wave operational cycle has been found to be produced for the following relay schedule:

   (a) Switch full negative = − 4 K

   (b) Full negative value = − 6 A

   (c) Switch full positive = + 4 K

   (d) Full positive value = + 6 A

   Figure 5.12 shows that the ± 6 A current control signal supplied to the TEC provides the best trade-off between accuracy (error less than 10%) and amount of switching. The largest error can be observed on the cooling half of the cycle. This is due to the slower dynamic response when the crystal is being force cooled by the TEC.

5. A more sophisticated approach to the control system design would be to modulate the current input to the TEC in proportion to how much temperature error there was present. This can be achieved with a PID controller, which we investigate in the next section.

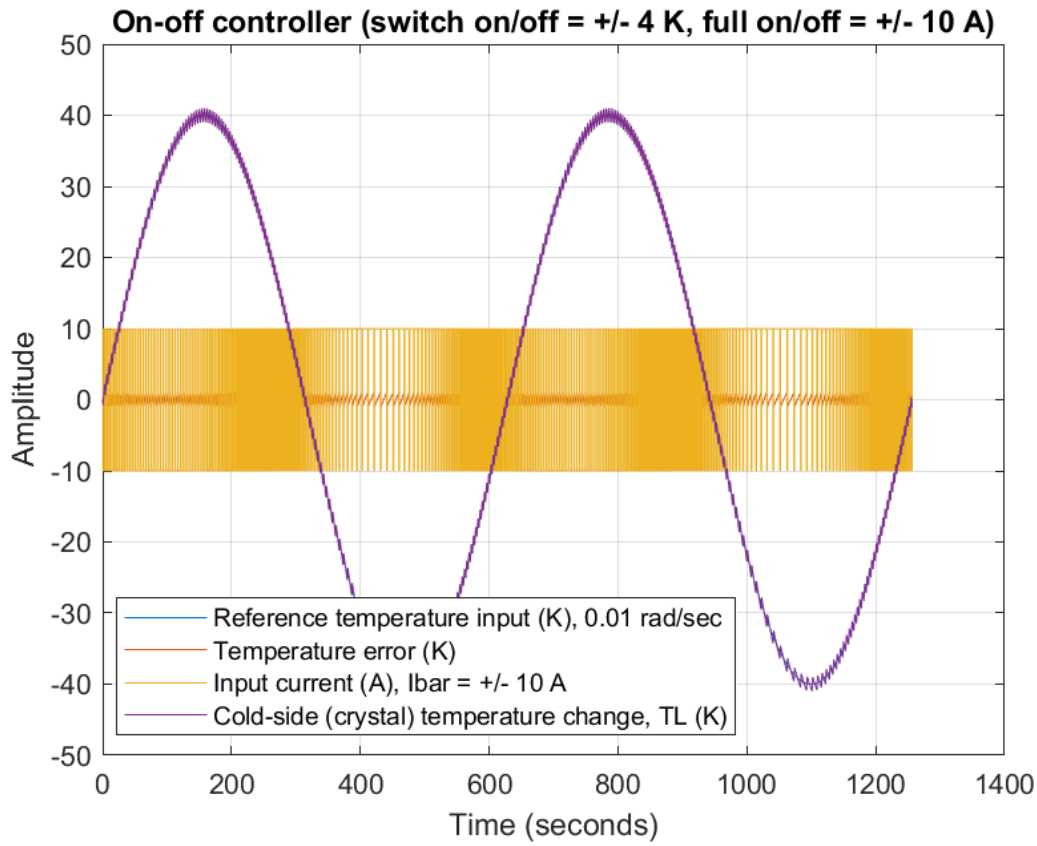

Fig. 5.9 Simulink nonlinear TEC model with an on-off controller - sine-wave response.

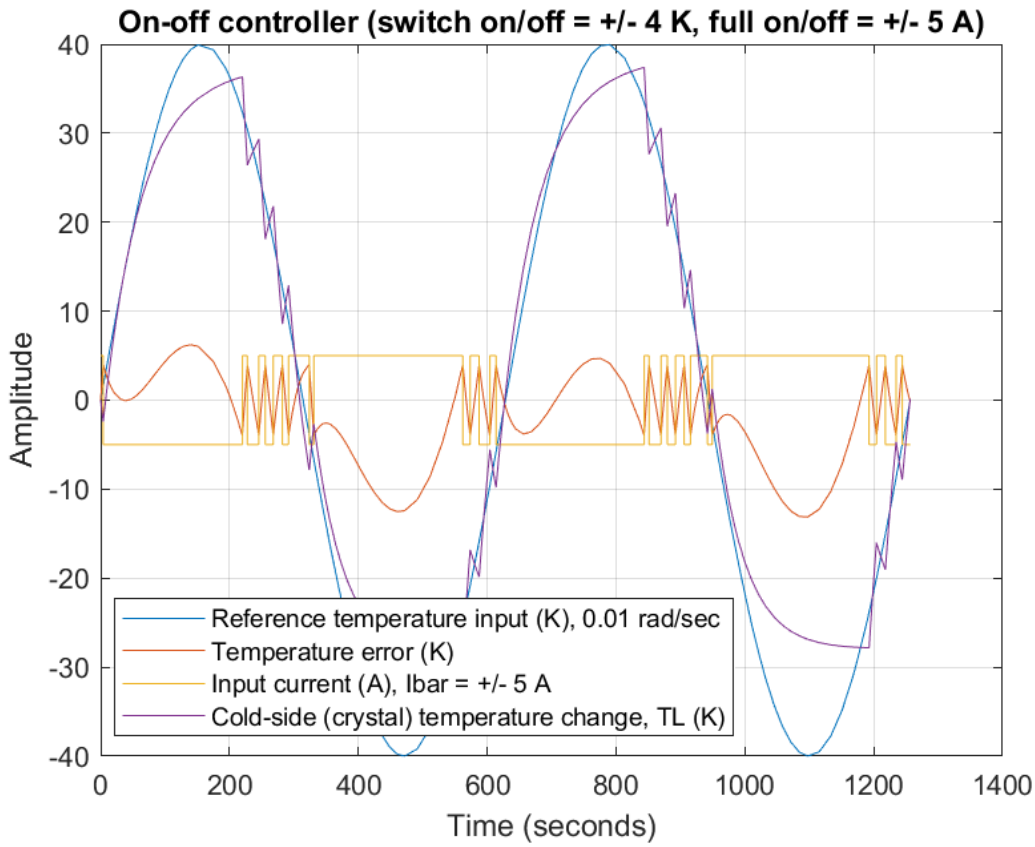

Fig. 5.10 Simulink nonlinear TEC model with an on-off controller - sine-wave response, with limited maximum magnitude of current at 5 A.

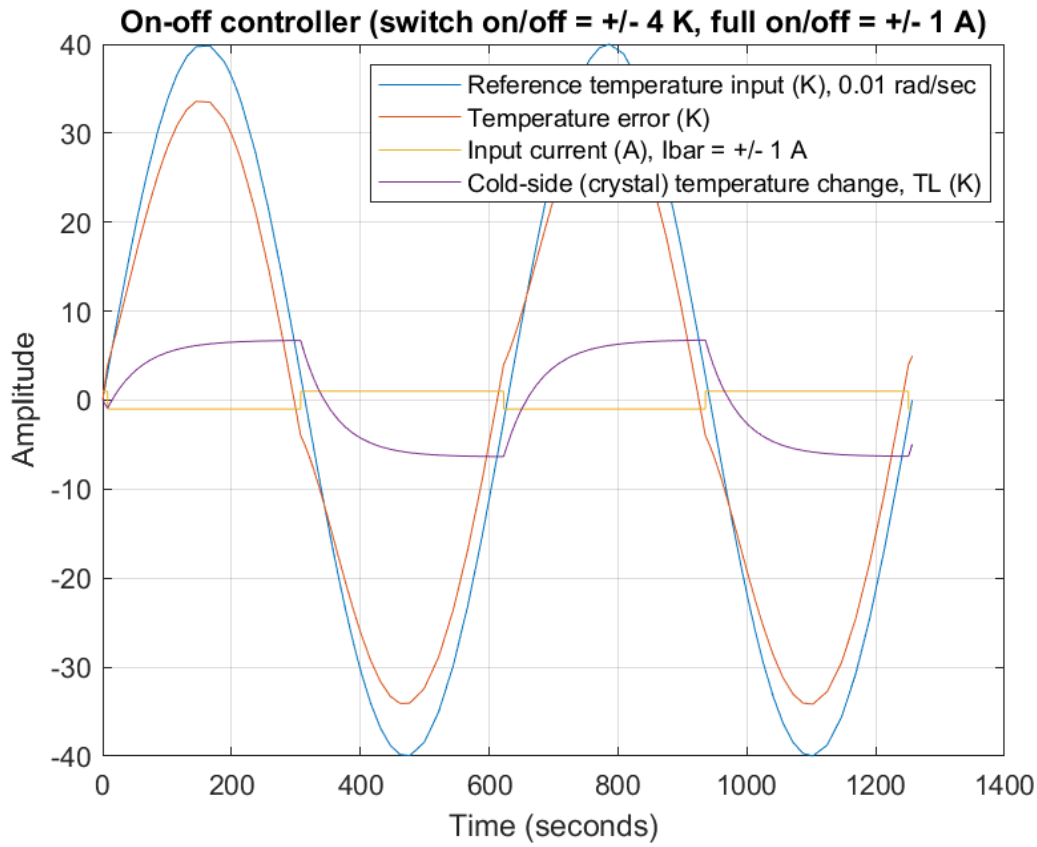

Fig. 5.11 Simulink nonlinear TEC model with an on-off controller - sine-wave response, with limited maximum magnitude of current at 1 A.

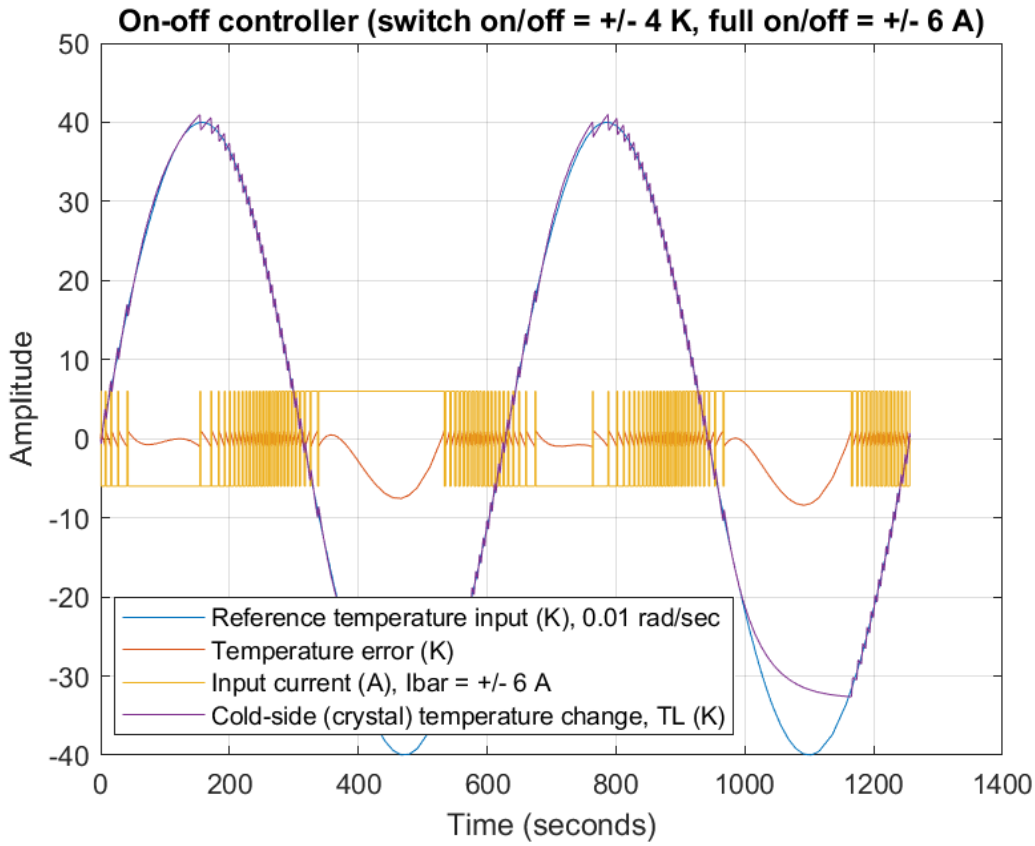

Fig. 5.12 Simulink nonlinear TEC model with an on-off controller - sine-wave response, with limited maximum magnitude of current at 6 A - best compromise between accuracy and potential TEC damage through switching.

5.3 PID control action

The parallel PID controller output is the sum of the proportional, integral and derivative actions, weighted independently by P, I and D, respectively. For example, for a continuous-time parallel-form PID controller, the transfer function is:

$$C_{par}(s) = P + I\left(\frac{1}{s}\right) + D\left(\frac{Ns}{s+N}\right) \tag{5.1}$$

where N is the filter coefficient, which determines the pole location of the filter in the derivative action of the block. The location of the filter pole depends on the Time domain parameter. When Time domain is Continuous-time, the pole location is $s = -N$.

The design of the PID controller using the Simulink PID Tuner involves the following tasks:

1. Develop the Simulink model of the process to be controlled and the PID controller. For our application the model is shown in Fig. 5.1.
2. Launch the PID Tuner. When launching, the software automatically computes a linear plant model from the Simulink model and designs an initial controller.
3. Tune the controller in the PID Tuner by manually adjusting design criteria in two design modes. Our pyroelectric TEC system design requirements (and controller parameters) are:
   (a) A settling time under 150 seconds gives transients of reasonable heating response times when compared with UCLA pyroelectric experiments [74].
   (b) An overshoot of less than 10% will avoid damage to the TEC components (which occurs at around 120 °C) when heating to a potential maximum temperature of 100 °C.
   (c) A rise time of around 5 seconds represents a crystal heating rate of around 12.4 K/min as used by the UCLA group in their experiments [74].
   (d) A zero steady-state error to the step reference input.
4. The tuner computes PID parameters that robustly stabilize the system. For our system the adjusted PID parameters are:
   (a) $P = -0.47647$
   (b) $I = -0.016725$

(c) $D = 1.1409$

and $N = 0.37466$.

5. Export the parameters of the designed controller back to the PID Controller block and verify controller performance against the nonlinear model in Simulink. The controller performance is analysed through unit-step, ramp and sine-wave responses in the following sections of this chapter.

5.3.1 Unit-step response

Figure 5.13 shows the closed-loop response with these settings. The tuned control system has a stable closed-loop response to a unit-step input, with

1. A rise time of 20 seconds
2. A settling time of 103 seconds
3. An overshoot of 8.87%
4. An infinite gain margin
5. A phase margin of 69 degrees at 0.0687 rad/sec

The response shows that the new controller meets all the design requirements. Figure 5.14 shows that the response for the cooling transient is also satisfactory.

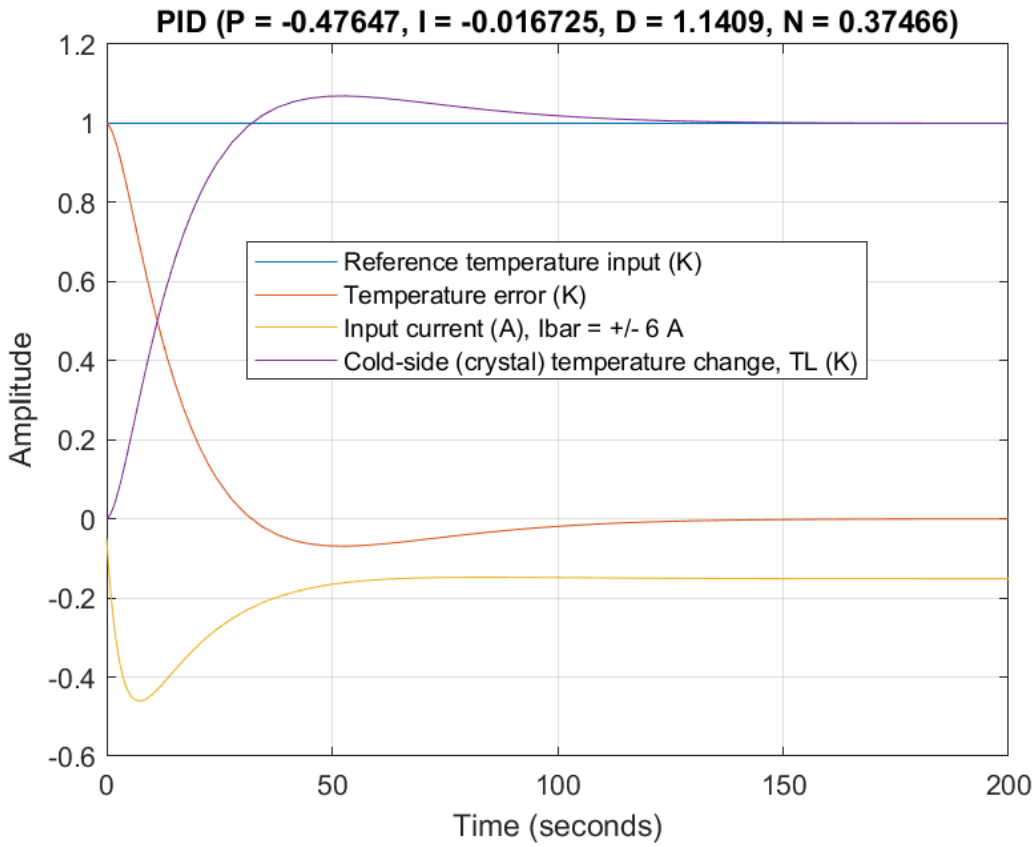

Fig. 5.13 Simulink nonlinear TEC model with a PID controller - unit-step response, at room temperature (heating transient).

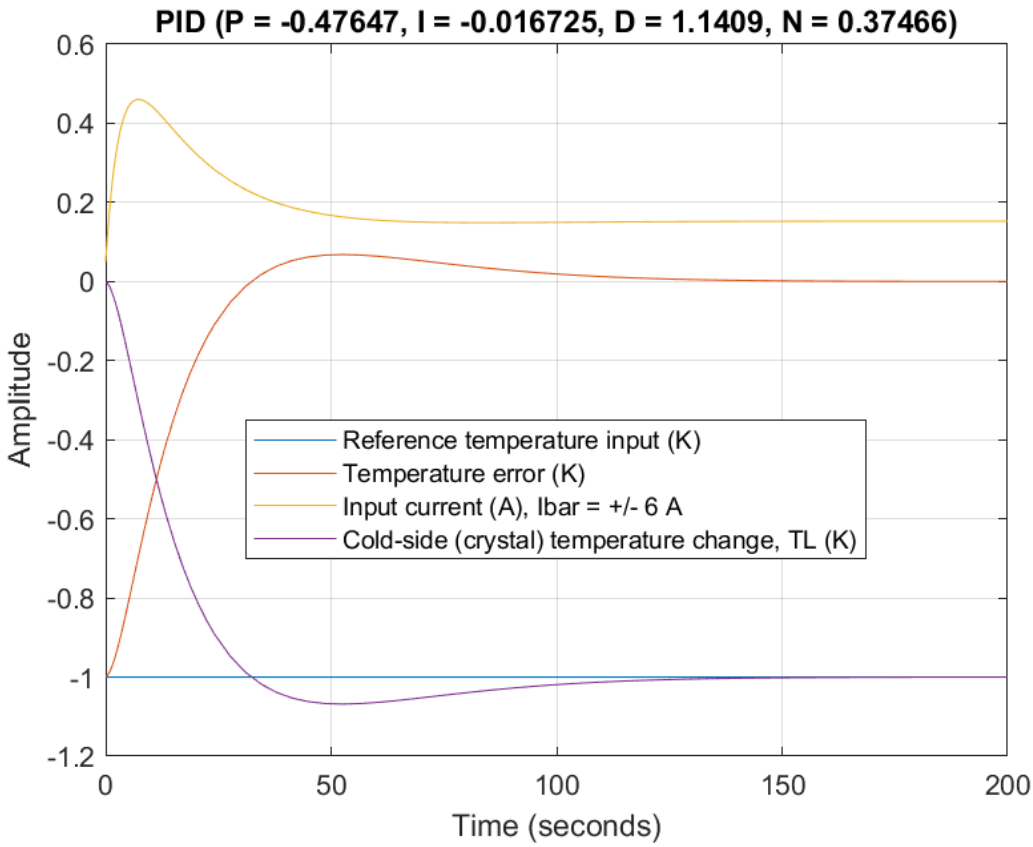

Fig. 5.14 Simulink nonlinear TEC model with a PID controller - unit-step response, at room temperature (cooling transient).

5.3.2 Ramp response

The ramp response in Fig. 5.15 shows an improved response when compared with that of the on-off controller. There is a smaller overshoot and no oscillations at steady-state. The error is kept at a smaller magnitude with the PID controller. Figure 5.16 shows that the response for the cooling ramp is also satisfactory with this controller.

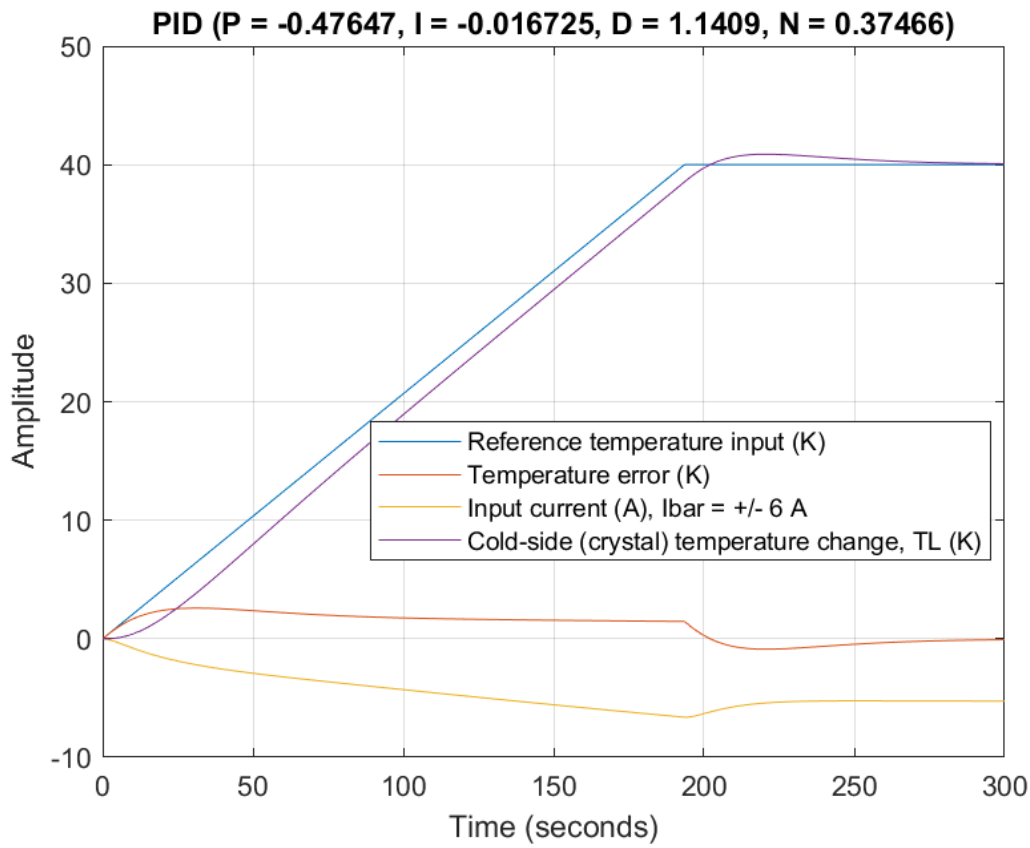

Fig. 5.15 Simulink nonlinear TEC model with a PID controller - heating ramp response, at room temperature.

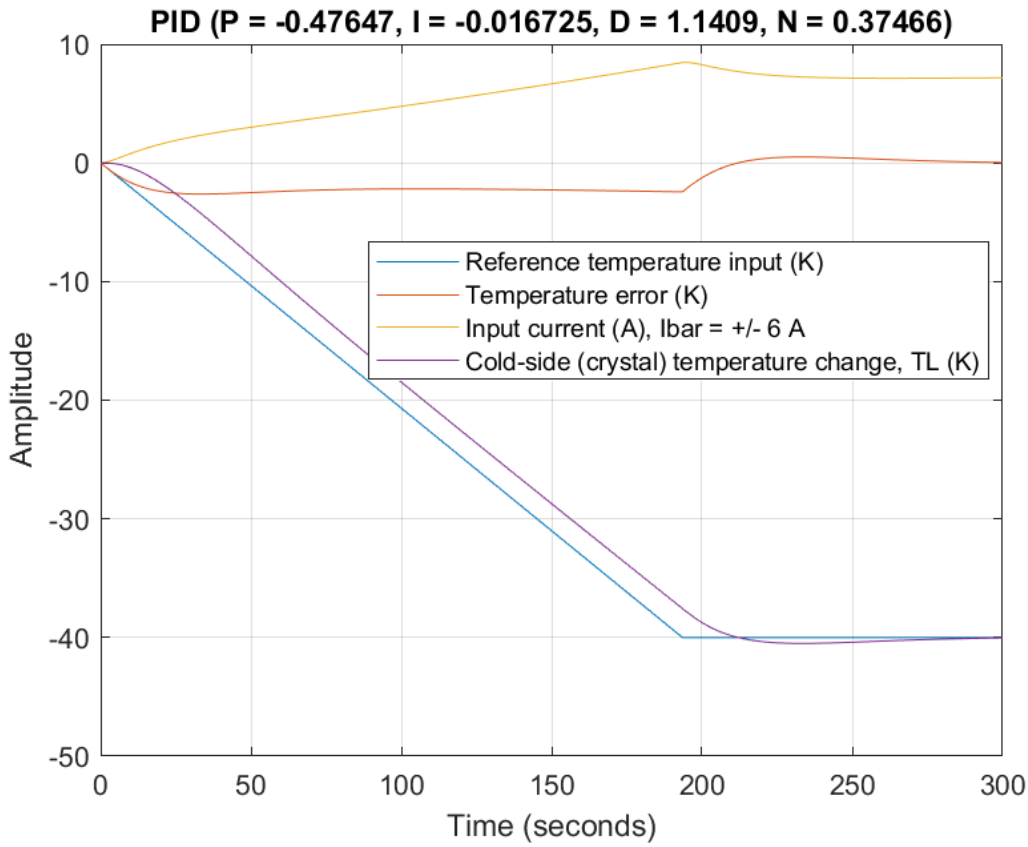

Fig. 5.16 Simulink nonlinear TEC model with a PID controller - cooling ramp response, at room temperature.

5.3.3 Sine-wave response

Of particular importance is the response to a cyclic temperature demand, which is shown in Fig. 5.17. In this plot, we can see that the system responds with improved accuracy when compared with the on-off controller.

1. When we increase the amplitude of the input signal to 40 K we still see a good response, as demonstrated in Fig. 5.18. The error is greater and subsequently the control system demands higher current inputs to the TEC in order to obtain the accuracy required.

2. In fact, we could cycle the system with a sine-wave amplitude of 20 K to achieve the total temperature change of 40 K (the known temperature change required to produce the 180 keV electric field required for ionisation and acceleration of the deuterium atoms). The system response is shown in Fig. 5.19. We start the cycle by initially cooling the crystal, then take it through a total 40 K change cyclically.

3. We could double the frequency, as shown in Fig. 5.20. However, we can see that the errors are greater (almost double) when the input frequency is increased. This is due to the thermal lag in the system temperature response.

4. The effect of increasing the input frequency further to 0.1 rad/sec is shown in Fig. 5.21. The response indicates that the system cannot be cycled this fast. This is to be expected as the Bode plot in Chapter 4 showed that the amplitude falls off at frequencies at above about 0.01 rad/sec, and at this frequency the output of the system is 90 degrees out of phase with the input. The system cannot meet this demand.

5. If we reduce the input frequency to 0.001 rad/sec, the system error is reduced and the accuracy of the response is increased, as can be seen in Fig. 5.22.

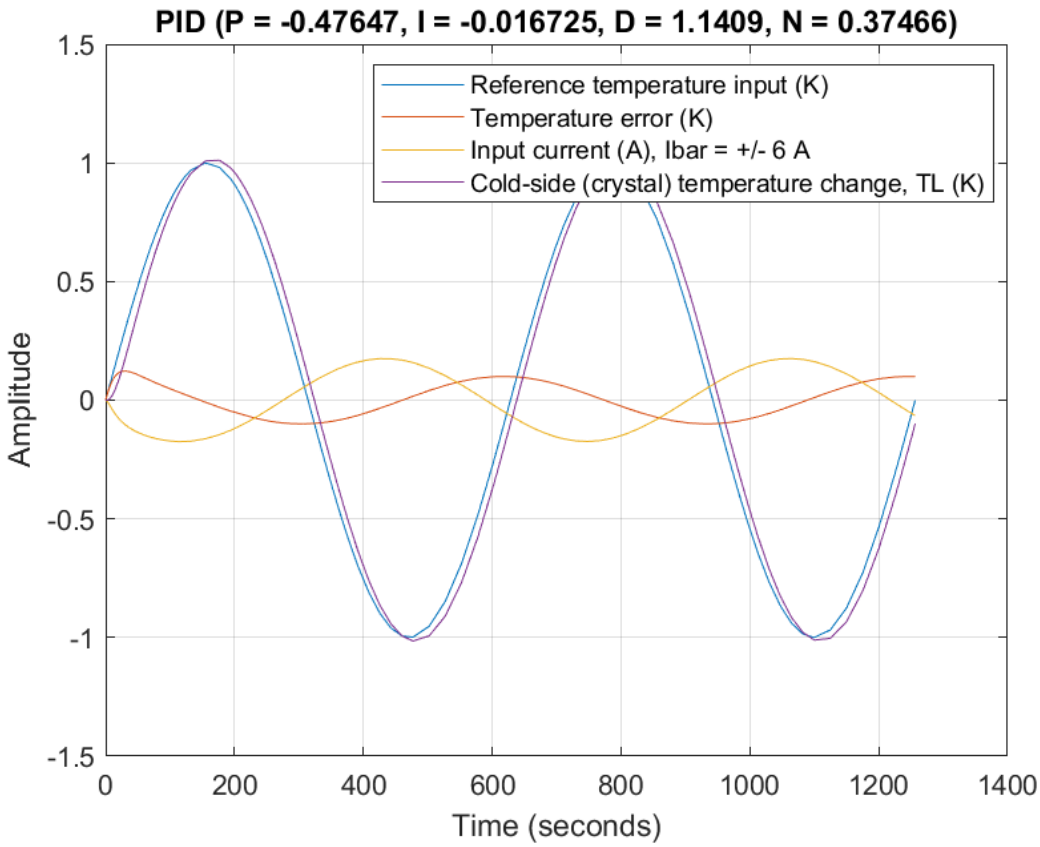

Fig. 5.17 Simulink nonlinear TEC model with a PID controller - 1 K amplitude, 0.01 rad/sec sine-wave response, at room temperature.

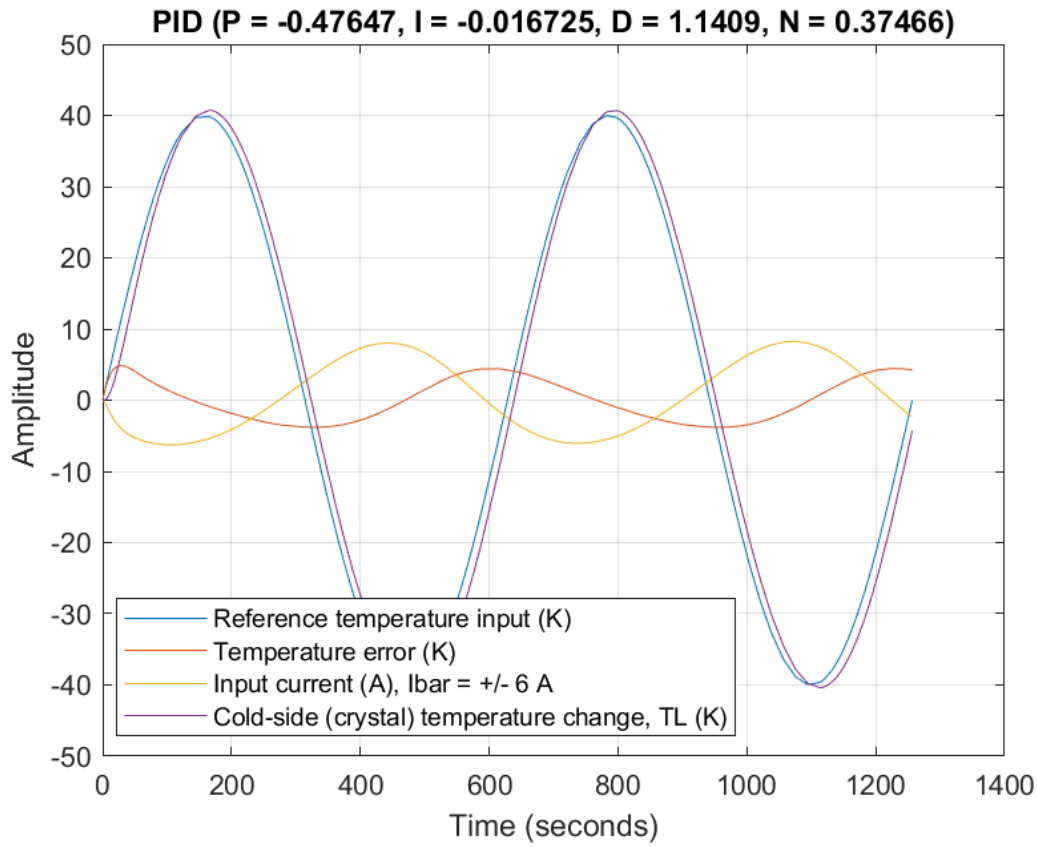

Fig. 5.18 Simulink nonlinear TEC model with a PID controller - 40 K amplitude, 0.01 rad/sec sine-wave response, at room temperature.

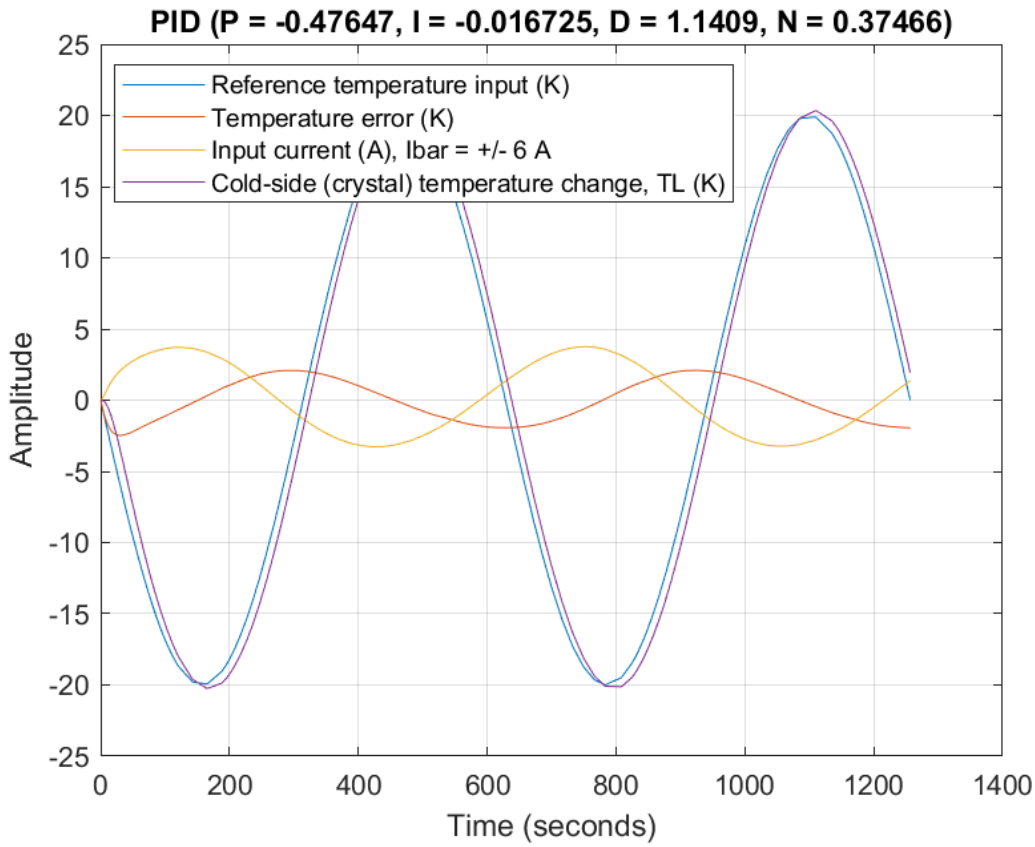

Fig. 5.19 Simulink nonlinear TEC model with a PID controller - 20 K amplitude, 0.01 rad/sec sine-wave response, at room temperature.

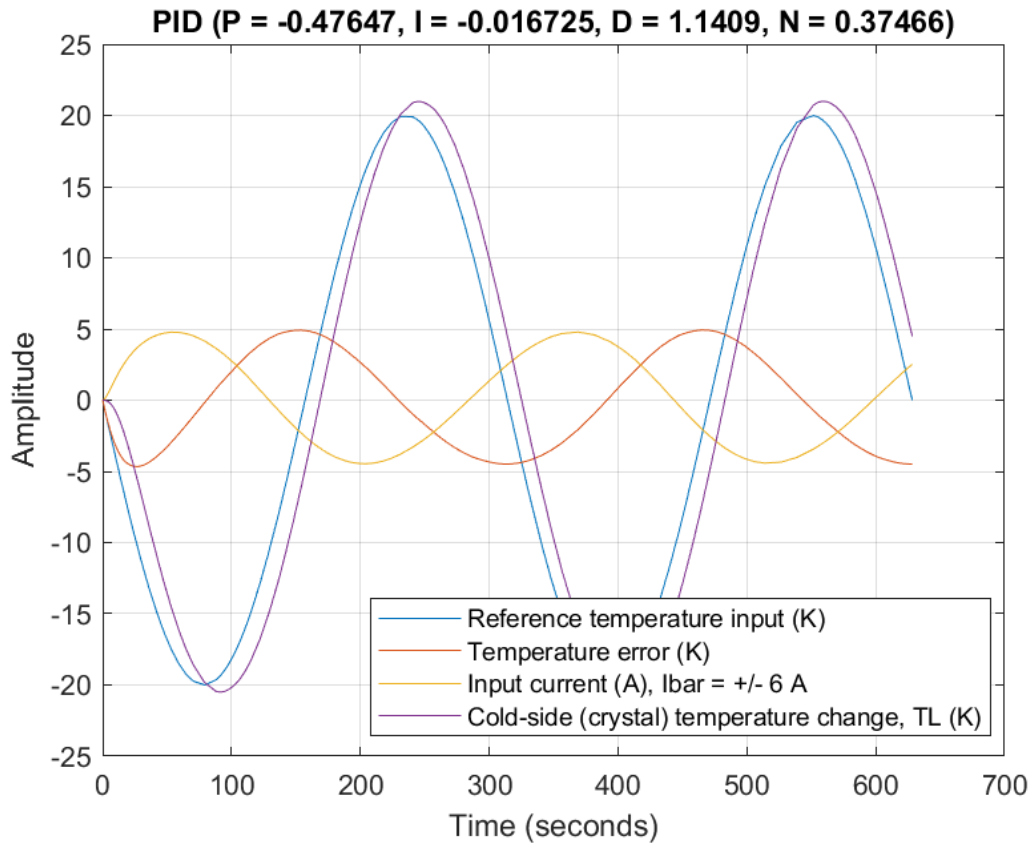

Fig. 5.20 Simulink nonlinear TEC model with a PID controller - 20 K amplitude, 0.02 rad/sec sine-wave response, at room temperature.

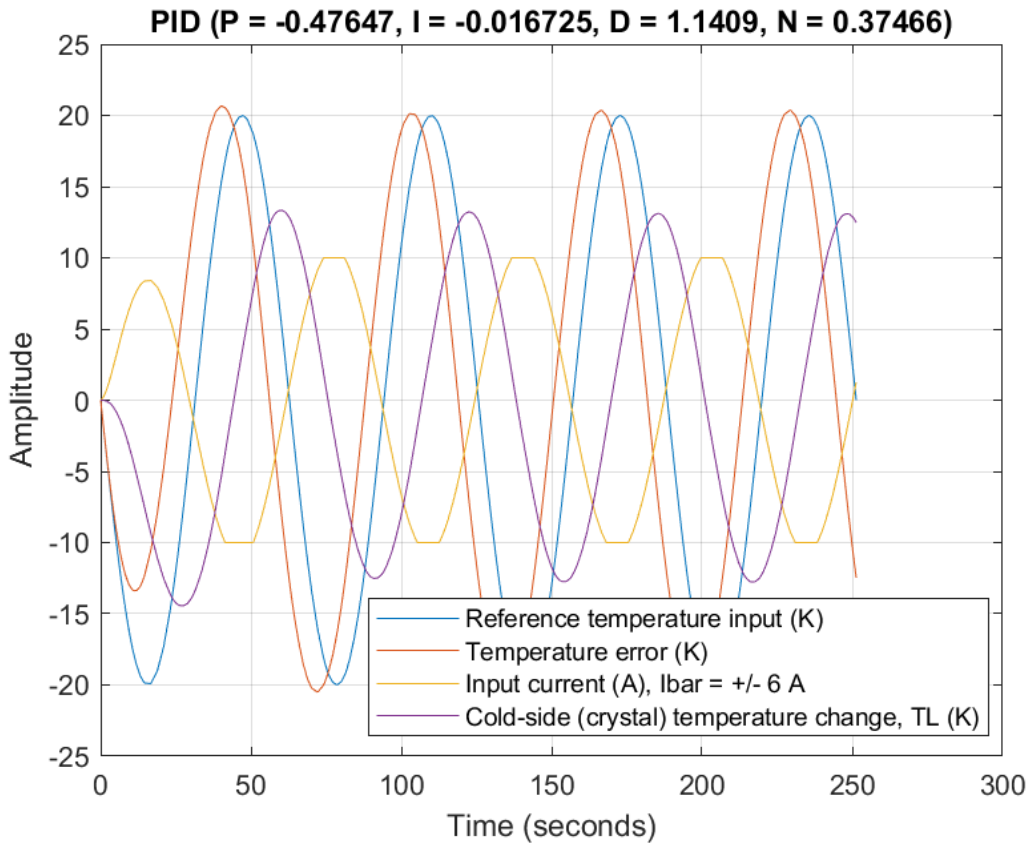

Fig. 5.21 Simulink nonlinear TEC model with a PID controller - 20 K amplitude, 0.1 rad/sec sine-wave response, at room temperature.

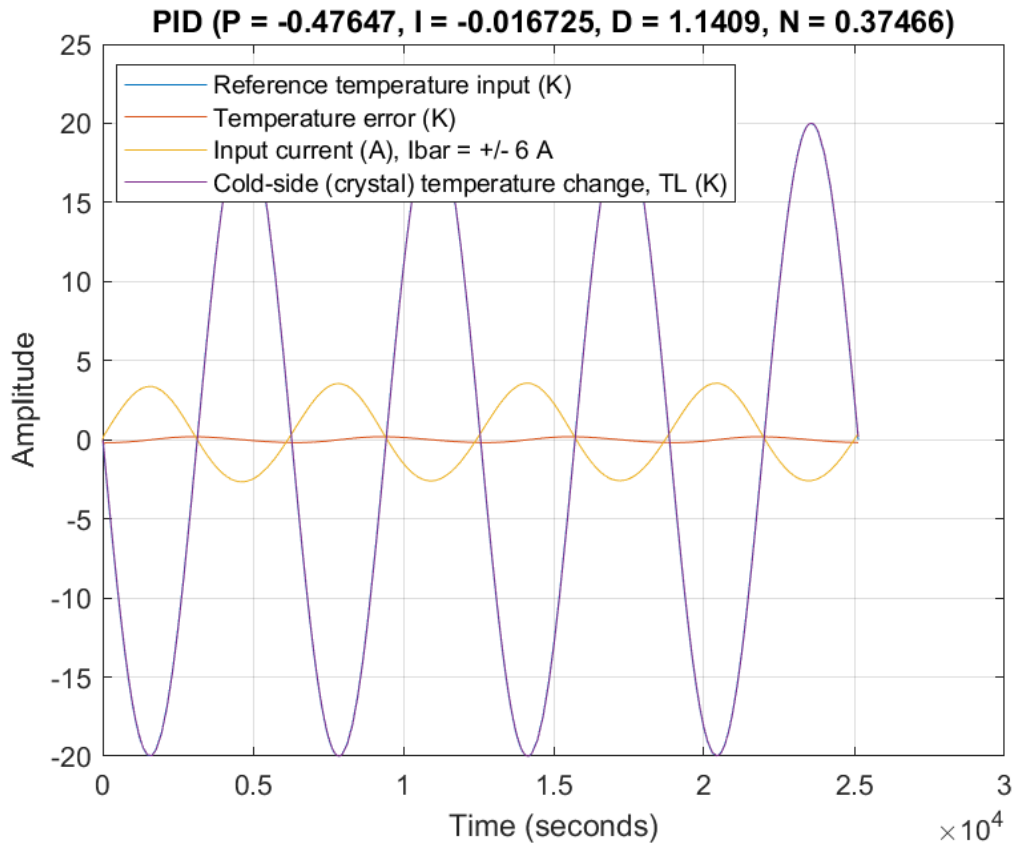

Fig. 5.22 Simulink nonlinear TEC model with a PID controller - 20 K amplitude, 0.001 rad/sec sine-wave response, at room temperature.

5.4 Summary

1. The on-off controllers result in either 100% full negative or full positive TEC current, which causes overshoots and undershoots in the crystal temperature, along with oscillations around the steady-state temperature.

2. The on-off controllers have been shown to provide poor control, and are not recommended for our pyroelectric TEC system heating/cooling processes.

3. The PID controllers have been shown to provide improved temperature control, with reduced error signals and no oscillations at steady-state.

4. Overall, the more sophisticated approach to the control system design was to modulate the current input to the TEC in proportion to how much temperature error there was present. This was achieved with the PID controller.

Having obtained good control over the heating and cooling cycles of a pyroelectric TEC system, we are now ready to expand our model and simulate the production of neutrons. Chapter 6 discusses the processes behind ion generation and acceleration, and the subsequent production of neutrons in a pyroelectric neutron generator. Equations are developed and verified using system identification techniques. We will then go on to consider the effects of changing the amplitude and frequency of temperature cycles when we consider the control system design for pyroelectric neutron production in Chapter 7.

Chapter 6

System dynamic model of a pyroelectric neutron generator

6.1 Introduction

A pyroelectric neutron source comprises pyroelectric crystals typically in a single or paired arrangement; the work presented in this chapter focuses on a single crystal, attached to a thermoelectric heater/cooler. These components are contained within a vacuum chamber which is partially filled with deuterium gas at low pressure, and which contains a deuterated target. When the pyroelectric crystal is thermally cycled, a change in the bound surface charge develops on the exposed polarised face. Through this pyroelectric effect, the crystal generates high voltages and a strong electric field in the chamber. The electric field is capable of ionising the deuterium gas and accelerating the ions into the deuterated target to produce a pulse of neutrons. In this chapter, we will model the pyroelectric neutron generator system using two approaches:

1. First, we will compare the UCLA experimental results, shown in Fig. 6.1 [74], with those of our theoretically derived model for the pyroelectric neutron generator system. This section builds upon our previously published work on pyroelectric neutron generator modelling, which was undertaken in 2017 [27].

2. Second, we will estimate the pyroelectric neutron generator model parameters using a system identification technique. We conducted an initial investigation into suitable estimation techniques in our second publication of 2017 [26]; this section of the chapter extends and improves upon that earlier work.

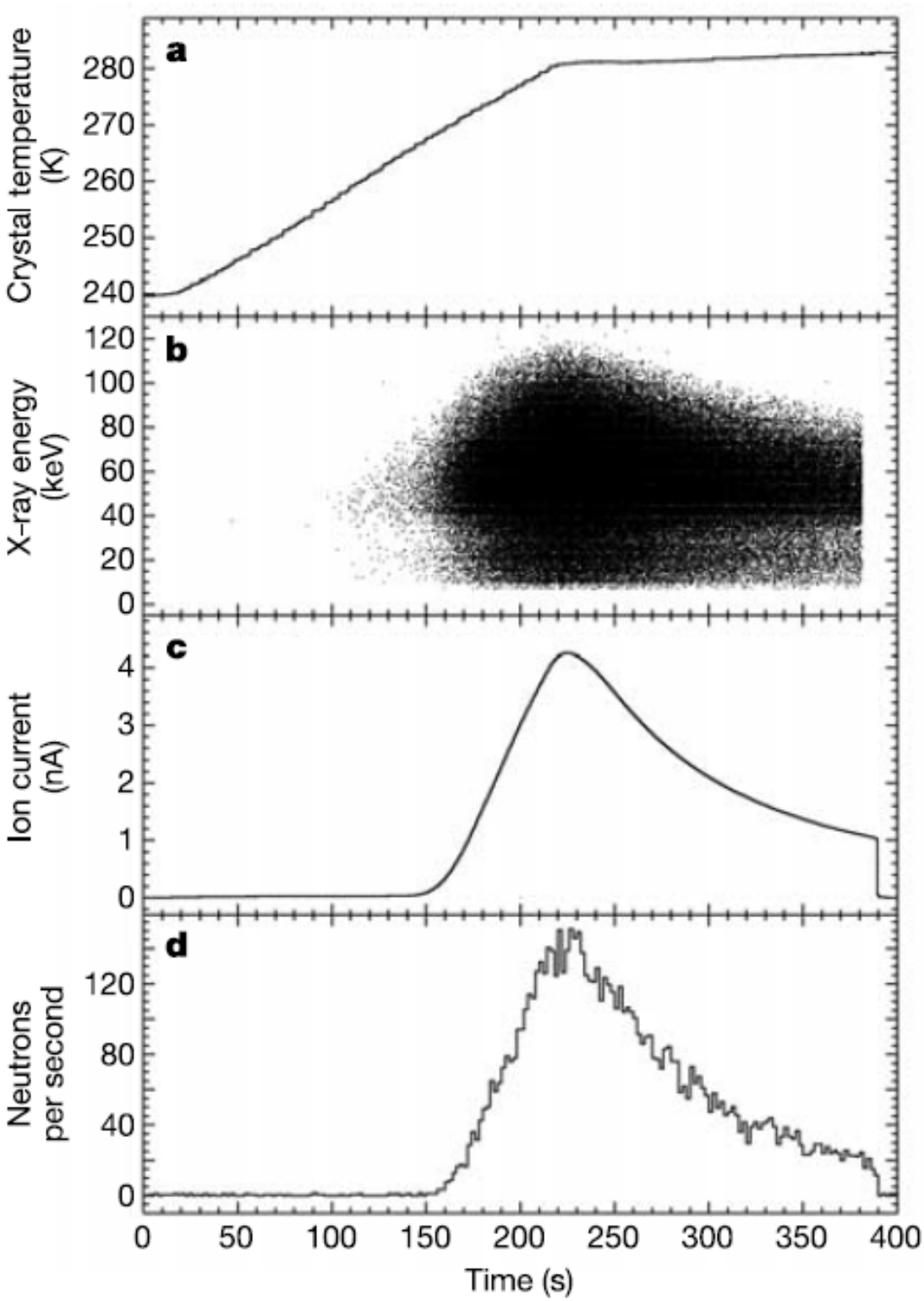

Fig. 6.1 Data from a single ULCA experiment run: a, Crystal temperature; b, X-rays detected; c, Faraday cup current; d, Neutrons detected [74].

6.2 Pyroelectric system describing equations

The data selected for identification is that of UCLA [74]. The UCLA system comprises a single z-cut, 1 cm radius, $LiTaO_3$ crystal with its $-z$ axis facing a deuterated target in a vacuum chamber containing deuterium gas at 0.7 Pa. In the UCLA experiments the crystal is heated from 240 K to 280 K, using a TEC, resulting in a decrease in spontaneous polarisation and leading to a system potential of around 100 keV for this particular system geometry. A tungsten tip was used in these experiments to generate a high electric field (> 25 Vnm^{-1}), sufficient for ionisation of deuterium and acceleration of the ions into a deuterated target. A neutron flux over 400 times the background level was reported.

Changes in the bulk crystal temperature, $\tilde{T}_L$, alter the lattice spacing of non-symmetrically located ions within pyroelectric crystals, such as lithium tantalate. The ion displacement varies the spontaneous polarization of the crystal, producing a displacement current, I, which is parallel to the crystal's polar axis [76]. We can estimate the electric current which is generated during the pyroelectric effect as [57]:

$$I = \gamma A \frac{dT_L}{dt} \tag{6.1}$$

where $\gamma = -190$ μC/K $\cdot$ m^2 is the value most often quoted as the pyroelectric coefficient for $LiTaO_3$ [45]. The UCLA publication [74] quotes a pyroelectric coefficient value based on the earlier work of Rosenblum et al. [82]. It is reported that heating a lithium tantalate crystal from 240 K to 265 K decreases its spontaneous polarization by 0.0037 Cm^2 (i.e. $\gamma = -148$ μC/K $\cdot$ m^2). We will use this experimentally derived value of the pyroelectric coefficient, as this was measured for the appropriate initial crystal temperature and the magnitude of the change applied in the UCLA experiments. The relationship between the pyroelectric current I and crystal voltage V may be expressed as

$$C\frac{dV}{dt} + \frac{V}{R} = I \tag{6.2}$$

where C is the crystal capacitance, which may be written as [45]

$$C = \varepsilon_o \varepsilon_{cr} \frac{A}{L} \tag{6.3}$$

and ε_0 is the standard permittivity of the vacuum; $\varepsilon_{cr} = 46$ is the relative permittivity of the $LiTaO_3$ [45] and $L = 0.01$ m is the length of the crystal used in the experiments [74]. In Eq. 6.2, R is the resistance of the $LiTaO_3$ crystal, which is expressed as

$$R = \frac{\rho A}{L} \tag{6.4}$$

where A is the area of the crystal, and ρ is the crystal resistivity. Specific values for $LiTaO_3$ crystal resistivity are difficult to obtain, and are not widely available. Roditi, a company who manufacture and distribute crystals for various applications, claim a value of bulk resistivity of $\rho = 4.5 \times 10^{10}$ Ω.cm for standard $LiTaO_3$ on their website [80]. However, for the same crystal, the webpage also has a value for bulk conductivity of $\sigma = 2.22 \times 10^{15}$ $\Omega^{-1}.\text{cm}^{-1}$. One of these values must be published in error, as we would reasonably expect the following relationship between the bulk conductivity and bulk resistivity:

$$\rho = \frac{1}{\sigma} \tag{6.5}$$

We contacted Roditi to ask for clarification on these values and the response, an email (J Brendel 2018, personal communication, 12 September), gave a range of values for $LiTaO_3$ bulk resistivity of between 10^{14} to 10^{15} Ω.cm. During the analysis of our pyroelectric neutron generator simulations, which are discussed in more detail later in this chapter, we found that a value of 1.3×10^{14} Ω.cm produced the most accurate results, when comparing the model generated signals to the UCLA experiment data [74]. With this value of resistivity, the resistance is calculated to be $R = 9.1 \times 10^{10}$ Ω.

Combining Eqs. 6.1 and 6.2 yields

$$C\frac{dV}{dt} + \frac{V}{R} = \gamma A \frac{dT_L}{dt} \tag{6.6}$$

We can now expand our previous small-perturbation analysis of the TEC model, developed in Chapters 3 and 4, to the linearised equation set for the typical pyroelectric neutron generation system. Our expanded variables set becomes:

$$\begin{aligned} T_L(t) &= \bar{T}_L + \tilde{T}_L(t) \\ T_H(t) &= \bar{T}_H + \tilde{T}_H(t) \\ V(t) &= \bar{V} + \tilde{V}(t) \\ I(t) &= \bar{I} + \tilde{I}(t) \end{aligned} \tag{6.7}$$

where each variable is considered to be the summation of a steady-state value (denoted by $\bar{X}$) and a small change (denoted by $\tilde{X}$) about that operating point. Equation set 6.7 can be substituted into 6.6, to obtain

$$C\frac{d(\bar{V}+\tilde{V})}{dt} + \frac{(\bar{V}+\tilde{V})}{R} = \gamma A \frac{d(\bar{T}_L+\tilde{T}_L)}{dt} \tag{6.8}$$

Eliminating the steady-state terms in Eq. 6.8, the following equation, Eq. 6.9, may be realised:

$$C\frac{d\tilde{V}}{dt} + \frac{\tilde{V}}{R} = \gamma A\frac{d\tilde{T}_L}{dt} \tag{6.9}$$

Taking the Laplace transform of Eq. 6.9, with steady-state initial conditions, yields

$$Cs\tilde{V} + \frac{\tilde{V}}{R} = \gamma As\tilde{T}_L \tag{6.10}$$

Then, we can rearrange Eq. 6.10 to obtain the transfer function

$$\frac{\tilde{V}}{\tilde{T}_L} = \frac{R\gamma As}{CRs+1} \tag{6.11}$$

where the time constant is $RC = 529$ seconds, and the gain is $R\gamma A = 1.9 \times 10^6$. Assuming that all the surface charge is converted into ions, a theoretical maximum ion current may be calculated from Eq. 6.11 by applying Eq. 6.12:

$$\tilde{q} = \frac{\tilde{V}}{R} \tag{6.12}$$

The total charge on the surface of the crystal is found by multiplying the crystal's surface potential, $\tilde{V}$, by the crystal's capacitance, C [45]

$$Q = C\tilde{V} \tag{6.13}$$

During the heating phase the system generates deuterons, and we can calculate the number of ions produced from the ion current, Eq. 6.12, by dividing through by the elementary charge, $e = 1.6 \times 10^{-19}$ C. We may assume that all the charge is converted into ions [45]

$$\phi = \frac{Q}{e} \tag{6.14}$$

where ϕ is the number of ions observed. Then, we can estimate that around half of the D-D fusions result in the neutron-producing branch, and the neutron production S, per thermal cycle, may then be obtained using

$$S = \frac{N_d\sigma\phi}{2} \tag{6.15}$$

where $N_d = 7.96 \times 10^{-10}$ (b-Å)$^{-1}$ [45] is the target density of deuterium atoms per unit volume and $\sigma = 259$ b-Å [45] is the calculated integrated cross section for D-D fusion.

6.3 Detectors

When modelling the UCLA experiments we need to take into account the behaviour of any detectors, which may affect the system signals that are recorded. The UCLA detector arrangement is shown in Fig. 1.7. There are three detectors used in the capture of the signals of interest:

1. The x-ray energy is measured using an Amptek XR-100T-CdTe x-ray detector.
2. The ion current is measured using a Faraday cup.
3. A liquid scintillator is used for the detection and pulse-shape identification of neutrons.

6.3.1 Amptek XR-100T-CdTe

The UCLA group used an Amptek XR-100T-CdTe x-ray and gamma ray detector [74]. Detailed information on the operation of this detector can be found on the Amptek website [1]. Amptek's standard XR-100T-CdTe detector consists of a 1 mm thick CdTe diode detector located behind a 4 mm (100 μm) Be window. The probability of a photon interaction somewhere in the thickness is the product of the probability of transmission through beryllium, Be, and the probability of interaction in the material. Detection efficiency is an important consideration for us, but according to Amptek [1], due to charge transport effects, defining it is somewhat subtle. If we consider the probabilities of interaction with the material, which are shown by the black line on Fig. 6.2, we can see that the efficiency remains above 0.3 for the entire energy range. The UCLA group observed that when the crystal reached 80 keV the field ionization rapidly turned on [74]; therefore, it is important that we have taken into account the detector efficiency at energies above this level.

6.3.2 Faraday cup

In the UCLA experiments [74] the ion current is measured using a Faraday cup. When a beam or packet of ions hits the metal, it gains a small net charge while the ions are neutralized. The metal can then be discharged to measure a small current proportional to the number of impinging ions. By measuring the electric current in the metal part of the cup circuit, the number of charges being carried by the ions in the vacuum part of the circuit can be determined. The current flow, I, through the circuit can be very accurately measured, and is directly proportional to the number of ions, ϕ, that have been intercepted by the Faraday cup [8]. The number of ions can be simply calculated from

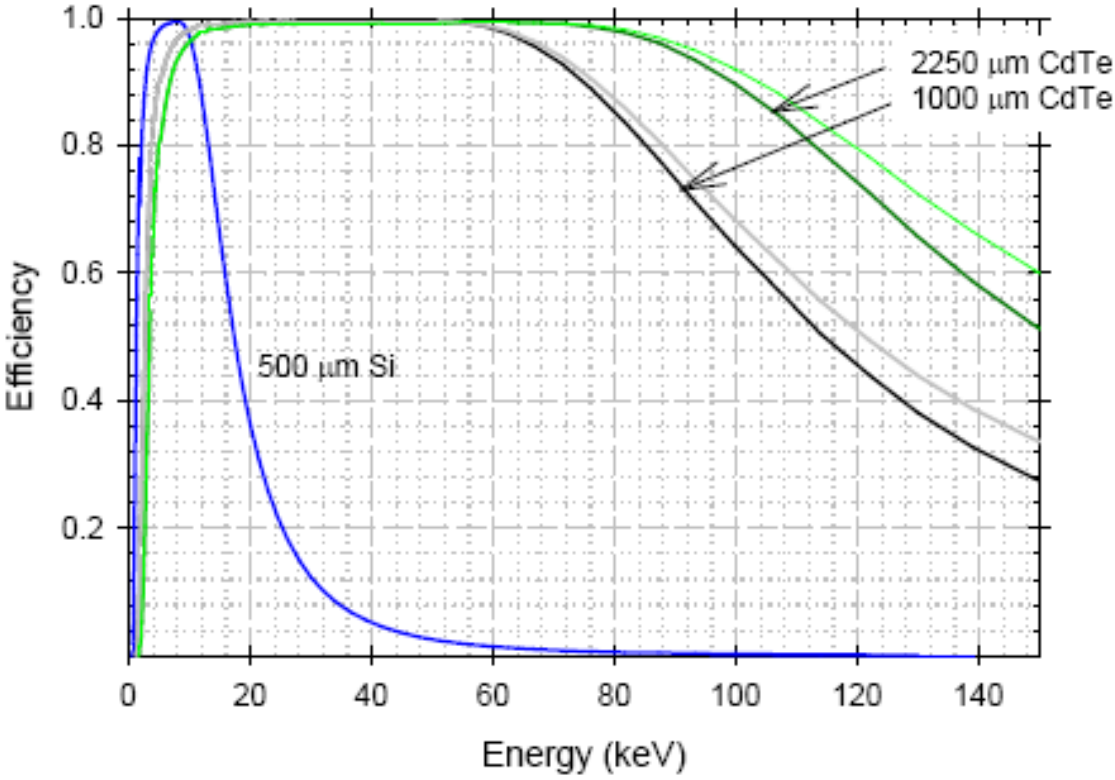

Fig. 6.2 Linear plot of interaction probability, computed by Amptek for their standard 1 mm CdTe detector [1]. The probabilities of interaction with the detector material are shown by the black line; the results for a 0.5 mm Si detector and for a CdTe stack detector, 2.25 mm thick, are shown for comparison purposes.

$$\frac{\phi}{t} = \frac{I}{e} \tag{6.16}$$

where t is the time of measurement.

The data recorded during the UCLA experiments [74], shown in Fig. 6.1, shows that the ion current is detected after around 150 seconds. The group reported that, only when the crystal potential reaches around 80 keV, does the field ionisation fully switch on. We will need to include this nonlinearity in the form of a deadband in our pyroelectric neutron generator model. The counting of charges collected per unit time in the Faraday cup may be impacted by two potential sources of error:

1. primary electrons that have been turned around, and are referred to as backscattered electrons, which temporarily leave the collecting surface, and

2. the emission of low-energy secondary electrons from the surface struck by the incident charge.

The UCLA group reported that ions striking the mesh and the surrounding aperture created secondary electrons that accelerated back into the crystal, increasing the x-ray signal [74]. NASA studies of Faraday cup detectors in 1965 [21] report that it is fundamentally impossible to distinguish between a new incident electron and one that has been backscattered or a fast secondary electron. These studies measured backscattering coefficients as low as 0.4% and as high as 62%, and secondary-electron yields ranging from 1.1 to 5.2% for a broad range of metal targets. We will need to take these coefficients into account in our model, and the appropriate magnitude to best replicate the UCLA experiment can be found through simulation trials.

6.3.3 Neutron detection

The UCLA group designed and constructed their own prototype neutron detector, built with funds from DARPA. The detector consisted of six liquid scintillator (BC-501A and NE213) cells (diameter, 127 mm; height,137 mm), for detection and pulse-shape identification of neutrons. Each scintillator was optically coupled to a 12 mm Hamamatsu R1250 photomultiplier tube (PMT). Most importantly for our simulation purposes, the UCLA group report an 18% 2.45-MeV neutron detection efficiency [74], which will be included in our full system model.

6.4 Comparison of Simulink results with UCLA experiment

Equations 6.11 and 6.12, for the crystal potential and the ion current respectively, can be added to our Simulink model for the pyroelectric TEC system. The resulting Simulink model is shown in Fig. 6.3. At the top of Fig. 6.3, we have our TEC Model, which we designed in Chapter 5 for the TEC, including, from left to right: the input signals (step, ramp and sine) with selector switch, the PID controller, the TEC current saturation block and the LPV TEC model. Then, working across the bottom of the diagram, again from left to right, we have our new components representing the thermal-to-pyroelectric system, a deadband for the ion current generation, deuterium ion count and, finally, we get to the output in neutron counts per second. The deadband represents the UCLA group's observation that only when the crystal reached 80 keV did the field ionization turn on [74]. We have also included three switches that give us the option to include the various detector parameters, which have been previously described, in the simulation.

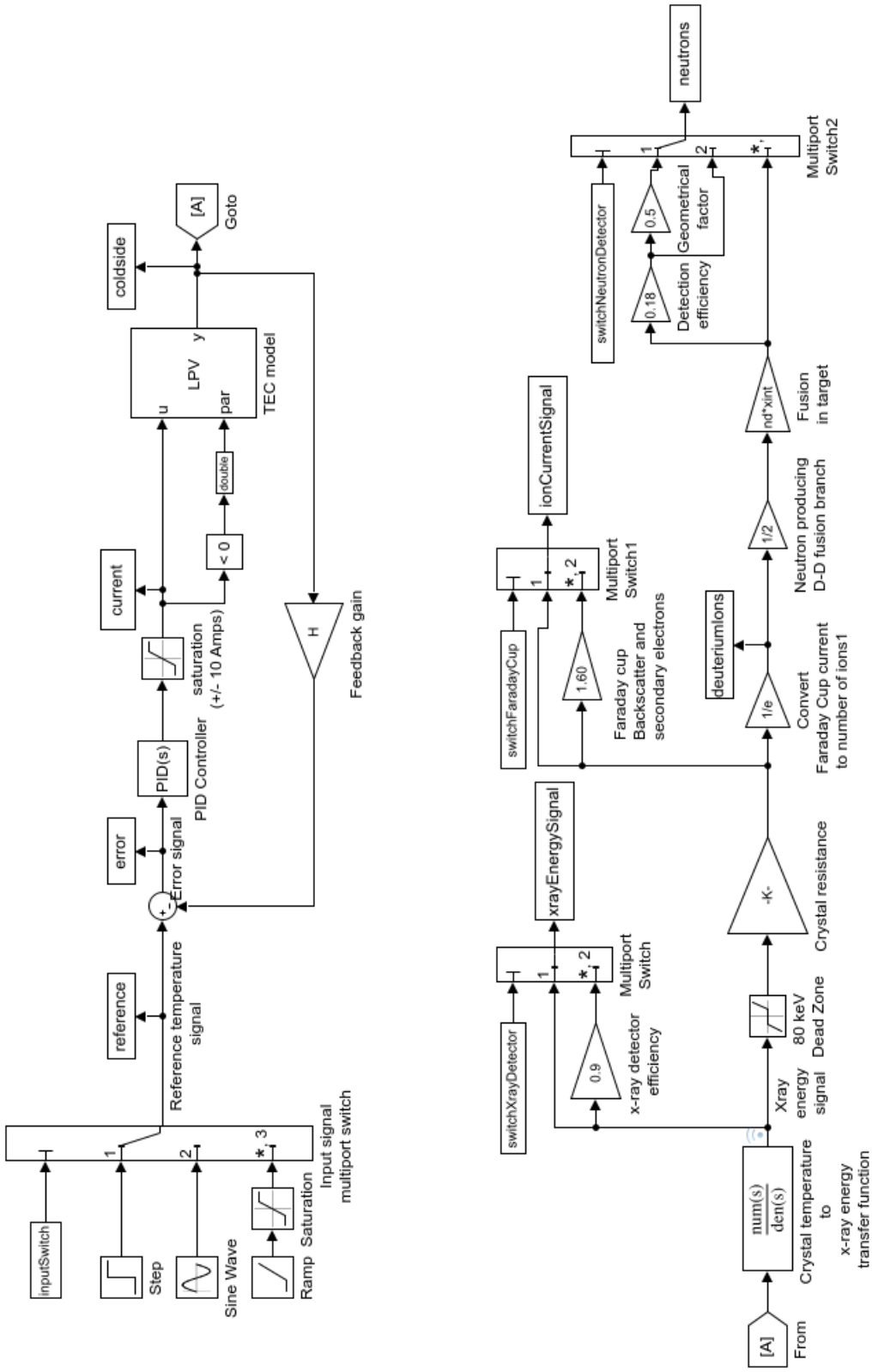

Fig. 6.3 Simulink model of the pyroelectric system.

For a simple visualisation of the accuracy of our results when compared to the UCLA experimental data, we can over-plot the original UCLA published graphs [74]. The graphs were read into MATLAB using the image read function of the image processing toolbox. The scale of each image was determined, and the simulation data was plotted on the same axis, for ease of comparison. The results are shown in the figures that follow.

1. **Crystal temperature and x-ray energy.** Figures 6.4 and 6.5 show very good agreement between the temperature profiles, and also between the x-ray energy signals for our Simulink pyroelectric system model. The dominant dynamic response of the temperature to x-ray energy sub-system has been captured. However, the magnitude may be affected by the efficiency of the detector used in the UCLA experiments [74]. We have used a detector efficiency of 90%, and the improvement in the accuracy of the magnitude of the detected x-ray energies can be seen in Fig. 6.5. The solid blue plot is the maximum predicted x-ray energy, and the dashed blue line shows the result when the detector efficiency is modelled.

2. **Ion current.** Figure 6.6 shows that the ion current output predicted by our model is approximately half of that observed by the UCLA group [74]. The timings of the peak in the ion current transients are in good agreement. The dashed blue plot in Fig. 6.6 shows the ion current output when a mid-range backscattering coefficient, of 30%, and a mid-range secondary-electron yield, of 3%, are added. Including this coefficient produces a more accurate prediction result for the UCLA experimental system.

3. **Deuterium ions per second.** Figure 6.7 shows our simulation of the number of deuterium ions produced, assuming 100% ionization efficiency. There is no comparison deuterium ion signal from the UCLA group's experiments.

4. **Neutrons per second.** The over-prediction of ions leads to an over-prediction of the ion current, and the number of neutrons per second that we simulate are detected, as seen in Fig. 6.8. The maximum neutron yield we have simulated is in good agreement with the maximum yield predictions made by the RPI group for a theoretically optimal system of a similar size [45].

   The observed neutron peak of the UCLA group experiments was around 400 neutrons per second, with a neutron detector efficiency of 18%. We simulate a peak count of 1400 neutrons per second. The UCLA group report that part of the ion beam struck outside the target and there was an oxide layer on the target [74]; this may well be a major factor contributing to the discrepancy of around 50% in the neutron counts

simulated by our model. Fig. 6.8 shows the result just taking into account the detector efficiency, and also the result with the addition of the geometrical considerations.

Comparison of our results with the UCLA experiments indicates that discontinuities and efficiency factors must be taken into account in order to reasonably predict the current system output. We have derived our pyroelectric neutron generator model structure from first principles and obtained a good representation of the dynamic response of the UCLA system. We can now use system identification techniques to estimate the best model parameters to fit a set of experimental input-output data relationships.

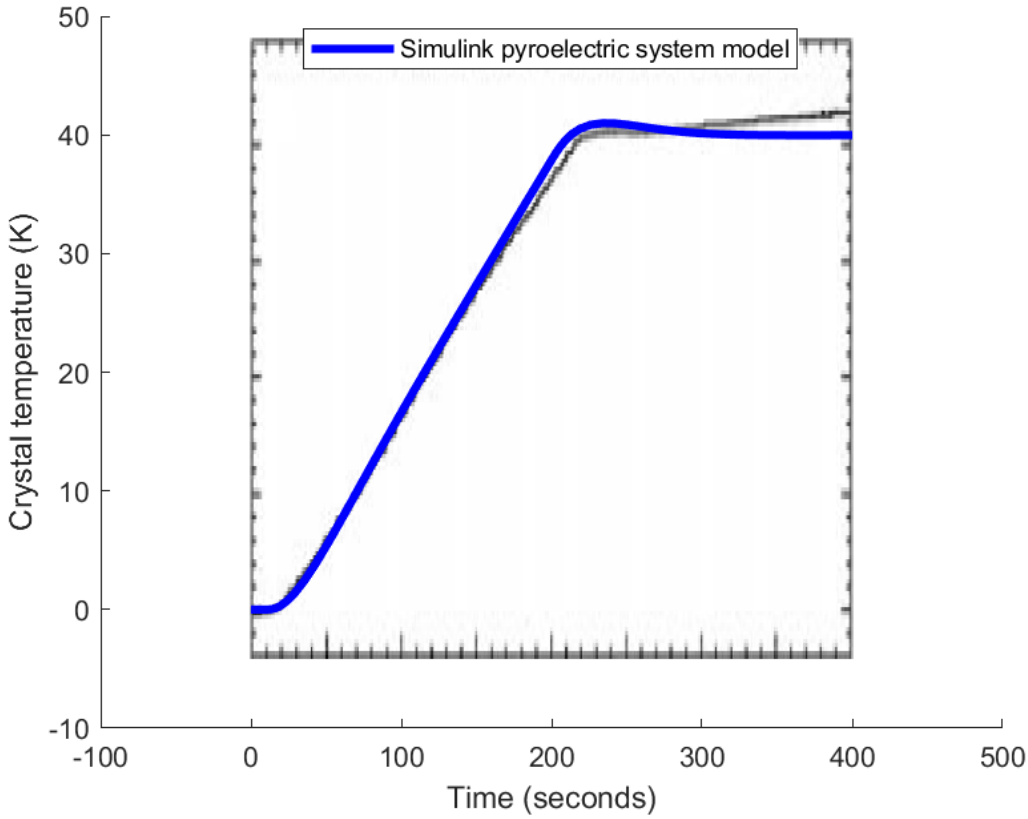

Fig. 6.4 Comparison of the UCLA crystal temperature with simulation.

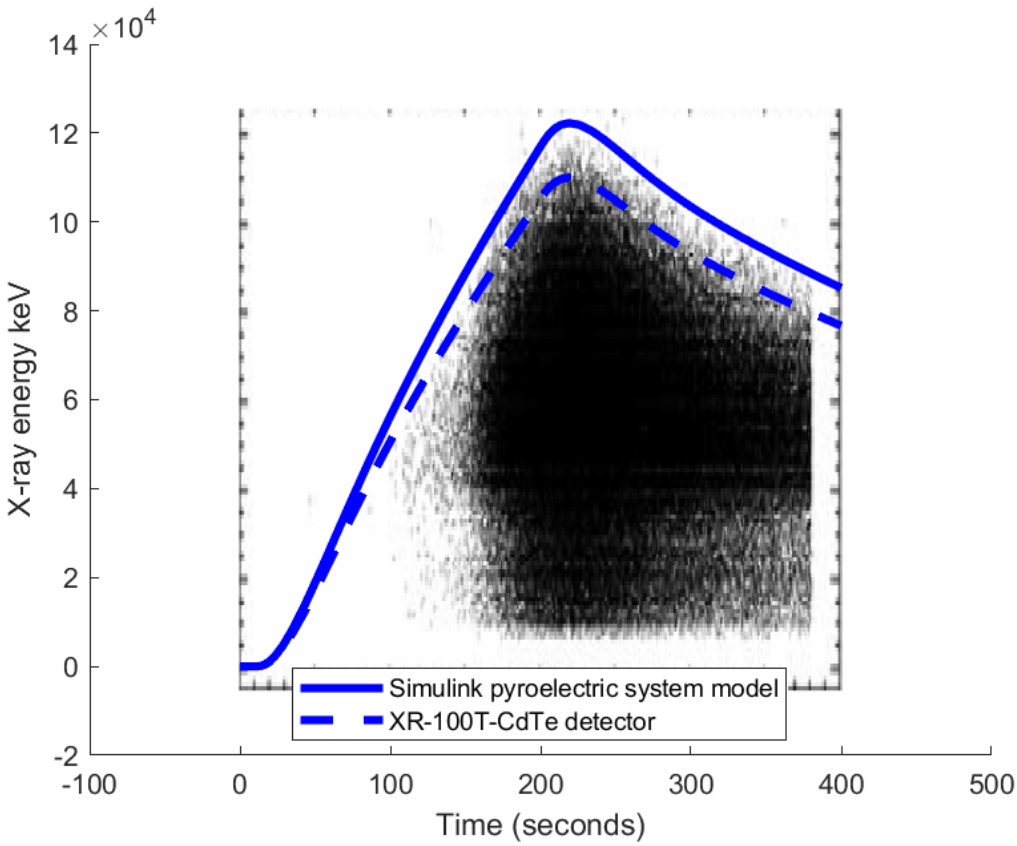

Fig. 6.5 Comparison of the UCLA x-ray energy with simulation.

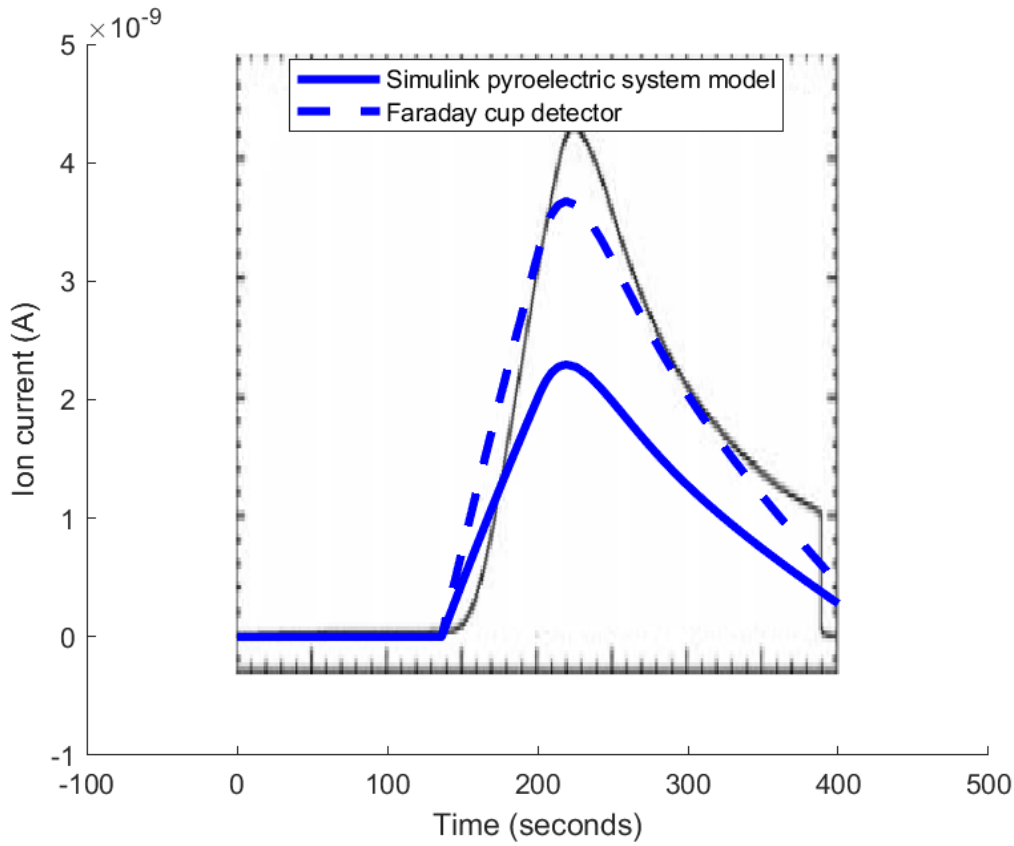

Fig. 6.6 Comparison of the UCLA ion current with simulation.

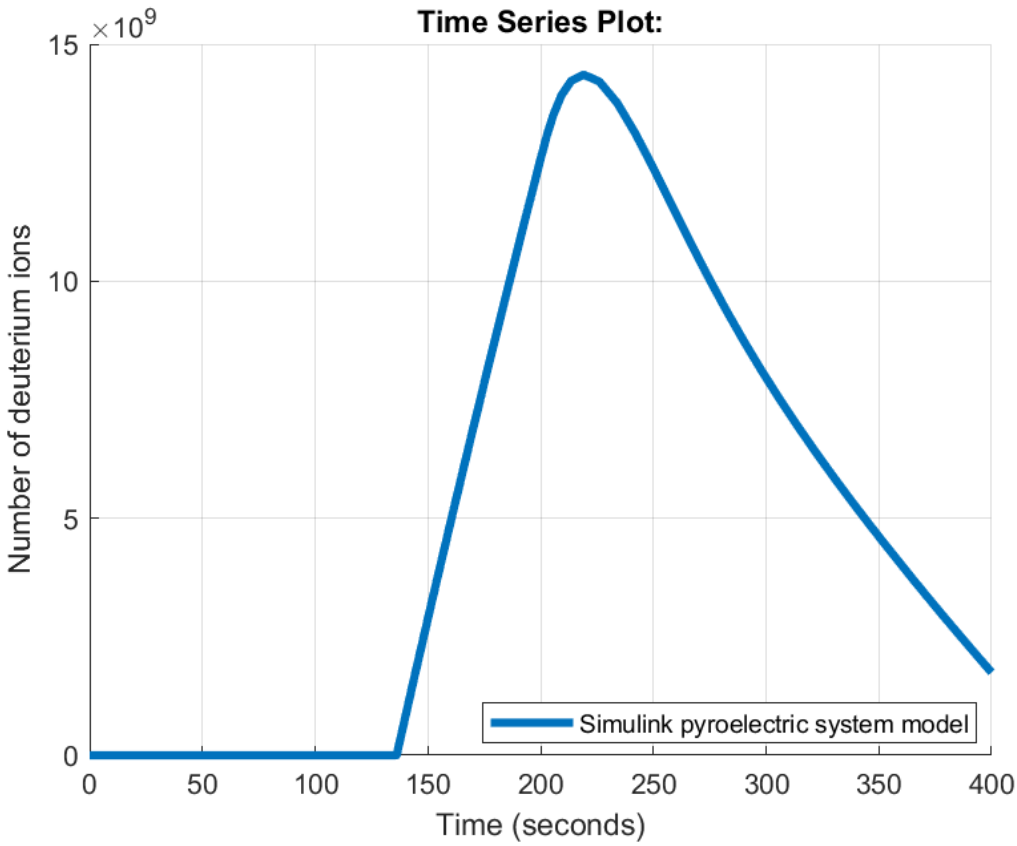

Fig. 6.7 Plot of simulated deuterium ions.

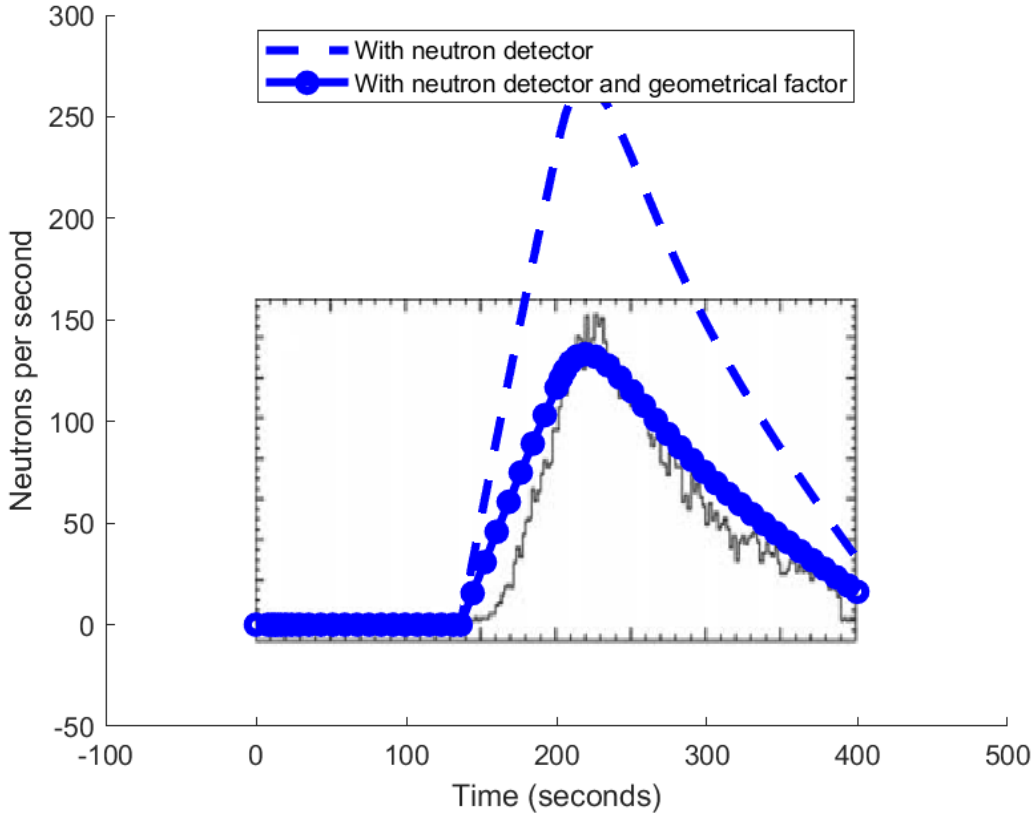

Fig. 6.8 Comparison of the UCLA neutron count rate with simulation.

6.5 System identification

This section presents our methods to construct, estimate and analyse grey-box models of the pyrofusion system from the UCLA measured data [74]. Our methods of system identification were trialled on data sets obtained from the publications of previous pyrofusion research groups. The results of our 2017 publication [26] indicated the promising potential application of these methods to the system identification of profusion device characteristics to support model verification, pulse characterisation and prediction of operational capabilities. The identified models were shown to exhibit satisfactory analogous cause-and-effect behaviour. However, the link between the estimated model parameters and the basic physics equations was not derived. In this section we aim to address this shortfall in our previous research.

Mathematical dynamic relationships between the input and output experimental data of each sub-system may be estimated with the implementation of the system identification algorithms in MATLAB. With consideration to the available system data from UCLA [74], three potential sub-systems may be identified:

1. crystal temperature to potential (x-ray energy),
2. potential to ion current, and
3. ion current to neutron flux.

We were unable to obtain the original data for the UCLA experiments; so, we used WebPlotDigitiser [81], which is an open source, semi-automated online tool, to reverse engineer the images of the data and extract the underlying numerical data. The results of this reverse engineering can be see in Figs. 6.9, 6.10 and 6.11. The temperature data is not digitised, as we use our previously designed TEC PID controller to generate the temperature profile input to the pyroelectric neutron generator system (see Fig. 6.3).

The selected time-domain data captures the important sub-system dynamics, such as the dominant time constants, system natural frequency and damping.

We used the MATLAB System Identification Toolbox to identify the models from the measured data. The following steps were taken:

1. **Process the data.** We import the data into the MATLAB workspace and create a data object for each transfer function using *iddata*. This data object takes the input and output data, and the sampling time. Each data value is assigned a time instant,

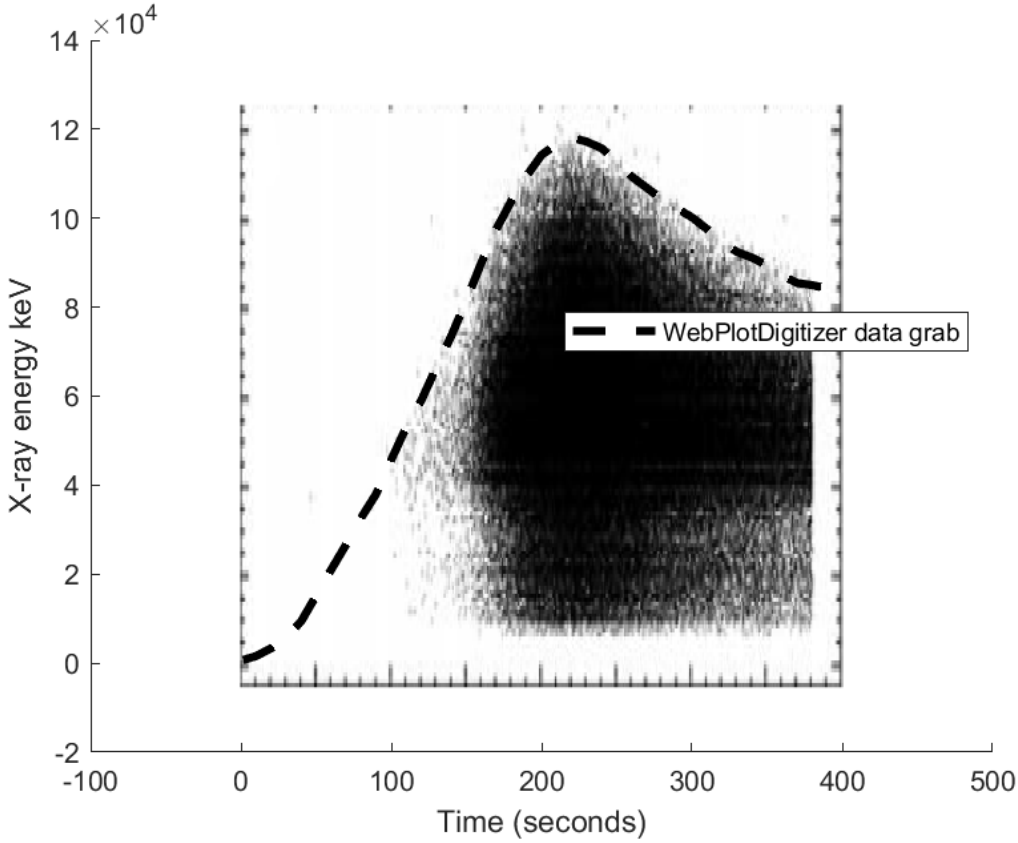

Fig. 6.9 Comparison of the UCLA x-ray plot with the numerical data from the reverse engineered images.

which is calculated from the start time and sample time. To replicate our input inter-sample behaviour, we use the default setting of a zero-order-hold; the zero-order hold maintains a piecewise-constant input signal between samples.

2. **Identify linear models.** We used *tfest* to identify the transfer function models, based on the *iddata* objects. The function *tfest* estimates a continuous-time transfer function, using the time-domain data. We specified the number of poles and zeros for each estimated transfer function based on the models we derived from our theory. We compare the structure and numerical values for each estimated model with the derived models later in this section. The MATLAB estimation algorithm we used was the *Instrument Variable (IV)* method. The method is also known as the Simplified Refined Instrumental Variable method for Continuous-time systems (SRIVC) [79].

3. **Compare the model output to measured data.** Then we used the *compare* function to simulate the response of estimated dynamic system models to the input data, and

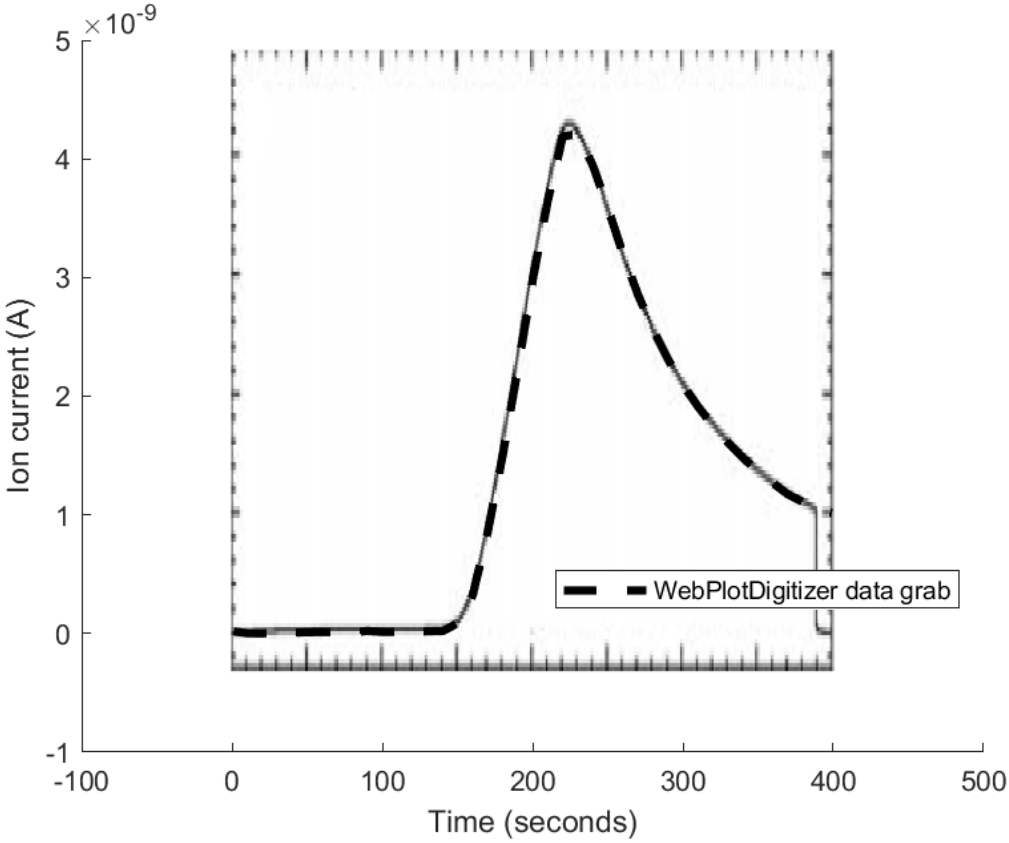

Fig. 6.10 Comparison of the UCLA ion plot with the numerical data from the reverse engineered images.

superimpose the output response over our digitised experimental data from UCLA [74]. The *compare* calculates the fit (in percentage) using [69]:

$$\text{fit} = 100\left(1 - \frac{||y - \hat{y}||}{||y - \text{mean}(y)||}\right) \tag{6.17}$$

where y is the measured data and $\hat{y}$ is the output of the estimated model.

Systems were represented as grey-box models, whose structures were based on our theoretical derivations of the transfer functions, and whose coefficients were estimated from the experimental data. The simulated model response comparison results are shown in Figs. 6.13, 6.14, and 6.15. Each plot can be used to evaluate the estimated candidate model identified from the measurement data, and also to validate the selected model through comparison of the time-domain models and the data. The plots also show the normalized root mean square error (NRMSE) measure of the goodness of the fit between simulated response and measurement data. The three sub-systems may be individually analysed:

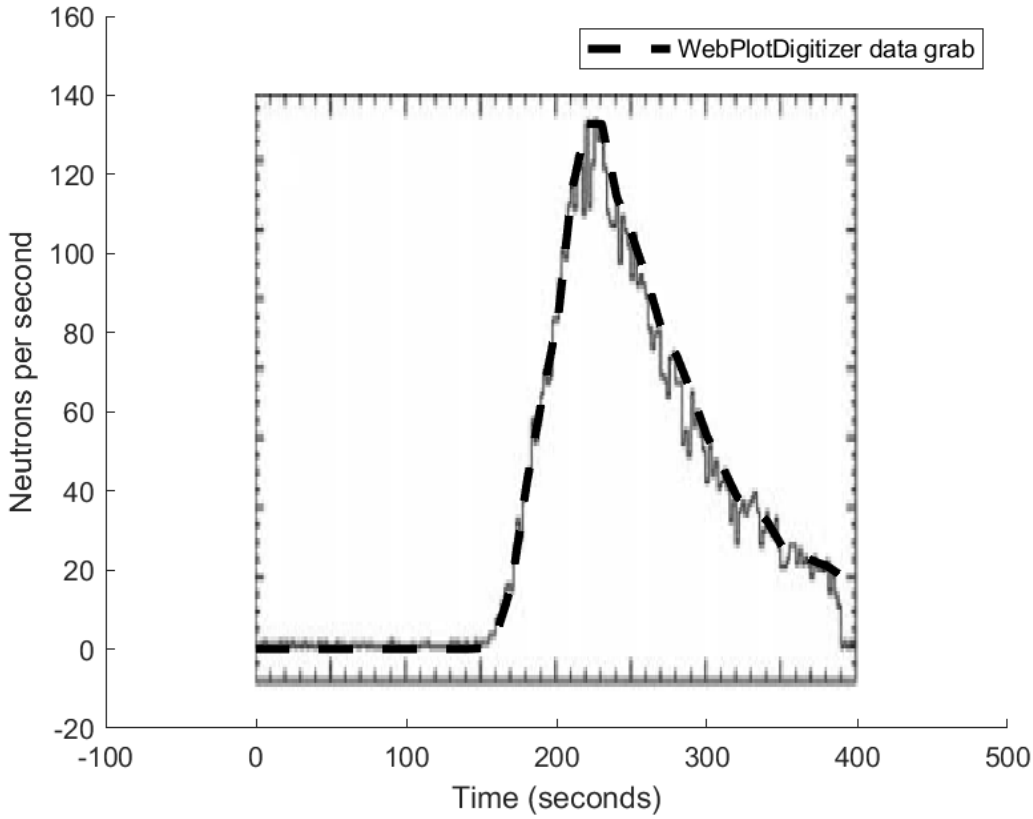

Fig. 6.11 Comparison of the UCLA neutron count rate plot with the numerical data from the reverse engineered images.

1. **Temperature to x-ray energy**. A linear model of first-order structure, based on our theoretically derived model structure, was estimated. This model simulates the temperature-potential experimental data relationship with a good fit of $\sim 90\%$. The result is shown by the blue line plotted in Fig. 6.13, where the grey line is the digitised x-ray data. Our derived transfer function model for the temperature to x-ray relationship, with numerical values, is

$$\frac{\tilde{V}}{\tilde{T}_L} = \frac{3270.4s}{s+0.001889} \approx \frac{1.9\times 10^6 s}{529s+1} \tag{6.18}$$

The estimated model was found to be

$$\frac{\tilde{V}}{\tilde{T}_L} = \frac{3584.3(s+0.009\times 10^{-5})}{(s+0.001466)} \approx \frac{3584.3s}{(s+0.001466)} \approx \frac{2.4\times 10^6 s}{682s+1} \tag{6.19}$$

Both models show good agreement: the estimated gain is 27% greater than the derived gain, and the time constant is 29% greater.

2. **Potential to ion current**. We estimated a first-order nonlinear Hammerstein-Wiener model, with an input deadband of [0, 80 keV]. The model estimation is shown to have a reasonably good fit of $\sim 72\%$. The Hammerstein-Wiener model is estimated using the function *nlhw*, which represents the decomposition of the input-output relationship into two or more interconnected elements [66]. The system dynamics are represented by a linear transfer function and the nonlinearities are captured using nonlinear functions of inputs and outputs of the linear system, as shown in Fig. 6.12. For our potential to ion current subsystem we applied a deadband input nonlinearity of [0, 80 keV].

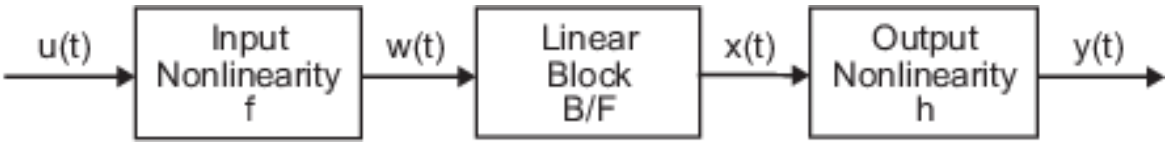

Fig. 6.12 The structure of Hammerstein-Wiener models [66].

In Fig. 6.12:
f is a nonlinear function that transforms input data $u(t)$ as $w(t) = f(u(t))$.
$w(t)$, an internal variable, is the output of the Input Nonlinearity block and has the same dimension as $u(t)$.
B/F is a linear transfer function that transforms $w(t)$ as $x(t) = (B/F)w(t)$.
$x(t)$, an internal variable, is the output of the Linear block and has the same dimension as $y(t)$.

We can compare the parameters of the estimated linear model with those we calculated for our derived Simulink model (the model is shown in Fig. 6.3). The estimated model and the derived model were both purely static gains (without any poles or zeros present in the structure). The models are in good agreement: the gain for our estimated model was $\approx 1 \times 10^{-13}$, which is around 15% greater than our calculated gain for the system including the Faraday cup efficiency, which was $5.4 \times 10^{-14} \times 1.6 = 8.7 \times 10^{-14}$.

3. **Ion current to neutron flux**. The first-order estimated models had a good percentage fit to the estimation data of $\sim 84\%$. The derived model is a static gain of 5.8×10^{10}, and we use this as our initial model for estimation. The final estimated model also has a structure with no zeros or poles, and a static gain of 2.9×10^{10}. This would imply that we need to reduce the gain of our derived model by 50% in order to get the best fit.

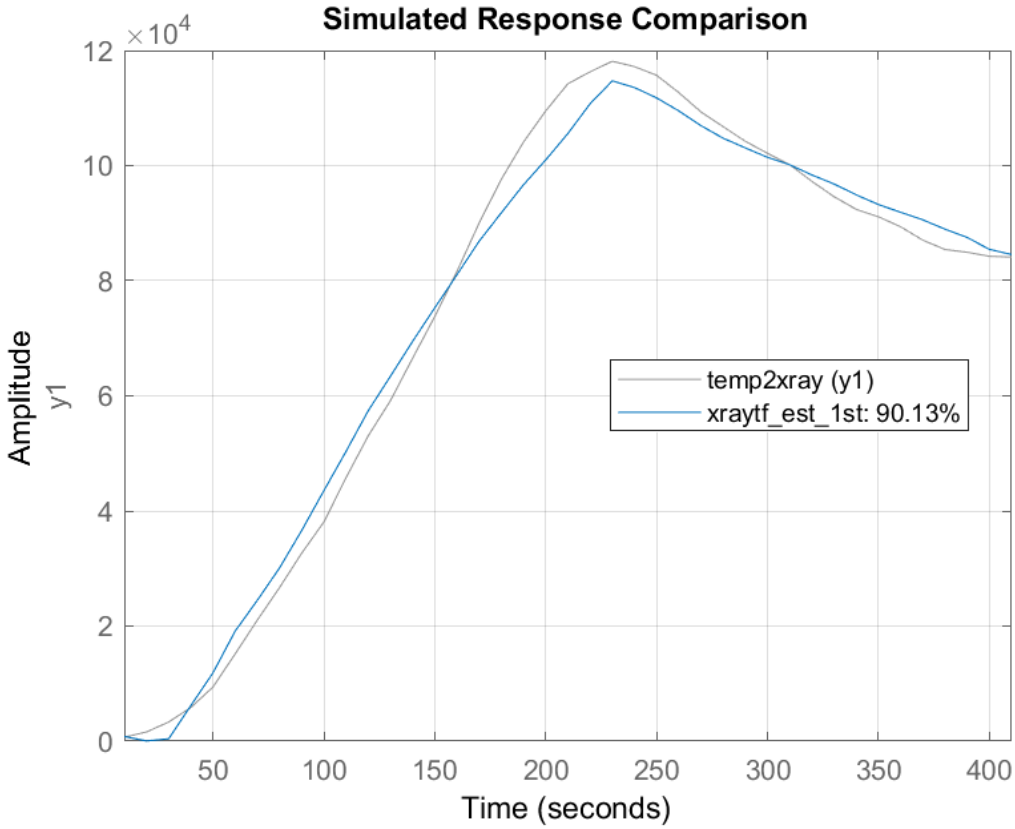

Fig. 6.13 Comparison of the UCLA system data and the estimated temperature to x-ray transfer function response. The original data is represented by the grey line, and the simulated response is plotted in blue.

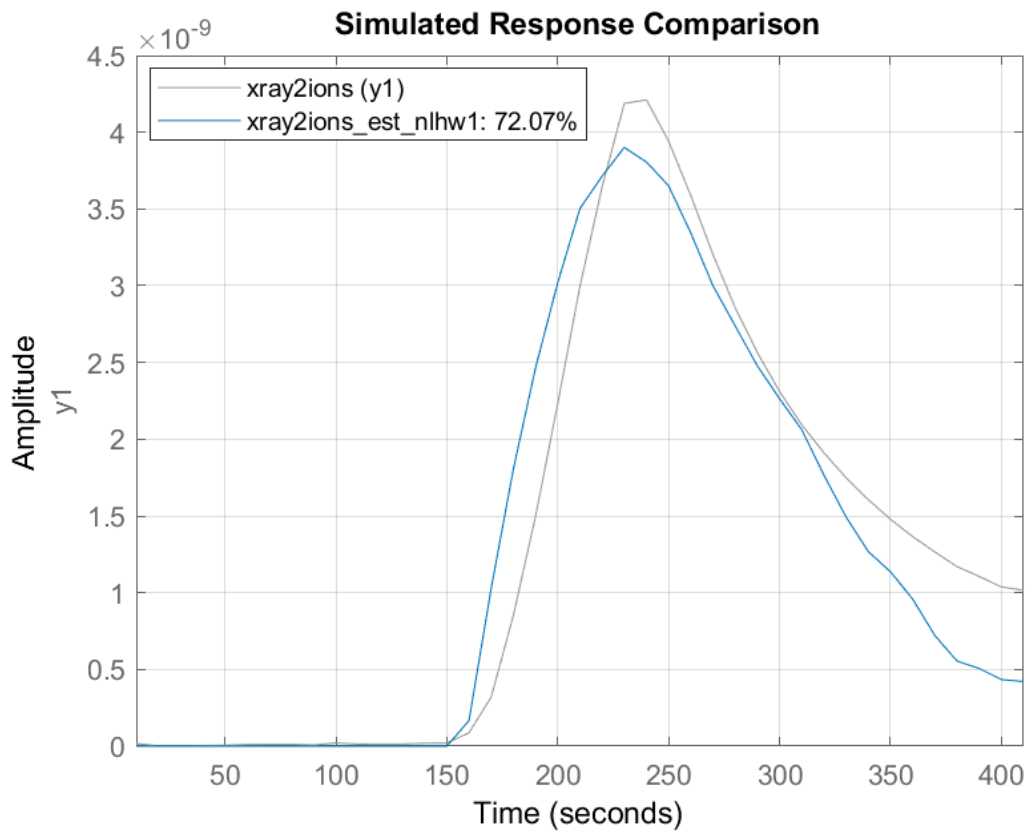

Fig. 6.14 Comparison of the UCLA system data and the estimated x-ray to ion current transfer function response. The original data is represented by the grey line, and the simulated response is plotted in blue.

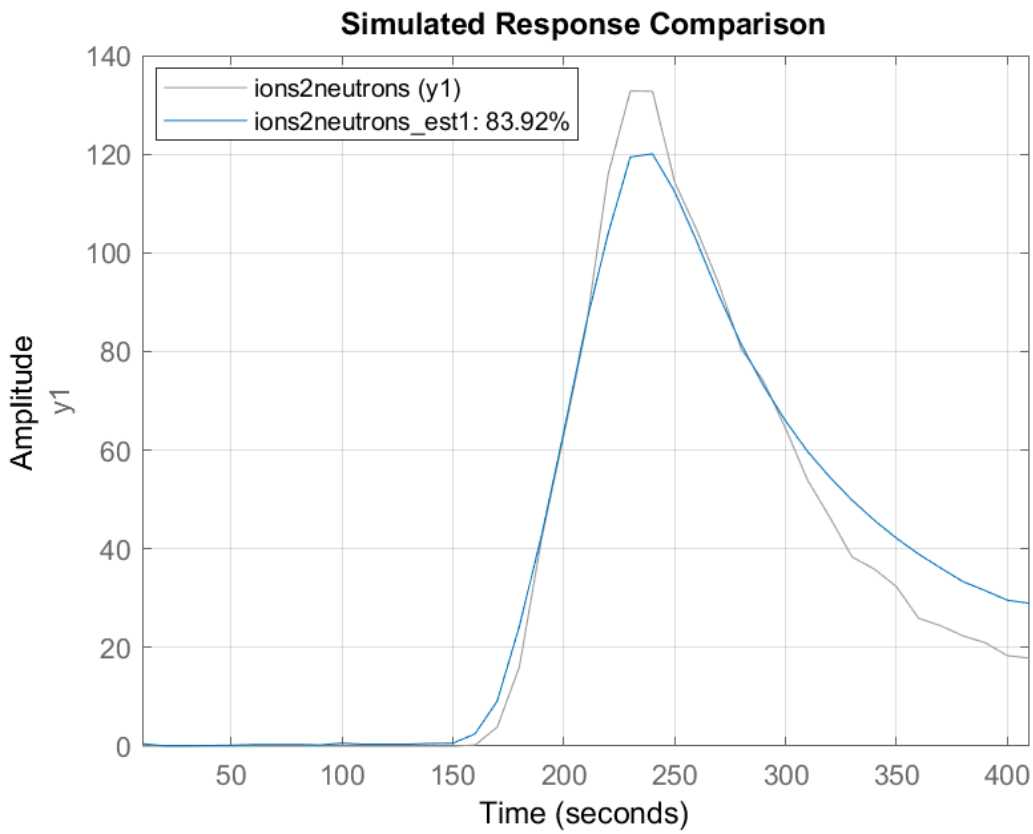

Fig. 6.15 Comparison of the UCLA system data and the estimated ion current to neutron counts per second transfer function response. The original data is represented by the grey line, and the simulated response is plotted in blue.

6.6 Summary

Our models have shown behavioural properties that reasonably resemble the performance of the UCLA pyroelectric neutron generation system [74]. We have identified the nonlinear dynamic characteristics for the UCLA pyrofusion system. We have investigated the physical identification of the model structures through use of digitised pyrofusion experiment data. The simulations in MATLAB/Simulink of a simple pyroelectric neutron source demonstrate the possibilities of investigation into the dynamic characteristics using methods of control engineering theory.

1. We have improved the modelling of the pyroelectric neutron generation system based on our previously published model and results [26, 27].

2. The dominant dynamic response of each sub-system has been captured and the theoretically derived model has been used to estimate more physically accurate transfer functions.

3. The nonlinearities of the system have been investigated and the initial steps towards their identification have been made.

4. The detector and geometrical considerations for the UCLA system have been identified; these parameters could be tuned to model other systems in the future.

5. Through our modelling process we can confirm that the UCLA group's neutron yield is not the theoretical maximum for an optimised system.

6. We have designated the same data set to be used for estimating and validating the model, so there is some risk that we may have overfitted our data. We were unable to get hold of any additional appropriate time-domain data for validation. In future work it is recommended that tests are run that provide an additional independent data set for cross-validation. This will be specified in Chapter 8.

In Chapter 7 we will analyse and compare the stability and controllability of the UCLA pyroelectric neutron system and a theoretically optimal pyroelectric neutron system. Control system design will be discussed, simulated and analysed. Finally, we will discuss the potential application of these neutron sources to low-power nuclear reactors.

Chapter 7

Pyroelectric neutron generator control system

7.1 Introduction

In the previous chapter we used simulation and system identification techniques to create a pyroelectric neutron generator model, which captures the dominant dynamic characteristics of the system. However, before we can consider the application of the generator, we must first analyse the potential controllability of pyroelectric neutron production. We must:

1. Estimate the pyroelectric neutron generation system dynamic response, stability and performance.
2. Determine the controllable pyroelectric system dynamics and controllability boundaries.
3. Understand the type of additional system equalization desirable to achieve better control.
4. Identify the maximum forcing function bandwidth compatible with reasonable control action.

Following this investigation, we can consider the feasibility of using this neutron generator system as a stable and reliable neutron source in a nuclear reactor. In Chapters 4 to 6, we derived a pyroelectric neutron generator model structure from the underlying physics principles. In order to simulate the cyclic, or repeated pulse operation, of our pyroelectric neutron system, we are required to make a few adjustments to our Simulink model, which include:

1. Extension of the x-ray deadzone to [-80,80] keV.
2. The addition of a block to output the absolute value of the ion current for the calculation of the ion production.
3. A switch on the ion production signal that only allows neutrons to be generated when the ions are accelerated towards the target.

The updates can be seen in the Simulink model in Fig. 7.1. The full system model has a multiloop control system, with temperature control in the inner loop, and the control of neutron production in the outer loop. We initially tuned single-input single-output PID controllers, and now we need to turn our attention to tuning multiloop PID controller architectures. We will follow a typical workflow [67], whereby we tune the compensator for the inner loop (the blue blocks in Fig. 7.1) first, by isolating the inner loop from the rest of the control system. Then we will tune the outer loop (the green blocks in Fig. 7.1) to achieve our desired closed-loop response.

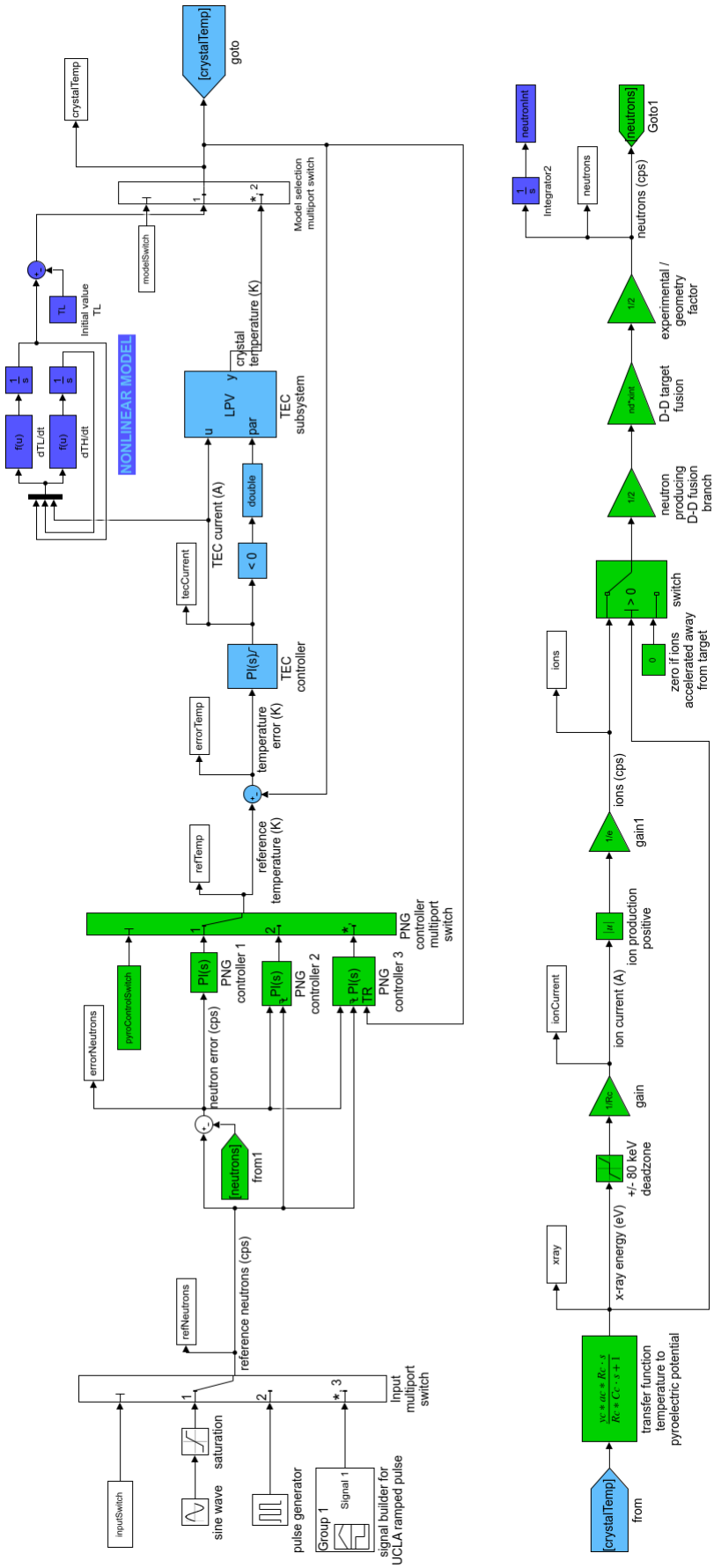

Fig. 7.1 Simulink single-crystal pyroelectric neutron generator multiloop control system.

7.2 Inner loop temperature controller design

In Chapter 5, we designed a control system for a TEC operating at 240 K to increase the pyroelectric crystal temperature to 280 K, for the purpose of generating neutrons. With consideration of our nuclear reactor application, we must optimise our TEC control system to operate at room temperature, that is, at ∼300 K. As we will be cycling our crystal temperature during the reactor transients, we will define the heating half-cycle as neutron producing. Our design objectives for the inner loop control system are:

1. Minimal closed-loop step response settling time.
2. Inner loop phase margin of at least 60 degrees.
3. Maximum inner-loop bandwidth.

The heating/cooling process can allow temperature overshoots of around 20% of the crystal temperature beyond the setpoint. TEC modules have operating temperature limits, and there are units available with a maximum operation temperature of around 200 °C, where this limit is defined by the reflow temperature of solder and sealing [70]. Temperature differences between hot and cold sides of around 70 + 273 K are safe for TEC operation. For our system, initially at room temperature (i.e. around 30 + 273 K), the change in setpoint must not exceed 60 K.

We can use the MATLAB supported rule-based methods to automatically tune our controller to achieve the optimal system design and to meet our requirements. However, these methods do not support nonlinear systems. We will need to use a linear plant model to automatically tune the PID controller gains, then fine-tune the design interactively as required.

We first isolate the inner loop (the blue blocks in Fig. 7.1); this removes the effect of the outer control loop on the open-loop transfer function of the inner loop. We can tune a one-degree-of-freedom PID controller, using the built-in *pidtune* MATLAB algorithm, which balances performance (response time) and robustness (stability margins) [67]. We can choose to specify a target value for the first 0 dB gain crossover frequency of the open-loop response. In Chapter 5, we identified the crossover frequency for the open-loop TEC system (i.e. without a controller) to be around 0.127 rad/sec. So, we can design and compare the performance of two controller options by specifying target values of 0.1 and 1 rad/sec gain crossover frequencies in the *pidtune* MATLAB algorithm. The controllers that result from the control design process are of the following PI form:

$$Kp + Ki\frac{1}{s} \tag{7.1}$$

where Kp and Ki have the following values:

1. Crossover frequency of 0.1 rad/sec: with $Kp = -0.612$, $Ki = -0.0504$.
2. Crossover frequency of 1 rad/sec: with $Kp = -6.7$, $Ki = -4.02$.

PI controllers are quite common in industry applications, since the derivative action is sensitive to measurement noise [67]. We have also moved the TEC current saturation from an external Simulink block to an internal controller parameter, such that the output of the PI controller will always be limited to ± 10 A.

We may now take each controller and simulate the closed-loop response for both the heating and cooling modes of operation. If the response for the cooling mode is unsatisfactory, we will need to consider gain scheduling of the PID controller. The resulting closed-loop TEC system unit-step and frequency response plots are shown in Fig. 7.2. The unit-step performance characteristics are compared in Table 7.1. We can see that:

1. Although the controller designs were based on the heating mode of operation, the resulting individual control system responses are the same for both heating and cooling. This is most clearly apparent on the Bode diagram, where the cooling cycle frequency response exactly overlays the heating response for each crossover target.
2. The unit-step response plot shows us that the response time increases with increasing target crossover frequency. The values of the rise time are easily compared in Table 7.1, where we can see the factor of approximately 10 increase between each successive controller design.
3. The controllers have reduced the low frequency gain to 0 dB. Each controller meets its crossover target well.

Comparing each of the controller performances against our design requirements, we can determine that controller 2 best meets our requirements. It is clear that the pyroelectric neutron generation system will not produce the demanded neutron output without either a good calibration of the neutron demand to temperature change required, or an outer closed-loop involving control on the neutron error. As our system is a multiloop control system, we must jointly tune both the inner and outer loops in order to get an acceptable design.

No.	Crossover frequency (rad/sec)	Peak response (K)	Overshoot %	Settling time (sec)	Rise time (sec)	Steady-state (K)
1	0.1	1.17	16.8	61.7	13.9	1
2	1.0	1.23	23.4	9.12	1.27	1

Table 7.1 Comparison of closed-loop TEC controller performance characteristics.

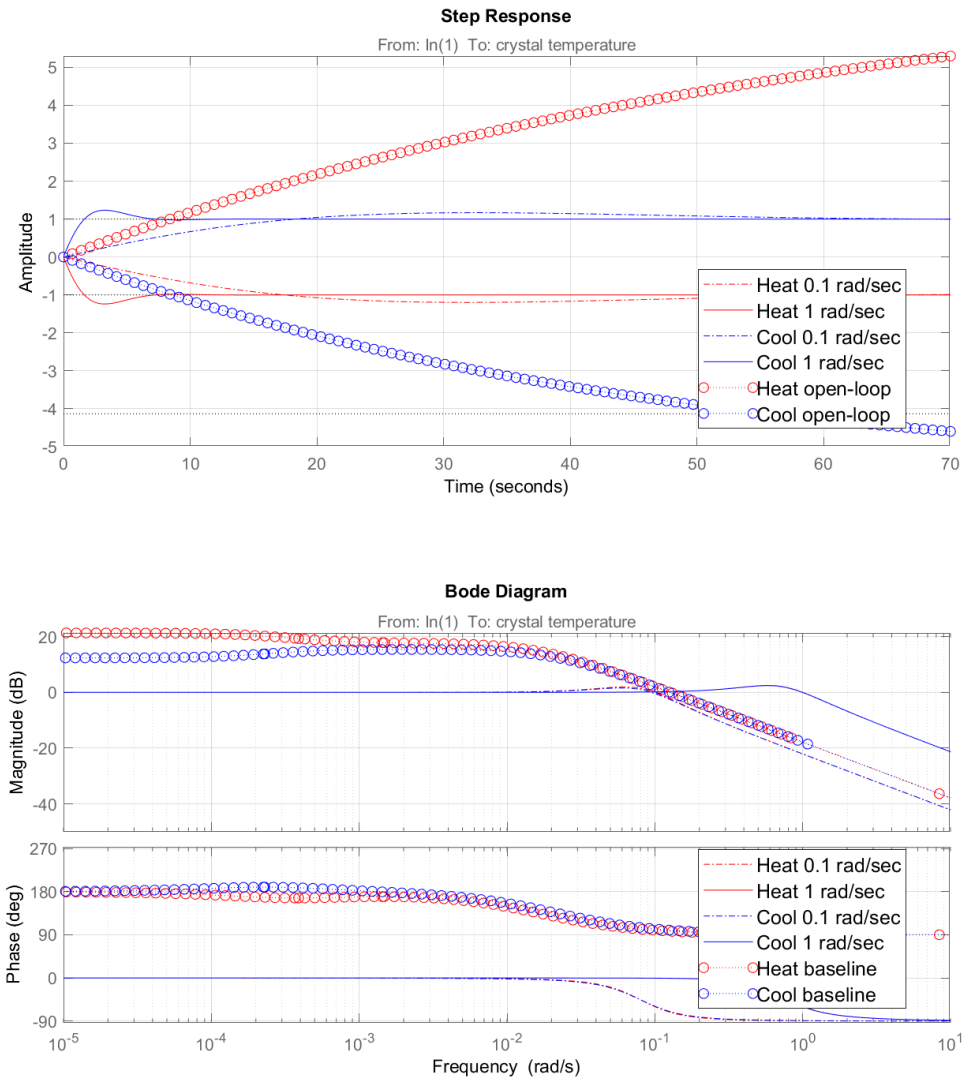

Fig. 7.2 Comparison of the TEC control system unit-step and frequency responses.

7.3 Outer loop neutron controller design

When designing multiloop control systems, the inner control loop is typically designed to be faster than the outer loop to reject disturbances before they propagate to the outer loop. In our case, we should design the outer loop to have a bandwidth of no more than 0.1 rad/s. We use a linearised pyroelectric neutron generator system model, and incorporate the inner TEC feedback control loop. Two crossover frequencies are considered for the outer control loop: 0.1 rad/sec and 0.01 rad/sec. We use the MATLAB algorithm *pidtune* for the neutron PID controller design. The optimised controller has the following I-only form:

$$Ki\frac{1}{s} \tag{7.2}$$

where

1. For a crossover frequency of 0.1 rad/sec: $Ki = 0.00154$, with a phase margin of 90.7 degrees.
2. For a crossover frequency of 0.01 rad/sec: $Ki = 0.0016$, with a phase margin of 100.7 degrees.

Figure 7.3 shows the response of the two neutron PI controllers.

1. The unit-step response shows that the multiloop control system, with the pyrolectric outer loop controller tuned for a 0.01 rad/sec crossover frequency, has a very sluggish response. This would be too slow for our reactor transient application, and the response actually increases (very slowly) to infinity (i.e. the system is unbounded and unstable).
2. The controller tuned for 0.1 rad/sec has a good response, with a final steady-state value of 1, a rise time of around 23 seconds, and no overshoot.
3. The Bode diagram clearly shows the systems to act like bandpass filters, from around 10^{-16} rad/sec to around 10^{-2} rad/sec. This indicates that the system should respond well to slow changing inputs with maximum frequencies in the region of 10^{-2} rad/sec.

The multiloop system controllers that we will take forward to the next section, for the nonlinear system cyclic pulse simulations in Simulink, are the inner loop TEC PI controller tuned at 1 rad/sec and the outer loop integral neutron controller tuned at 0.1 rad/sec.

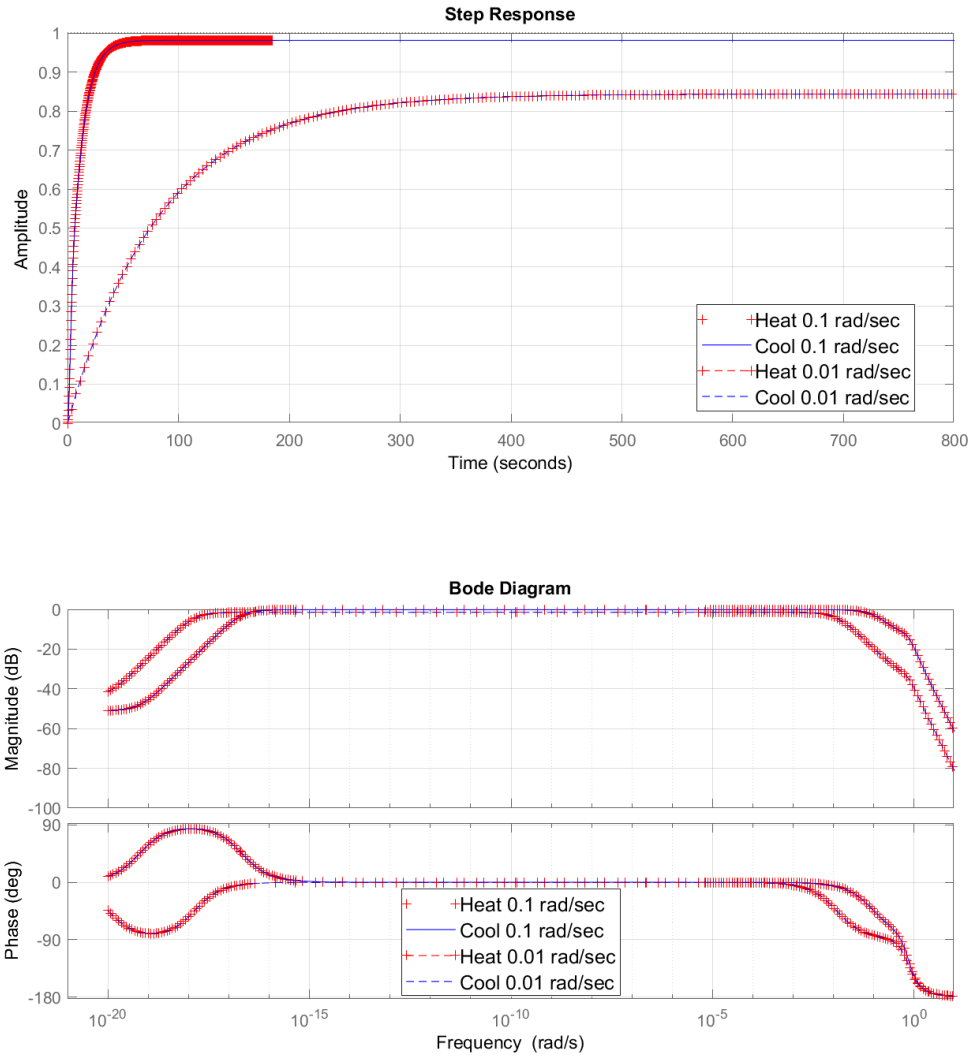

Fig. 7.3 Comparison of the two pyroelectric neutron generator multiloop controller designs, with an inner control loop (temperature) crossover frequency of 1 rad/sec, and an outer loop (neutrons) target crossover frequency of 0.1 rad/sec or 0.01 rad/sec.

7.4 Repeated pulse and positive half-cycle sine-wave responses

In this section, we will investigate how our first pass controller system responds to dynamic inputs when coupled with the nonlinear plant dynamics. In each case, the controllers and input combinations under investigation are:

1. An inner loop PI TEC controller, with a ± 10 A output current saturation, and 1 rad/sec crossover frequency; and an outer loop I-only pyroelectric controller with 0.1 rad/sec crossover frequency.
   (a) Positive half-cycle sine-wave input, with 800 counts per second (cps) magnitude and 0.01 rad/sec frequency.
   (b) A repeated pulse input with an amplitude of 800 cps, period of 600 seconds, pulse width of 50% and zero phase delay.
2. A inner loop PI TEC controller, with a ± 10 A output current saturation, and 1 rad/sec crossover frequency; and an outer loop I-only pyroelectric controller with 0.1 rad/sec crossover frequency; **and additionally with an external reset trigger.** The action of the external reset is explained in the following section.
   (a) Positive half-cycle sine-wave input, with 800 cps magnitude and 0.01 rad/sec frequency.
   (b) A repeated pulse input with an amplitude of 800 cps, period of 600 seconds, pulse width of 50% and zero phase delay.
3. An inner loop PI TEC controller, with ± 10 A output current saturation, and 1 rad/sec crossover frequency; and an outer loop I-only pyroelectric controller with 0.1 rad/sec crossover frequency, **external reset trigger, and additionally with tracking mode enabled.** The action of the enabled tracking mode is explained in the following section.
   (a) Positive half-cycle sine-wave input, with 800 cps magnitude and 0.01 rad/sec frequency.
   (b) A repeated pulse input with an amplitude of 800 cps, period of 600 seconds, pulse width of 50% and zero phase delay.

The results of the simulations are shown in Figs. 7.4 to 7.9. The main observations from the simulation results are as follows:

1. **Neutron I-only controller:**

(a) **Positive half-cycle response.** Figure 7.4 shows a reasonable neutron response. The production of generated neutrons lags the demand and there is an error of around 40 cps at each peak. The multiloop controller shows good inner loop (temperature) control. However, the main issue with this controller response is the continually increasing crystal temperature - ideally, we would want the temperature to decrease back to room temperature between each half-cycle. The TEC current demand looks reasonable, it only once peaks at the saturation value - this could be avoided with a controller that reduces the temperature between peak demands. The x-ray energy and ion current signals look reasonable - both are positive, and they are repeatable, i.e the signals do not increase or drift between the peaks in neutron demand.

(b) **Pulse response.** Figure 7.5 shows that the PI controller response to a pulse demand is not as good as the previous half-cycle response. The first neutron pulse demand results in a series of spikes, which overshoot the setpoint. The error in neutrons increases over the transient, with the controller finally unable to produce a satisfactory second pulse. The temperature exceeds the safe operational limits for the device, and the error in this signal increases over the transient. The TEC current saturates several times over the duration of the two pulses. The x-ray energy switches from positive to negative several times (due to the temperature fluctuations) and the ion current signal has a similar shape.

The two responses indicate that we need to include an external reset in the controller to reset the output when the neutron demand signal has a falling edge - this should cause the temperature demand to return the crystal to room temperature between cycles.

2. **Neutron I-only controller with reset trigger:** We specify an external trigger condition that causes the controller block to reset the integrator and filter to initial conditions. Our external trigger condition is a falling neutron demand.

(a) **Positive half-cycle response.** Figure 7.6 can be compared to the I-only controller response. The neutron output looks very similar - the error at peak demand is, again, around 40 cps. The temperature change response has improved, and we can see that it now successfully returns to 0 K (i.e. back to room temperature) between each positive half-cycle. This is accompanied by increased saturation of the controller output (TEC current), and oscillations on the falling neutron edge. There are also accompanying oscillations in the x-ray energy and ion current.

(b) **Pulse response.** Figure 7.7 can be compared to the I-only controller response, and we can see that there is no improvement in the performance.

The oscillations in temperature are due to the TEC actuator having its own closed-loop dynamics. The neutron controller is in an outer loop and sees the temperature dynamics as an inner loop, or a cascaded saturated dynamic. We need to remove the falling-edge TEC current and temperature oscillations using a tracking coefficient on the output of the inner loop. This will ensure that when we transfer control from one control loop to the other there is no big transient. A successful multiloop anti-windup control strategy in MATLAB requires feeding back the actuator output to the tracking port of the controller block [67].

3. **Neutron I-only controller with reset trigger and tracking mode for anti-windup:**

   (a) **Positive half-cycle response.** We enable the tracking mode of the I-only controller, so that the difference between the inner loop feedback signal (the actual crystal temperature) and the block output is fed back to the integrator input with a gain $K_t = 1$. Figure 7.8 shows no improvement in the overall neutron production. However, the oscillations that were previously seen on the falling edge of the crystal temperature signal have been removed. It is to be noted that there is an increase in successive temperature change peaks from 42 K to 50 K. The TEC current signal has fewer saturation peaks, and has a much smoother response than the previous controllers. The x-ray energy and ion current have no oscillations or spikes in their response.

   (b) **Pulse response.** Figure 7.9 shows a greater level of improvement in its response when compared to the previous controller. The spikes in neutron generation have gone, and both pulse demands are achieved. There is an increasing overshoot from one pulse to the next - however, this overshoot is around 27% - this is deemed to be acceptable. Again, the temperature profile is damped and shows an increase from one pulse to the next. The TEC current demand has less saturation, and both the x-ray energy and the ion current response have been damped. The temperature rate limit is breached for 30 seconds at the start of each pulse when the rate is approximately 1 K/sec. Following this initial period, the rate reduces to around 0.07 K/sec for 200 seconds of each pulse. The cooling rate at the end of the pulse is also around 1 K/sec for 40 seconds.

The best response is seen with the I-only controller with reset trigger and tracking mode for anti-windup. The multiloop pyroelectric neutron generator control system shows a good response to both the positive half-cycle and the pulse in neutron demand.

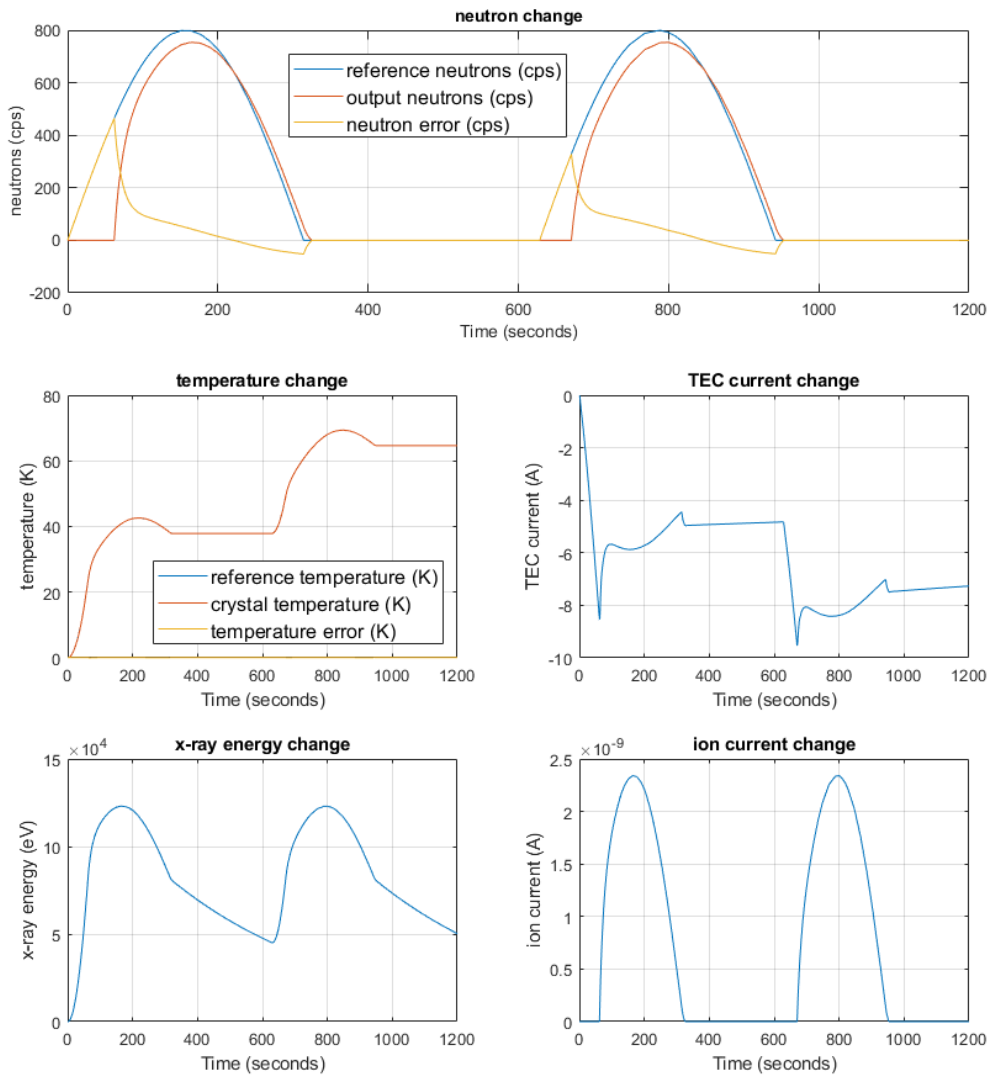

Fig. 7.4 Positive half-cycle response for the multiloop control system - with a temperature PI controller, and a neutron I-only controller.

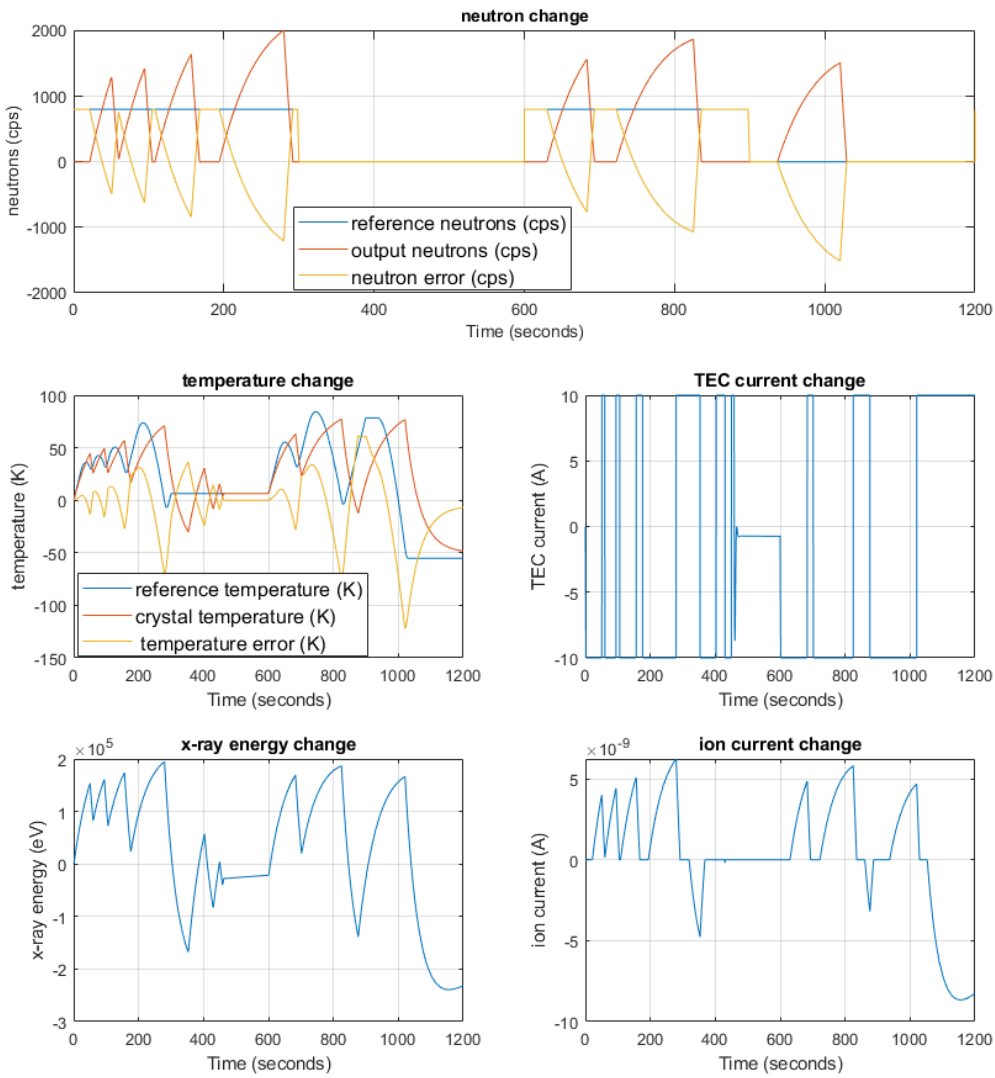

Fig. 7.5 Pulse response for the multiloop control system - with a temperature PI controller, and a neutron I-only controller.

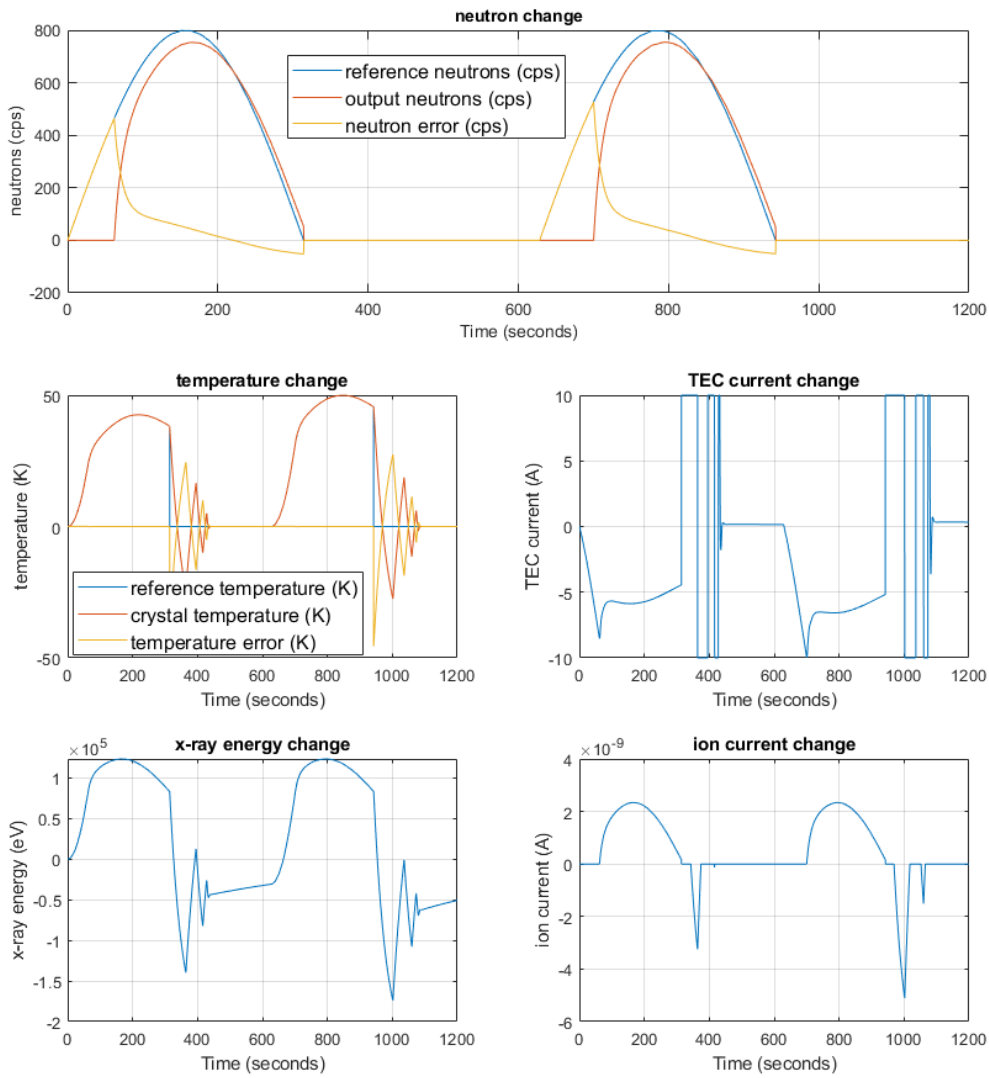

Fig. 7.6 Positive half-cycle response for the multiloop control system - with a temperature PI controller, and a neutron I-only controller **with external reset trigger**.

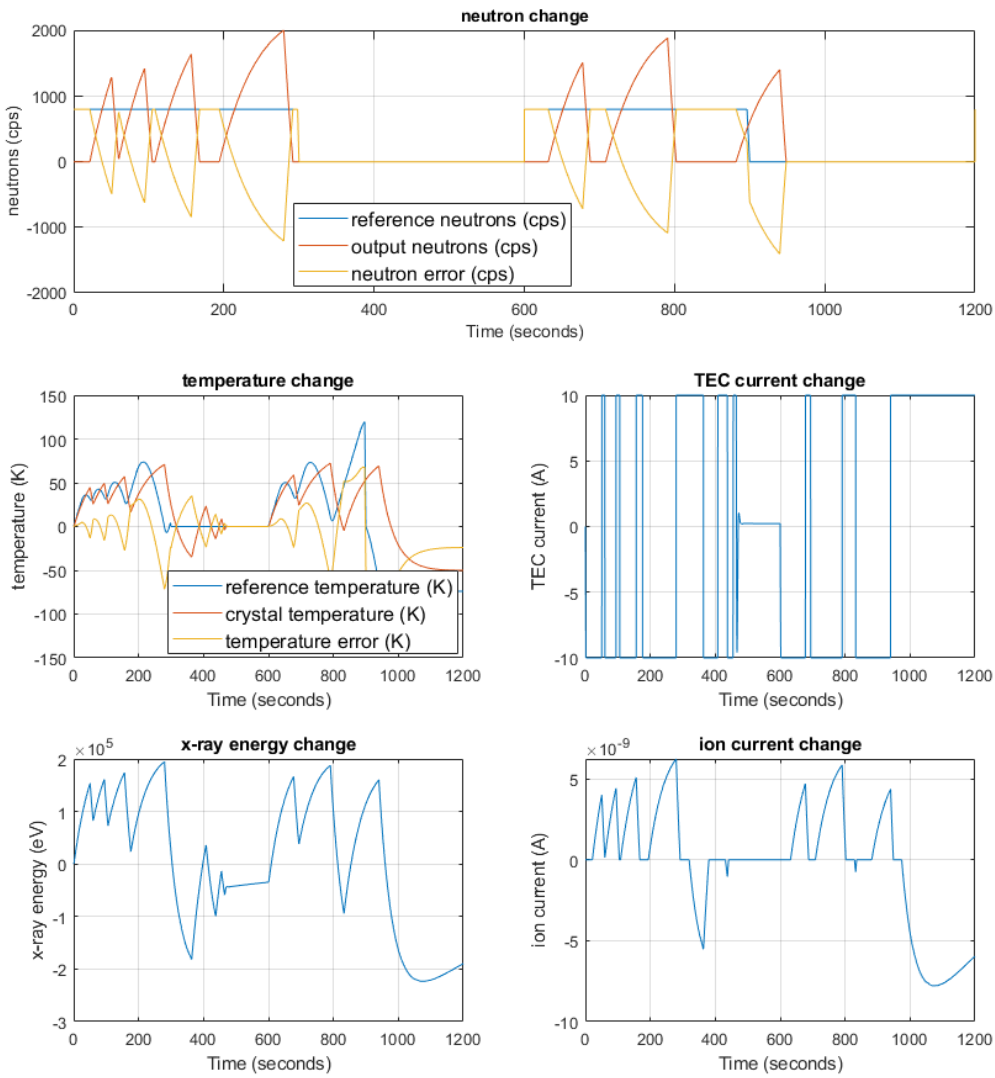

Fig. 7.7 Pulse response for the multiloop control system - with a temperature PI controller, and a neutron I-only controller **with external reset trigger**.

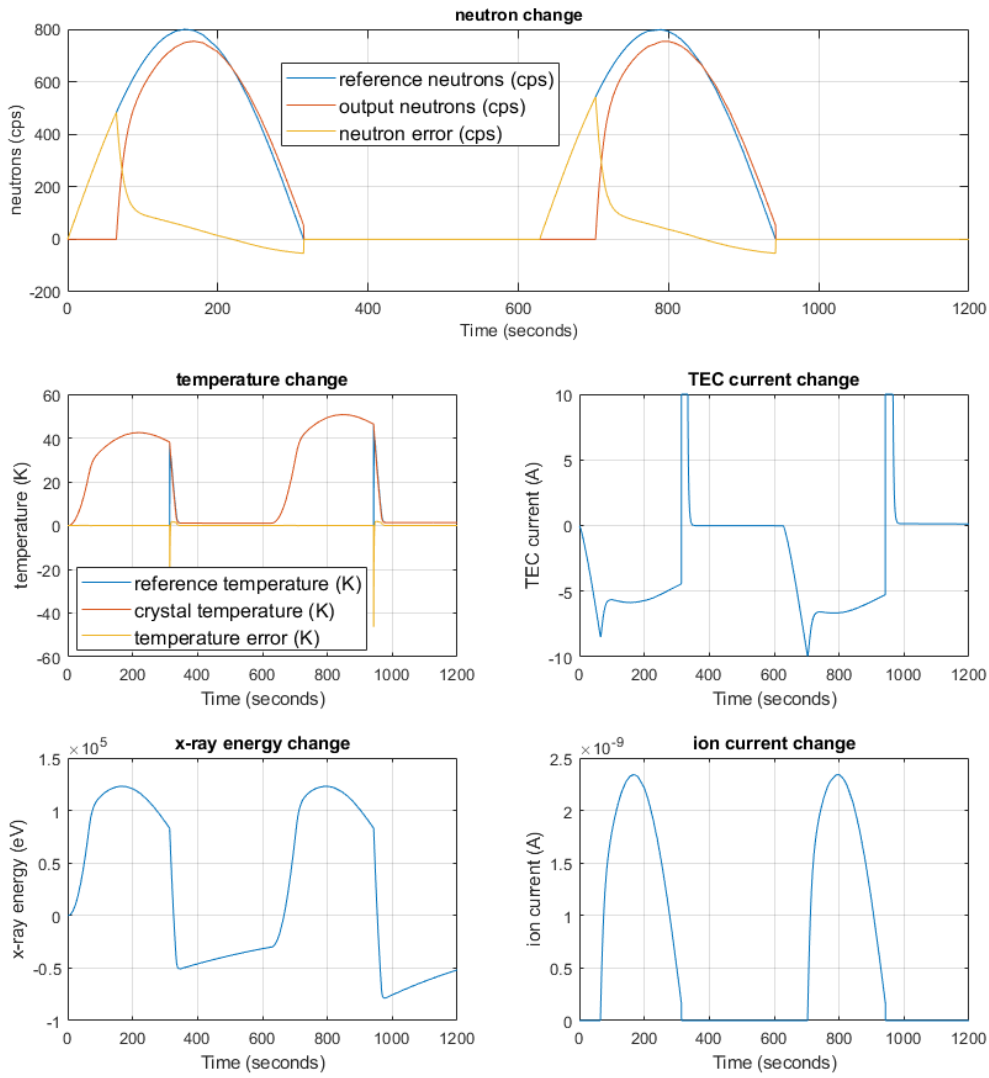

Fig. 7.8 Positive half-cycle response for the multiloop control system - with a temperature PI controller, and a neutron I-only controller **with external reset trigger and tracking mode for anti-windup**.

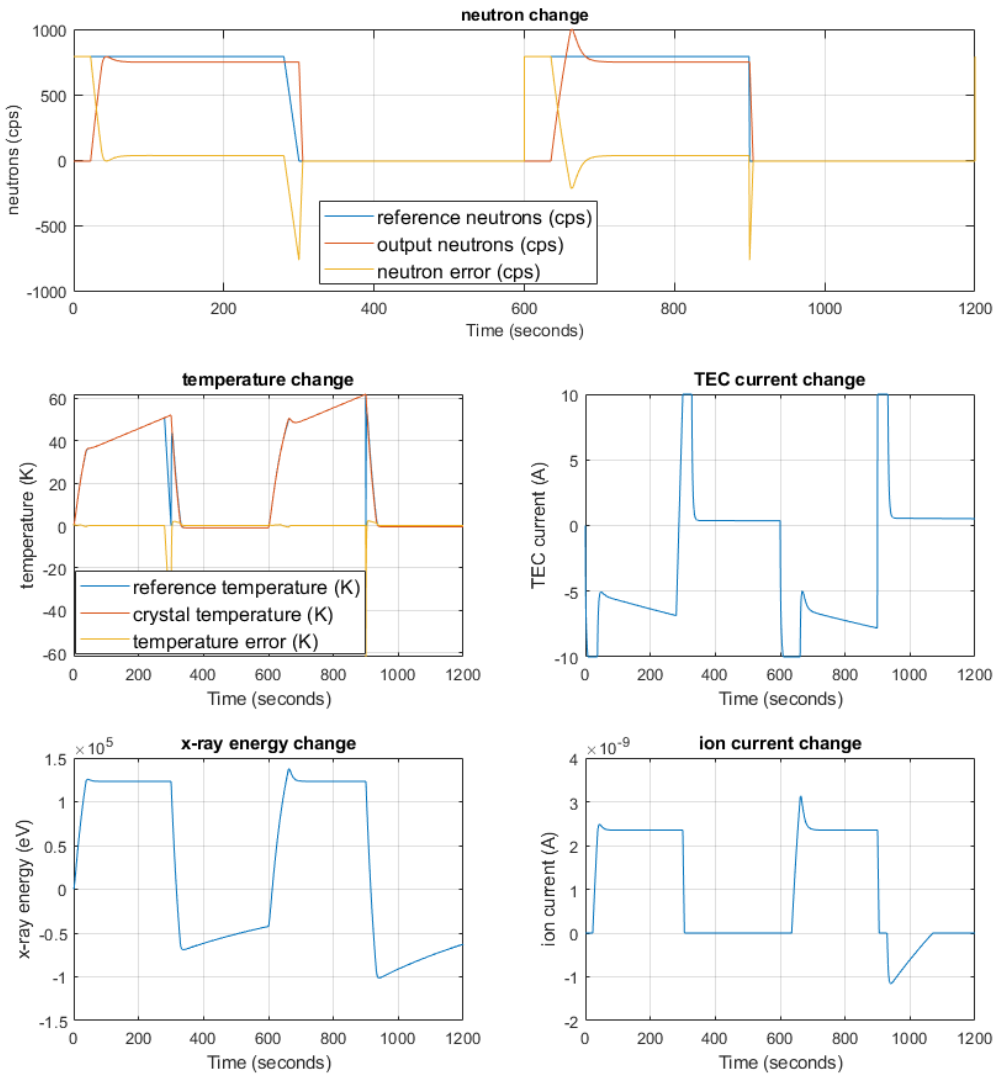

Fig. 7.9 Pulse response for the multiloop control system - with a temperature PI controller, and a neutron I-only controller **with external reset trigger and tracking mode for anti-windup**.

Having identified a suitable set of trajectories for neutron production in Fig. 7.9, we now look to optimise over these by parametrisation. The input pulses are generated using the MATLAB *Pulse Generator* block. The block waveform parameters, Amplitude, Pulse Width, Period, and Phase Delay, determine the shape of the output waveform. The following diagram shows how each parameter affects the waveform [68].

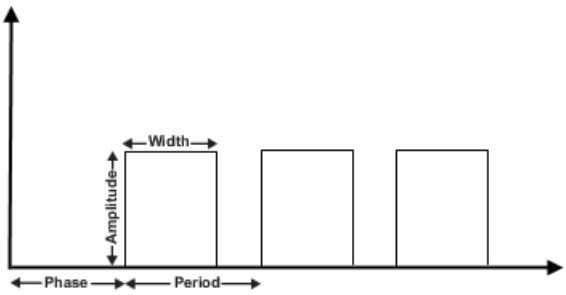

Fig. 7.10 Pulse generator parameter effects [68].

The UCLA experiments showed that it takes around 150 seconds of heating the crystal to start generating 800 neutrons per second. We want to thermally cycle our system, so we will take 150×2 seconds as our period. The amplitude of our pulse will be set at 800 neutrons per second. We will investigate the operation of the generator over a range of pulse widths (i.e. 10%, 25%, 50%, and 75% of the period). The pulse width (or duty cycle) is specified as the percentage of the pulse period that the signal is on.

The plots in Fig. 7.11 show the results. Each of the four plots in the left-hand column compares an ideal rectangular pulse (dashed-black outline) with the system's neutron output (cps) (blue plot). The plots in the right-hand column show the total number of neutrons produced over 600 seconds. For each pulse width, we calculate the Normalised Root Mean Square Error (NRMSE) between the ideal pulse and the modelled pulse, using the MATLAB function *goodnessOfFit*, with the cost function 'NRSME' specified [69]. The fit values are shown in Table 7.2, and vary between -0.4450 and -0.3560, with the former being the worst fit.

Although the pulse width of 10% has the best fit to the ideal pulse data, it can be seen that the pulse amplitude only reaches a maximum of 400 cps. The longer pulse widths of 50% and 75% produce more neutrons overall; however, we can see that there are increasing overshoots when transitioning from low to high states in successive pulses. The performance of repeated pulses at these longer pulse widths is not reliable. The pulse width of 25% seems to be the best compromise between the number of neutrons produced, and the repeatability of the pulses.

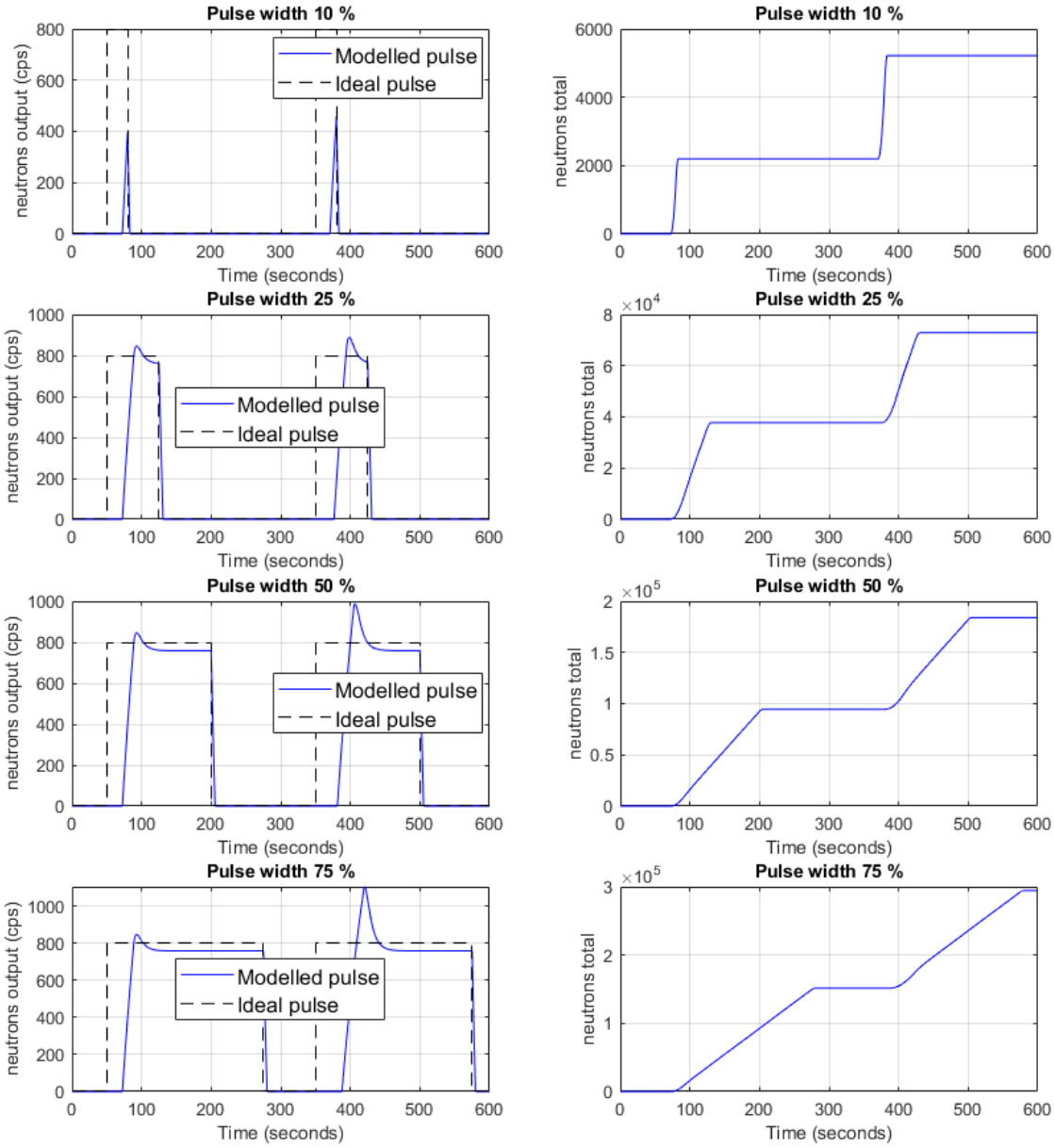

Fig. 7.11 Effect of pulse width variation on output neutron pulse and total neutrons produced.

Pulse Width	NRSME
10	-0.3560
25	-0.3615
50	-0.3679
75	-0.4450

Table 7.2 Comparison of NRMSE values for variation in pulse width.

7.5 The parallel pyroelectric neutron generator actuator problem

If we are to consider the potential of utilising pyroelectric neutron sources in reactor control applications, we will need to have several devices operating in an array. There are several ways in which the control of an array can be achieved. In this section, we will investigate the problem of operating pyroelectric neutron generators in parallel. Figure 7.12 shows the Simulink block diagram for two parallel pyroelectric neutron generators. Both devices are driven by the same setpoint signal, and the outputs of the devices are combined to generate the total neutron production signal. We have developed the model so that two input types can be considered: a step demand and a repeated pulse. The array controller was designed using the method that we used to design the controllers for the individual devices. In this section, we will report and discuss the results for the best performing controller design: an I-only controller (with a target crossover closed-loop frequency of 0.01 rad/sec and a resulting integrator gain of $Ki = 0.00512$), with external reset trigger that is inserted into the forward path to improve the closed-loop response of the array.

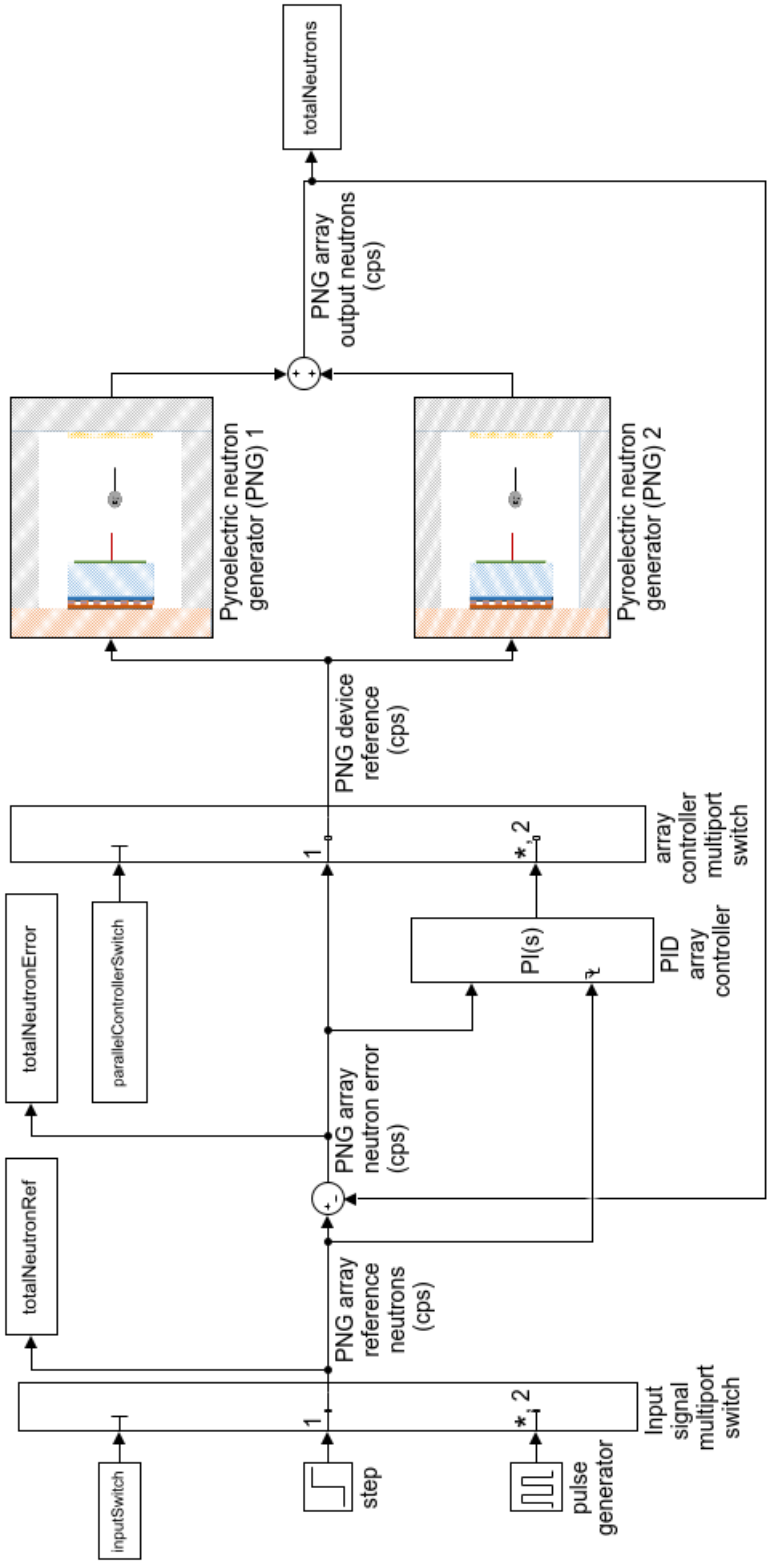

Fig. 7.12 Simulink block diagram of the parallel pyroelectric neutron generator array control system.

7.5.1 Repeated pulse response

Figure 7.13 shows the response of the controller array to a repeated pulse demand of 1600 neutrons/second, with a 400 second period and a 50% pulse width. Figure 7.14 shows the response of the individual devices, and as each device responded in exactly the same way, only one response is shown. From the figures we can see that:

1. The total pulsed demand is not quite met. The total generated pulse peaks reach a maximum of around 1470 cps at 200 seconds following the rising edge of each demand. The falling edge of each demand appears to be well controlled.

2. The individual devices produce half of the total neutrons generated by the array. The temperature of the crystal is well controlled, and rises with each successive pulse. However, the temperature change remains well below the maximum ∼70 K for the TEC. The maximum rate of change of temperature is 0.3846 K/sec, which is just under double the limit of 0.2 K/sec that was suggested by UCLA as safe enough to prevent crystal damage [74]. However, more research is required into the damage caused by the rate of change of temperature in lithium tantalate crystals.

3. The TEC current hits the saturation limit on the falling and rising edges of each pulse. However, the maximum duration of this saturation is around 23 seconds.

4. The x-ray energy cycles with the pulse, and the magnitude looks reasonable, reaching a maximum of around 120 keV at the pulse peaks.

5. The ion current also looks to be sensible, and peaks at around 2.3 nA.

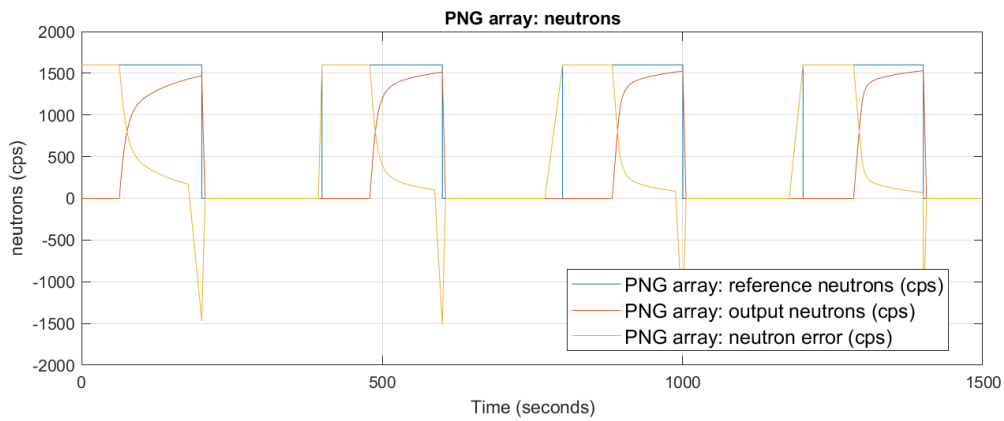

Fig. 7.13 Repeated pulse response of the parallel pyroelectric neutron generator array.

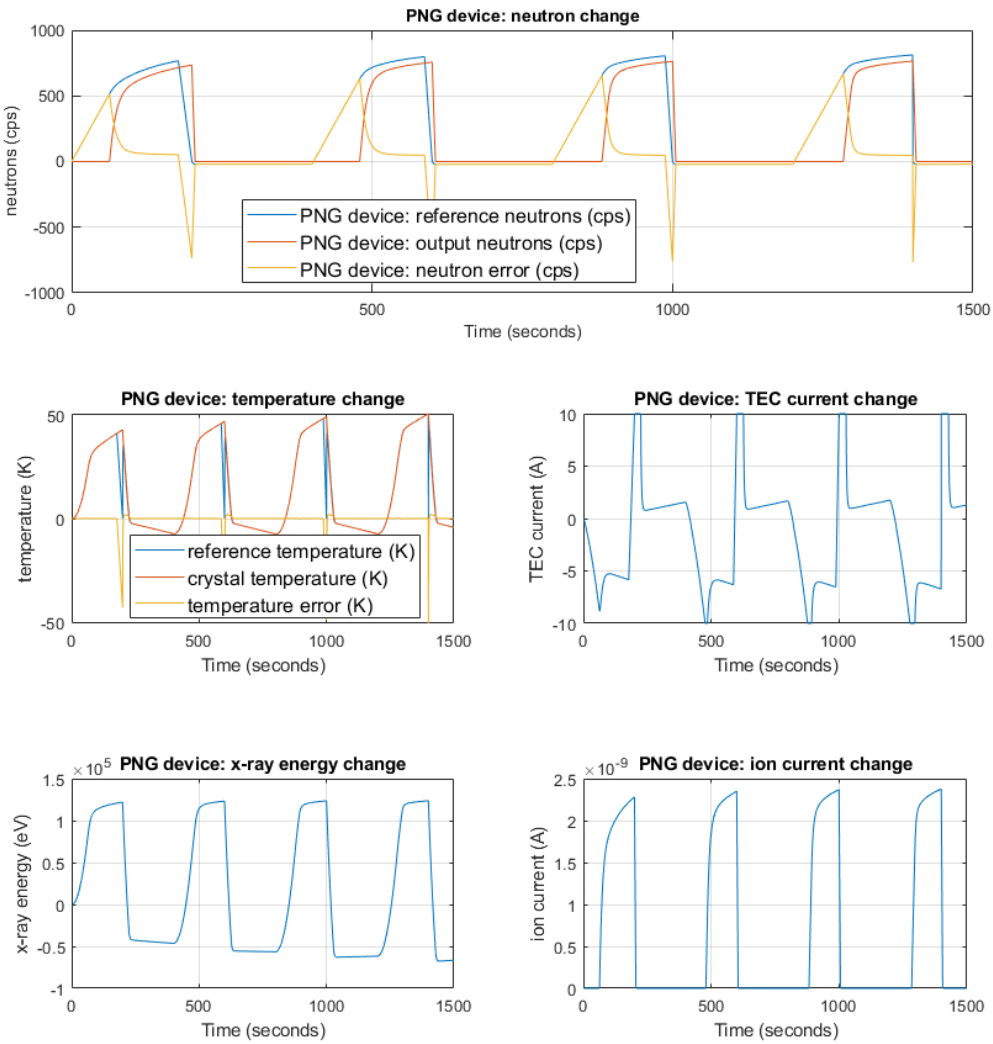

Fig. 7.14 Repeated pulse response of an individual pyroelectric neutron generator in the array.

7.5.2 Step response

Figure 7.15 shows the response of the controller array to a step demand of 1600 neutrons/second, and Fig. 7.16 shows the response of an individual device. From the figures we can see that

1. The overall constant step demand of 1600 cps is not met.
2. However, the array is able to produce a peak combined output of 1600 cps at around 500 seconds, for a maximum duration of 232 seconds. The rising edge of the pulse is seen at 64 seconds and the falling edge starts at 732 seconds, yielding a maximum pulse duration of 661 seconds.
3. The individual devices produce half of the total neutrons generated by the array. The temperature of the crystal is well controlled, until the TEC current becomes fully saturated at 752 seconds. The temperature change rises above the maximum ∼70 K for the TEC. The maximum rate of change of temperature is 2.8 K/sec, which is well above the limit of 0.2 K/sec that was suggested by UCLA as safe enough to prevent crystal damage. However, as we previously stated, more research is required into the damage caused by the rate of change of temperature in lithium tantalate crystals.
4. The x-ray energy reaches a maximum of around 130 keV.
5. The ion current also looks to be sensible, and peaks at 2.5 nA.

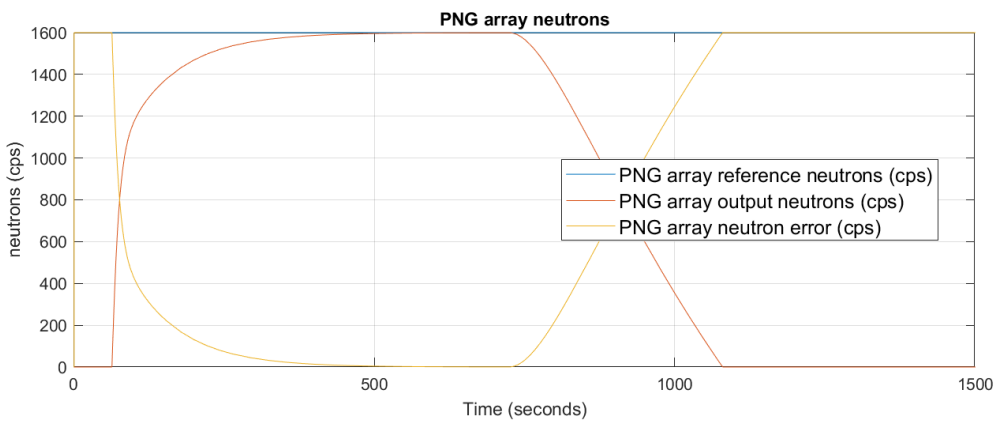

Fig. 7.15 Step response of the parallel pyroelectric neutron generator array.

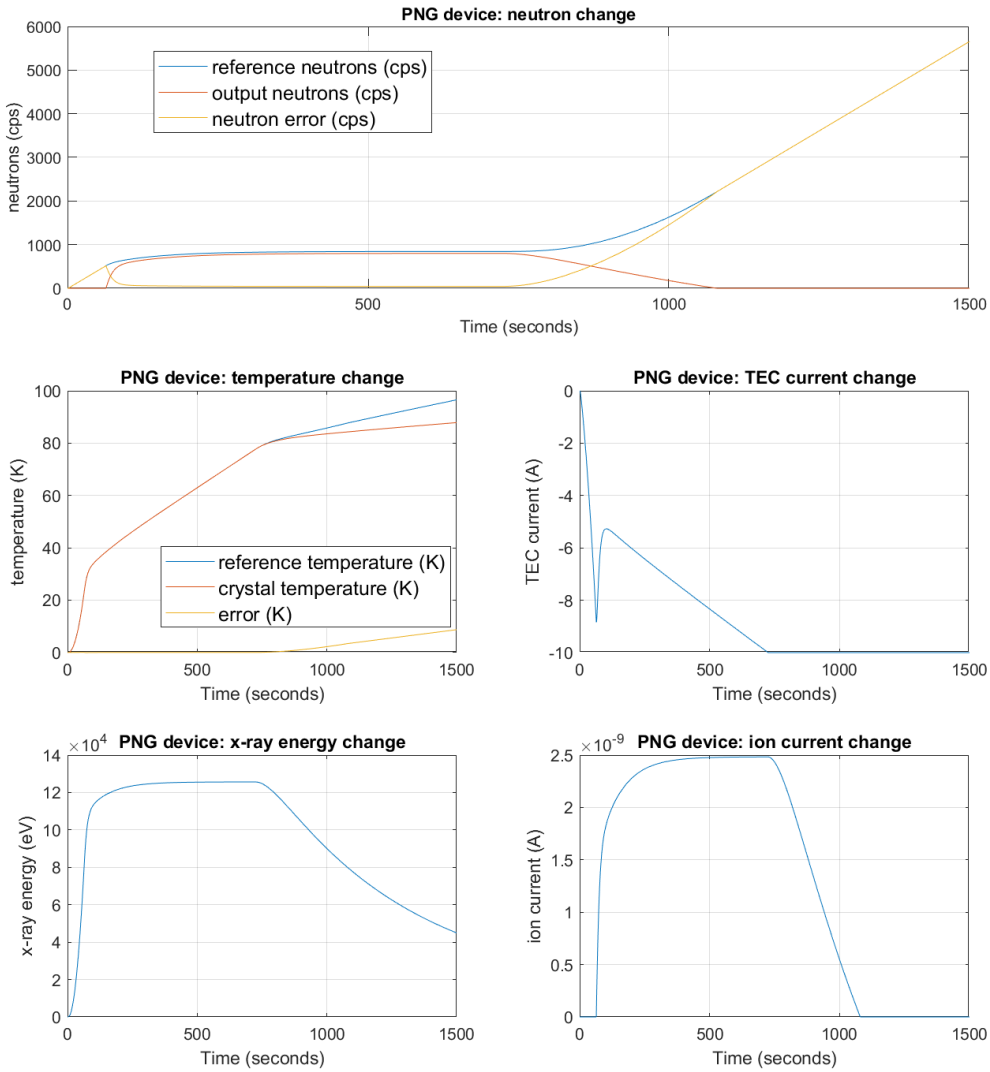

Fig. 7.16 Step response of an individual pyroelectric neutron generator in the array.

7.6 Pyroelectric neutron generator driven subcritical reactor transient

In this section, we will undertake a preliminary investigation into the feasibility of using a pyroelectric neutron generator array as an external neutron source to drive a subcritical reactor transient. The VR-1 zero-power reactor at the Czech Technical University would be convenient for performing such pulsed-source experiments. In 2019, a research team at the VR-1 performed several experiments using a pulsed external neutron source to determine the accuracy of the reactor kinetics parameters [12].

The simplest model of a reactor that we can consider is known as the point kinetics model. Several studies have shown good agreement between the point kinetic equations and experimental results at low frequencies (i.e. less than 20 rad/sec) [72]. These lumped-parameter equations are known to be satisfactory when the reactor is not very far from critical, i.e. when $k \approx 1$ [48]. The point kinetics equations, assuming a one neutron energy group reactor (that is one in which the production, diffusion and absorption of neutrons occur at thermal energy), may be written as [48]:

$$\frac{dn}{dt} = \frac{\rho - \beta}{l} n + \Sigma_{i=1}^{i=m} \lambda_i C_i + q \tag{7.3}$$

$$\frac{dC_i}{dt} = \frac{\beta_i}{l} n - \lambda_i C_i \tag{7.4}$$

where l is the neutron generation time,
$\rho = \frac{k-1}{k}$ is the reactivity (where k is the effective multiplication factor),
β is the effective delayed neutron fraction and is different for each reactor,
λ_i is the decay constant for the decay of precursor group i,
C_i is the number of delayed neutron precursors in group i,
q is the source of neutrons extraneous to the fission process (i.e. pyroelectric neutrons),
β_i is the proportion of fission reactions that result in the production of a delayed neutron precursor in group i.

Since, in the point kinetics equations, the neutron density is assumed to have a fixed spatial distribution, n may be regarded as an integral or volume-averaged property that is proportional to the instantaneous neutron density at some point in the reactor, such as the total number of neutrons, fission rate, power or average power density. We shall use the total number of neutrons, because the output of our pyroelectric neutron source is neutrons in

counts per second.

We can reduce the mathematical complexity of determining the reactor response to step changes in reactivity by representing all the delayed neutron precursors with a single mean decay constant. Applying this approximation, the kinetics equations can be written as

$$\frac{dn}{dt} = \frac{\rho - \beta}{l} n + \lambda C + q \tag{7.5}$$

$$\frac{dC}{dt} = \frac{\beta}{l} n - \lambda C \tag{7.6}$$

The parameters β, λ and l are assumed to be constant; and for the VR-1 reactor we may take the following values: $\beta = 0.00772$, $\lambda = 0.08518\ \mathrm{s}^{-1}$ and $l = 4.571 \times 10^{-5}$ seconds.

When we are considering the VR-1 reactor, the system output is the neutron flux and the input can be a reactivity perturbation, $\tilde{\rho}$, or a time-dependent neutron source, $\tilde{q}$. We call the two transfer functions the reactivity transfer function and the source transfer function, respectively. The system represented by Eqs. 7.5 and 7.6 is nonlinear, since ρ is functional of n [48]. In order to obtain the source transfer function, we can linearise by considering small deviations about some equilibrium value. In linearising we make the following substitutions:

$$\begin{aligned} n &= \bar{n} + \tilde{n} \\ C &= \bar{C} + \tilde{C} \\ \rho &= \bar{\rho} + \tilde{\rho} \\ q &= \bar{q} + \tilde{q} \end{aligned} \tag{7.7}$$

Making these substitutions into Eqs. 7.5 and 7.6, we obtain

$$\frac{d(\bar{n} + \tilde{n})}{dt} = \frac{(\bar{\rho} + \tilde{\rho}) - \beta}{l} (\bar{n} + \tilde{n}) + \lambda (\bar{C} + \tilde{C}) + \bar{q} + \tilde{q} \tag{7.8}$$

$$\frac{d(\bar{C} + \tilde{C})}{dt} = \frac{\beta}{l} (\bar{n} + \tilde{n}) - \lambda (\bar{C} + \tilde{C}) \tag{7.9}$$

If we now expand these equations, we get

$$\frac{d\bar{n}}{dt} + \frac{d\tilde{n}}{dt} = \frac{\bar{\rho}\bar{n} + \bar{\rho}\tilde{n} + \tilde{\rho}\bar{n} + \tilde{\rho}\tilde{n} - \beta\bar{n} - \beta\tilde{n}}{l} + \lambda\bar{C} + \lambda\tilde{C} + \bar{q} + \tilde{q} \tag{7.10}$$

$$\frac{d\bar{C}}{dt} + \frac{d\tilde{C}}{dt} = \frac{\beta\bar{n}}{l} + \frac{\beta\tilde{n}}{l} - \lambda\bar{C} - \lambda\tilde{C} \tag{7.11}$$

If we now remove the steady-state and higher-order terms, we obtain the following set of small perturbation equations:

$$\frac{d\tilde{n}}{dt} = \frac{\tilde{\rho}\bar{n} + \bar{\rho}\tilde{n} - \beta\tilde{n}}{l} + \lambda\tilde{C} + \tilde{q} \tag{7.12}$$

$$\frac{d\tilde{C}}{dt} = \frac{\beta\tilde{n}}{l} - \lambda\tilde{C} \tag{7.13}$$

Applying the Laplace transform (with all initial conditions set equal to zero), and rearranging, we may obtain the source transfer function:

$$\frac{\tilde{n}}{\tilde{q}} = \frac{s+\lambda}{s^2 + \left(\lambda + \frac{\beta-\bar{\rho}}{l}\right)s - \frac{\bar{\rho}\lambda}{l}} \tag{7.14}$$

Figure 7.17 shows the Simulink block diagram for the VR-1 reactor and the pyroelectric neutron generator array. The frequency response plot of the linearised subcritical VR-1 reactor and pyroelectric neutron generator array is shown in Fig. 7.18, and it indicates that this system could accept forcing functions with frequencies of up to 0.1 rad/sec.

Figures 7.19 and 7.20 show the change in reactor neutron density for an array of four pyroelectric neutron generators. The I-only controller for this array was designed using the same method as we used for the previous array, and the integral gain for optimal closed-loop performance was found to be $Ki = 0.00256$.

1. The responses seen are typical of the results to be expected from repetitively pulsing a subcritical reactor configuration - the neutron density, increases with the addition of pyroelectric neutrons. The falling edge of each neutron pulse is accompanied by a decrease in the reactor neutron density. This decrease shows an immediate fall caused by the prompt response of the reactor, followed by a delayed neutron 'tail'.

2. The pulse width that is generated by the array becomes slightly narrower with each successive pulse, and the pulse height ever so slightly increases.

3. The response of the shutdown reactor is less than that of the reactor when it is at around one rod worth of subcriticality.

4. It is to be noted that the model we have implemented is linear and does not account for increasing reactivity in the VR-1.

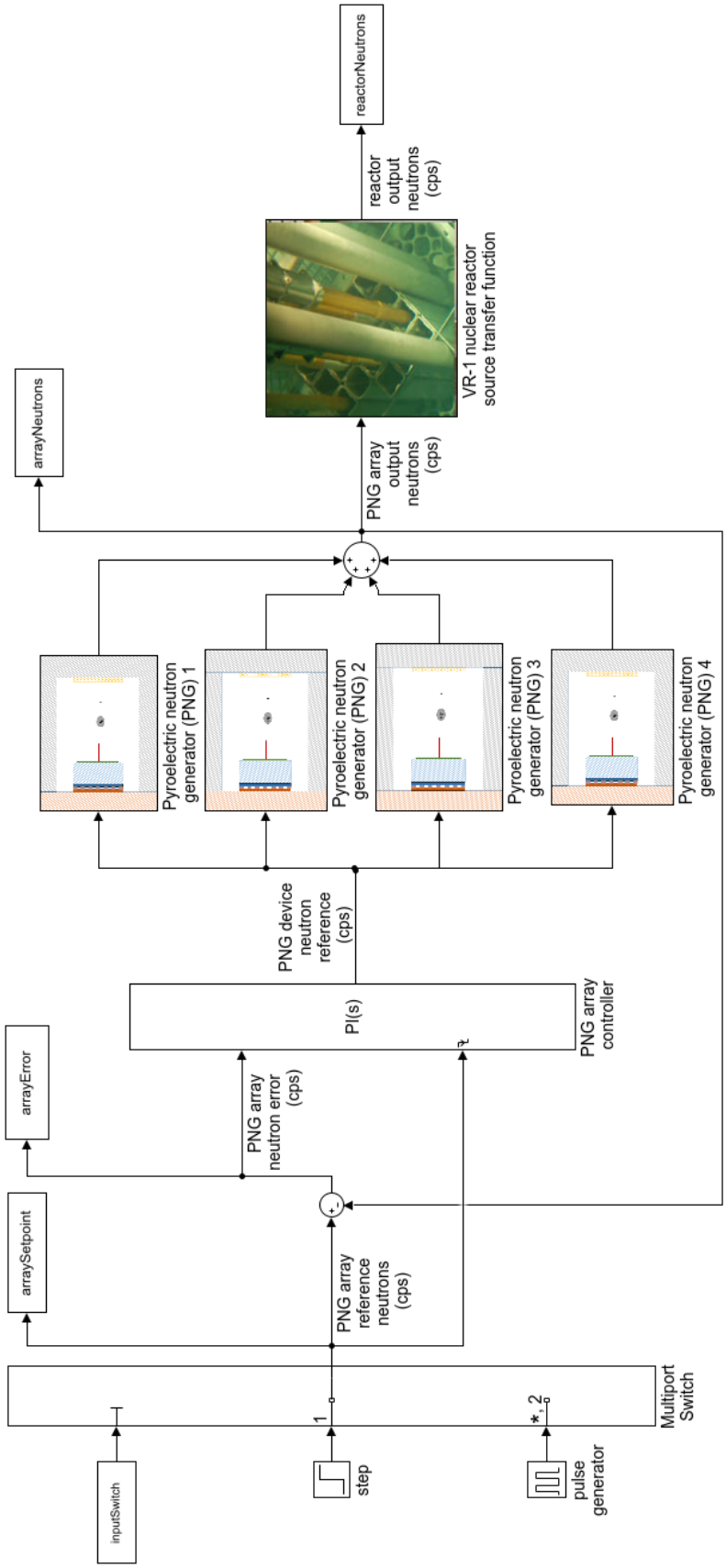

Fig. 7.17 Simulink block diagram of the VR-1 reactor and pyroelectric neutron array.

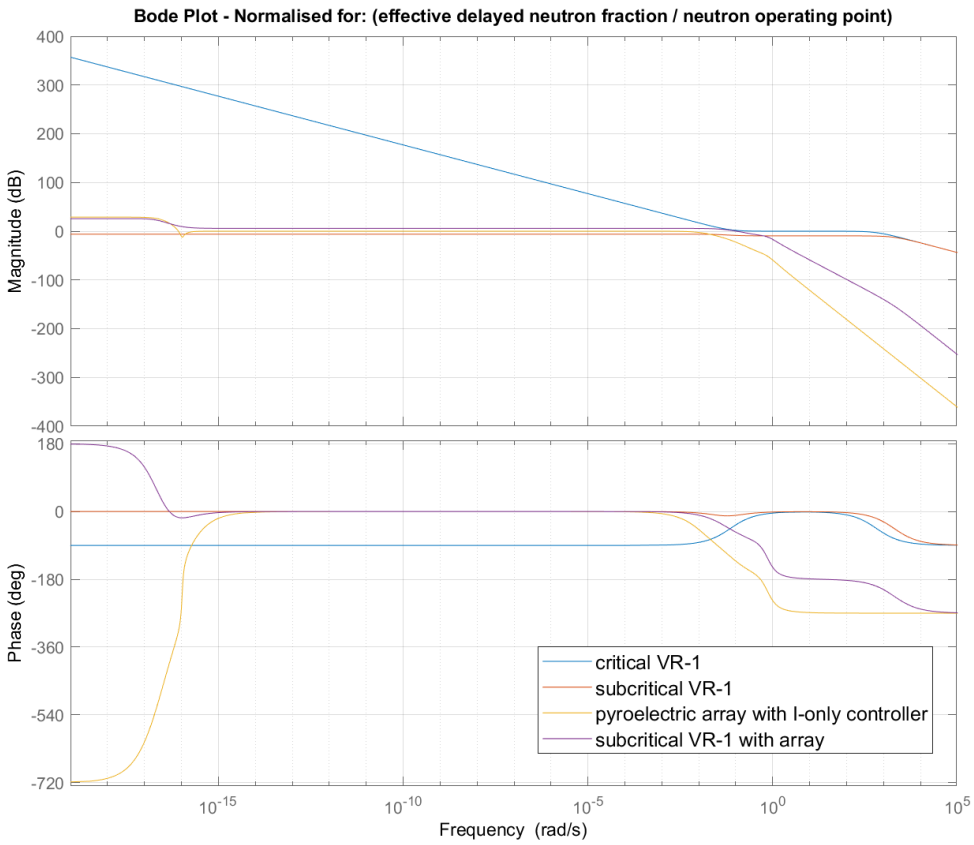

Fig. 7.18 VR-1 reactor and pyroelectric neutron array frequency responses.

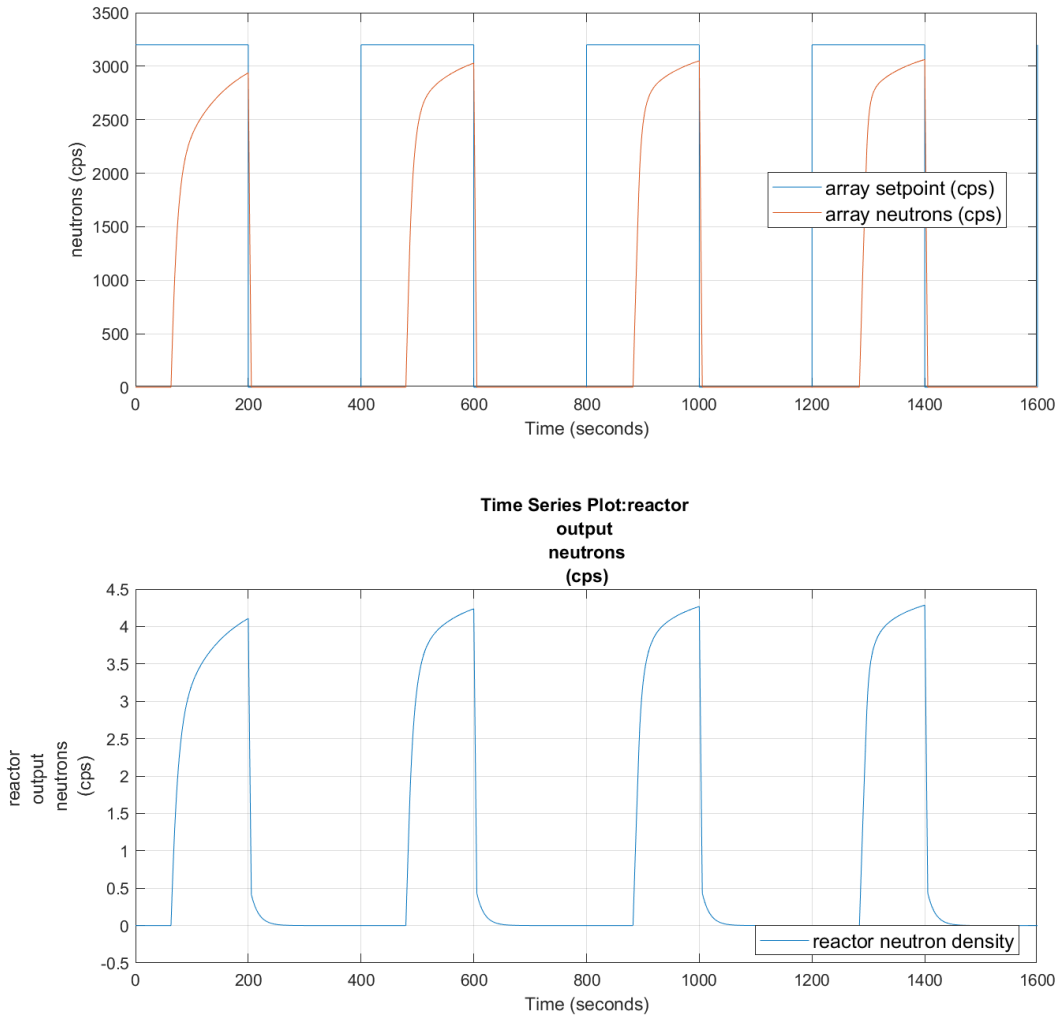

Fig. 7.19 Subcritical (shutdown reactor −7 $) VR-1 response to a pyroelectric neutron pulse.

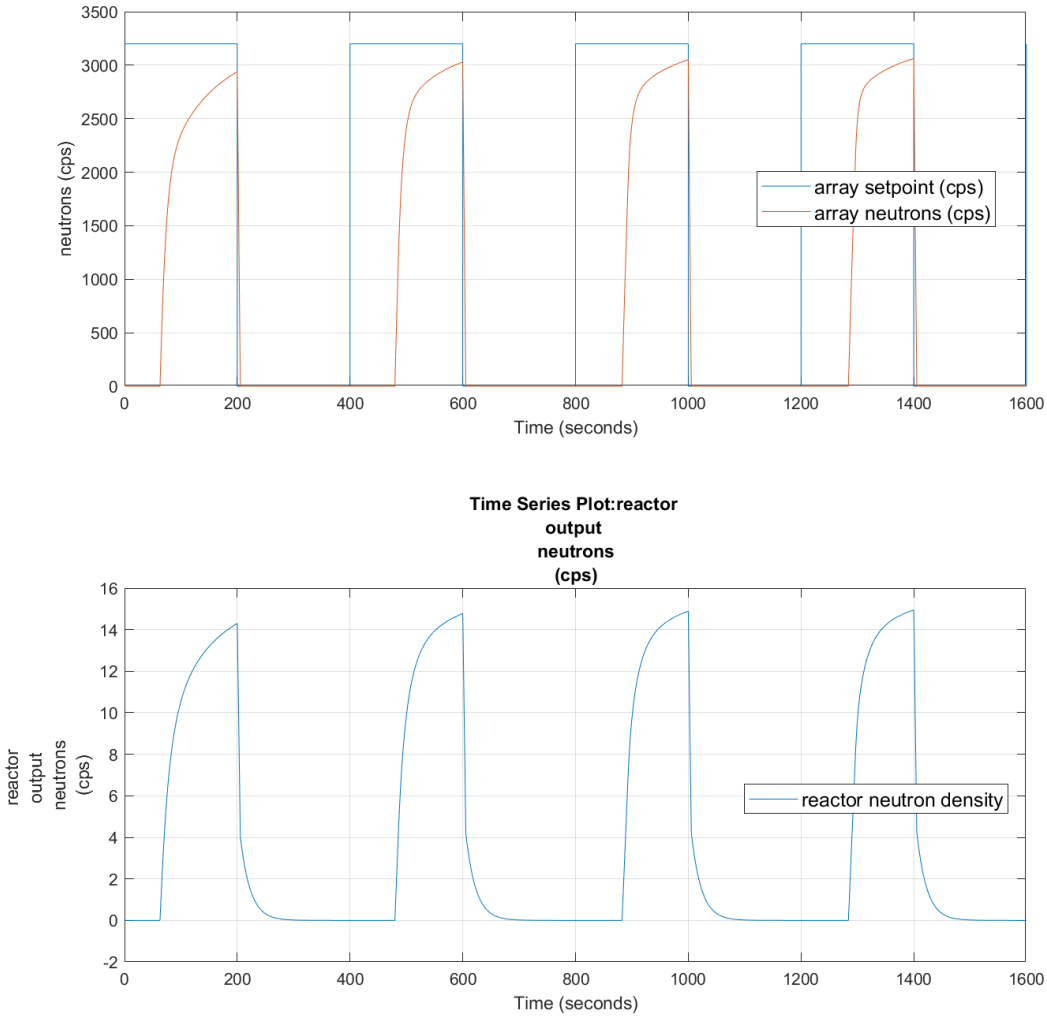

Fig. 7.20 Subcritical (approximately one rod worth −2 \$) VR-1 response to a pyroelectric neutron pulse.

7.7 Summary

We have analysed the potential controllability of pyroelectric neutron production, and the applicability of an array of devices as a pulsed neutron source in a subcritical reactor. Our main conclusions are:

1. The best form of controller for a single pyroelectric neutron generator is a multiloop control system, where there is a PI inner control loop for the crystal temperature, and an outer control loop containing an I-only controller, with an external reset trigger and the tracking mode enabled, for the neutron output.

2. A single device had the best performance when the control system was designed so that the inner loop crossover frequency was 1 rad/sec and the outer loop had a crossover frequency which was ten times less, at 0.1 rad/sec.

3. The maximum forcing function bandwidth has been found to be approximately 10^{-2} rad/sec, and given the current capability of the UCLA device, the maximum neutron output of each pyroelectric device has been limited to 800 cps.

4. From our preliminary analysis, it would seem that an array of pyroelectric neutron generators is capable of following a pulse demand in neutrons with a reasonable level of accuracy. The continuous step demand is rather more challenging for the array, and a continuous output can only be maintained for around 600 seconds.

5. Although the count rates seen in the simulated VR-1 subcritical system are small, we have confirmed the viability of coupling a pyroelectric neutron generator array with a zero power reactor. The device could be used to generate experimental data for kinetics parameter validation [12].

Chapter 8

Future research, recommendations and conclusions

8.1 General summary and conclusions

It will be recalled from Chapter 1 that the primary goals of this research were the modelling and control system design for the dominant dynamic characteristics of a pyroelectric neutron generator. The simulations and system identification tasks reported in Chapters 3-7 have accomplished the thesis goals, and in addition have revealed other facets of pyroelectric neutron dynamics. The total effort can be summarised under two major headings:

1. Status of the pyroelectric neutron generator model.
2. Extensions to the model and the control system design.

8.2 Status of the existing pyroelectric neutron generator model

Our Simulink pyroelectric neutron generator model has been developed in Chapters 3-7, and the status of this model can be summarised in the following points:

1. Chapter 3. Accurate modelling of the TEC was identified early on as a primary goal for successful pyroelectric neutron generator simulation. The performance of our model has been verified through simulation and comparison with more accurate theoretical models, and with an experimentally derived model. We performed a parameter-variation sensitivity study and a stability analysis. These indicated that the

TEC model performance is dependent on both the model operating point values and the hot-side and cold-side thermal masses.

2. Chapter 4. We applied our TEC model to the appropriate pyroelectric system thermal masses, and studied the system stability. We found the pyroelectric TEC system response to be sluggish with large overshoots - confirming the requirement for an inner loop TEC control system.

3. Chapter 5. We investigated the application of different simple controller types to our pyroelectric TEC system and found that simple PI control yields good closed-loop performance.

4. Chapter 6. We have shown that, for the particular UCLA experiment [74] case, the developed Simulink pyroelectric neutron generator model adequately captures the dominant non-linear system dynamics, and represents the available experimental data well.

5. Chapter 7. We designed a multiloop control system for a pyroelectric neutron generator device, where there is a PI inner control loop for the crystal temperature, and an outer control loop containing an I-only controller, with an external reset trigger and the tracking mode enabled, for the neutron output. The multiloop control system behaves in a suitable fashion, and the overall system has all the features of good closed-loop control (stability, accuracy, and simplicity). We have shown that pyroelectric neutron production can potentially be controlled, and an array of devices could be applied as a pulsed neutron source in a subcritical reactor.

8.3 Extensions to the model and control system design

Our major recommendations for model extension can be summarised in the following points:

1. Chapters 3-5. The TEC simulation results would benefit from thermal cycling validation experiments.

2. Chapters 3-5. A simulation comparison of paired crystal systems would indicate the potential dynamic advantages. It is anticipated that, due to the position of each crystal in a paired arrangement, they may require independent temperature control.

3. Chapter 6. The existing pyroelectric neutron generator devices are not yet optimal in their performance. We recommend further investigations into tip and target age-

ing, pressure control, and verification of the limit for the rate of change of crystal temperature.

4. Chapter 6. There is a lack of suitable identification data sets from pyroelectric neutron generator experiments, and, due to this, there is a risk that we have over-fitted our data. We recommend that further on-the-bench experiments are performed to provide a more extensive transient database for model cross-validation.

5. Chapter 6. The detector and geometrical considerations for the UCLA system have been identified; these parameters could be tuned to model other systems in the future.

6. Chapter 6. The geometry factor is arguably one of the weaker assumptions. It is obvious that this is required to reasonably replicate the system response, and more work will be required to substantiate this factor.

7. Chapter 6. Thermal gradients, charge leakage through the crystal, temperature dependence of material properties, parasitic capacitance, and spontaneous discharges all likely contribute to the slight discrepancies between the potential predicted by our model and the measured potential in the UCLA experiments.

8. Chapter 6. A question also remains as to the adaptivity of the model performance to capturing the system dynamics of different pyroelectric plant geometries and materials.

9. Chapter 7. When designing the multiloop control system, we assumed ideal temperature sensors and neutron detectors. It is recommended that the associated efficiencies or system dynamics are attributed to these components in the feedback loops to investigate the robustness of the control system design.

10. Chapter 7. The application of optimal control theory should be considered. A control law that maximises the neutron output, whilst constraining the TEC current and/or rate of change of crystal temperature, could improve the system performance.

11. Chapter 7. Lastly, the control system design and reactor application results presented will require validation with experiments at the VR-1 reactor.

8.4 Application of the pyroelectric neutron model

Some appreciation of the scope of the potential model application has been revealed during our studies. The main applications can be listed under two headings:

1. Pre-experimental analysis
   (a) simulation of experiments
   (b) predict critical areas and parameters
   (c) guidance for experimental design
2. Post-experimental analysis
   (a) interpretation and generalisation of results

The experimental data taken for model development and validation was the best available at the time, however limited. The existing data has indicated that consistent repeatable results could be possible with hardware improvements. It is thought that the future transition from the domain of research to that of nuclear reactor application will present significant challenges, including: geometry, scalability and material restrictions on hardware and component selection; integration of radiation-hardened and radiation-tolerant components, such as sensors and control circuits; self-containment of the device, and the ageing of the device.

References

[1] Amptek. XR-100CdTe X-ray & Gamma Ray Detector, 2019. URL http://amptek.com/products/xr-100cdte-x-ray-and-gamma-ray-detector/#5.

[2] J.R. Anderson. Thermoelectric air conditioner for submarines. *Advanced Energy Conversion*, 2:241–248, 1962.

[3] T. Anderson, R. Edwards, K. Bright, A. Kovanen, Y. Danon, B. Moretti, J. Musk, M. Shannon, and D. Gillich. Preliminary results from pyroelectric crystal accelerator. *AIP Conference Proceedings*, 1336, 2011.

[4] A.J. Antolak, A.X. Chen, K.N. Leung, D.H. Morse, and T.N. Raber. Radiatively heated high voltage pyroelectric crystal pulser. *Nuclear Instruments and Methods in Physics Research A*, 735:379–381, 2014.

[5] K.J. Astrom and T. Hägglund. Automatic tuning of simple regulators. *IFAC 9th World Congress, Budapest*, pages 1867–72, 1984.

[6] K.J. Astrom and T. Hägglund. Automatic tuning of simple regulators with specification on phase and amplitude margins. *Automatica*, 20:645–51, 1984.

[7] K.J. Astrom and T. Hägglund. A frequency domain method for automatic tuning of simple feedback loops. *23rd IEEE Conference on Decision and Control, Las Vegas*, pages 299–304, 1984.

[8] U. Bahr, U. Röhling, C. Lautz, K. Strupat, M. Schurenberg, and F. Hillenkamp. A charge detector for time-of-flight mass analysis of high mass ions produced by matrix-assisted laser desorption/ionization (MALDI). *International Journal of Mass Spectrometry and Ion Processes*, pages 9–21, 1996.

[9] S.P. Banks. *State-space and Frequency Domain Methods in the Control of Distributed Parameter Systems*. Peter Peregrinus Ltd, 1983.

[10] S.P. Banks. *Control Systems Engineering*. Prentice-Hall, 1986.

[11] M. Bayssie, J.D. Brownridge, N. Kukhtarev, T. Kukhtarev, and J.C. Wang. Generation of focused electron beam and x-rays by the doped $LiNbO_3$ crystals. *Nuclear Instruments and Methods in Physics Research B*, 241:913–916, 2005.

[12] T. Bily, J. Rataj, O. Humel, and O. Chvala. Effect of kinetics parameters on transient calculations in external source driven subcritical VR-1 reactor. *Annals of Nuclear Energy*, 123:97–108, 2019.

[13] P.F. Braunlich and J.P. Carrico. Feasibility study of exoelectron imaging as an NDT method for laser surface damage of nonlinear optical materials and laser glass. *Bendix Research Laboratories Semi-Annual Technical Report No. 1*, AFCRL-TR-73-0068: 97–108, 1973.

[14] J. Brownridge and S. Raboy. Pyroelectric response in $LiNbO_3$ and $LiTaO_3$ to temperature changes. *arXiv Physics e-prints*, 2001.

[15] J.D. Brownridge. Pyroelectric x-ray generator. *Nature*, 358:287–288, 1992.

[16] J.D. Brownridge and S.M. Shafroth. Using static charge on pyroelectric crystals to produce self–focusing electron and ion beams and transport through tubes. *Journal of Electrostatics*, 63:249–259, 2005.

[17] R.L. Byer and C.B. Roundy. Pyroelectric coefficient direct measurement technique and application to an nsec response time detector. *IEEE Trans. Sonics & Ultrasonics*, 3:333–338, 1972.

[18] R.P. Bywaters and H.A. Blum. The transient behavior of cascade thermoelectric heat pumps. *Energy Conversion*, 10:193–200, 1970.

[19] A.S. Chepurnov, V.Y. Ionidi, O.O. Ivashchuk, A.S. Kubankin, A.N. Oleinik, and A.V. Shchagin. Pyroelectric neutron generator for calibration of neutrino and dark matter detectors. *Journal of Physics: Conference Series*, 675:1–3, 2016.

[20] A.S. Chepurnov, V.Y. Ionidi, O.O. Ivashchuk, M.A. Kirsanov, E.P. Kitsyuk, A.A. Klenin, A.S. Kubankin, R.M. Nazhmudinov, I.S. Nikulin, A.N. Oleinik, A.A. Pavlov, A.V. Shchagin, and P.N. Zhukova. Compact neutron generator with nanotube ion source. *Journal of Instrumentation*, 13, 2018.

[21] A.J. Cohen and K.F. Korul. Backscattering and secondary-electron emission from metal targets of various thicknesses. *NASA Technical Note, NASA-TN-D-2782*, 1965.

[22] Kurt J. Lesker Company. Kurt J. Lesker Company, 2020. URL https://www.lesker.com/.

[23] Y. Danon. A novel compact pyroelectric x-ray and neutron source. *Rensselaer Polytechnic Institute, Final Technical Report, DOE NEER Grant DE-FG07-04ID14596*, 2007.

[24] Y. Danon. Pyroelectric crystal $D-D$ and $D-T$ neutron generators. *2nd International Workshop on Fast Neutron Detectors and Applications, Ein Gedi, Israel, November 6-11 2011*, 2011.

[25] Y. Danon and T. Fullem. Electrostatics of pyroelectric accelerators. *Journal of Applied Physics*, 106:74–101, 2009.

[26] A.M. Darbyshire and K.D. Atkinson. Identification and system parameter estimation methods for a pyrofusion neutron source. In *NPIC & HMIT 2017, San Francisco, CA, June 11-15*, pages 1983–1990, 2017.

[27] A.M. Darbyshire and K.D. Atkinson. A multi-mode state-space dynamic model for pyrofusion neutron sources. In *NPIC & HMIT 2017, San Francisco, CA, June 11-15*, pages 1972–1982, 2017.

[28] A.M. Daskalakis. Optimization of pyroelectric neutron generators. *MSc Thesis, Rensselaer Polytechnic Institute*, 2011.

[29] J. Duderstadt and L. Hamilton. *Nuclear Reactor Analysis*. Wiley and Sons, 1976.

[30] K. Dutton, S. Thompson, and B. Barraclough. *The Art of Control Engineering*. Prentice Hall, 1997.

[31] J.L. Ellsworth, V. Tang, S. Falabella, B. Naranjo, and S. Putterman. Neutron production using a pyroelectric driven target coupled with a gated field ionization source. In *22nd International Conference on the Application of Accelerators in Research and Industry, Forth Worth, TX, United States, 2-10 August 2012*, volume 1525, pages 128–132. LLNL, 2012.

[32] Control Engineering. Auto-tuning control using Ziegler-Nichols, 2019. URL https://www.controleng.com/articles/auto-tuning-control-using-ziegler-nichols/.

[33] T.A. Fox, R.A. Mueller, and D. Fieno. Pulsed-neutron-source studies with the NASA zero power reactor ii. *NASA Technical Note*, pages TN D–5956, 1970.

[34] G. Franklin, J.D. Powell, and A. Emami-Naeini. *Feedback Control of Dynamic Systems*. Pearson, 2015.

[35] J. Geuther, Y. Danon, F. Saglime, and B. Sones. Electron acceleration for x-ray production using paired pyroelectric crystals. *Sixth International Meeting on Nuclear Applications of Accelerator Technology, San Diego, California, United States, 1-5 June 2003*, pages 591–595, 2003.

[36] J.A. Geuther. Enhanced neutron production from pyroelectric fusion. *Applied Physics Letters*, 90:174103–1–3, 2007.

[37] J.A. Geuther. Applications of pyroelectric particle accelerators. *Nuclear Instruments and Methods in Physics Research B*, 261:110–113, 2007.

[38] J.A. Geuther. Radiation generation with pyroelectric crystals. *PhD Dissertation, Rensselaer Polytechnic Institute*, 2007.

[39] J.A. Geuther and Y. Dannon. Electron and positive ion acceleration with pyroelectric crystals. *Journal of Applied Physics*, 97:074109–1–5, 2005.

[40] J.A. Geuther and Y. Danon. Pyroelectric electron acceleration: Improvements and future applications. *DOE NEER: Highlights of Recent and Current Research -I*, 2003.

[41] D. Gillich, Y. Danon, G. Geuther, B. Marus, and B. McDermot. Deuterium ionization for pyroelectric crystal accelerators. *Detection Technologies for Homeland Security Applications*, pages 927–928, 2007.

[42] D. Gillich, Y. Danon, A. Kovanen, and B. Herman. Pyroelectric crystal-generated neutron production: Preliminary results using a portable vacuum system. *Transactions of the American Nuclear Society*, 99:283–284, 2008.

[43] D. Gillich, Y. Danon, A. Kovanen, B. Herman, and W. Labarre. Tip length optimization for a pyroelectric crystal neutron source. *Transactions of the American Nuclear Society*, 98:393–394, 2008.

[44] D. Gillich, A. Kovanen, B. Herman, T. Fullem, and Y. Danon. Pyroelectric crystal neutron production in a portable prototype vacuum system. *Nuclear Instruments and Methods in Physics Research Section A: Accelerators, Spectrometers, Detectors and Associated Equipment*, 602:306–310, 2009.

[45] D.J. Gillich. Particle acceleration with pyroelectric crystals. *PhD Dissertation, Rensselaer Polytechnique Institute*, 2009.

[46] S. Gotoh. Transfer function measurement of ionization chambers with the use of uncorrelated reactor noise. *Journal of Nuclear Science and Technology*, 3:359–362, 1966.

[47] P.E. Gray. *The Dynamic Behavior of Thermoelectric Devices*. John Wiley and Sons, Inc., 1960.

[48] D.L. Hetrick. *Dynamics of Nuclear Reactors*. American Nuclear Society, 1993.

[49] T. Hägglund and K.J. Astrom. Automatic tuning of PID controllers based on dominant pole design. *FDAC Adaptive Control of Chemical Processes, Frankfurt am Main*, pages 205–210, 1985.

[50] B.J. Huang and C.L. Duang. System dynamic model and temperature control of a thermoelectric cooler. *International Journal of Refrigeration*, 23:197–207, 2000.

[51] B.J. Huang, , C.J. Chin, and C.L. Duang. A design method of thermoelectric cooler. *International Journal of Refrigeration*, 23:208–218, 2000.

[52] Czech Technical University in Prague. Training reactor VR-1, 2019. URL http://www.reaktor-vr1.cz/en/.

[53] Del Mar Photonics Inc. Lithium tantalate crystal - material properties, 2019. URL http://www.dmphotonics.com/LiTaO3_crystal/Lithium%20Tantalate%20Crystal.htm.

[54] A. Kolros, O. Humel, M. Kriz, and J. Kos. Equipment for neutron measurements at VR-1 Sparrow training reactor. *Applied Radiation and Isotopes*, 68:570–574, 2010.

[55] A. Kovanen, Y. Danon, and D. Gillich. X-ray production using stacked pyroelectric crystals. *Transactions of the American Nuclear Society*, 98:406–407, 2008.

[56] K.S. Krane. *Introductory Nuclear Physics*. Wiley, 1988.

[57] A.S. Kubankin, A.S. Chepurnov, O.O. Ivashchuk, V.Y. Ionidi, I.A. Kishin, A.A. Klenin, A.N. Oleinik, and A.V. Shchagin. Optimal speed of temperature change of a crystal in a pyroelectric x-ray radiation source. *American Institute of Physics Advances*, 8:1–5, 2018.

[58] J. Kubatova and P. Pokorny. Combined measurements of thermostimulated processes in $LiNbO_3$ surfaces. *Proceedings of the 5th International Symposium Electrets, in Heidelberg, Germany, 4-6 September 1985*, pages 214–219, 1985.

[59] N. Kukhtarev, T. Kukhtareva, M. Bayssie, J. Wang, J.D. Brownridge, and V. Rotaru. Generation of focused electron beam and x-rays by pyroelectric and photogalvanic crystals. *Tenth International Conference on Nonlinear Optics of Liquid and Photorefractive Crystals*, 6026:113–122, 2005.

[60] N. Kukhtarev, T. Kukhtareva, J.C. Wang, J.D. Brownridge, and T. Hudson. Pyroelectric and photo-galvanic effects for generation of the focused electron beam, x-rays, photo-actuation and electric micro-propulsion. *ISE 12: 12th International Symposium on Electrets, Salvador, Bahia - Brazil, 11-14 September 2005*, pages 479–482, 2005.

[61] Los Alamos National Laboratory. A technical tour of the t-2 nuclear information service, 2019. URL http://t2.lanl.gov/nis/tour/u235nf.gif.

[62] S.B. Lang. Pyroelectricity: From ancient curiosity to modern imaging tool. *Physics Today, American Institute of Physics*, 66:31–36, 2005.

[63] K. Leung. Cylindrical neutron generator. *U.S. Patent No. 6,907,097 B2*, 2005.

[64] W.S. Levine. *The Control Handbook*. IEEE Press, 1996.

[65] MathWorks. Mathworks - MATLAB, 2019. URL https://uk.mathworks.com.

[66] Mathworks. What are Hammerstein-Wiener models?, 2019. URL https://uk.mathworks.com/help/ident/ug/what-are-hammerstein-wiener-models.html.

[67] Mathworks. pidtune, 2019. URL https://uk.mathworks.com/help/control/ref/pidtune.html.

[68] Mathworks. Pulse generator, 2019. URL https://uk.mathworks.com/help/simulink/slref/pulsegenerator.html.

[69] MathWorks. compare, 2020. URL https://uk.mathworks.com/help/ident/ref/compare.html.

[70] Meersetter. TEC / Peltier Element Design Guide, 2019. URL https://www.meerstetter.ch/compendium/tec-peltier-element-design-guide.

[71] T.A. Melhorn. NRL plasma formulary. *Naval Research Laboratory Publication, Washington, DC 20375-5320,NRL/PU/6790–18-640*, 2018.

[72] D.A. Moen. Reactor frequency response based on pulsed neutron technique. *Retrospective Theses and Dissertations*, 4490:1–142, 1971.

[73] M.S. Mohamed, M.G. Hassan, and A.A. Aly. An intelligent robust fuzzy temperature control of a thermoelectric cooler. *International Journal of Applied Engineering Research*, 13:1–7, 2018.

[74] B. Naranjo, J. Gimzewski, and S. Putterman. Observation of nuclear fusion driven by a pyroelectric crystal. *Nature*, 434:1115–1117, 2005.

[75] M.M. Nasseri. A virtual experiment on pyroelectric X-ray generator. *Nuclear Instruments and Methods in Physics Research B*, 358:255–257, 2015.

[76] A. Odon. Modelling and simulation of the pyroelectric detector using MATLAB/simulink. *Measurement Science Review*, 10,6:195–199, 2010.

[77] K. Ogata. *Modern Control Engineering*. Prentice-Hall, 2002.

[78] K.O. Ott and R.J. Neuhold. *Nuclear Reactor Dynamics*. American Nuclear Society, 1985.

[79] S. Pan, R.A. Gonzales, J.S. Welsh, and C.R. Rojas. Consistency analysis of the simplified refined instrumental variable method for continuous-time system. *Automatica*, 113:1–10, 2020.

[80] Roditi. Lithium tantalate properties, 2019. URL http://www.roditi.com/SingleCrystal/Lithium-Tantalate/LiTaO3-Properties.html.

[81] A. Rohatgi. WebPlotDigitizer, 2019. URL https://automeris.io/WebPlotDigitizer/.

[82] B. Rosenblum, P. Braunlich, and J.P. Carrico. Thermally stimulated field emission from pyroelectric $LiNbO_3$. *Applied Physics Letters*, 25:17–19, 1974.

[83] G.I. Rosenman, V.I. Pechorskii, Y.L. Chepelev, E.I. Boikova, and L.E. Issakova. Exoemission of pyroelectrics. *Physica Status Solidi (b) - Basic Solid State Physics*, 120, 1983.

[84] S. Schlesinger. Terminology for model credibility. *Simulation*, 32:103–104, 1979.

[85] S.M. Shafroth and J.D. Brownridge. Self-focused electron beams produced by pyroelectric crystals on heating or cooling in dilute gases. *Applied Physics Letters*, 79, 3364, 2001.

[86] S. Shaojing and Q. Qin. Temperature control of thermoelectric cooler based on adaptive NN − PID. *IEEE International Conference on Electrical and Control Engineering, Wuhan, China, 25-27 June 2010*, pages 2245–2248, 2010.

[87] S. Skogestad. Simple analytic rules for model reduction and PID controller tuning. *Journal of Process Control*, 13(4):291–309, 2003.

[88] W.M. Stacey. *Nuclear Reactor Physics*. Wiley-Vch, 2007.

[89] K. Sumita, Y.Kaneko, R. Kurokawa, T. Adachi, K. Ogawa, and K. Miyoshi. A pulsed neutron source for thermal reactor physics. *Journal of Nuclear Science and Technology*, 4:328–338, 2012.

[90] V. Tang, G. Meyer, G. Schmid, C. Spadaccini, P. Kerr, B. Rusnak, S. Sampayan, B. Naranjo, and S. Putterman. Neutron production from feedback controlled thermal cycling of a pyroelectric crystal stack. *LLNL Review of Scientific Instruments*, UCRL-JRNL-233604:1–13, 2007.

[91] V. Tang, G. Meyer, S. Falabella, G. Guethlein, S. Sampayan, P. Kerr, B. Rusnak, and J. Morse. Intense pulsed neutron emission from a compact pyroelectric driven accelerator. *Journal of Applied Physics*, 105(026103), 2009.

[92] V. Tang, J. Morse, G. Meyer, S. Falabella, G. Guethlein, P. Kerr, H.G. Park, B. Rusnak, S. Sampayan, G. Schmid, C. Spadaccini, and L. Wang. Crystal driven neutron source: A new paradigm for miniature neutron sources. *Conference on Accelerator Applications in Research and Industry*, 1099:870–873, 2009.

[93] Ferro Tec. Thermoelectric technical reference, 2019. URL https://thermal.ferrotec.com/technology/thermoelectric-reference-guide.

[94] W. Tornow. Production of 14 MeV neutrons using pyroelectric crystals: Reconverting solar energy into nuclear fusion energy. *International Journal of Energy Sciences (IJES)*, 4:101–107, 2014.

[95] W. Tornow, S. M. Shafroth, and J. D. Brownridge. Evidence for neutron production in deuterium gas with a pyroelectric crystal without tip. *Journal of Applied Physics*, 104: 034905–1–8, 2008.

[96] W. Tornow, W. Corse, S. Crimi, and J. Fox. Neutron production with a pyroelectric double-crystal assembly without nano-tip. *Nuclear Instruments and Methods in Physics Research A*, 624:699–707, 2010.

[97] J.G. Truxal. *Control Engineers' Handbook*. McGraw-Hill Book Company, 1958.

[98] A. Tsai and C. Cui. *Handbook of Crystal Growth: Crystal Growth of Quasicrystals*. Elsevier, 2015.

[99] L.E. Weaver. *Reactor Dynamics and Control State Space Techniques*. American Elsevier Publishing Company, Inc., 1968.

[100] R.W. Whatmore. Pyroelectric devices and materials. *Reports on Progress in Physics*, 49(12):1335–1386, 1986.